

https://dspace.org/

The compressible shear layer of a Mach Reflection

Hall, Russell Edward

2016-10-11
http://hdl.handle.net/10539/21157

Downloaded from a DSpace repository. https://dspace.org/

The Compressible Shear Layer of a Mach Reflection

Russell Edward Hall

A dissertation submitted to the Faculty of Engineering and the Built Environment, University of the Witwatersrand, Johannesburg, in fulfilment of the requirements for the degree of Master of Science in Engineering.

Johannesburg, May 2016

Declaration

I declare that this dissertation is my own, unaided work, except where otherwise acknowledged. It is being submitted for the degree of Master of Science in Engineering in the University of the Witwatersrand, Johannesburg. It has not been submitted before for any degree or examination at any other university.

Signed this 5th day of May 2016

Russell Edward Hall

This dissertation is dedicated to my parents

Brian and Sue

who have always encouraged, supported and motivated me throughout my studies

Acknowledgements

I would like to thank my supervisor Professor B. W. Skews for his advice, guidance and supervision for this dissertation. I really appreciated the countless discussions regarding this topic and various other compressible flow phenomena. Thank you for instilling in me the patience required for the experimental work as well as for allowing me the freedom to conduct the research in a direction that interested me. It was a privilege to present aspects of this work at an international conference.

Thanks also go to Mr R. T. Paton for introducing me to the field of compressible gas dynamics during my undergraduate vacation work. Thank you for the use of the excellent LaTeX template used to produce this document and for assistance with the experimental and computational work throughout. Thank you for always encouraging me during the challenging times and for the insightful comments on this topic.

To the NWE Workshop Staff: huge thanks are owed for the excellent manufacture of the test pieces used during the study. Special mention goes to Mr S. Riekert and Mr M. van Wyk for assistance throughout the design process of the wedges and for their manufacturing expertise.

To Mr M. F. Boer: thank you for helping with the preparation of the large scale test pieces and for the motivation throughout. To my colleagues at the university: Dean, Matthew, Bright and Brendan, thank you for the help with the experimental setup and for the numerous discussions regarding this topic.

A final thank you goes to my parents who have always supported and encouraged me throughout my studies.

Abstract

The Mach Reflection occurring in pseudo-steady flows has been studied for well over a century. A Mach Reflection consists of incident and reflected shocks, a Mach stem and a shear layer. Three Shock Theory proposed by von Neumann in the 1940's shows good agreement to experimental data in the strong shock domain ($M_s > 2$) however, poor agreement is obtained in the weak shock domain ($M_s < 1.5$).

A pseudo-steady Single Mach Reflection (SMR) was studied in a large scale facility for a single wedge angle, a complimentary study was undertaken in a conventional shock tube over a wide range of wedge angles. The Mach numbers used were in the range $1.27 \leq M_s \leq 1.59$ and the wedge angles $25^\circ \leq \theta_w \leq 38^\circ$. A shadowgraph flow visualisation system was used in conjunction with a single shot camera to obtain high resolution images. Various shock angles were measured as well as the triple point trajectory from the leading edge of the wedge. As expected, poor agreement to Three Shock Theory was obtained in the current (M_s, θ_w) domain.

The spread angle of the shear layer was measured from the triple point. An oblique shock analysis was used to obtain the theoretical velocity and density ratio across the shear layer as well as other properties such as shear velocity (ΔU) and convective Mach number (M_c). The analysis revealed that the effect of compressibility on the growth of the shear layer was negligible. The spread angle increased with increasing incident shock strength and wedge angle. A comparison to the theoretical models of Papamoschou and Rikanati et al. showed good agreement for some wedge angles and intermediate Mach numbers. Recommendations for future work include increasing the Mach number and wedge angle range as well as the implementation of different flow visualisation setups.

Published Work

Aspects of this thesis have been published in the following reference:

- Hall, R. E., Skews, B. W. (2015) *The Compressible Shear Layer of a Mach Reflection*; in *Proceedings of the 30th International Symposium on Shock Waves*; Tel-Aviv, Israel; Springer Berlin Heidelberg (In Press).

Contents

Declaration i

Acknowledgements iii

Abstract iv

Published Work v

Contents vi

List of Figures x

List of Tables xvii

List of Acronyms xviii

1 Introduction 1

1.1 Shock Waves in Gases 2

1.2 Shock Wave Reflection 2

1.2.1 Transition criteria for Mach Reflection types 5

1.2.2 Oblique Shock Theory 8

1.3 Three Shock Theory 10

1.3.1 Modifications to Three Shock Theory 13

1.4 Shock Polars 22

1.5 Previous work by Rubidge 23

1.6 Motivation 25

2 Literature Survey **26**

2.1 Shock Tubes 26

2.2 Flow Visualisation 28

2.3 Compressible Shear Layers 29

2.3.1 Introduction 29

2.3.2 Previous Experimental Work and Development on Shear Layers 30

2.3.3 The Kelvin Helmholtz Instability 46

3 Objectives **50**

4 Experimental Facilities and Method **51**

4.1 Overview 51

4.2 The Large Blue Shock Tube (LBST) 51

4.2.1 Overview of the LBST 51

4.2.2 LBST Test Pieces 52

4.2.3 Operating Procedure of the LBST 53

4.2.3.1 Start up procedure 53

4.2.3.2 Testing procedure 53

4.2.3.3 Shut down procedure 55

4.2.3.4 Precautions . . . 55
4.3 The Michael Seitz Automated Shock Tube (MSAST) . . . 56
4.3.1 Overview of the MSAST . . . 56
4.3.2 MSAST Test Pieces . . . 58
4.3.3 Operating Procedure of the MSAST . . . 58
4.3.3.1 Start up procedure . . . 58
4.3.3.2 Testing procedure . . . 59
4.3.3.3 Shut down procedure . . . 59
4.3.3.4 Precautions . . . 60
4.4 Optical Visualisation . . . 61

5 Numerical Method **63**

5.1 Computational Fluid Dynamics . . . 63
5.1.1 Physical Geometry . . . 63
5.1.2 Mesh . . . 64
5.1.3 Settings . . . 64
5.1.3.1 Solver Settings . . . 65
5.1.3.2 Solution Initialisation . . . 65
5.1.3.3 Preliminary Results and Wedge Angle Selection . . . 66

6 Results and Discussion **67**

6.1 Experimental Results . . . 67
6.1.1 LBST Experimental Results . . . 67
6.1.2 MSAST Experimental Results . . . 73

6.1.3 Comparison of LBST and MSAST Results 86
6.2 Three Shock Theory for Mach Reflection 88
6.2.1 Ben-Dor 1987 Validation 88
6.2.2 Comparison of Three Shock Theory to Experimental Results 94
6.2.3 Theoretical results for Complimentary Wall Angle ($\theta_w + \chi$) 96
6.3 Oblique Shock Analysis: MSAST Experimental Results 98
6.4 Shear Layer Growth Calculations 103
6.4.1 Spread Angle Comparison to Experimental Results 106

7 Conclusions **110**

8 Recommendations for Future Work **112**

References **114**

A Detailed Test Piece Drawings **117**

A.1 LBST Test Pieces 117
A.2 MSAST Test Pieces 125

B MSAST Experimental Images **137**

C Supplementary Three Shock Theory Results **142**

D Digital Appendix **146**

List of Figures

1.1 Galilean transformation of a shock wave from the laboratory to stationary shock reference frame [1] 2

1.2 Possible shock wave reflections as classified in Ben-Dor [1] 3

1.3 (a) Regular Reflection (RR), (b) Mach Reflection (Mach Reflection (MR)) . . 3

1.4 Illustration of MR types (a) Direct Mach Reflection (DiMR) (b) Stationary Mach Reflection (StMR) (c) Inverse Mach Reflection (InMR), adapted from Ben-Dor [1] 4

1.5 The shock wave reflection process model[1]. Schematic showing effect of M_1^L on the pressure jump 5

1.6 Single Mach Reflection (SMR)[1] 6

1.7 Transitional Mach Reflection (TMR)[1] 6

1.8 Experimental verification of analytical transition criteria for imperfect Nitrogen and other gases. $P_0 = 15$ torr, $T_0 = 300$K[2] 7

1.9 Oblique shock wave parameters[1] 8

1.10 Mach Reflection occurring on a plane wedge 10

1.11 Three Shock Theory schematic with definition of parameters 11

1.12 Definition of parameters used in Skews[8] 13

1.13 Variation of incidence angle with reflection angle for $\xi = 0.8$[8] 14

1.14 Various solution types for values of F with θ_e as a parameter[8] 16

1.15 Limit curves for values of ϵ [8] 16

1.16 Zoomed in shadowgraph of the DMR analysed by Ben-Dor[10, 11]. $M_s = 2.71 \pm 0.01$, $\theta_w = 47.1°$, $T_0 = 296$K, $p_0 = 760$ torr and $\chi = 3° \pm 0.5°$. 17

1.17 Pressure behind the reflected shock (P_{20}) vs Complimentary Wall Angle ($\theta_w + \chi$) as a function of Mach number. Solid lines indicate Three Shock Theory calculated theoretically[12] 19

1.18 Measured shock angles with dashed line calculated from three shock theory[12] (a) ω_{IR} (b) ω_{IM} 19

1.19 Normalised minimum experimental error values with mean value indicated by a dashed line[12] (a) Pressure difference (b) θ difference 20

1.20 Measured shock angles with dashed line calculated from three shock theory and line T from the modified theory[12] (a) ω_{IR} (b) ω_{IM} 21

1.21 Modified three shock theory proposed by Olim and Dewey[12] 21

1.22 Shock Polar solution of a Single Mach Reflection[1] 22

1.23 Kelvin-Helmholtz Instability (KHI) occurring along a Mach reflection shear layer for a 30° wedge, $M_s = 1.61$ [13] 24

1.24 Shear layer average width [13] 24

2.1 Shock tube initial conditions before diaphragm burst [3] 27

2.2 Shock tube after diaphragm burst [3] 27

2.3 Schematic layout of a typical monochrome schlieren visualisation system (adapted from Kleine[16]) 28

2.4 Schematic of a plane shear layer with definition of some parameters (adapted from Brown and Roshko[17]) 29

2.5 Plane mixing layer [17] 30

2.6 Shadowgraph of mixing layer showing measurement of growth rate [17] 31

2.7 Shadowgraph of mixing layer for density ratio of 7 [17] 31

2.8 Shear layer growth rates (filled symbols represent visual growth rates from experimental photographs) [17] 33

2.9 Vorticity thickness vs λ for $s = 1$ [17] 33

2.10 Experimental apparatus (a) Parallel to shear layers (b) Normal to shear layers (c) Magnification of nozzle exits [19] 35

2.11 Shear layer spreading rates $\delta_{\rho m}$ vs ϕ with λ_ρ as a parameter [19] 36

2.12 Vortex reference frame showing large structures and induced velocities [20] . . 37

2.13 Vorticity (maximum slope) thickness for $s = 1/7, 1, 7$ [20] 39

2.14 Experimental apparatus ($M_2 = 1.4$ test conditions) [21] 40

2.15 Spreading rate variation with M_1 [21] 41

2.16 Spreading rate variation with λ [21] 41

2.17 Experimental apparatus [22] 42

2.18 Visual thickness growth rate versus $\Delta U/U_c$ [22] 45

2.19 Normalised pitot thickness growth rate versus M_{c_1} [22] 45

2.20 Growth rates as a function of S [24] with data from Brown and Roshko[17]. Dotted lines from Dimotakis[20] 47

2.21 Spread angle of the shear layer as a function of Mach number [14] 49

4.1 Large Blue Shock Tube Schematic 51

4.2 Schematic of the Michael Seitz Automated Shock Tube (MSAST) 56

4.3 Flow Visualisation Layout 62

5.1 A typical geometry for a 30° Wedge 63

5.2 Refined mesh in the vicinity of the triple point for a 30° Wedge, $M_s = 1.46$. 64

5.3 Contours of density of a Single Mach Reflection occurring on a 30° Wedge, $M_s = 1.61$ 66

6.1 Shear layer development for the 30° Wedge. $M_s = 1.37$. (a) $3100\mu s$, (b) $3200\mu s$, (c) $3300\mu s$, (d) $3350\mu s$, (e) $3400\mu s$, (f) $3600\mu s$, (g) $3800\mu s$ 69

6.2 Shear layer development for the 30° Wedge. $M_s = 1.44$. (a) $3000\mu s$, (b) $3100\mu s$, (c) $3150\mu s$, (d) $3200\mu s$, (e) $3300\mu s$, (f) $3400\mu s$ 70

6.3 Measured Shear Layer Thickness from the LBST 71

6.4 Shear layer development for the 30° Wedge. $M_s = 1.27$. (a) $3800\mu s$, (b) $4000\mu s$, (c) $4200\mu s$, (d) $4400\mu s$, (e) $4600\mu s$, (f) $4800\mu s$ 72

6.5 Single Mach Reflection with highlighted features (Incident Shock, Reflected Shock, Mach Stem, Triple Point Trajectory - Black, Wedge Surface - White): (a) $\theta_w = 25°$. $M_s = 1.585$, Time Delay: $1550\mu s$ (b) $\theta_w = 30°$. $M_s = 1.583$, Time Delay: $1550\mu s$ 74

6.6 Shear layer development for the 25° Wedge. Corresponding Incident Shock Mach number and time delay: (a) $M_s = 1.309$, $1925\mu s$ (b) $M_s = 1.447$, $1750\mu s$ (c) $M_s = 1.585$, $1550\mu s$. Shear layer development for the 30° Wedge: (d) $M_s = 1.309$, $1900\mu s$ (e) $M_s = 1.441$, $1700\mu s$ (f) $M_s = 1.583$, $1550\mu s$ . . . 75

6.7 Single Mach Reflection with highlighted features (Incident Shock, Reflected Shock, Mach Stem, Triple Point Trajectory - Black, Wedge Surface - White): (a) $\theta_w = 35°$. $M_s = 1.587$, Time Delay: $1550\mu s$ (b) $\theta_w = 38°$. $M_s = 1.593$, Time Delay: $1500\mu s$ 76

6.8 Shear layer development for the 35° Wedge. Corresponding Incident Shock Mach number and time delay: (a) $M_s = 1.313$, $1925\mu s$ (b) $M_s = 1.447$, $1750\mu s$ (c) $M_s = 1.587$, $1550\mu s$. Shear layer development for the 38° Wedge: (d) $M_s = 1.304$, $1850\mu s$ (e) $M_s = 1.442$, $1650\mu s$ (f) $M_s = 1.593$, $1500\mu s$ . . . 77

6.9 (a) $\theta_w = 35°$, $M_s = 1.587$ Original Image (b) Image corrected for grid distortion with virtual grid overlaid in red 79

6.10 Schematic of measured angles 80

6.11 χ vs M_s 81

6.12 ω_{IR} vs M_s 82

6.13 ω_{RS} vs M_s 82

6.14 ω_{IM} vs M_s 83

6.15 ω_{MS} vs M_s 84

6.16 θ_E vs M_s 84

6.17 ω_{IR} vs $\theta_w + \chi$ 85

6.18 ω_{IM} vs $\theta_w + \chi$ 85

6.19 Comparison of facility wedge sizes (dimensions in mm) 86

6.20 Comparison of SMR's obtained at $M_s = 1.44$ in the (a) LBST (b) MSAST . . 86

6.21 Confluence of three shocks at the triple point of a Mach Reflection with definition of angles and flow regions 89

6.22 Shock Polar representation of Ben-Dor's data 91

6.23 Shock Angle (ϕ) vs Shear Layer Divergence (ϵ) 91

6.24 Shock Angle (ϕ) vs M_{03} 92

6.25 Reflected Shock Angle (ϕ_1) vs Velocity and Density Ratio 93

6.26 Comparison of experimental shock angles to Three Shock Theory for ω_{IR} . . 95

6.27 Comparison of experimental shock angles to Three Shock Theory for ω_{IM} . . 95

6.28 Triple Point Trajectory (χ) vs Complimentary Wall Angle ($\theta_w + \chi$) for $M_s = 1.30$ 96

6.29 Flow Mach Number vs Complimentary Wall Angle ($\theta_w + \chi$) for $M_s = 1.30$ . . 97

6.30 Shock Angle (ϕ) vs Complimentary Wall Angle ($\theta_w + \chi$) for $M_s = 1.30$ 97

6.31 Pressure difference across the shear layer 98

6.32 Divergence across the Shear Layer 99

6.33 Velocity difference across the Shear Layer 100

6.34 Convective Mach Number 100

6.35 Velocity Ratio across the Shear Layer 102

6.36 Density Ratio across the Shear Layer 102

6.37 Visual Growth Rate (δ'_{viz}) vs λ 104

6.38 Convective Velocity Ratio (r_c) vs Velocity Ratio (r) 104

6.39 Visual Growth Rate (δ'_{viz}) vs Convective Velocity Ratio (r_c) 105

6.40 Visual Growth Rate (δ'_{viz}) vs Density Ratio (s) 106

6.41 Visual Growth Rate (δ'_{viz}) comparison to theory from Papamoschou and Roshko[22] 107

6.42 Spread angle comparison to theory from Papamoschou and Roshko[22] 109

6.43 Spread angle comparison to theory from Rikanati et al.[14] 109

A.1 30° Wedge Assembly 118

A.2 30° Wedge Rear Support Assembly 119

A.3 30° Wedge Channel 120

A.4 30° Wedge Attachment Foot 121

A.5 30° Wedge Corner Attachment Foot 122

A.6 30° Wedge Channel Attachment Foot 123

A.7 30° Wedge Rear Support 124

A.8 25° Wedge Model 126

A.9 25° Wedge Model CNC Path 127

A.10 25° Wedge Model Mounting Holes 128

A.11 30° Wedge Model Modification 129

A.12 30° Wedge Model Modification Side View 130

A.13 35° Wedge Model 131

A.14 35° Wedge Model CNC Path 132

A.15 35° Wedge Model Mounting Holes 133

A.16 The 25° and 35° Wedge Spacer 134

A.17 38° Wedge Model 135

A.18 The 38° Wedge Spacer 136

B.1 Single Mach Reflection with highlighted features for the $\theta_w = 25°$ wedge (Incident Shock, Reflected Shock, Mach Stem, Triple Point Trajectory - Black, Wedge Surface - White): (a) $M_s = 1.309$, Time Delay: $1925\mu s$ (b) $M_s = 1.447$, Time Delay: $1750\mu s$ 138

B.2 Single Mach Reflection with highlighted features for the $\theta_w = 30°$ wedge (Incident Shock, Reflected Shock, Mach Stem, Triple Point Trajectory - Black, Wedge Surface - White): (a) $M_s = 1.309$, Time Delay: $1900\mu s$ (b) $M_s = 1.441$, Time Delay: $1700\mu s$ 139

B.3 Single Mach Reflection with highlighted features for the $\theta_w = 35°$ wedge (Incident Shock, Reflected Shock, Mach Stem, Triple Point Trajectory - Black, Wedge Surface - White): (a) $M_s = 1.313$, Time Delay: $1925\mu s$ (b) $M_s = 1.447$, Time Delay: $1750\mu s$ 140

B.4 Single Mach Reflection with highlighted features for the $\theta_w = 38°$ wedge (Incident Shock, Reflected Shock, Mach Stem, Triple Point Trajectory - Black, Wedge Surface - White): (a) $M_s = 1.304$, Time Delay: $1850\mu s$ (b) $M_s = 1.442$, Time Delay: $1650\mu s$ 141

C.1 Triple Point Trajectory (χ) vs Complimentary Wall Angle ($\theta_w + \chi$) for $M_s = 1.44$ 143

C.2 Triple Point Trajectory (χ) vs Complimentary Wall Angle ($\theta_w + \chi$) for $M_s = 1.585$ 143

C.3 Flow Mach Number vs Complimentary Wall Angle ($\theta_w + \chi$) for $M_s = 1.44$ . . 144

C.4 Flow Mach Number vs Complimentary Wall Angle ($\theta_w + \chi$) for $M_s = 1.585$. 144

C.5 Shock Angle (ϕ) vs Complimentary Wall Angle ($\theta_w + \chi$) for $M_s = 1.44$ 145

C.6 Shock Angle (ϕ) vs Complimentary Wall Angle ($\theta_w + \chi$) for $M_s = 1.585$ . . . 145

List of Tables

1.1 Comparison of results for analytical three shock theory model by Law and Glass[7] to experimental results 12

1.2 Comparison of results for analytical three shock theory models to experimental results for Figure 1.16 18

4.1 Large Blue Shock Tube (LBST) Specifications 52

4.2 LBST Test piece dimensions 53

4.3 Michael Seitz Automated Shock Tube (MSAST) Specifications 57

4.4 MSAST Test piece dimensions 58

4.5 Flow Visualisation Equipment Specifications 61

4.6 Flow Visualisation Layout Specifications 62

5.1 Pressure Inlet Initial Conditions 65

5.2 Preliminary CFD Results for the LBST 66

6.1 Measured angles and calculated shear layer data 71

6.2 Comparison of Ben-Dor's[10] results to the numerical code 93

List of Acronyms

CFD Computational Fluid Dynamics.

KHI Kelvin-Helmholtz Instability.

LBST Large Blue Shock Tube.

MR Mach Reflection.

MSAST Michael Seitz Automated Shock Tube.

SMR Single Mach Reflection.

TMR Transitional Mach Reflection.

TST Three Shock Theory.

Chapter 1 Introduction

This chapter serves as a general introduction to the dissertation. The broad topic is the compressible shear layer of a Mach Reflection (MR). The general laws governing the propagation of shock waves in gases is described and the relevant reflection types that have been classified by Ben-Dor [1] for pseudo-steady flows are covered in detail. A detailed review of three shock theory is provided and modifications to the theory are covered. The most recent work undertaken in the research area is discussed.

1.1 Shock Waves in Gases

A shock wave is a discontinuity through which an abrupt change in pressure, temperature and density occur. Steady flow concepts can be applied to a moving shock wave (often studied in the laboratory) by attaching a frame of reference to it. The flow field is then known as pseudo-steady, this is shown in Figure 1.1. A shock wave propagates with constant velocity V_s from left to right into a fluid of velocity V_i with induced velocity V_j behind it. By imposing a velocity equal to the shock velocity on the flow field the shock is brought to rest and allows for steady flow theories to be utilised for analysis.

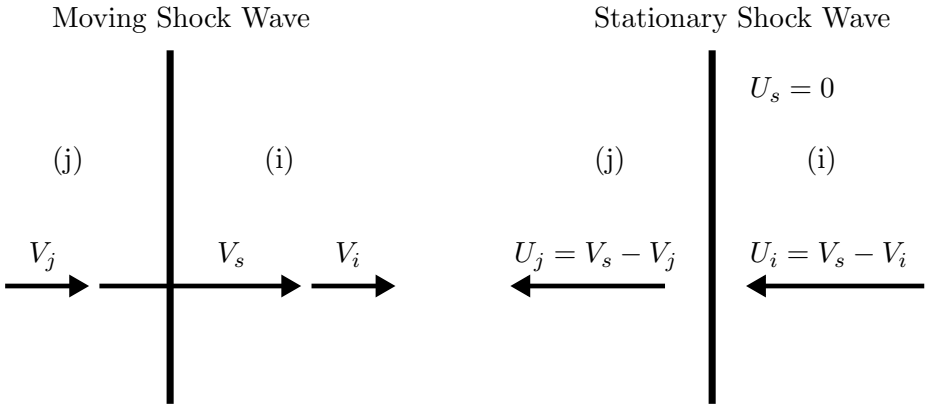


Figure 1.1: Galilean transformation of a shock wave from the laboratory to stationary shock reference frame [1]

1.2 Shock Wave Reflection

When a supersonic flow encounters a change in surface geometry a shock wave reflection takes place to maintain boundary conditions. The reflection can take many forms and is formally classified into three categories depending on the flow, namely: steady, pseudo-steady and unsteady reflections [1]. Shown in Figure 1.2 are the possible reflection types that can occur, where those not pertinent to this study have been greyed out.

In general, the reflections either take the form of a Regular Reflection (RR) or an Irregular Reflection (IR). A RR consists of two shock waves, namely the incident (i) and reflected (r) shocks. IR is divided into two sub-domains where the reflection either takes the form of a MR or falls into the so called weak shock domain of von Neumann Reflection (vNR), Vasilev Reflection (VR) or Guderley Reflection (GR). A Mach Reflection (MR) consists of three shock waves namely the incident shock (i), reflected shock (r) and Mach stem (m) that meet at the triple point (t). A slipstream (s) exists due to flow passing through the incident and reflected shocks differing to the flow passing through the Mach stem (m). The Mach stem

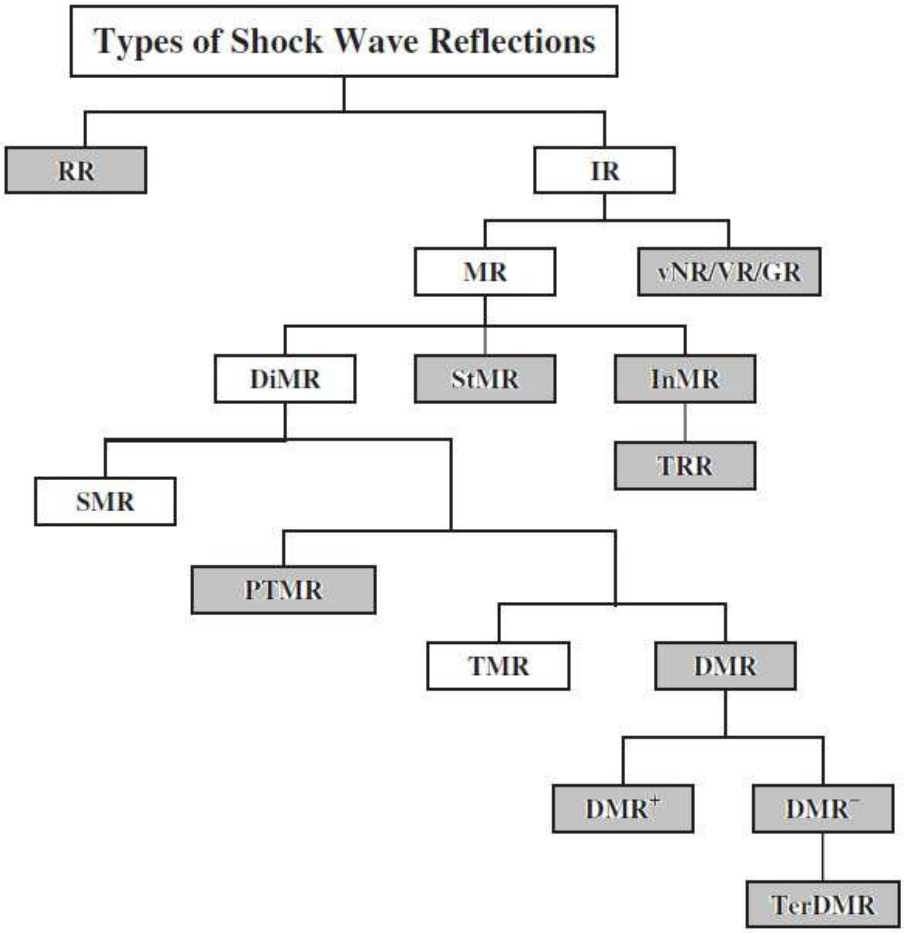


Figure 1.2: Possible shock wave reflections as classified in Ben-Dor [1]

may be curved along its length but meets the wedge surface perpendicularly at the reflection point (R). Experimentally it is slightly inclined due to the presence of the viscous boundary layer growing on the wedge surface. Shown in Figure 1.3 is a schematic of a RR and MR:

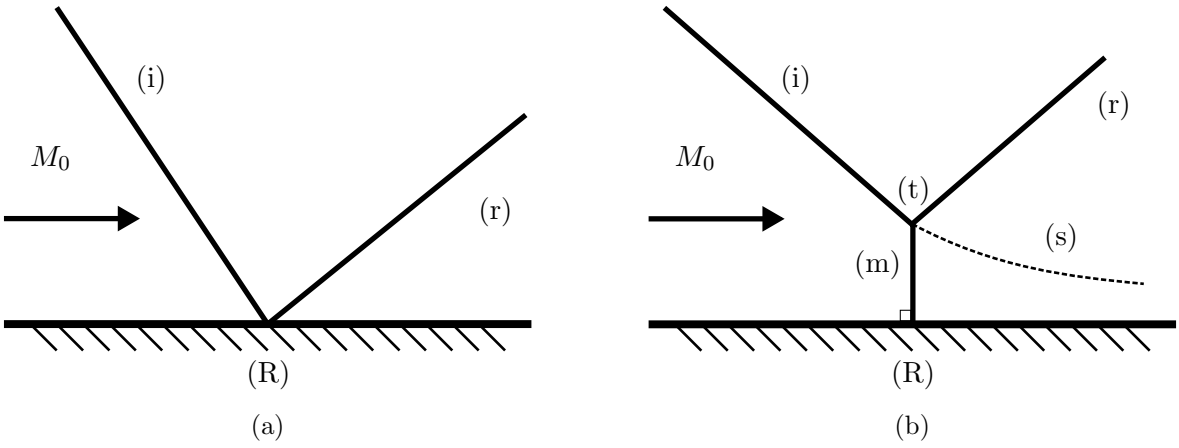


Figure 1.3: (a) Regular Reflection (RR), (b) Mach Reflection (MR)

There are three possible MR configurations depending on the triple point trajectory shown in Figure 1.4. If the triple point moves away from the reflecting surface it is known as a Direct Mach Reflection (DiMR), if it moves parallel it is known as a Stationary Mach Reflection (StMR) and if it moves towards the reflecting surface it is known as a Inverse Mach Reflection (InMR).

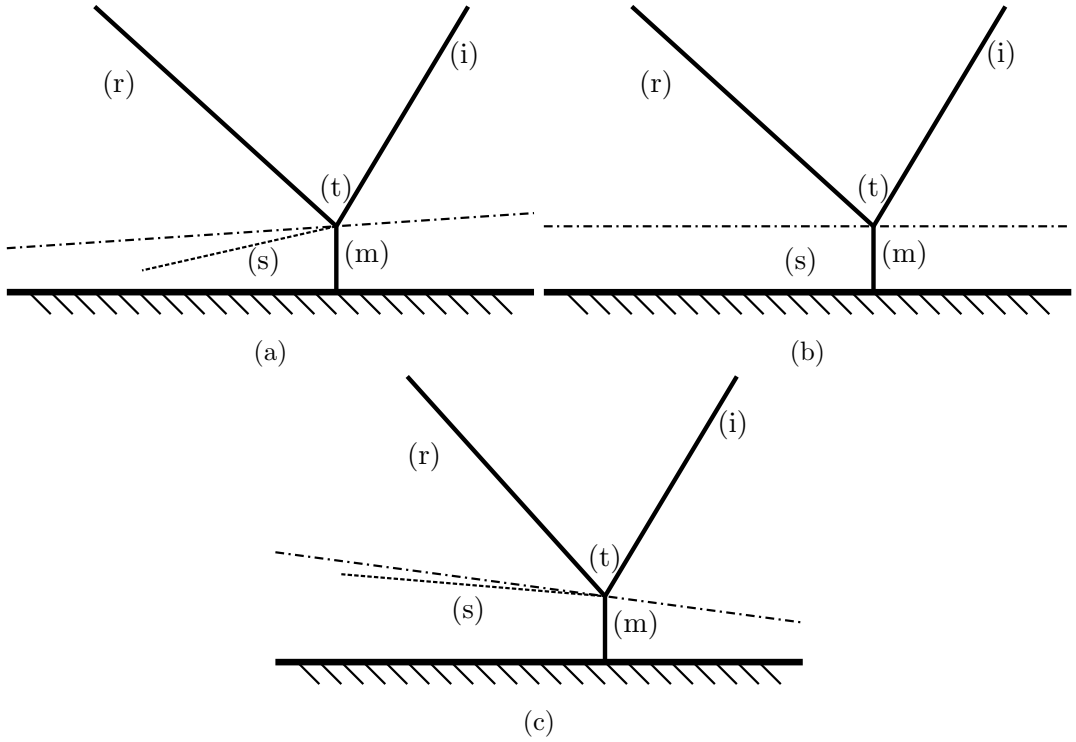


Figure 1.4: Illustration of MR types (a) Direct Mach Reflection (DiMR) (b) Stationary Mach Reflection (StMR) (c) Inverse Mach Reflection (InMR), adapted from Ben-Dor [1]

The process of shock wave reflection consists of two sub-processes [1], namely:

- The reflection of the planar shock wave over the reflecting surface: *Shock-reflection*
- The deflection of the shock-induced flow around the reflecting surface: *Flow-deflection*

A simple case of the sub-process interaction is shown in Figure 1.5. The reflection type is a Mach reflection formed on a plane wedge. The bow shock (B) forms upstream of the wedge and extends to point b due to the flow deflection process. The Mach reflection assumes its usual form with incident (i) and reflected (r) shock, Mach stem (m) and shear layer (not shown). The pressure behind the reflected shock and Mach stem is constant in region (2). In the laboratory reference frame the incident shock strength is M_s and the shock-induced flow Mach number is M_1^L. The dotted line is the boundary between the two sub-processes and interaction is dependent on M_1^L:

- $p_b < p_2$: The pressure gap is bridged by an expansion band propagating towards (2)
- $p_b > p_2$: The pressure gap is bridged by a compression band propagating towards (2)

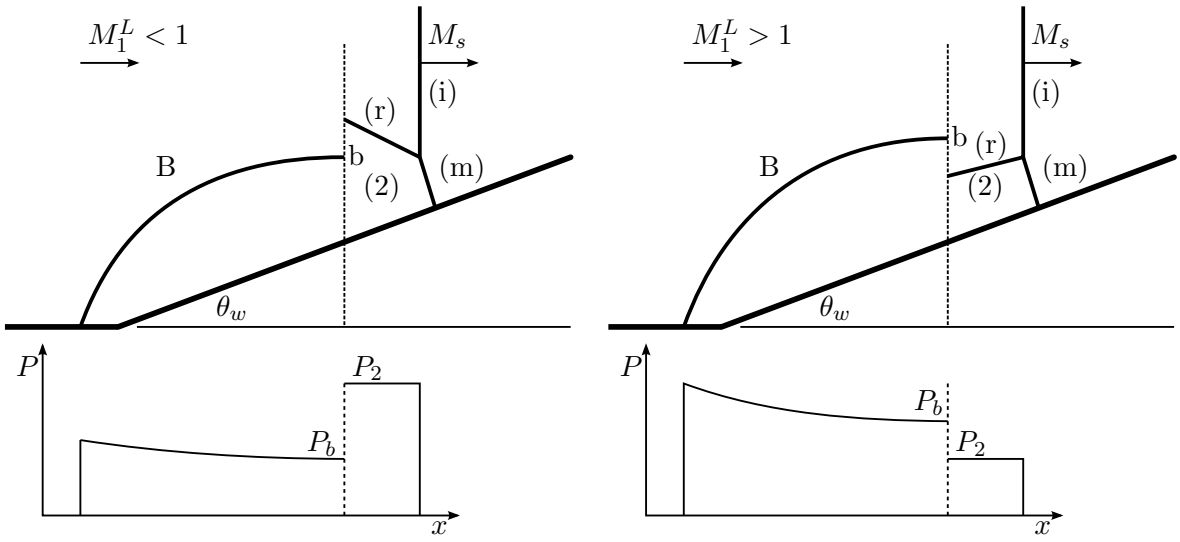


Figure 1.5: The shock wave reflection process model[1]. Schematic showing effect of M_1^L on the pressure jump

1.2.1 Transition criteria for Mach Reflection types

Ben-Dor and Glass[2] were the first to classify the domains of pseudo-steady shock wave reflection over a Mach number range of $2 \leq M_s \leq 8$ and for wedge angles ranging between $2° \leq \theta_w \leq 60°$. Irregular Reflection for strong incident shocks can be classified into three domains, namely: Single Mach Reflection (SMR), Transitional Mach Reflection (TMR) and Double Mach Reflection (DMR) (DMR is beyond the scope of this thesis).

The transition criteria are as follows[2]:

- When the flow downstream is subsonic with respect to the triple point ($M_{2t} < 1$), a SMR (shown in Figure 1.6) occurs
- When the flow downstream is supersonic with respect to the triple point ($M_{2t} = 1$), a kink (k) forms in the reflected shock and a TMR (shown in Figure 1.7) occurs
- When the flow downstream is supersonic with respect to the kink (k) ($M_{2k} = 1$), a DMR occurs

Using the above mentioned transition criteria, Ben-Dor and Glass verified these transitions experimentally[2] with the inclusion of real-gas effects. This is shown in the (M_s,θ_w) plane (in Figure 1.8) for imperfect Nitrogen (a diatomic gas) with other experimental results included.

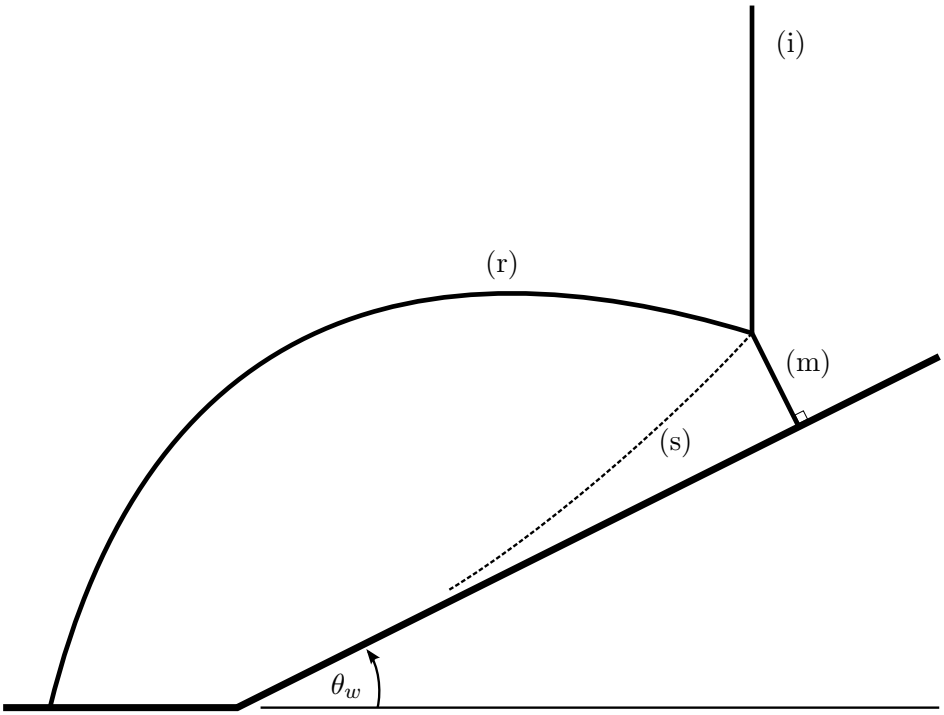


Figure 1.6: Single Mach Reflection (SMR)[1]

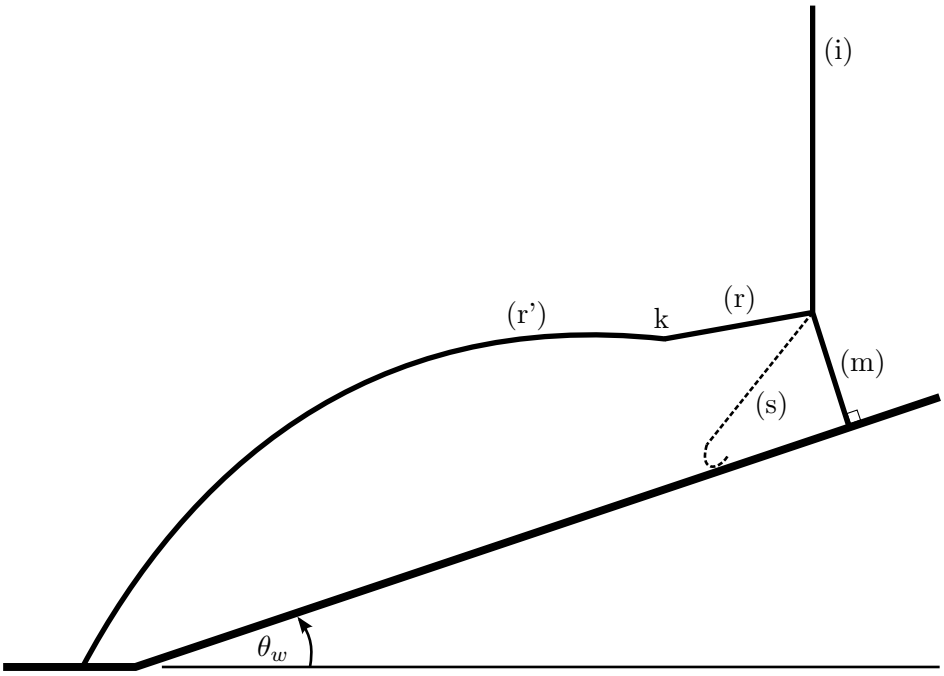


Figure 1.7: Transitional Mach Reflection (TMR)[1]

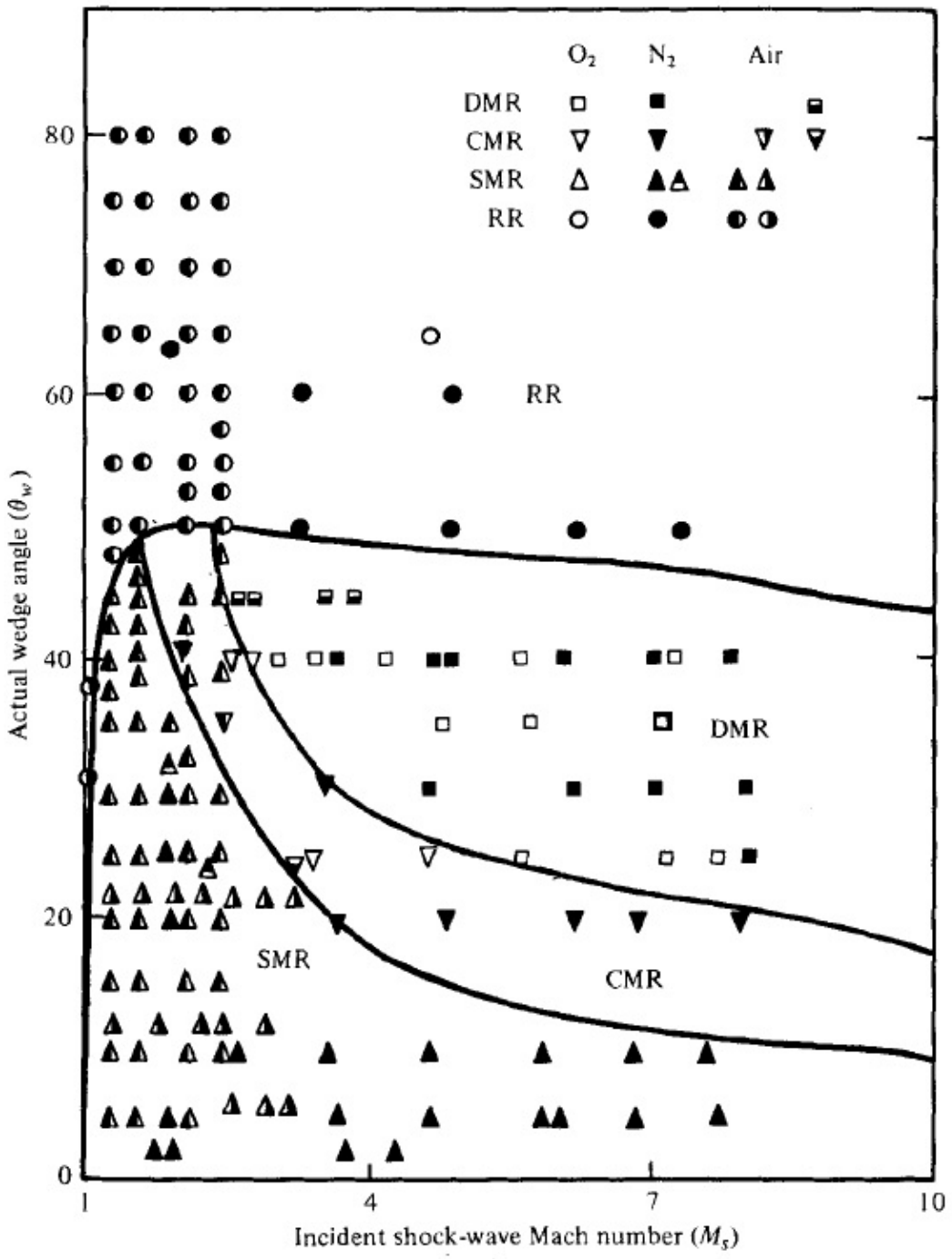


Figure 1.8: Experimental verification of analytical transition criteria for imperfect Nitrogen and other gases. $P_0 = 15$ torr, $T_0 = 300$K[2]

1.2.2 Oblique Shock Theory

Consider an oblique shock wave shown in Figure 1.9. The angle of incidence between the incoming flow and the shock is denoted by β. The flow passing through the shock is deflected by angle θ from state (i) to (j).

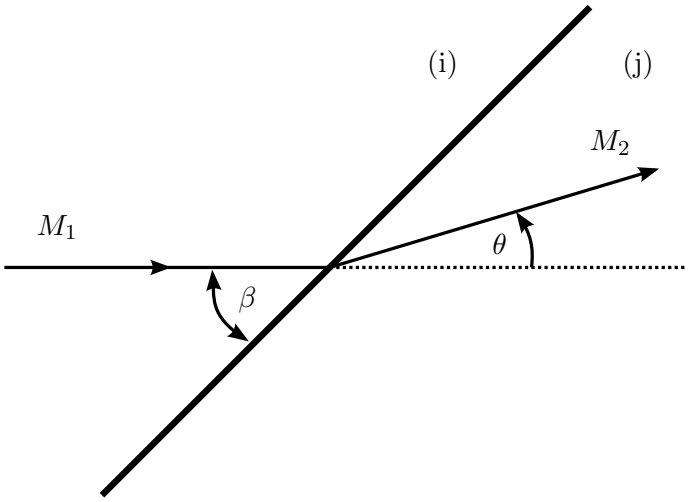


Figure 1.9: Oblique shock wave parameters[1]

The changes across an oblique shock wave are governed by the normal component of free-stream velocity [3] where the conversion is given by:

$$M_{n1} = M_1 sin\beta \tag{1.1}$$

The flow Mach number M_2 can be calculated by Equation 1.2 [3]:

$$M_2 = \frac{M_{n2}}{sin(\beta - \theta)} \tag{1.2}$$

The pressure and density ratios across an oblique shock can be calculated by using Equations 1.3 and 1.4 [3], where γ is the specific heat ratio of the fluid:

$$\frac{p_2}{p_1} = 1 + \frac{2\gamma\left(M_{n1}^2 - 1\right)}{\gamma + 1} \tag{1.3}$$

$$\frac{\rho_2}{\rho_1} = \frac{(\gamma + 1)\, M_{n1}^2}{(\gamma - 1)\, M_{n1}^2 + 2} \tag{1.4}$$

The normal Mach number of the flow behind the oblique shock wave can be calculated using Equation 1.5 [3]:

$$M_{n2}^2 = \frac{M_{n1}^2 + \frac{2}{\gamma-1}}{\frac{2\gamma}{\gamma-1}M_{n1}^2 - 1} \tag{1.5}$$

The ratio of sound speeds can be calculated using Equation 1.6 [4]:

$$\frac{a_2}{a_1} = \frac{\left[(\gamma-1)\,M_1^2 sin^2\beta + 2\right]^{1/2}\left[2\gamma M_1^2 sin^2\beta - (\gamma-1)\right]^{1/2}}{(\gamma+1)\,M_1 sin\beta} \tag{1.6}$$

The flow deflection angle θ can be calculated using Equation 1.7 [3] and is know as the $\theta - \beta - M$ relation as it specifies the deflection angle θ as a function of M_1 and β.

$$tan\theta = \frac{2cot\beta\left(M_1^2 sin^2\beta - 1\right)}{M_1^2\left(\gamma + cos2\beta\right) + 2} \tag{1.7}$$

1.3 Three Shock Theory

The MR configuration was first described analytically by von Neumann[5, 6] and is known as Three Shock Theory (TST). Consider an incident shock wave of strength M_s encountering a wedge with wall angle θ_w resulting in a Mach Reflection shown in Figure 1.10. The triple point follows a linear trajectory where angle χ is the trajectory angle with respect to the wedge surface.

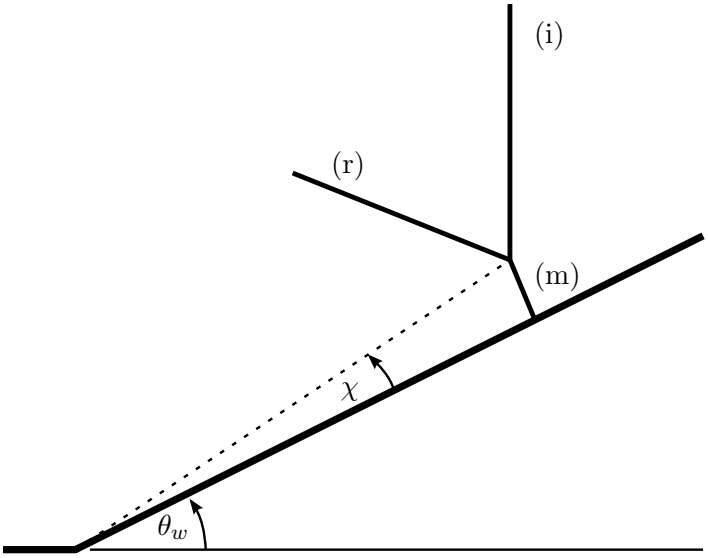


Figure 1.10: Mach Reflection occurring on a plane wedge

Transforming the Mach Reflection to a frame of reference attached to the triple point (shown in Figure 1.11) allows Equations 1.3 to 1.7 to be used to obtain the pressure, temperature, density and velocity in each of the regions (1), (2) and (3). The following boundary conditions are applied:

$$p_2 = p_3 \tag{1.8}$$

The flow states in (2) and (3) are separated by a shear layer across which the pressure must be equal. It is assumed that the shear layer is infinitely thin and the flow is inviscid [1], therefore the flow either side of the shear layer must remain parallel:

$$\theta_1 \mp \theta_2 = \theta_3 \tag{1.9}$$

The above boundary condition implies that there are two possible solutions to Equation 1.9 where Equation 1.10 below is referred to as standard Three Shock Theory as it yields a MR. The non-standard Three Shock Theory yields a vN/G/V Reflection[1].

$$\theta_1 - \theta_2 = \theta_3 \tag{1.10}$$

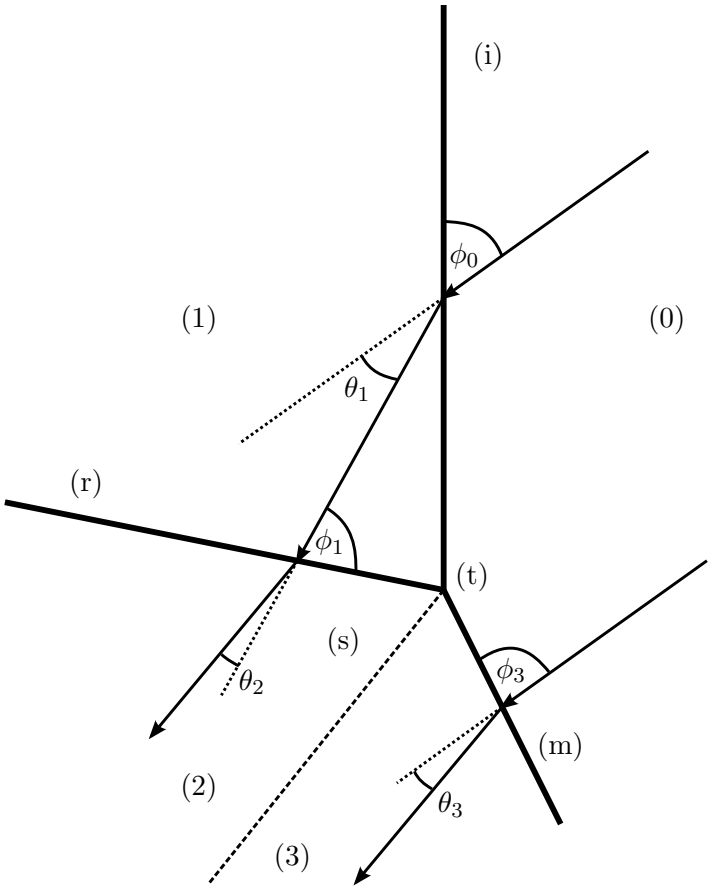


Figure 1.11: Three Shock Theory schematic with definition of parameters

From Figure 1.10 and 1.11 the following relationships can be derived:

$$\phi_0 = 90^\circ - \chi - \theta_w \tag{1.11}$$

If the Mach number of the incident shock M_s is known then the inflow Mach number M_0 can be calculated from:

$$M_0 = \frac{M_s}{sin\,(\phi_0)} \tag{1.12}$$

An analytical model of three shock theory was determined by Law and Glass[7] in the range $2 < M_s < 8$. The Mach stem is only slightly curved for small wedge angles ($\theta_w < 25°$) and strong shocks ($M_s > 2.5$), therefore the assumption is made:

$$\phi_3 = 90° - \chi \tag{1.13}$$

Equation 1.13 implies that the Mach stem *at the triple point* is perpendicular to the wedge surface even though the Mach stem may be curved[7]. The analytical method uses shock polars to obtain the solution graphically as follows (note p_0 and T_0 are constant):

1. Construct shock polar I with known conditions p_0, T_0 and a chosen M_0
2. Define a range of ϕ_0 values and calculate M_s and $\theta_w + \chi$ using Equations 1.11 and 1.12
3. Construct shock polar R at θ_1 for each ϕ_0 value
4. The intersection of I and R is the three shock solution, angle χ can then be determined from Equation 1.13
5. Repeat steps 1 to 4 for the same ϕ_0 value and different M_0
6. Curves of $\theta_w + \chi$ are then plotted on χ vs M_s
7. The triple point trajectory for constant θ_w is then obtained by subtracting χ from the $\theta_w + \chi$ values obtained in step 6

The analytical solution shows good agreement with experimental data except for large θ_w angles. In general the overall agreement can be subdivided into the following regions shown in Table 1.1(adapted from Law and Glass[7]):

Table 1.1: Comparison of results for analytical three shock theory model by Law and Glass[7] to experimental results

M_s Range	θ_w Range [°]	Agreement and χ deviation
1.45< M_s <2.5	$\theta_{w(e)} < \theta_w$ <35	Very good with minimum χ deviation
2.5< M_s <7	35< θ_w <40	Good with χ deviation of $\pm 0.5°$
2.5< M_s <7	$\theta_{w(e)} < \theta_w$ <25	Fair to poor with χ deviation greater than 0.5°
1.45< M_s <2.5	40< $\theta_w < \theta_{w(max)}$	Fair to poor with χ deviation greater than 0.5°

1.3.1 Modifications to Three Shock Theory

Skews[8] investigated the effect of relaxing the normal three shock theory boundary conditions for a weak shock of strength $\xi = 0.8$. A definition of the parameters used in the results is shown in Figure 1.12 for clarity.

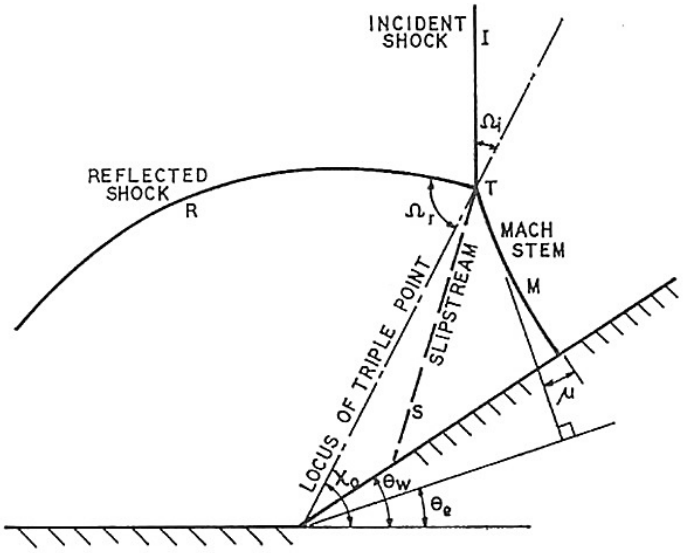


Figure 1.12: Definition of parameters used in Skews[8]

The available experimental data (at the time) are plotted in Figure 1.13, indicating the transition to Mach reflection occurs at $\Omega_i = 55°$ and does so in a continuous manner. Smith[9] considered the flow in the upper domain without restricting the results imposed by the three shock theory, these curves and labelled points on Figure 1.13 are defined as follows:

- Curve **r**: The theoretical prediction for Regular Reflection
- Curve **TST**: The theoretical prediction for Mach Reflection i.e. the three shock theory solution
- Curve **s**: The reflected shock to be positioned at the Mach angle to the incoming flow i.e. vanishing strength
- Curve **p**: The reflected shock is perpendicular to the incoming flow
- Curve **c**: The catch-up criterion i.e. the flow is sonic in region (2). On the concave side the flow is subsonic. Between curves s and c the flow is supersonic
- Curve **e**: The maximum and minimum deflection possible as the reflected shock angle is varied

- Point **er**: The maximum incidence angle where RR is possible
- Point **st**: The intersection of the TST and RR curves where the reflection type is a StMR
- Point **es**: The extreme sonic point, where no solutions are possible at higher angles of incidence

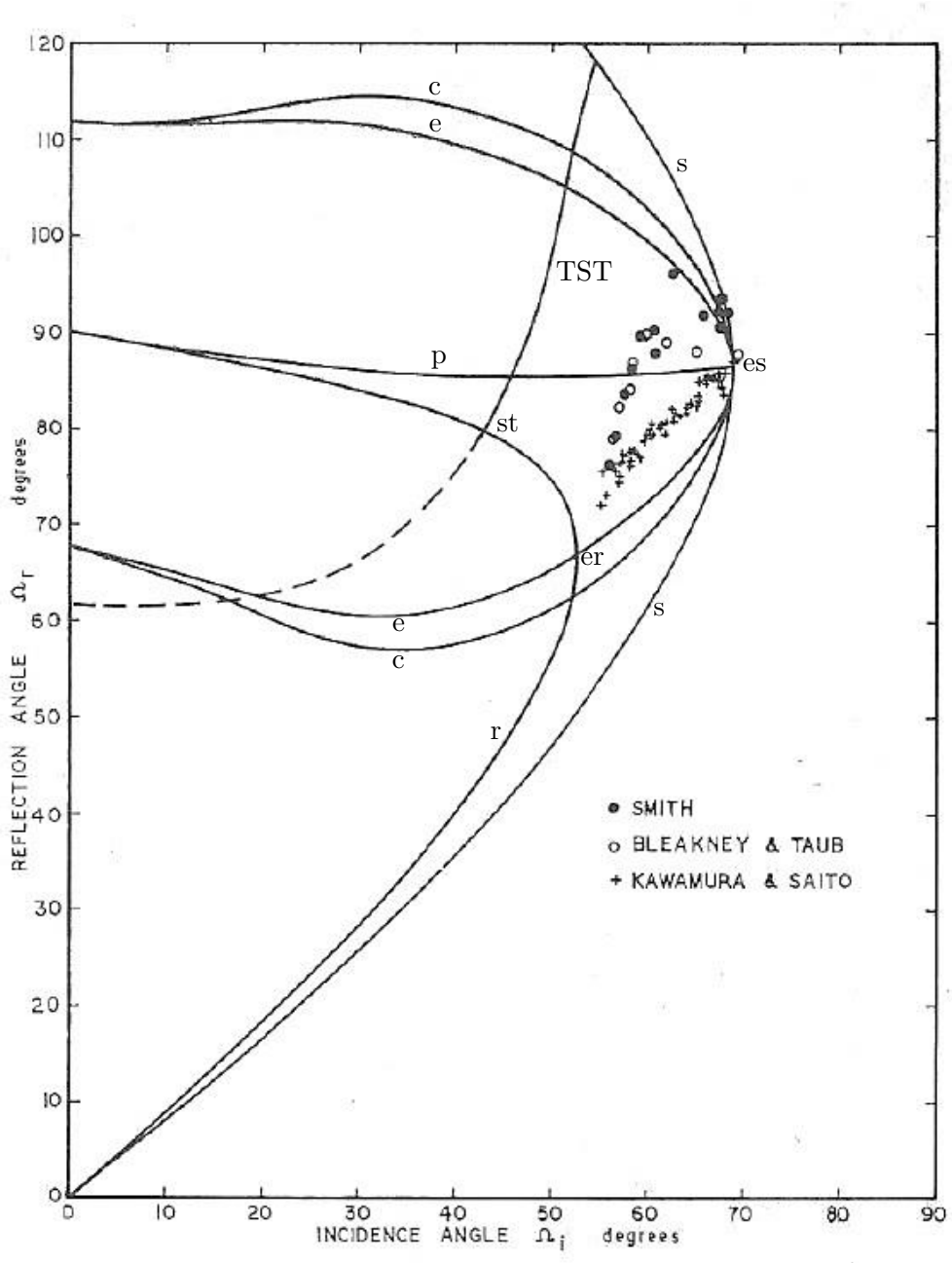


Figure 1.13: Variation of incidence angle with reflection angle for $\xi = 0.8$[8]

Skews considered the strength and inclination of the shock waves that are physically observable and restricted his computations to the near field surrounding the triple point[8]. The

so-called "equilisation zone" at the triple point was ignored as it violates the boundary conditions imposed by three shock theory. The pressure *immediately* behind the reflected shock and Mach stem do not have to be the same, for this reason a measure of their relative value is defined as:

$$F = (p_2/p_0 - p_1/p_0)/(p_3/p_0 - p_1/p_0) \tag{1.14}$$

where F is termed the pressure defect. For the normal three shock theory: $F = 1$ with $p_2 = p_3$, whilst a value of $F = 0$ gives $p_2 = p_1$: where the reflected shock is of vanishing strength. The slipstream is not a discontinuity but rather a region of mixing that grows from the triple point. The fact that a pressure defect exists does not violate the assumption that the pressure is continuous across the slipstream[8]. A direction deficit is also defined by angle ϵ where positive values indicate flow divergence and vice versa.

The possible solution types for $\epsilon = 0$ are presented in Figure 1.14. The effective wall angle (θ_e) is taken as a parameter with the pressure deficit being varied. The solutions can be classified into the following sub-domains (corresponding to Figure 1.14):

(a): For low values of θ_e, the solution reaches a maximum incidence angle on the upper branch of curve **e**. This corresponds to a minimum triple point trajectory χ_0.
(b): The solution forms two curves with the maximum incidence angle on the lower branch of curve **e** and minimum incidence angle on the upper branch of curve **e**. Between the two intersections with curve **e** there is no solution for Mach reflection.
(c): The solutions divide into an upper and lower branch with the maximum incidence angle occurring on the lower branch of curve **e**.
The maximum incidence angle decreases as θ_e is increased until it reaches the point **er** for Regular Reflection where $\chi_0 = \theta_w$.
(d): The solution is discontinuous for higher θ_e values where the maximum incidence angle occurs on the curve **r**. Mach Reflection is still possible within the region bound by curve **r**. Lower incidence angles are possible on the concave side of curve **r**.

The comparison with available experimental data proves to be inconclusive when $\epsilon = 0$. Computations performed with positive and negative ϵ values are presented in Figure 1.15. The experimental curve (shown by the dotted line) intersects the limiting loops and gives the possible range of ϵ values where solutions are possible. It is indicated that between θ_e values of 0° and 12° the flow directions must diverge. The solution also permits flow convergence for larger values of θ_e[8].

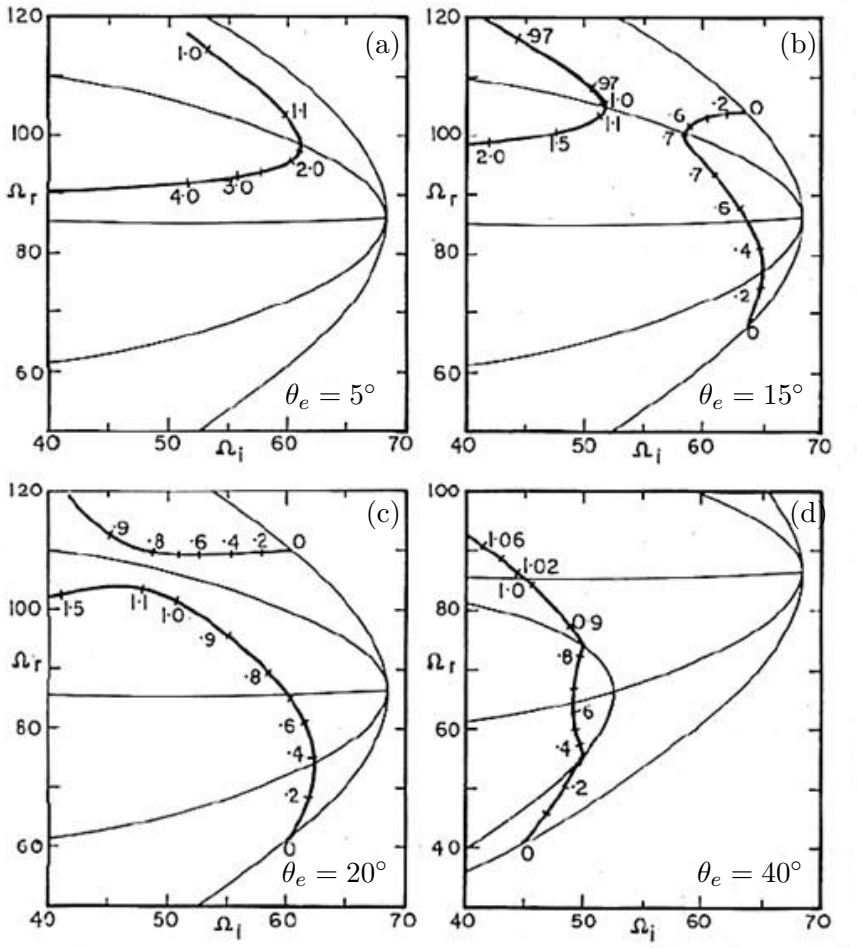


Figure 1.14: Various solution types for values of F with θ_e as a parameter[8]

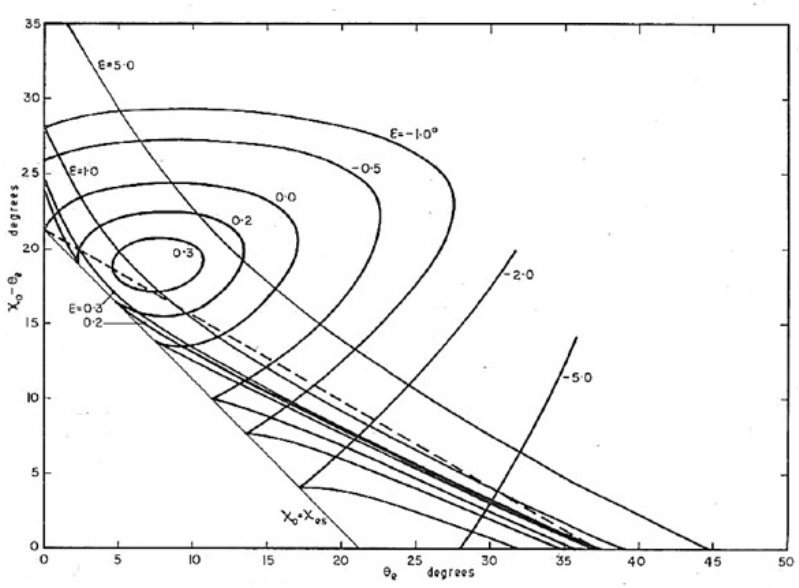


Figure 1.15: Limit curves for values of ϵ [8]

Ben-Dor[10] proposed modifications to simple three shock theory that took into account real-gas effects and the boundary layer growth either side of the slipstream. The analytical models were applied to one experimental case of a DMR shown in Figure 1.16. The measured triple point trajectory was used in the analytical model.

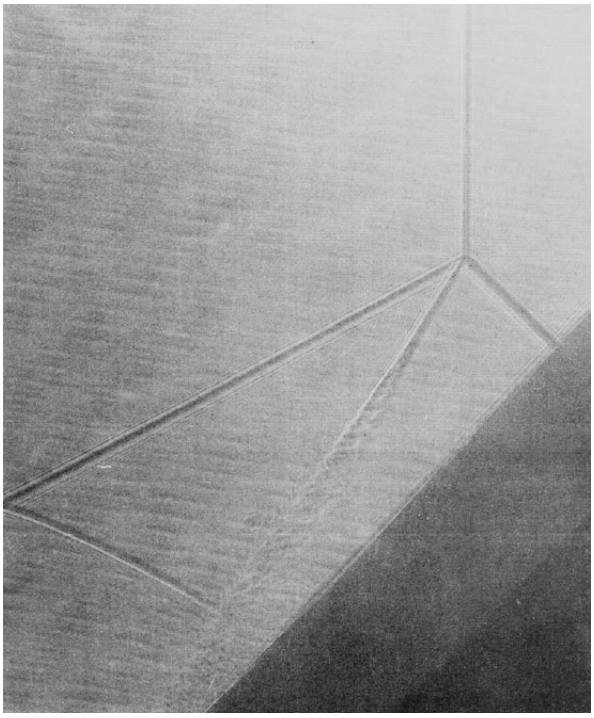


Figure 1.16: Zoomed in shadowgraph of the DMR analysed by Ben-Dor[10, 11]. $M_s = 2.71 \pm 0.01$, $\theta_w = 47.1°$, $T_0 = 296$K, $p_0 = 760$ torr and $\chi = 3° \pm 0.5°$.

In a frame of reference attached to the triple point trajectory, the angle ϕ_0 was measured to be $39.9° \pm 0.5°$: this is in total agreement with Equation 1.11. The following angles are defined in order to compare experimentally measured angles to the analytical model predictions:

ω_{IR}: The angle between the incident and reflected shocks:

$$\omega_{IR} = 180° + \theta_1 - \phi_0 - \phi_1 \tag{1.15}$$

ω_{IM}: The angle between the incident shock and Mach stem:

$$\omega_{IM} = 180° + \phi_0 - \phi_3 \tag{1.16}$$

ω_{RS}: The angle between the reflected shock and shear layer:

$$\omega_{RS} = \phi_1 - \theta_2 \tag{1.17}$$

ω_{MS}: The angle between the Mach stem and shear layer:

$$\omega_{MS} = \phi_3 - \theta_3 \tag{1.18}$$

The above equations result in the expected: $\omega_{IR} + \omega_{IM} + \omega_{RS} + \omega_{MS} = 360°$. Using simple three shock theory, i.e. the perfect-gas solution, resulted in a large discrepancy between the experimental and analytical values by about 5°. Due to the Mach number being greater than 2, real-gas effects were included in the analytical solution. This resulted in a much improved solution but ω_{RS} still differed by 2°.

The second analytical model included viscous effects along the slipstream where the displacement thickness was calculated (equivalent to boundary layer growth on a flat plate). The displacement thickness δ was then used to calculate an angular displacement of the slipstream at a characteristic length x_{char}. This length was chosen to be the thickness of the incident shock thickness[10].

A third analytical model included both real-gas effects and viscous effects. Unfortunately this method proved to be in worse agreement than the perfect-gas solution. A summary of the results from Ben-Dor[10] is provided in Table 1.2. The inclusion of viscous effects into the simple three shock theory model provides excellent agreement with experimental results. Further analytical work was conducted by Ben-Dor using this analytical model[11] by incorporating the results of Skews[8]. The viscous model was replaced with a simple divergence angle ϵ measured from the experimental image. In Figure 1.16 the value is measured to be $4° \pm 0.1$. The boundary condition given in Equation 1.10 then becomes $\theta_1 - \theta_2 = \theta_3 - \epsilon$[11]. The results are provided in Table 1.2. When the experimental value of ϵ was used, the results were found to be worse than the viscous model. When real-gas effects were introduced into the divergence model, the results showed very good agreement. The reason for this is the reflected shock angle ω_{IR} is dependent on conditions in region (2) behind the reflected shock; this gas has been double shocked and is at a very high temperature, therefore requiring real-gas effects to be accounted for[11].

Table 1.2: Comparison of results for analytical three shock theory models to experimental results for Figure 1.16

	Type of model	$\omega_{IR}[°]$	$\omega_{IM}[°]$	$\omega_{RS}[°]$
Reference	Experimental Results	118 ±1	132 ±1	32 ±1
Ben-Dor 1987[10]	TST with a Perfect-Gas	123.19	132.74	27.16
	TST with Real-Gas Effects	117.32	131.95	29.81
	TST with Viscous Effects	118.02	131.70	32.32
	TST with Real-Gas and Viscous Effects	120.04	130.70	27.09
Ben-Dor 1990[11]	TST with Divergence ϵ	123.25	133.95	30.11
	TST with Real-Gas Effects and ϵ	117.38	133.19	31.65

Olim and Dewey[12] proposed a revised three shock solution in the weak shock domain ($M_s < 1.5$). The new analytical solution was based on an experimental observation that the pressure behind the reflected shock increased linearly with the triple point trajectory as shown in Figure 1.17. It is well documented that the agreement between experiments and three shock theory is poor for weaker shocks[12].

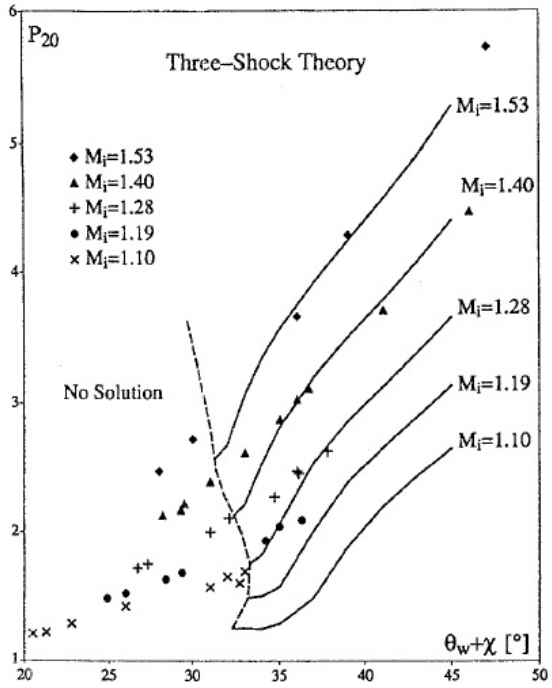
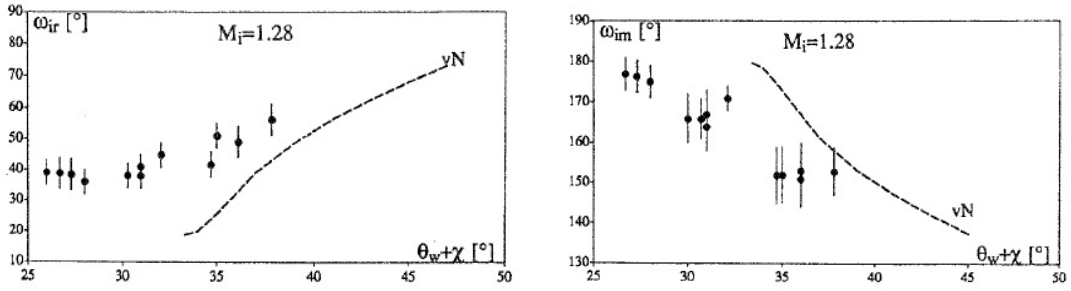


Figure 1.17: Pressure behind the reflected shock (P_{20}) vs Complimentary Wall Angle ($\theta_w + \chi$) as a function of Mach number. Solid lines indicate Three Shock Theory calculated theoretically[12]

A series of experiments were carried out where the angle between the incident and reflected shocks (ω_{IR}) and incident and Mach stem (ω_{IM}) were measured as shown in Figure 1.18.



(a) (b)

Figure 1.18: Measured shock angles with dashed line calculated from three shock theory[12] (a) ω_{IR} (b) ω_{IM}

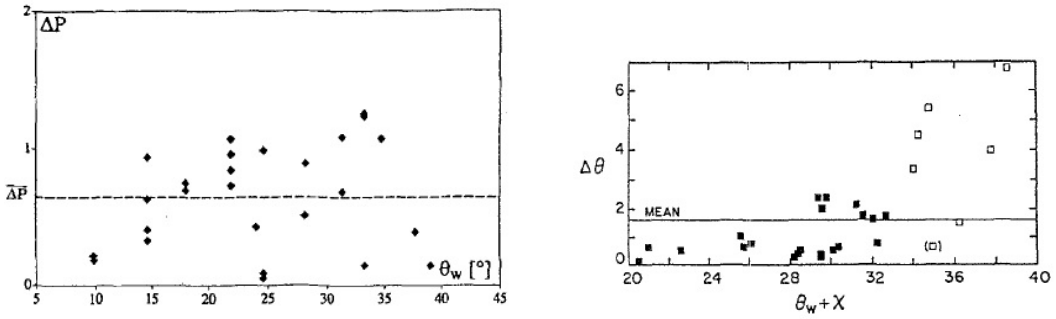
The measured angles together with the triple point trajectory and incident shock strength were used to determine the pressure behind the reflected shock (P_{20}) and Mach stem (P_{30}). The net deflection across the incident and reflected shocks ($\theta_1 - \theta_2$) and Mach stem (θ_3) was calculated using oblique shock theory. An analysis of the results revealed a divergence between the two streams of several degrees and the pressure behind the Mach stem being slightly larger for most cases. A separate test was conducted that produced a Double Mach Reflection at $M_s = 2.21$ and $\theta_w = 41.8°$, this type of reflection is easier to measure the shock angles due to the reflected and Mach stem shocks being planar at the triple point. An oblique shock analysis was used to determine the divergence of the two flows and pressure difference. The pressure difference was normalised by the pressure behind the incident shock:

$$|P_{30} - P_{20}| / P_{10} = 0.128 \tag{1.19}$$

Likewise, the divergence at the slipstream was calculated:

$$|\theta_1 - \theta_2 - \theta_3| = 0.8° \tag{1.20}$$

The above Equations 1.19 and 1.20 were used as a measure of the minimum experimental error. The pressure difference and divergence calculated for the previous experiments was then normalised by the minimum experimental error values. A value of 1 or less for the normalised pressure difference meant that acceptable accuracy was obtained in the measurements as shown in Figure 1.19:

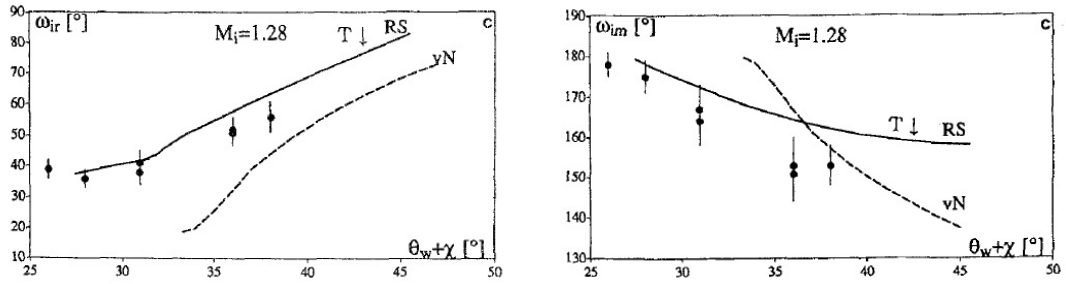


(a) (b)

Figure 1.19: Normalised minimum experimental error values with mean value indicated by a dashed line[12] (a) Pressure difference (b) θ difference

From the above Figure 1.19 it was concluded that the pressure difference across the shear layer was insignificant compared to the shear layer divergence. A revised three shock solution was derived based off the previously mentioned relationship between the triple point trajectory

and P_{20}, more details on the theory can be found in Olim and Dewey[12]. Figure 1.20 shows the much improved agreement between the measured angles and the new theory; with a much closer agreement obtained between the pressure P_{20} and the linear theory shown in Figure 1.21.



(a) (b)

Figure 1.20: Measured shock angles with dashed line calculated from three shock theory and line T from the modified theory[12] (a) ω_{IR} (b) ω_{IM}

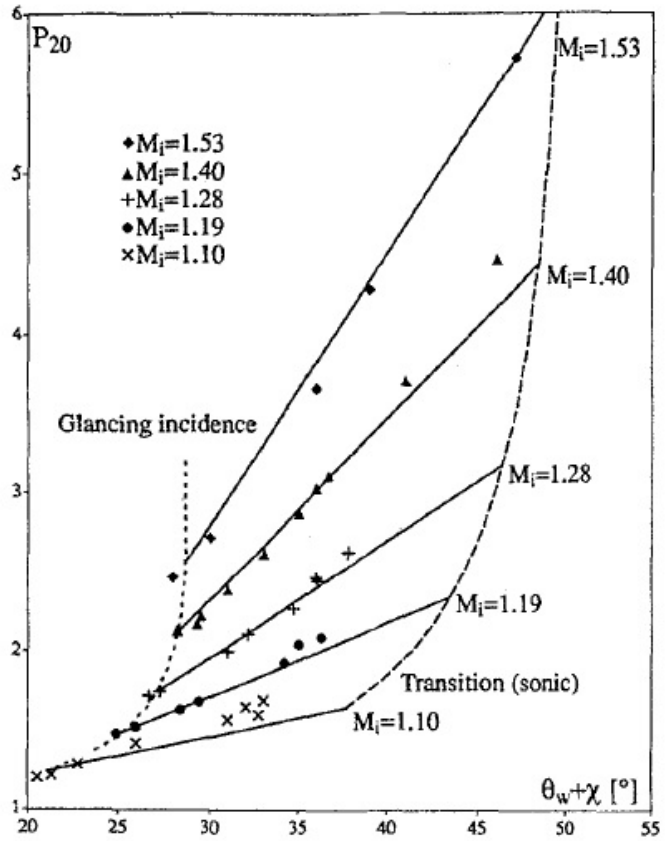


Figure 1.21: Modified three shock theory proposed by Olim and Dewey[12]

1.4 Shock Polars

A useful means to analyse the flow deflection process in a Mach Reflection is by means of a shock polar[1] as shown in Figure 1.22. The flow deflection (θ_i^T) is measured with respect to the triple point trajectory, explained in Section 1.3. The I-polar represents the locus of all states obtainable by the flow in Region (0) passing through an oblique shock wave. Region (1) is the origin of the R-polar and is labelled (1) in Figure 1.22. The R-polar represents the locus of all states obtainable by the flow in Region (1) passing through any oblique reflected shock wave. The R-polar is drawn in the opposite direction to the I-polar due to the boundary conditions of the SMR. Region (3) behind the Mach stem is also on the I-polar and is always a strong shock solution ($M_3 < 1$). The intersection of the I and R-polar yields the three shock solution at point (2) and (3) as the pressures are the same in Regions (2) and (3) as is the net flow deflection.

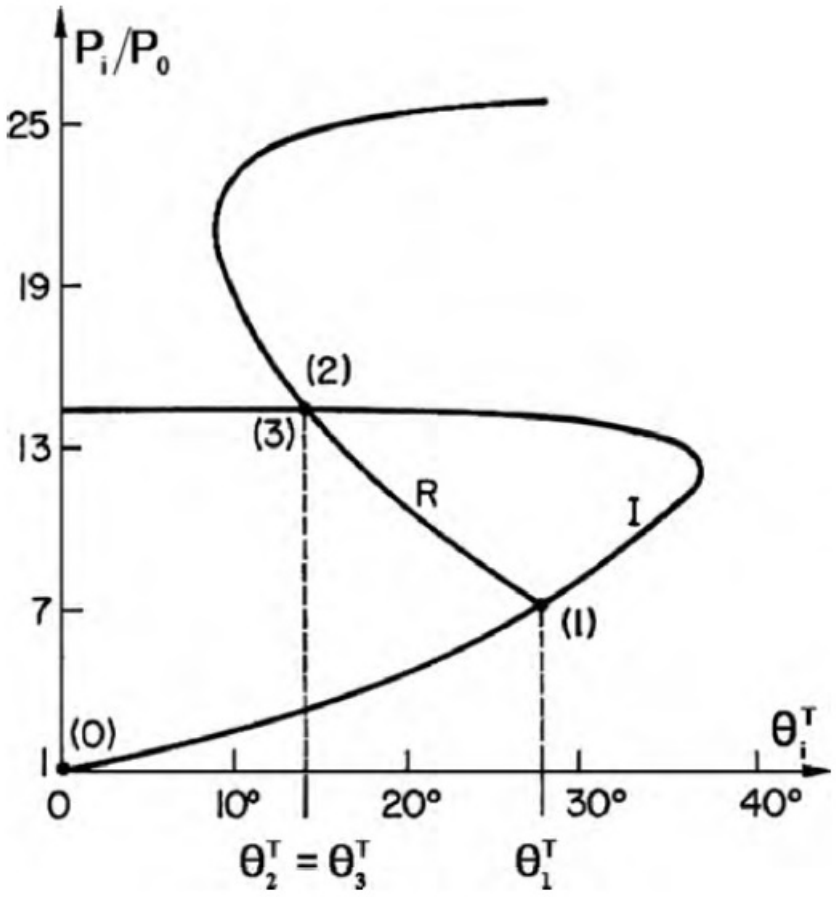


Figure 1.22: Shock Polar solution of a Single Mach Reflection[1]

1.5 Previous work by Rubidge

Rubidge and Skews[13] investigated the Kelvin-Helmholtz Instability (KHI) occurring along the shear layer of a Mach reflection. A double diaphragm shock tube was used that produced repeatable shock Mach numbers. The Mach numbers tested were $1.33, 1.45$ and 1.6. The test section used was 180mm high by 76mm wide with 300mm diameter viewing windows. Six different test pieces were used for the experiment, with four wedges having parabolic entrances of different lengths and two wedges having plane entrances. A schlieren optical system was used to visualise the flow along with a wire grid placed on the one window for scaling and measurement purposes. It was found that greatest sensitivity for visualising the KHI structures was achieved when the camera side knife edge was orientated perpendicular to the shear layer.

It was found that as the Mach reflection developed on the test piece, the shear layer grows in length and width from the triple point, as expected. The KHI along the shear layer was found to be present across the Mach number range with a shorter time to develop as the Mach number was increased. There are distinct differences between the parabolic and plane wedges: the shear layer terminates above the surface for the parabolic wedges whilst in the plane case it extends to the wedge surface indicating an interaction with the boundary layer. For the plane wedges the shear layer appears more curved in nature due to the immediate formation of the Mach reflection. The KHI loops are larger for the plane wedges and are not consistent between images with this attributed to their interaction with the boundary layer itself. Figure 1.23 shows the KHI development for the plane ($30°$) wedge.

Measurements were taken of various flow features to track the development of the KHI along the shear layer. Figure 1.24 is the KHI thickness, clearly showing the apparent linear development of the shear layer. A comparison to Rikanati et al. [14] was made of slipstream spread with the results indicating a spread angle that was roughly double that obtained by Rubidge and Skews[13]. This was attributed to the measurement technique used by Rikanati et al. [14]. The effect of the boundary layer on the shear layer is apparent when comparing the two plane wedges. A clear thickening of the boundary layer is apparent near where the shear layer contacts the wedge surface, this is most noticeable for the larger wedge angle ($38°$) and requires further investigation.

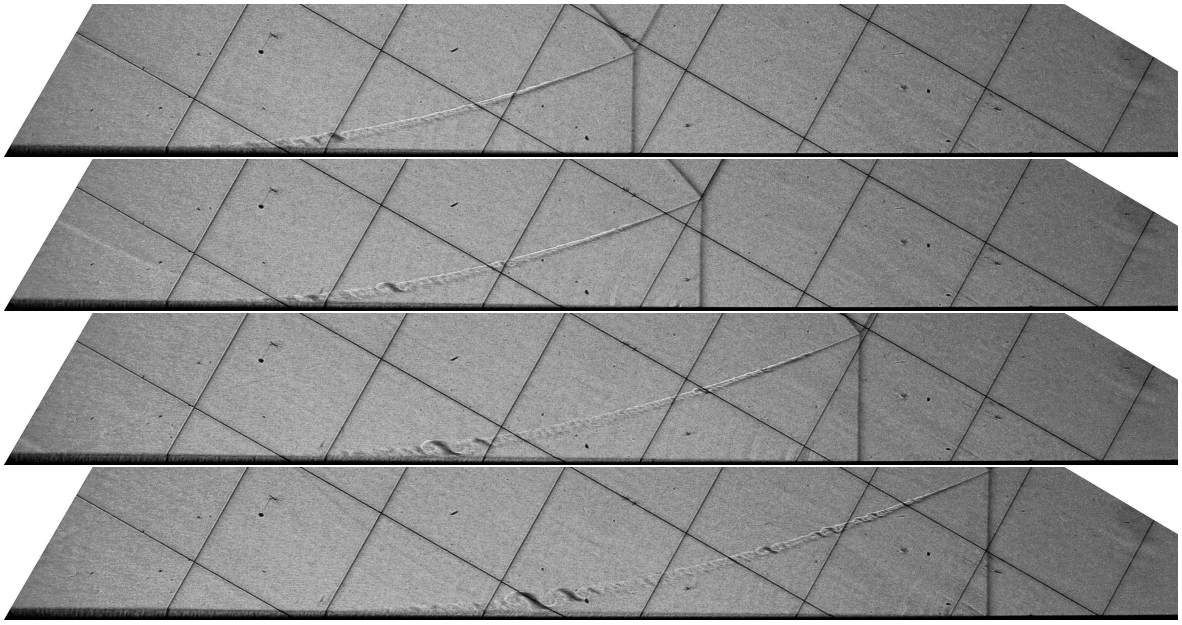


Figure 1.23: KHI occurring along a Mach reflection shear layer for a 30° wedge, $M_s = 1.61$ [13]

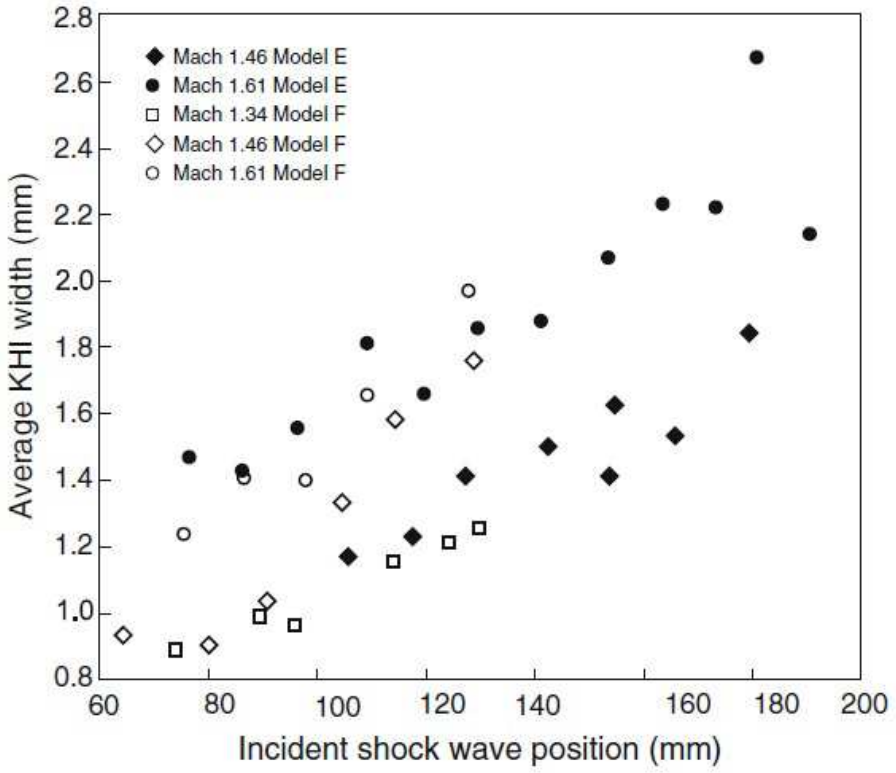


Figure 1.24: Shear layer average width [13]

1.6 Motivation

It is clear that Three Shock Theory fails to predict shock angles in the weak shock domain ($M_s < 1.5$) and is in good agreement for strong shocks ($M_s > 2$). There have been few attempts at relaxing the boundary conditions imposed on the shear layer; the most notable being that of Skews[8] for very weak shocks and Ben-Dor[10, 11] for strong shocks. There exists a range of Mach reflection that has not been accounted for ($1.5 < M_s < 2.7$) by previous work utilising a modified Three Shock Theory and serves as the motivation for this dissertation. It is noted that there have been previous studies of Mach Reflection, but the focus has rather been on the RR⇌SMR or SMR⇌TMR transition etc. and not on the shear layer growth itself. The work done by Rubidge and Skews[13] will serve as a basis for this research as measurements were taken of the shear layer as seen in Figure 1.24. There have been numerous studies on the growth of a shear layer where two streams of different velocity and density meet at a splitter plate (discussed in Section 2.3); these could serve as a useful tool to characterise the shear layer growth occurring in a Mach Reflection.

Chapter 2 Literature Survey

This chapter provides relevant literature on shock tubes and the flow visualisation of gases in Sections 2.1 to 2.2. Previous theoretical and experimental work conducted on shear layers is provided in Section 2.3.

2.1 Shock Tubes

A shock tube is an experimental apparatus for producing shock waves for research purposes. The general layout consists of a tube that is separated into a high and low pressure section by a diaphragm. The high pressure and low pressure regions are referred to as the driver and driven sections respectively. A diaphragm is a thin sheet of polymer plastic or metal that is clamped in place between the two sections. To initiate a test the driver section is pressurised, this is shown in Figure 2.1. The diaphragm then bursts at its natural burst pressure or is manually burst by some mechanical means. A shock wave propagates into the driven section and an expansion wave into the driver, this is shown in Figure 2.2. The contact surface is the interface between the driver and driven test gas and has identical pressure and velocity properties as the fluid behind the shock [3]. The pressure ratio $\frac{p_4}{p_1}$ of the driver gas to driven gas can be expressed as a function of M_1, γ_1, γ_4 and $\frac{a_1}{a_4}$ [15]. This is known as Ideal Shock Tube Theory (ISTT) and is given by Equation 2.1:

$$\frac{p_4}{p_1} = \left[1 + \frac{2\gamma_1}{\gamma_1 + 1}\left(M_{s1}^2 - 1\right)\right]\left[\frac{1}{1 - \left(\frac{\gamma_4 - 1}{\gamma_1 + 1}\right)\left(\frac{a_1}{a_4}\right)\left(M_{s1} - \frac{1}{M_{s1}}\right)}\right]^{\frac{2\gamma_4}{\gamma_4 - 1}} \tag{2.1}$$

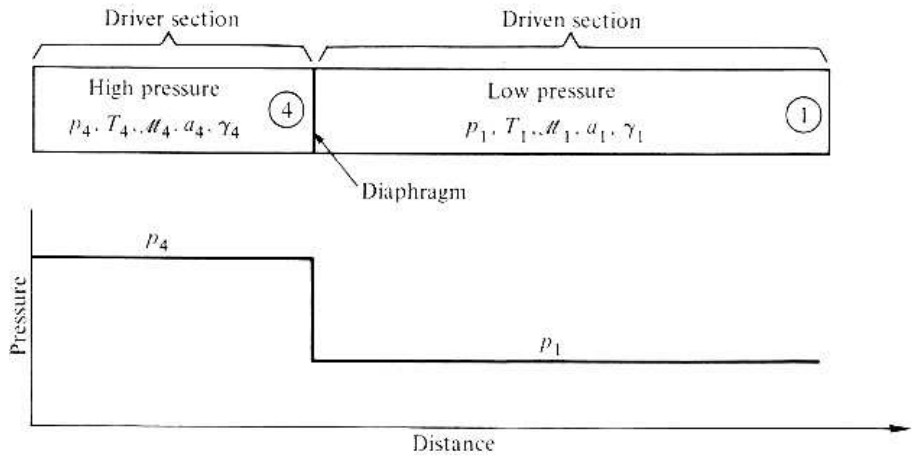


Figure 2.1: Shock tube initial conditions before diaphragm burst [3]

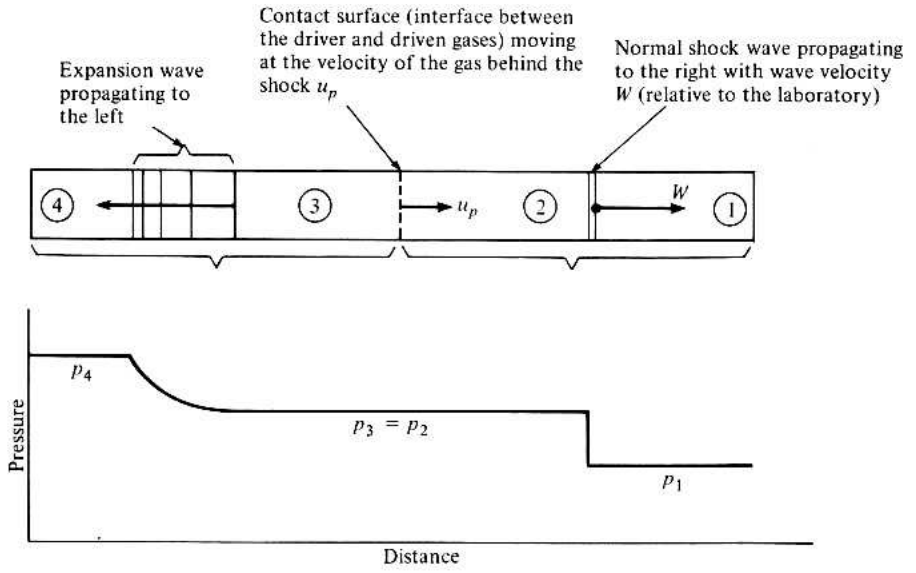


Figure 2.2: Shock tube after diaphragm burst [3]

2.2 Flow Visualisation

Density sensitive flow visualisation techniques rely on the refractive index of the gas varying with density. Light passing through the gas is diffracted by varying amounts depending on the density gradient of the gas; this allows density gradients within the flow to be visualised[16]. The simplest form is known as shadowgraph, this visualises changes in density gradient and is therefore suited to shock waves, slipstreams and zones of high turbulence[16]. In order to visualise gradual density changes such as those occurring in compression regions or across expansions fans, the schlieren technique is used; this visualises the flow density gradient in a certain direction. A schematic of a z-configuration schlieren setup is shown in Figure 2.3, the direction of highest sensitivity is that perpendicular to the knife edge before the camera[16].

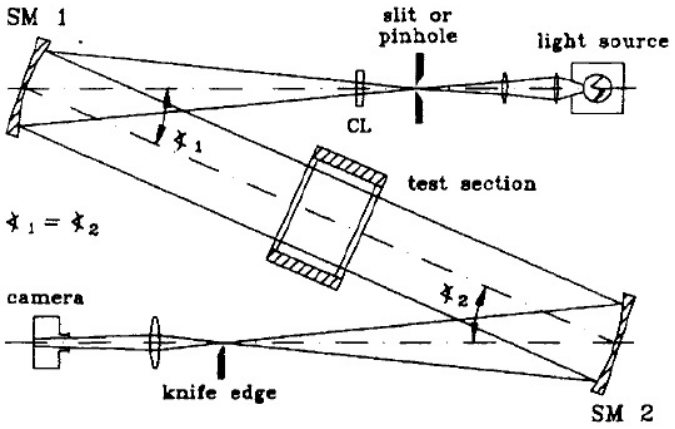


Figure 2.3: Schematic layout of a typical monochrome schlieren visualisation system (adapted from Kleine[16])

2.3 Compressible Shear Layers

2.3.1 Introduction

A shear layer is an interface between two fluids travelling at different velocities that may have differing properties such as density and temperature. A method for creating a shear layer for experimental studies is by means of a splitter plate, where two plane flows (of velocities U_1, U_2 and densities ρ_1, ρ_2) meet at $x = 0$. The shear layer thickness is defined by δ_{viz} at distance x from the trailing edge. The higher speed flow is always defined as having flow velocity U_1 and density ρ_1. The following ratios appear extensively in literature and are defined as:

$$r = \lambda_u = U_2/U_1 \tag{2.2}$$

$$s = \lambda_\rho = \rho_2/\rho_1 \tag{2.3}$$

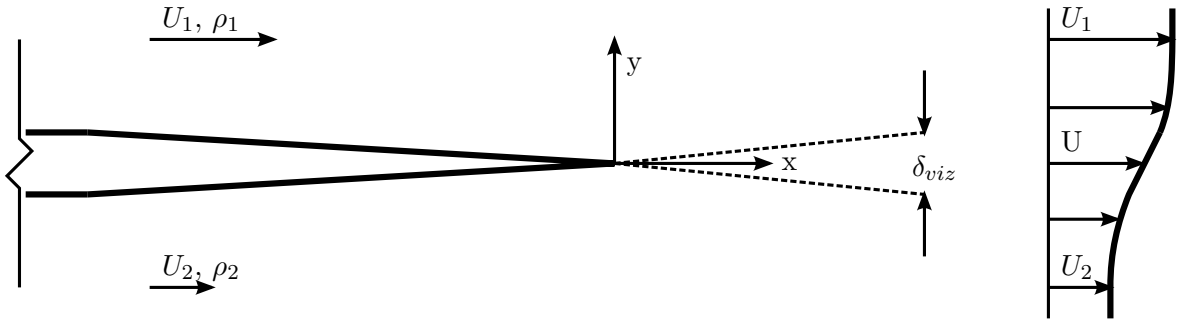


Figure 2.4: Schematic of a plane shear layer with definition of some parameters (adapted from Brown and Roshko[17])

A comprehensive historical review of the available shear layer literature is provided in Section 2.3.2 where the experiments were all steady flows. A review of the relevant work undertaken on the KHI occurring in shear layers is provided in Section 2.3.3.

2.3.2 Previous Experimental Work and Development on Shear Layers

Brown and Roshko [17] investigated planar turbulent mixing between two streams of different gases. Previous studies of supersonic jets showed a decrease in the mixing layer spread angle with increase in Mach number. The increase in Mach number causes a change in density ratio across the jet boundary. A good approximation was found between a plane mixing layer and the initial mixing region of an axisymmetric jet and therefore a suitable comparison can be made between the two. For a planar mixing layer with helium and nitrogen as the test gases,the same density ratio can be obtained as that of a Mach 5.5 supersonic air jet. An experimental apparatus was constructed to study plane mixing layers whereby two streams of different gases meet at a splitter plate as shown in Figure 2.5. Two nozzles supply the test gases from gas bottles into the test section. The side walls are adjustable in order to remove pressure gradients within the gas stream. Control valves downstream of the two nozzles allow the pressure of each stream to be maintained at the desired operating value before it reaches the test section. The entire test section is enclosed in a cylinder with viewing windows built in, this allows density sensitive optical techniques to be utilised for photographing the mixing layer.

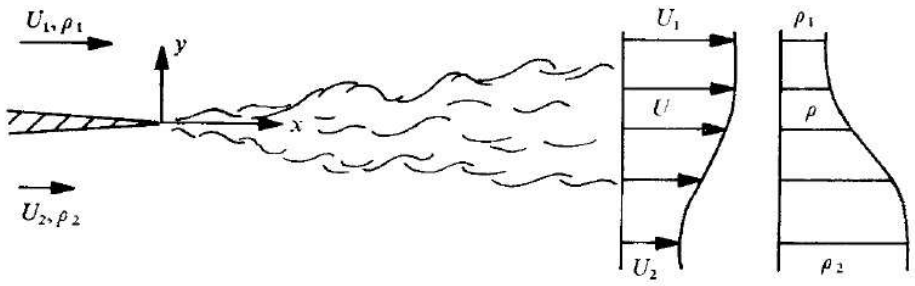


Figure 2.5: Plane mixing layer [17]

Through the use of spark shadow pictures it was shown that the mixing layer is dominated by large coherent structures for all density ratios. An example of an image obtained is shown in Figure 2.6 for a velocity ratio of $U_1/U_2 = \sqrt{7}$.

Shown in Figure 2.7 is flow of the same velocity ratio as above but with $\rho_2/\rho_1 = 7$. This leads to an increase in density ratio of 49 (compared to Figure 2.6) and a corresponding decrease in the spreading angle of about 2.

The velocity ratio was then increased to $U_1/U_2 = 7$ and the density ratio was varied between 1/7, 1 and 7. The spreading rates were higher at this velocity ratio. The visual growth δ_{viz} is determined by drawing tangents from the virtual origin along the edges of the mixing layer as seen in Figure 2.6. The visual growth rate is simply given by $\delta'_{viz} = \delta_{viz}/(x - x_0)$, where

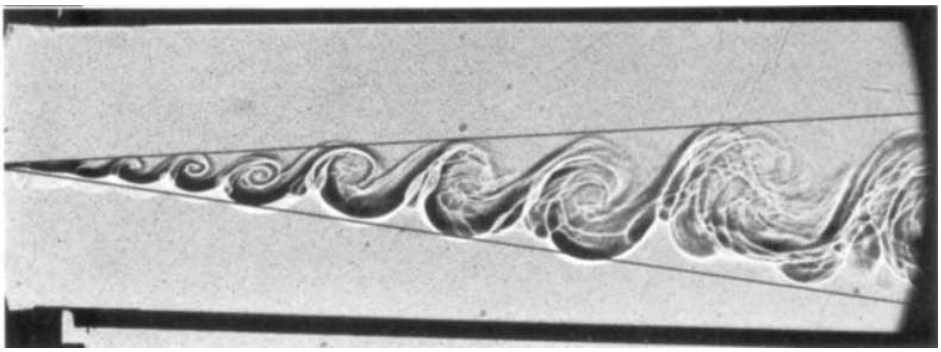


Figure 2.6: Shadowgraph of mixing layer showing measurement of growth rate [17]

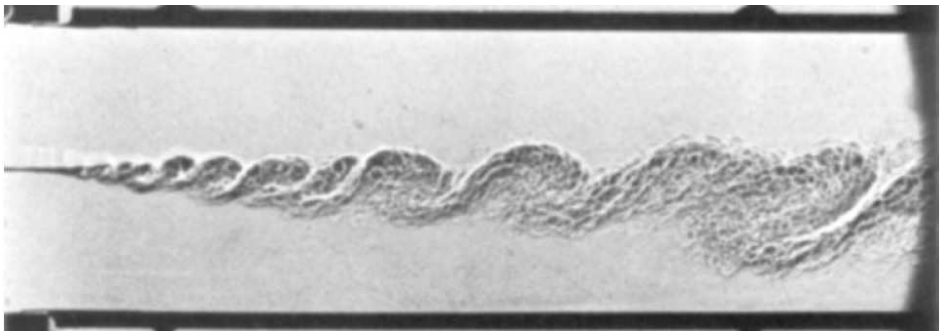


Figure 2.7: Shadowgraph of mixing layer for density ratio of 7 [17]

x_0 is the virtual origin. The visual growth rates are plotted against $(U_1 - U_2)/(U_1 + U_2)$ in Figure 2.8. The growth rates are assumed be in the form:

$$\delta'_{viz} = const.\frac{U_1 - U_2}{U_1 + U_2} \tag{2.4}$$

Constant lines are plotted in Figure 2.8 of $\delta_{viz} = 0.51$, 0.38 and 0.28 for density ratio of 7, 1 and 1/7. The density ratio has a small effect on the spreading rates as mentioned above. Density fluctuations were measured by traversing probes capable of measuring dynamic pressure and density in a streamwise direction. The origin x_0 is determined from a plot of the thickness at each traverse location. The velocity-profile maximum-slope thickness is defined as:

$$\delta_\omega = \frac{U_1 - U_2}{(\partial U/\partial y)_{max}} \tag{2.5}$$

And the x derivative used to define the spreading rate:

$$\delta'_\omega = \frac{\delta_\omega}{x - x_0} \tag{2.6}$$

Shown in Figure 2.9 is a plot of the spreading rate with results of various investigators [17].The vorticity thickness growth rate δ_ω is plotted against parameter λ defined as:

$$\lambda = \frac{U_1 - U_2}{U_1 + U_2} = \frac{1 - r}{1 + r} \tag{2.7}$$

The line of best-fit is given as:

$$\delta_\omega^{'} = 0.181\lambda \tag{2.8}$$

This line intersects the y-axis at $\delta_{\omega 0}^{'} = 0.181$ for $U_2 = 0$. Further attempts were made to fit concave down curves based on the Abramovich-Sabin relation and by locating the dividing streamline[17] but with limited success.

It is evident from the shadowgraph images of the mixing layer that the spacing between vortices and the vortex diameter increases with distance from the splitter plate. Due to the fact that each vortex convects near the average speed of the layers $\frac{1}{2}(U_1 + U_2)$, a decrease in frequency is implied with increase in vortex diameter. This leads to the conclusion that the vortices must amalgamate and this happens continuously as distance from the splitter plate increases. Experimental measurements of the vortex velocity were conducted and the velocities varied between $0.45U_1$ and $0.60U_1$ with an average of $0.53U_1$. The mean eddy spacing was found to be invariant of velocity and density ratio, depending only on layer thickness. An estimate of the mean vortex spacing is defined as:

$$\bar{l} = 3\delta_{\omega 0} \tag{2.9}$$

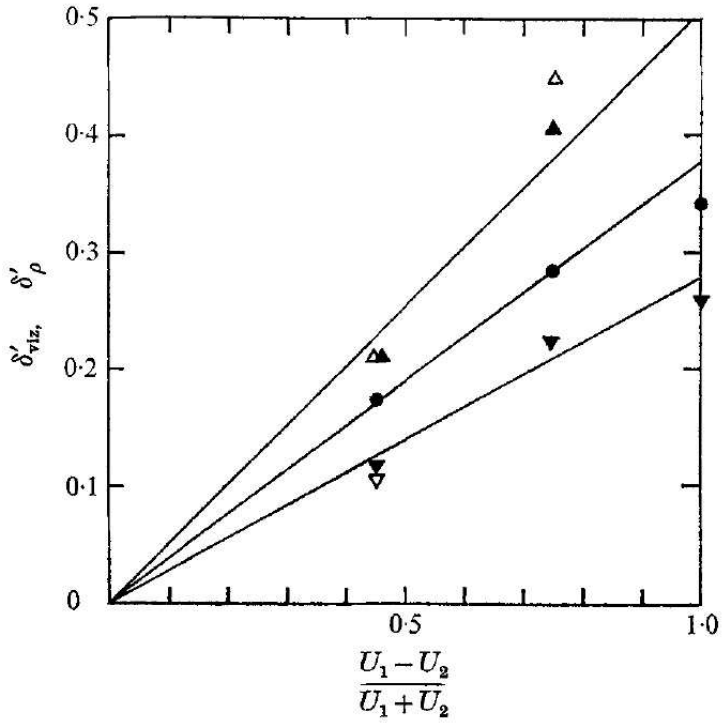


Figure 2.8: Shear layer growth rates (filled symbols represent visual growth rates from experimental photographs) [17]

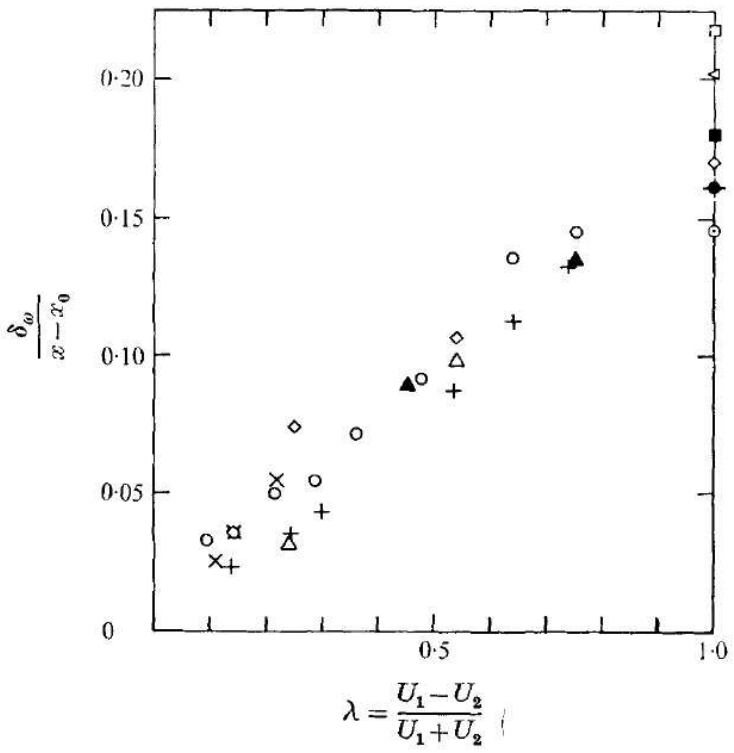


Figure 2.9: Vorticity thickness vs λ for $s = 1$ [17]

Bogdanoff [18] denotes a parameter M^+ to correlate the effect of compressibility on the growth rates of two-dimensional shear layers. The structures in the shear layer are assumed to travel at a mean velocity U_w with negligible drag force acting on them. Equating the dynamic pressures across the two freestreams with respect to the structures:

$$\rho_1 \left(U_1 - U_w\right)^2 = \rho_2 \left(U_w - U_2\right)^2 \tag{2.10}$$

Through the use of Equation 2.10, the Mach numbers of the structures may be found with respect to each freestream:

$$\left(U_1 - U_w\right)/a_1 = M_1 \left(1 - \lambda_u\right) / \left(1 + \lambda_\rho^{-\frac{1}{2}}\right) \tag{2.11}$$

and

$$\left(U_w - U_2\right)/a_2 = M_1 \left(1 - \lambda_u\right) / \left[\left(1 + \lambda_\rho^{-\frac{1}{2}}\right) \lambda_\gamma^{\frac{1}{2}}\right] \tag{2.12}$$

The geometric average of Equations 2.11 and 2.12 is then defined as M^+:

$$M^+ = \frac{M_1 \left(1 - \lambda_u\right)}{\left(1 + \lambda_\rho^{-\frac{1}{2}}\right) \lambda_\gamma^{\frac{1}{4}}} \tag{2.13}$$

The decrease in shear layer thickness with increasing Mach number observed experimentally was compared to the maximum linear instability growth rates from Blumen et al.[18]. The vorticity thickness measured experimentally was used as the ordinate, normalised with respect to δ_w for $\lambda_\rho = 1$ and $M_1 = 0$. The decrease in maximum growth rates of the Kelvin-Helmholtz instabilities was considered to be an important factor that contributes to the decrease in shear layer growth rate as M^+ increases.

Bogdanoff [19] measured the spreading rate of low speed shear layers using interferometry at a velocity ratio $\lambda_u = 0$ and with density ratios λ_ρ of 0.2 to 0.7. The experiment was conducted at higher velocities and at a smaller scale than previous work and at similar Reynolds numbers. This reduced the effect of buoyancy on the shear layer and the momentum deficit caused by a splitter plate. The apparatus (shown in Figure 2.10) consisted of three nozzles and two splitter plates with two shear layers originating from the outside nozzles. The flow is enclosed by optical flats aligned parallel to the nozzle walls using a alignment pins and a laser beam. The interferogram fringes were read at fixed distances from the nozzle exits until a distance x_{max} where the two shear layers interfered with the wake of the flow. The non-dimensional concentration profiles (defined by $c = (\rho - \rho_1)/(\rho_2 - \rho_1)$) were each given the same statistical weighting and hand fitted with curves. The maximum shear layer thickness $\delta_{\rho m}$ was obtained by measuring the 20 and 80 percent points on each profile and fitting a straight line between them. The intercept between this line and the 0 and 100 percent concentration levels is then defined as $\delta_{\rho m}$.

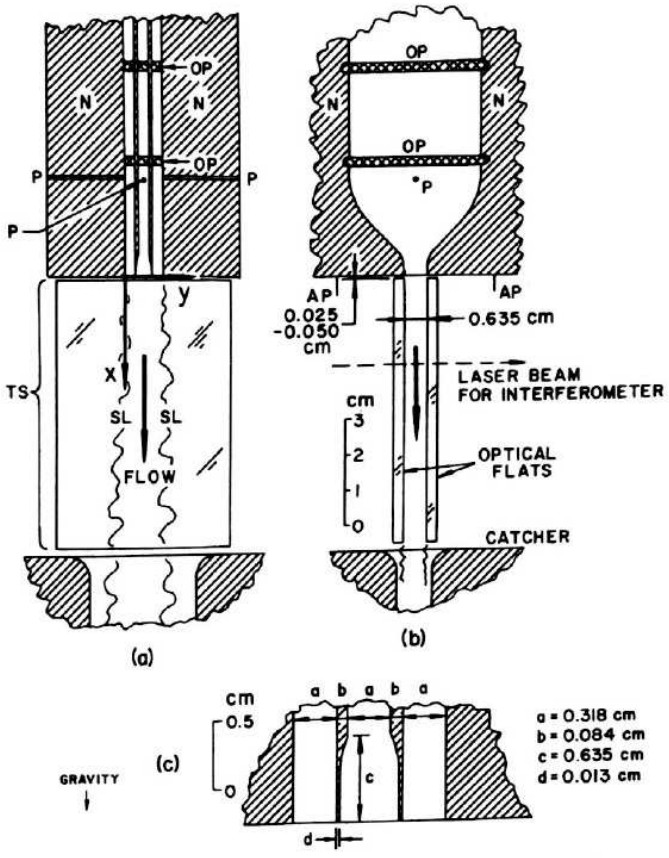


Figure 2.10: Experimental apparatus (a) Parallel to shear layers (b) Normal to shear layers (c) Magnification of nozzle exits [19]

Using Bogdanoff's previous work [18] on the convective velocity of the structures in the shear layer, the maximum shear layer thickness could be calculated for a fixed λ_ρ (shown as curves

a and b in Figure 2.11). These curves show a good agreement with the experimental data (Brown and Roshko's [17] data is included as flagged data points). The experiment allowed for results that were not affected by buoyancy with the resulting shear layers showing a high degree of self-similiarity. As the density ratio increases the shear layer profile broadens and shifts towards the low speed stream. Previous experimental work was shown to have been affected by buoyancy.

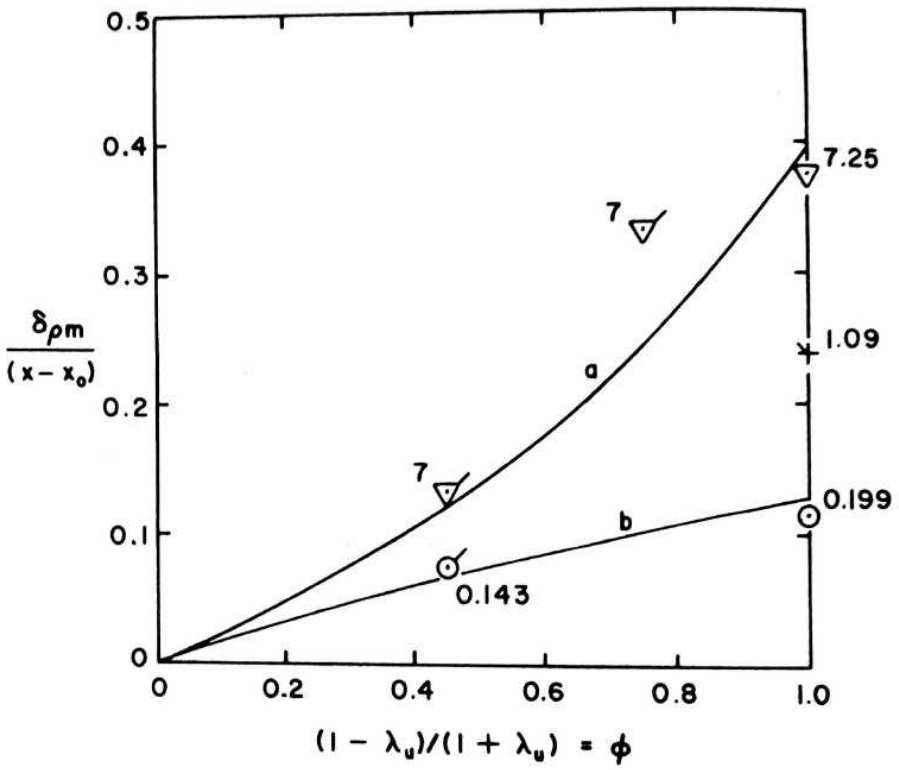


Figure 2.11: Shear layer spreading rates $\delta_{\rho m}$ vs ϕ with λ_ρ as a parameter [19]

Dimotakis [20] investigated the effect of velocity and density ratio on the entrainment ratio and growth of the shear layer. A spatially growing shear layer entrains different amount of fluid from each of the free streams (in favour of the high speed side) and this leads to a mixed fluid composition. It is well known that the large scale vortex structures convect with a constant velocity U_c. Using a Galilean reference moving at U_c allows a vortex fixed frame of reference to be used for analysis. In this frame of reference (shown in Figure 2.12) the high speed side would be travelling at $U_1 - U_c$ while the low speed side would be travelling in the opposite direction at $U_c - U_2$.

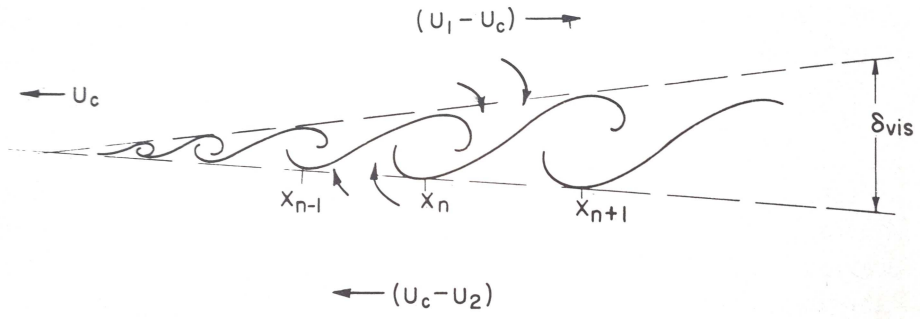


Figure 2.12: Vortex reference frame showing large structures and induced velocities [20]

To begin the analysis, a velocity $-U_c$ is imposed on the splitter plate and vortex x_n is defined at an instant between vortex pairings as seen in Figure 2.12. The fluid induction velocity to the vortex frame velocity ratio is expressed as a dimensionless function:

$$\epsilon\,(r, s) = \frac{U_1 - U_c}{U_c - U_2} = \frac{1 - r_c}{r_c - r} \tag{2.14}$$

where $r_c = U_c/U_1$.

Using the above Equation 2.14 and the argument proposed by Bogdanoff [18], the freestream velocity ratio with respect to the vortices is given by:

$$\frac{1 - r_c}{r_c - r} = s^{1/2} \tag{2.15}$$

Equation 2.15 can then be normalized with respect to r_c:

$$r_c\,(r,s) = \frac{1 + rs^{1/2}}{1 + s^{1/2}} \tag{2.16}$$

The above Equation 2.16 reveals the following information:

- The convection velocity r_c increases linearly with r
- For equal densities ($s = 1$), $r_c = (1 + r)/2$ i.e the mean speed $\bar{r}$
- For a heavy high speed fluid ($\rho_1 > \rho_2$), the vortex velocity U_c exceeds the mean speed of the layer $\bar{U} = (U_1 + U_2)/2$
- For a light high speed fluid ($\rho_2 > \rho_1$), the converse occurs
- Good agreement is shown with Brown and Roshko's [17] data of $r_c(r = 0.38, s = 7) = 0.55$

The growth of the shear layer is taken to be linear in time. By assuming that the vortex pairings are constant and using the mean vortex spacing to position ratio $(l/x) = 0.68(1 - r)/(1 + r)$ obtained from Brown and Roshko[17] leads to:

$$\frac{\delta}{x} = \epsilon \left[\frac{1 - r}{r_c} - \left(1 - \frac{1 + r}{2r_c}\right) \left(\frac{\frac{l}{x}}{1 + \frac{l}{2x}} \right) \right] \tag{2.17}$$

By substituting in for r_c from Equation 2.16 and (l/x) the prediction of the two-dimensional shear layer growth is given by:

$$\frac{\delta}{x} = \epsilon \left(\frac{1 - r}{1 + rs^{1/2}} \right) \left[1 + s^{1/2} - \frac{1 - s^{1/2}}{1 + 2.9\left(\frac{1+r}{1-r}\right)} \right] \tag{2.18}$$

For $s = 1$ the above Equation 2.18 reduces to the familiar form:

$$\frac{\delta}{x} = c \left(\frac{1 - r}{1 + r} \right) \tag{2.19}$$

Show in Figure 2.13 is Brown and Roshko's [17] data for density ratios of $1/7, 1$ and 7 plotted against $(1 - r)/(1 + r)$. The solid lines represent the calculated values of δ_ω/x with the constant $\epsilon = 0.17/2$.

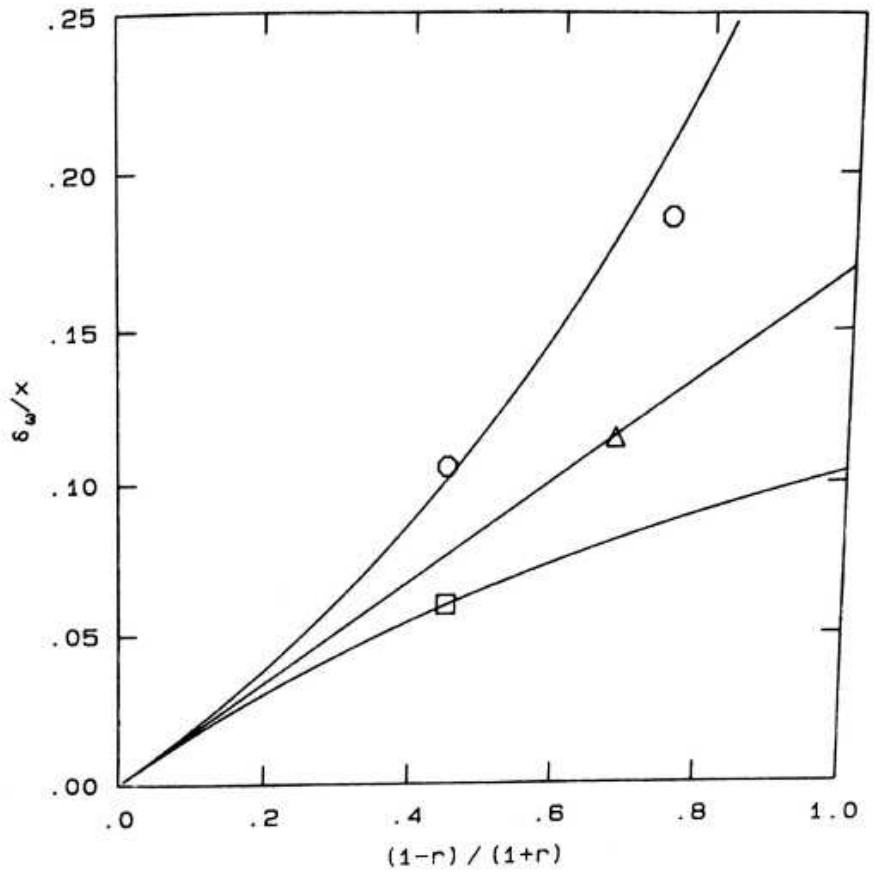


Figure 2.13: Vorticity (maximum slope) thickness for $s = 1/7, 1, 7$ [20]

Chinzei et al. [21] investigated the spreading of two stream supersonic turbulent mixing layers. A high pressure reservoir feeds through a pressure regulator before being divided into two streams by a splitter plate. An orifice and nozzle are adjusted on each side to control the velocity ratio. A schematic of the apparatus used is shown in Figure 2.14. The free stream Mach number was $M_1 = 2.3$ on the high velocity side and the low velocity Mach number M_2 varied between $0, 0.19, 0.49, 0.65, 0.80$ and 1.4. Compression and expansion waves form in the test section due to the trailing edge of the splitter plate, this was accounted for by transforming the measured flow fields using isentropic relations into uniform pressure fields.

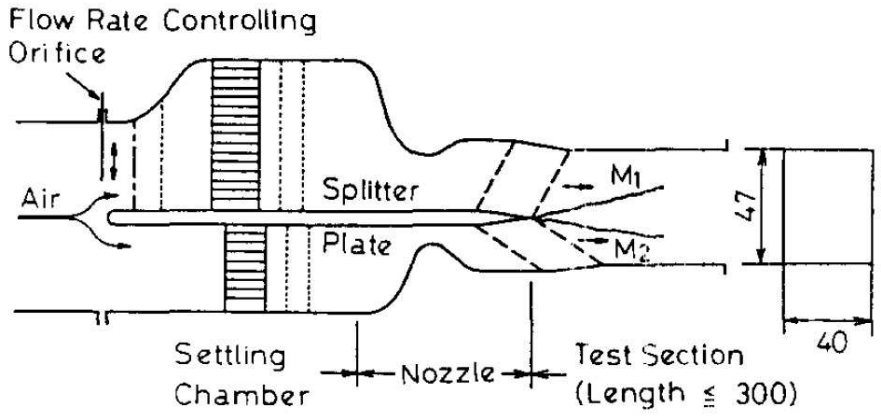


Figure 2.14: Experimental apparatus ($M_2 = 1.4$ test conditions) [21]

The mixing layer thickness b is the distance between the two points where the velocity $U = (0.1)^{0.5}(U_1 - U_2) + U_2$ and $U = (0.9)^{0.5}(U_1 - U_2) + U_2$. The spreading rate db/dx was then obtained by using a linear least square fit. The spreading rates were normalised by the Langley curve incompressible value of $(db/dx)_{0i} = 0.115$. Shown in Figure 2.15 is the experimental data showing good agreement with the Langley curve. In order to represent the effect of compressibility a parameter is introduced, denoted by $\lambda = (1-r)/(1+r)$. The incompressible relation $db/dx \approx \lambda$ is shown as a dotted line in Figure 2.16. The experimental data better fit the upper dotted line if λ is small, indicating a dependence on r for compressible flows. Using Bogdanoff's geometric average Mach number relation M^+ and under the assumption that the Langley curve in Figure 2.15 is valid for two stream mixing layers if plotted against $2M^+$[21] for a fixed value of λ, then the following relation is obtained:

$$\lambda = (M_1 - M_2\beta) \,/\, (M_1 + M_2\beta) \tag{2.20}$$

Where $\beta = \frac{a_2}{a_1}$ is the ratio of sound speeds. The experiment used $M_1 = 2.3$ and is plotted as the solid line on Figure 2.16, showing a good agreement with experimental data. The spreading rates are dominated by λ for low M_1 values (i.e an incompressible velocity ratio

effect [21]), whilst at much higher M_1 values the effect of compressibility governed by M^+ is apparent.

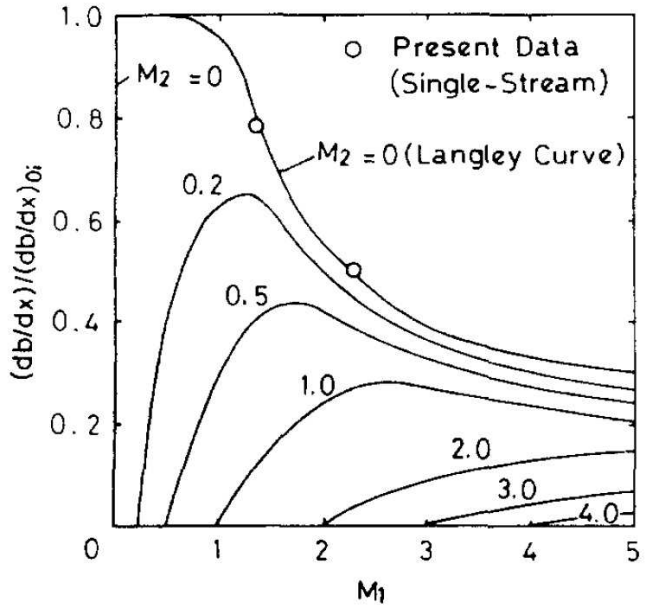


Figure 2.15: Spreading rate variation with M_1 [21]

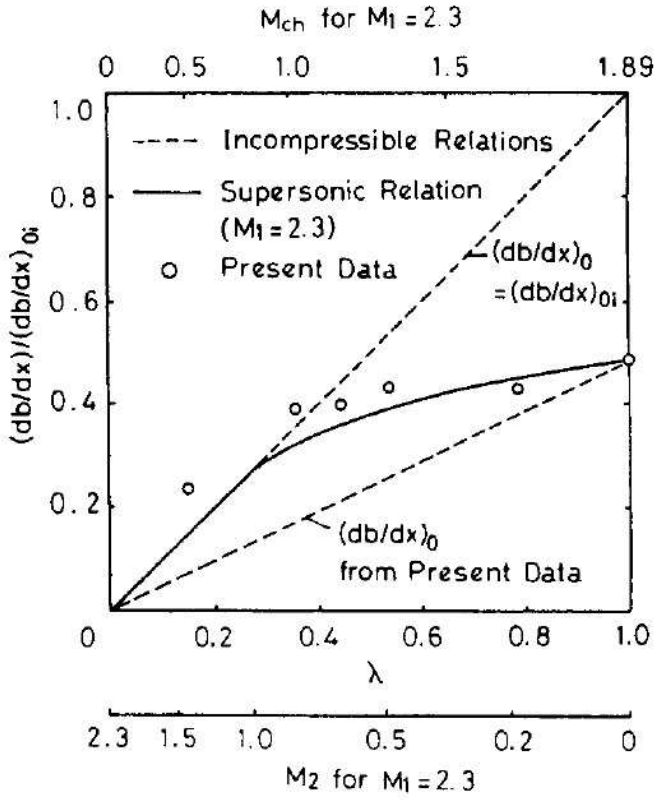


Figure 2.16: Spreading rate variation with λ [21]

Papamoschou and Roshko [22] investigated the growth of compressible turbulent shear layers. The experimental apparatus consisted of a two-stream blow-down supersonic wind tunnel where each stream is supplied independently (a schematic is shown in Figure 2.17). The test gas is supplied from an array of gas bottles where it passes through a pressure regulator and fast opening solenoid valve. From here it enters a settling chamber before it is expanded to the desired Mach number by a shaped centrebody. The test gases meet at a 0.3mm thick trailing edge. Streamwise pressure gradients are minimised by adjusting the upper and lower walls of the test section. Ten combinations of gases at Mach numbers ranging from 0.2 to 4 were tested with schlieren visualisation revealing large scale structures as observed in previous experiments. A pitot probe mounted on a pivot downstream of the trailing edge is used for taking measurements across the shear layer.

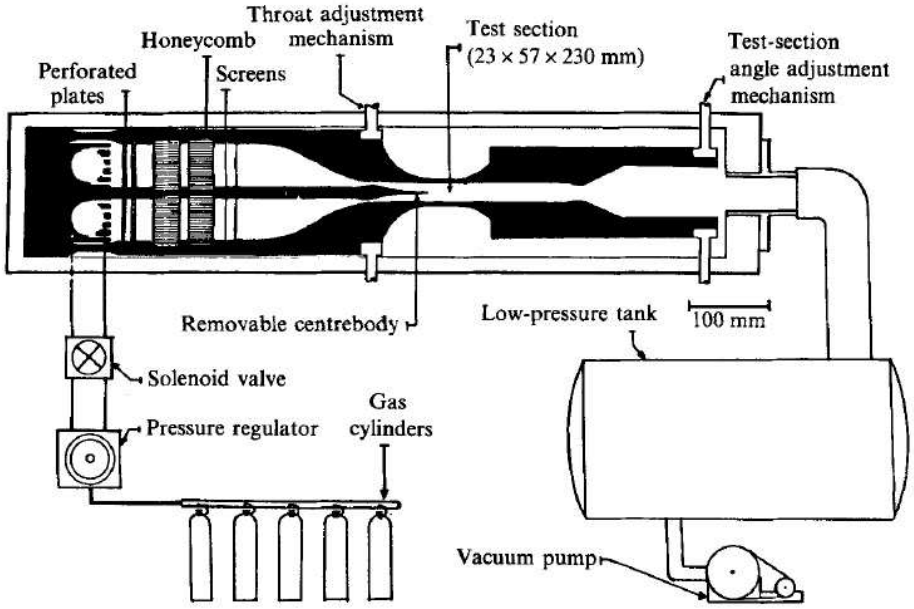


Figure 2.17: Experimental apparatus [22]

From the schlieren images it was observed that the shear layers all had low spreading rates when compared to previous subsonic experiments. The pitot thickness data revealed that the shear layers grow linearly which is expected as they are fully turbulent. In order to compare to previous experiments, the pitot thickness δ_{pit} is related to the visual thickness δ_{viz} and vorticity thickness δ_{ω} by the following relations (derived from Brown [17] and other experiments[22]):

$$\delta_{\omega} = 0.5\delta_{viz} \tag{2.21}$$

$$\delta_{pit}/\delta_{viz} = 0.8 \tag{2.22}$$

In order to correlate the effect of compressibility on the growth rate of the shear layer it is important to note that a flow with a high Mach number M_1 may have a similar velocity to the other stream ($U_1 \approx U_2$) and therefore a small velocity difference with respect to either sound speed. Therefore the work of Bogdanoff[18] was chosen as a starting point with the convective Mach number M^+. Using a reference frame attached to the convecting structures as discussed previously, the convective Mach numbers are defined as:

$$M_{c_1} = \frac{U_1 - U_c}{a_1} \tag{2.23}$$

$$M_{c_2} = \frac{U_c - U_2}{a_2} \tag{2.24}$$

Using the same argument posed by Bogdanoff the following relation is derived (the same as in Dimotakis[20]):

$$\frac{U_c}{U_1} = \frac{1 + \frac{U_2}{U_1}\left(\frac{\rho_2}{\rho_1}\right)^{1/2}}{1 + \left(\frac{\rho_2}{\rho_1}\right)^{1/2}} \tag{2.25}$$

For gases of the same specific heat ratio, the convective velocity is defined as:

$$U_c = \frac{a_2 U_1 + a_1 U_2}{a_1 + a_2} \tag{2.26}$$

The effect of compressibility on the growth rate is better expressed as a function of M_{c_1} and is assumed to be:

$$\delta^{'} = f\left(\frac{U_2}{U_1}, \frac{\rho_2}{\rho_1}, \frac{\gamma_2}{\gamma_1}, M_{c_1}\right) \tag{2.27}$$

In order to understand the effect of M_{c_1} on the growth rate it is normalised with respect to the incompressible growth rate (denoted subscript 0) for the same velocity and density ratio (the effect of specific heat ratios is thought to be negligible). The growth rate is thought to be in the form:

$$\delta_0^{'} \approx \frac{\Delta U}{U_c} \tag{2.28}$$

Using Equation 2.25 this becomes (with inclusion of constant 0.17 from Brown[17]):

$$\delta'_{vis,0} = 0.17\frac{\Delta U}{U_c} = 0.17\frac{\left[1-\frac{U_2}{U_1}\right]\left[1+\left(\frac{\rho_2}{\rho_1}\right)^{1/2}\right]}{1+\frac{U_2}{U_1}\left(\frac{\rho_2}{\rho_1}\right)^{1/2}} \tag{2.29}$$

Shown in Figure 2.18 is the prediction of Equation 2.29 plotted against visual growth rates obtained experimentally in Brown [17], good agreement is obtained for density ratios of 7, 1 and 1/7. In order to compare to Papmoschou's experiment, Equation 2.29 can be related using Equation 2.22 to the incompressible pitot thickness, resulting in:

$$\delta'_{pit,0} = 0.14\frac{\left[1-\frac{U_2}{U_1}\right]\left[1+\left(\frac{\rho_2}{\rho_1}\right)^{1/2}\right]}{1+\frac{U_2}{U_1}\left(\frac{\rho_2}{\rho_1}\right)^{1/2}} \tag{2.30}$$

The normalised growth rate $\delta'_{pit}/\delta'_{pit,0}$ is plotted against M_{c_1} in Figure 2.19. This decreases as M_{c_1} increases until it levels off for $M_{c_1} > 0.8$ where the value remains approximately constant. This can be compared to the incompressible growth rate by noting that when the higher density gas is the high velocity stream, the growth rate is smaller and vice versa. It is implied therefore that the growth rate increases with decreasing velocity ratio. From Figure 2.19 it is clear that the reduction in growth rate occurs whilst M_{c_1} is still subsonic, one such explanation for this is that energy removal decreases the vortex amalgamation process, resulting in a decreased growth rate.

Ragab and Wu [23] investigated the stability characteristics of supersonic mixing layers of differing velocity and temperature ratios. Further work was done on substantiating the convective Mach number M^+ using spatial linear stability analysis for various velocity profiles. The growth rate of the shear layer reaches a maximum value at a particular velocity ratio for a set Mach number, temperature ratio and frequency. The convective Mach number M^+ was found to correlate compressibility effects on the growth rate of the shear layer. The spreading rates of compressible and incompressible shear layers at the same velocity and density ratio were found to depend on convective Mach number, this agrees with the work of Papamoschou and Roshko[22].

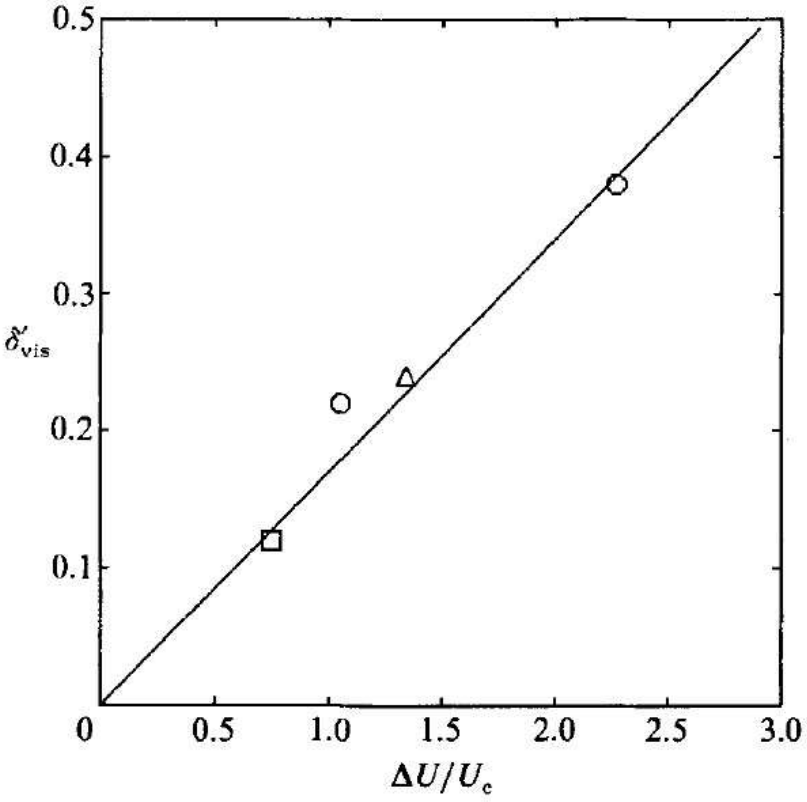


Figure 2.18: Visual thickness growth rate versus $\Delta U/U_c$ [22]

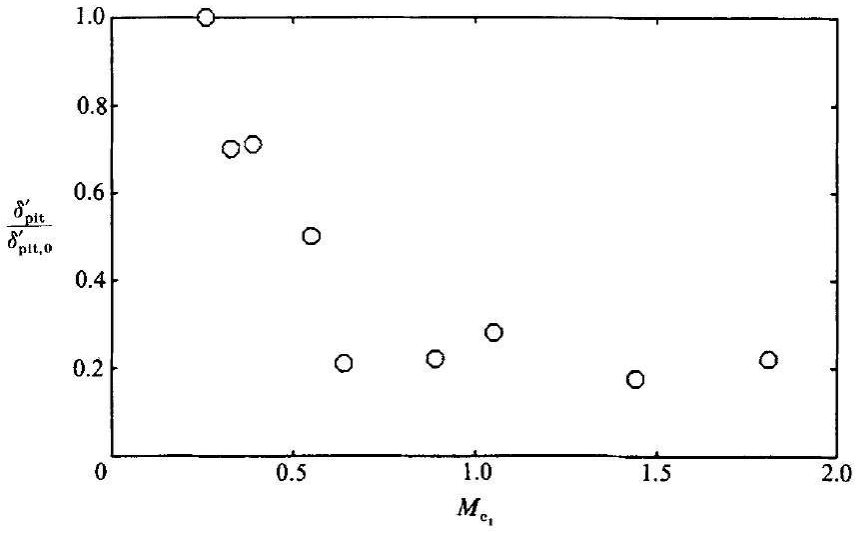


Figure 2.19: Normalised pitot thickness growth rate versus M_{c_1} [22]

2.3.3 The Kelvin Helmholtz Instability

The Kelvin-Helmholtz Instability occurs along a shear layer, which is the result of two fluids flowing with different tangential velocities close to each other. When the layer is perturbed, it breaks down into a series of vortices that cause mixing of the two fluids. The KHI plays an important role in the study of turbulence and occurs in other instabilities such as the Richtmyer-Meshkov and Rayleigh-Taylor instabilities[24]. The vortices evolve in a self-similar manner by amalgamating as discussed in Brown and Roshko[17], Dimotakis[20] and Papamoschou and Roshko [22].

Rikanati, Alon and Shvarts [24] derived a statistical model based on the growth of a single vortex in the shear layer and the amalgamation process with neighbouring vortices. The mixing layer growth was derived non-empirically for equal densities across the shear layer and is defined as:

$$\delta h_{max}\left(x\right) = 0.4\left(\frac{U_1 - U_2}{U_1 + U_2}\right)x \tag{2.31}$$

The mixing layer growth is dominated by the vortex amalgamation process and is found to be independent of density ratio. Using the assumption of Dimotakis[20]: for density ratios differing from 1, the vortices drift toward the higher density side of the shear layer. The growth of the mixing layer is then defined:

$$\delta h_{max}\left(x\right) = 0.4\left(\frac{S}{1 - 2f_d\left(\rho_1/\rho_2\right)S}\right)x = g_R\left(S, \rho 1/\rho 2\right)x \tag{2.32}$$

where:

$$f_d\left(\rho_1/\rho_2\right) = \frac{U_d}{\left(U_1 - U_2\right)} = \frac{1}{2}\left|\frac{1 - \sqrt{\rho_2/\rho_1}}{1 + \sqrt{\rho_2/\rho_1}}\right| \tag{2.33}$$

$$S\left(U_1, U_2\right) = \frac{U_1 - U_2}{U_1 + U_2} \tag{2.34}$$

The drift velocity U_d affects the growth of the mixing layer as the drift direction is always into the higher density fluid:

- Growth rates are inhibited if the higher density fluid is on the slower side
- Growth rates are enhanced if the higher density fluid is on the faster side

The resulting growth rates $g_R(S)$ are plotted in Figure 2.20 with data from Brown and Roshko[17], with the current model a good agreement is obtained.

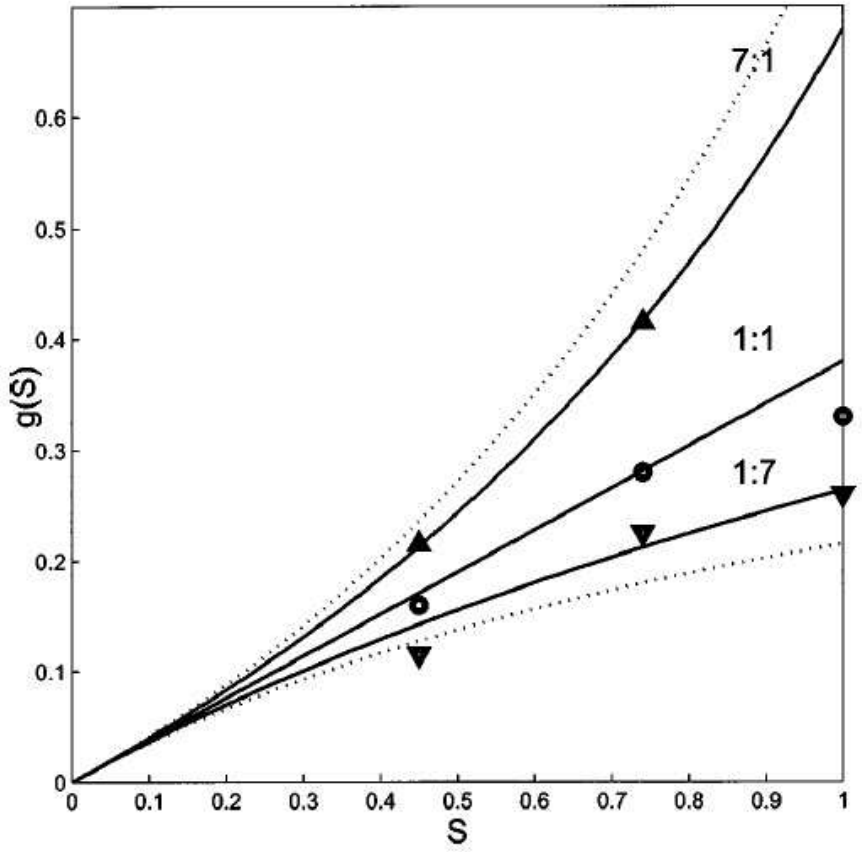


Figure 2.20: Growth rates as a function of S [24] with data from Brown and Roshko[17]. Dotted lines from Dimotakis[20]

Rikanati et al. [14] used growth rates of large-scale KHI shear flows to model the shear layer growth occurring in a Mach Reflection. The thickening of the shear layer was found to be caused by secondary turbulent mixing. The width of the shear layer is expected to grow as a function of time:

$$\delta h\left(t\right) = c\Delta U t \tag{2.35}$$

where δh is the width of the mixing layer, ΔU is shear velocity and $c = 0.19 \pm 0.01$ derived experimentally in Brown and Roshko[17]. Experimentally the growth of the shear layer is measured spatially from the triple point. The spatial growth is related to the temporal growth by assuming that the mixing layer fluid flows downstream at the average velocity of the two fluids:

$$\delta h\left(x\right) = 2c\left[\left(U_1 - U_2\right) / \left(U_1 + U_2\right)\right] x \tag{2.36}$$

where U_1 and U_2 represent the fluid velocities across the shear layer and x is the distance from the triple point. The above Equation 2.36 is corrected for fluids of different densities (see Rikanati, Alon and Shvarts [24]) and for high Mach number shear velocities i.e. $\Delta U/a > 1$. The mixing layer width is then defined:

$$\delta h\left(x\right) = \left(0.38 \pm 0.02\right) \frac{S}{1 - 2f_d\left(\rho_1, \rho_2\right) S} \times x f_{HiMach}\left(\frac{\Delta U}{a}\right) \tag{2.37}$$

where f_{HiMach} is based on a parametric fit of results in Ragab and Wu [23]. The other variables are defined previously in Equations 2.33 and 2.34:

$$f_{HiMach}\left(\frac{\Delta U}{a}\right) = 0.5\left(1 - tanh\left(2\left(\frac{\Delta U}{a} - 1.2\right)\right)\right) \tag{2.38}$$

The spread angle of the shear layer from the triple point is then defined as:

$$\theta_{spread} = arctan\left(\frac{\delta h\left(x\right)}{2x}\right) \tag{2.39}$$

To calculate the required variables in the regions across the shear layer, Three Shock Theory was used as discussed in Section 1.3. Theoretical predictions are shown as curves in Figure 2.21 with θ_w as a parameter. The wall angles ranged from $\theta_w = 45°$ (solid line), $\theta_w = 40°$ (dashed-dotted line), $\theta_w = 30°$ (upper dashed line) and $\theta_w = 20°$ (lower dashed line).

As expected the spread angle increases as a function of Mach number until a value of 8° where the effect of f_{HiMach} in Equation 2.37 influences the shear layer. Experimental results are plotted on Figure 2.21 with the same wedge angles as the theoretical predictions. Ambient air was used as the test gas with $P_0 = 10.1$ kPa and $M_s = 1.55, 1.9, 2.3, 2.78$. The spread angle was measured from the interferogram images by drawing two straight lines from the triple point bounding the mixing layer. The uncertainty in measurements was estimated at half the thickness of a single fringe.

Good agreement is shown in Figure 2.21 apart from the $M_s = 1.55$ experiments, for $M_s < 2$ with $\theta_w = 30°$ and for $M_s < 2.4$ with $\theta_w = 20°$. This can be attributed to Shear Reynolds number, calculated by:

$$Re = \frac{\Delta U l}{\nu} \tag{2.40}$$

Where l is the characteristic length scale chosen according to the typical height of the Mach stem and ν is the average kinematic viscosity across the shear layer. For $Re > 2 \times 10^4$ good agreement is obtained with experiments. Interestingly for experiments conducted at different P_0 initial conditions and the same M_s, good agreement is obtained for higher P_0 due to higher densities across the shear layer and therefore smaller kinematic viscosity and larger Reynolds numbers.

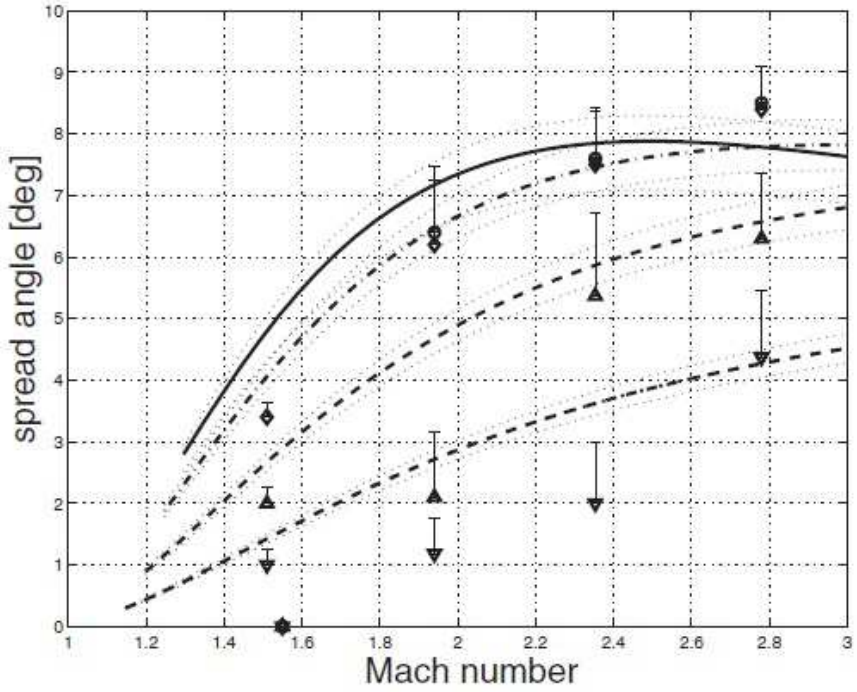


Figure 2.21: Spread angle of the shear layer as a function of Mach number [14]

Chapter 3 Objectives

The research objectives are formulated from the motivation outlined in Section 1.6 and are as follows:

- Characterise the growth of the compressible shear layer of a Mach reflection
  - Compare Three Shock Theory to experimental shock angles
  - Utilise Three Shock Theory to obtain theoretical velocity and density ratios across the shear layer. Compare theoretical to experimental growth rates
  - Assess the self-similarity of the shear layer using a large scale shock tube
- Utilise Computational Fluid Dynamics (CFD) to aid in design of the wedge angles to be tested and for experimental comparison where possible

Chapter 4 Experimental Facilities and Method

4.1 Overview

Two different shock tubes were used for the experimental research. Single shot high resolution photography was used to capture images of the flow field at a specified delay. This chapter covers the facilities used and outlines the operating procedures involved. Engineering Drawings may be found in Appendix A.

4.2 The Large Blue Shock Tube (LBST)

4.2.1 Overview of the LBST

The Large Blue Shock Tube (LBST) consists of a circular driver connected to a rectangular driven section, a schematic is shown in Figure 4.1. The driver is fitted with wooden inserts to decrease the driver volume, this decreases the downtime between tests. The pressure vessel is mounted on rails that allow the vessel to be decoupled from the driven section to change the diaphragm between tests. The driver is bolted to the driven section by 16 M32 bolts that are tightened and loosened by using a pneumatic torque wrench. The driven section consists of three 2m long rectangular sections with an internal height of 450mm and width of 100mm.

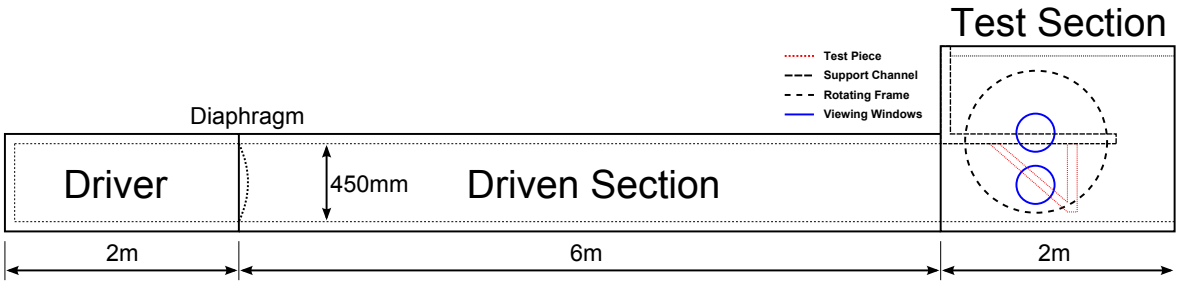


Figure 4.1: Large Blue Shock Tube Schematic

The test section is bolted to the end of the driven section and has an identical cross-section. The viewing windows are 315mm diameter and are mounted in a 1.1m diameter frame at a fixed radius. The frame can rotate, this allows different regions of the test section to be viewed. The test pieces are mounted upside down to a steel channel in the test section by two M10 cap screws. The viewable region of the test piece is covered with a thin layer of double sided tape to create a seal against the window and to prevent the glass from being scratched. Under normal conditions the shock tube is operated manually and uses a single diaphragm, controlled burst technique. A diaphragm of required thickness is inserted between the driver and driven section of the tube and secured by bolting the two flanges together. The driver is then pressurised to the required pressure for the test. The diaphragm is manually burst using a spring loaded pricking device initiated by the operator. A shock wave forms in the driven section and propagates into the test section where it is visualised.

Table 4.1: LBST Specifications

Specification	**Detail**
Driver Length:	2m
Driver Diameter:	450mm
Driver Gas:	Air
Maximum Driver Pressure:	10 Bar
Operation:	Manual Diaphragm Pricking
Expansion Chamber Length:	6m
Expansion Chamber Gas:	Air
Expansion Chamber Pressure:	Atmospheric
Mach Number Range:	$1.1 \leq M_s \leq 1.5$
Test Section Length:	2m
Test Section Dimensions:	450mm×100mm
Viewing Windows:	Borosilicate Glass (BK7) 315mm Diameter 25mm Thickness

4.2.2 LBST Test Pieces

The test pieces were manufactured out of 100mm wide standard steel channel with the wedge angles being chosen from the preliminary study in Section 5.1. The top surface of the channel was polished to a fine surface finish to ensure boundary layer effects were minimised and then spray-painted matte black to eliminate surface reflections affecting the optical visualisation. The sides of the channel were then machined down to 98.5mm to ensure a tight fit in the test section. Only the side sections of the wedge in the viewing area of the window was covered

in double-sided tape. The leakage past the wedge not lined with tape was assumed to be minimal in the experiment and was therefore deemed acceptable. The critical dimensions of each test piece are outlined in Table 4.2:

Table 4.2: LBST Test piece dimensions

Wedge Angle [°]	**Surface Length** [mm]	**Height** [mm]	**Length** [mm]	**Width** [mm]
30	778.4	386.3	674.1	98.5
40	600.4	385.9	459.9	98.5

4.2.3 Operating Procedure of the LBST

Ensure the laboratory compressor is switched on and the supply tank is pressurised to the required pressure for testing. The supply pressure must be above 6 bar in order to tighten the bolts of the driver sufficiently.

4.2.3.1 Start up procedure

1. Switch on all instrumentation: oscilloscope, signal conditioners and delay box
2. Ensure the oscilloscope Volt/division and Time/division settings are correct for the testing planned for the day
3. Check the pressure transducers are connected correctly using the channel selector on the signal conditioner box
4. Switch on the camera, ensure it is set to "Quick-response remote" for use with the infra-red remote
5. Remove the covers on the parabolic mirrors for the optical visualisation

4.2.3.2 Testing procedure

The testing procedure is continued from the previous day where the driver has been decoupled from the driven section and the ruptured diaphragm has been removed from the driver flange.

1. Obtain the required number of diaphragms for testing and affix these to the driver flange using a small piece of masking tape

2. Latch the diaphragm pricker into the locked position by pulling it back against the spring. Ensure the string is attached to the release arm
3. Slide the driver vessel towards the driven section and bolt it closed using the pneumatic wrench
4. Close the supply valve and open the release valve on the control panel
5. Open the supply line at the wall
6. Set the trigger box delay to the desired value for the test (in μs)
7. Arm the trigger delay box and oscilloscope
8. Lock the laboratory doors using the switch at the wall. This sounds an alarm notifying persons in the area that a test is to be conducted
9. Switch off all lights in the room. The operator must wear a head lamp to monitor the driver pressurisation process
10. Close the release valve on the control panel
11. Slowly open the supple valve on the control panel, the driver will begin to pressurise
12. Once the desired pressure has been reached, close the supply valve on the control panel
13. Switch off the operator headlamp and open the camera shutter using the infra-red remote
14. Pull the string connected to the diaphragm pricker, the shock tube will then fire
15. Close the camera shutter using the infra-red remote
16. Switch on all room lights
17. Open the release valve on the control panel
18. Record the Δt value displayed on the oscilloscope in order to obtain the Mach number of the shock wave
19. Record the burst pressure, Δt, image number and trigger box delay of the test in the logbook
20. Loosen the bolts on the driver section, decouple the driver vessel and remove the burst diaphragm from the driver flange
21. Vent the driven section of the shock tube using the pneumatic hose attached to the release valve

4.2.3.3 Shut down procedure

1. Close the supply line valve at the wall and vent any remaining pressure in the supply line using the release ball valve
2. Close the valve at the wall and vent any remaining pressure in the pneumatic wrench line
3. Replace the covers on the parabolic mirrors
4. Switch off all instrumentation: oscilloscope, signal conditioners and delay box
5. Switch off the camera, remove the memory card and save the images to a hard drive

4.2.3.4 Precautions

- Hearing protection must be worn when operating the pneumatic wrench
- Hearing protection must be worn for the duration of the test procedure
- Inspect the driven section of the shock tube for any foreign bodies before running a test
- Sound the secondary siren before initial driver pressurisation and at approximately half the required burst pressure
- Ensure the area downstream of the test section is clear of any debris before testing
- Clean the test section windows and parabolic mirrors with a soft cloth and acetone regularly to obtain clear images
- Regularly check and tighten the bolts securing the test piece to the mounting channel and the bolts securing the window frames to the test section

4.3 The Michael Seitz Automated Shock Tube (MSAST)

4.3.1 Overview of the MSAST

The Michael Seitz Automated Shock Tube (MSAST) was designed and used for experimental research by Michael Seitz as part of his PhD Thesis[25]. The general layout of the shock tube is shown in Figure 4.2. The shock tube uses an automated double diaphragm bursting technique, which results in highly repeatable testing conditions.

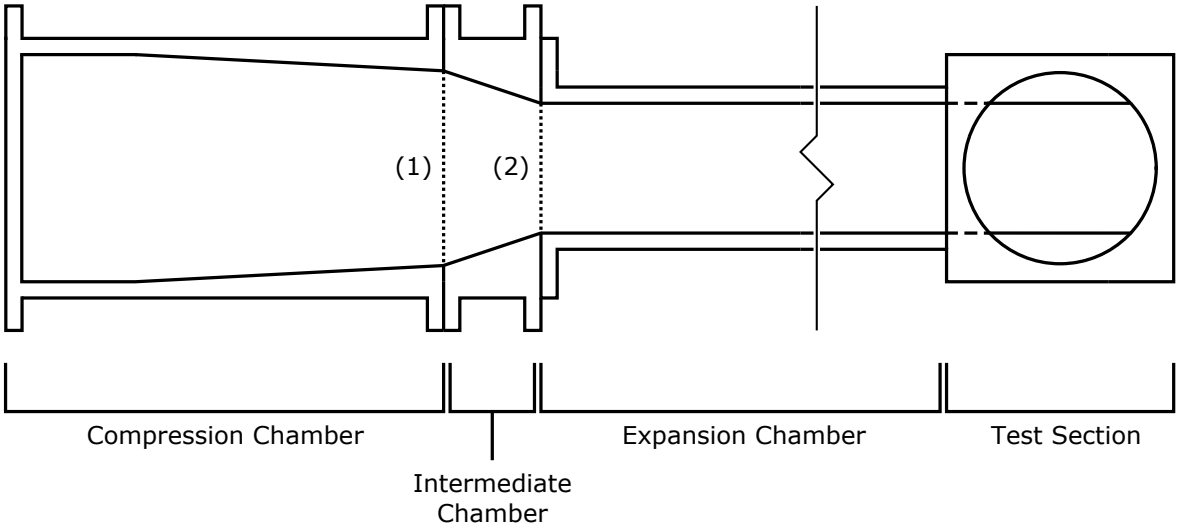


Figure 4.2: Schematic of the Michael Seitz Automated Shock Tube (MSAST)

The compression chamber is a circular pressure vessel with internal diameter 300mm that is certified to a maximum pressure of 20 bar. The vessel has polyurethane rubber inserts to reduce the area near vessel exit to a square 180 by 180mm. Inserts are used in the intermediate chamber as well to reduce the area to its final rectangular cross-section of 180 by 76mm. The area reduction from the compression chamber to the expansion section results in an increase in Mach number[25]. The expansion chamber is 180 by 76mm rectangular cross-section made from cast-iron sections bolted together. The test section bolts on to the end of the expansion section and houses two 300mm diameter optical windows. The window frames are mounted on hinges, this allows for easy changing of test pieces when required. The test pieces are mounted in the test section from the end wall by three M8 bolts. The top and bottom walls of the test section have ports for pressure transducer readings to be taken. Two ports in the expansion section (just before the test section) are used for obtaining the Mach number of the test; this is recorded by the automation software and used when calibrating the diaphragms. Transverse waves formed from the finite rupture of the diaphragm are dampened by means of thick-pile carpeting fixed to the top and bottom walls of the expansion chamber[25]. The specifications of the MSAST operating under normal conditions are outlined in Table 4.3.

Table 4.3: MSAST Specifications

Specification	**Detail**
Driver Length:	2m
Driver Diameter:	300mm
Driver Gas:	Air
Maximum Driver Pressure:	20 Bar
Operation:	Automated
Expansion Chamber Length:	6m
Expansion Chamber Gas:	Air
Expansion Chamber Pressure:	Atmospheric
Mach Number Range:	$1.1 \leq M_s \leq 1.8$
Test Section Length:	450mm
Test Section Dimensions:	180mm×76mm
Viewing Windows:	Borosilicate Glass (BK7) 250mm Diameter 55mm Thickness

Under normal operating conditions the shock tube is controlled by an automated computer program. Once diaphragms of specific thickness have been calibrated, the operator selects the required Mach number of the test. The required diaphragms are positioned at station (1) and (2) in Figure 4.2 and the compression and intermediate chambers are closed hydraulically. Both chambers are then pressurised simultaneously to the required pressure with the compression chamber at a higher pressure. To initiate a test the intermediate chamber is vented to atmosphere, this causes the diaphragm at (1) to rupture. A steep compression/shock then ruptures the diaphragm at (2), sending a shock wave into the expansion chamber where it is visualised in the test section. A 25mm spaced square grid is bolted to one of the viewing windows and is visible in the experimental images; this is used for scaling purposes as well as for optical distortion corrections. To obtain higher Mach numbers the expansion chamber may be evacuated. The shock tube was calibrated by Seitz[25] over a range of $1.2 \leq M_s \leq 1.7$. The expansion section was evacuated and leak-tested down to a pressure of 2 torr[25].

4.3.2 MSAST Test Pieces

The test pieces were manufactured from aluminium stock and machined to a final width of 75mm to fit into the test section. A range of wedge angles was required for testing in the MSAST with the final angles consisting of a 25°, 30°, 35° and 38° wedge angle. The 30° and 38° wedges was the same as that used by Rubidge and Skews[13]. The 30° wedge was used without a spacer to ensure the apex was visible during testing. A new spacer was manufactured from PVC for the 25° and 35° wedges to maximise the portion of the wedge surface visible in the test section windows. The sides of the spacer and wedge were lined with tape to ensure a tight seal against the windows once the test section was bolted closed. The critical dimensions of each test piece are outlined in Table 4.4:

Table 4.4: MSAST Test piece dimensions

Wedge Angle [°]	**Surface Length** [mm]	**Height** [mm]	**Length** [mm]	**Width** [mm]
25	244.3	107.3	221.4	75
30	300.0	155	259.8	75
35	237.2	140	194.3	75
38	266.4	168	212	75

4.3.3 Operating Procedure of the MSAST

Ensure the high pressure laboratory compressor is switched on and the supply tank is pressurised to the required pressure for testing.

4.3.3.1 Start up procedure

1. Switch on the automated computer system and signal conditioners
2. Open the pressure control valve at the wall, ensuring sufficient pressure is available for the days testing
3. Check the pressure transducers are connected correctly using the channel selector on the signal conditioner box
4. Switch on the camera, ensure it is set to "Quick-response remote" for use with the infra-red remote
5. Remove the covers on the parabolic mirrors for the optical visualisation

4.3.3.2 Testing procedure

The testing procedure is continued from the previous day where the test section doors and the compression and intermediate chambers are open.

1. Use the cleaning high pressure line to remove any diaphragm material from the expansion chamber, test section and vent tube
2. Secure the diaphragm required for the test to the flanges of the compression and intermediate chambers
3. Close the test section door and tighten the securing bolts using the hand spanner
4. Close the room door
5. Use the testing wizard on the automated computer to set the test Mach number and light source delay (in μs)
6. Before the chambers begin pressurisation, switch off the room lights and then open the camera shutter using the infra-red remote
7. The shock tube will be fired automatically at the correct pressure ratio by the automated computer
8. Once the test is over, close the camera shutter using the infra-red remote and then turn on the room lights
9. Before opening the compression and intermediate chambers, ensure the tube has depressurised to atmospheric conditions
10. Loosen the securing bolts and open the test section door

4.3.3.3 Shut down procedure

1. Close the pressure control valve at the wall
2. Replace the covers on the parabolic mirrors
3. Switch off the automated computer system and signal conditioners
4. Switch off the camera, remove the memory card and save the images to a hard drive

4.3.3.4 Precautions

- Hearing protection must be worn when cleaning the expansion section of the tube
- Hearing protection must be worn for the duration of the test procedure
- Ensure the test piece is securely fastened
- Ensure the test section door is securely closed before each test
- Do not leave the test section doors closed overnight
- Clean the test section windows and parabolic mirrors regularly (with a soft cloth and acetone), to obtain clear images

4.4 Optical Visualisation

A standard z-configuration shadowgraph flow visualisation technique was used. Two optical rails were positioned at approximately 10° to the central parallel light beam passing through the test section. To eliminate astigmatism, a cylindrical lens (f = 25mm) was used after the first cut-off. For the LBST testing, parabolic mirrors of diameter 350mmm were used whilst for the MSAST testing parabolic mirrors of diameter 254mm were used. A rail guided laser was used in the initial setup to ensure correct alignment of the optical equipment. The light passing through the test section windows was made perpendicular to the glass, this is important as any optical misalignment would cast a shadow across the shear layer. A 0.5mm thick aluminium plate was used with the light passing through a 0.3mm diameter hole to act as the cut-off. Table 4.5 details the specifications of the equipment used. The layout of the optical setup is shown in Figure 4.3 with the descriptions provided in Table 4.6.

Table 4.5: Flow Visualisation Equipment Specifications

Camera	
Specification	**Detail**
Camera Manufacturer:	Nikon
Model:	D90
Resolution:	12.2 Megapixel (4288×2848)
Format:	RAW
ISO Setting:	800-1600
Shutter Setting:	Quick-response Infrared Remote
Light Source	
Specification	**Detail**
Manufacturer:	Hamamatsu
Type:	Xenon Flash Lamp
Model:	SQ type L2437
Exposure Time	1.5μs

Two pressure transducers located in the test section of the shock tube were used to measure the arrival and velocity of the shock wave as it propagated towards the test section. In the LBST, this signal was sent to an oscilloscope that outputted a TTL-out signal when the shock passed the first transducer. A delay box received this signal and was used to trigger the xenon light source at the required delay for the test. In the MSAST, the operator specified the delay required using the shock tube computer program.

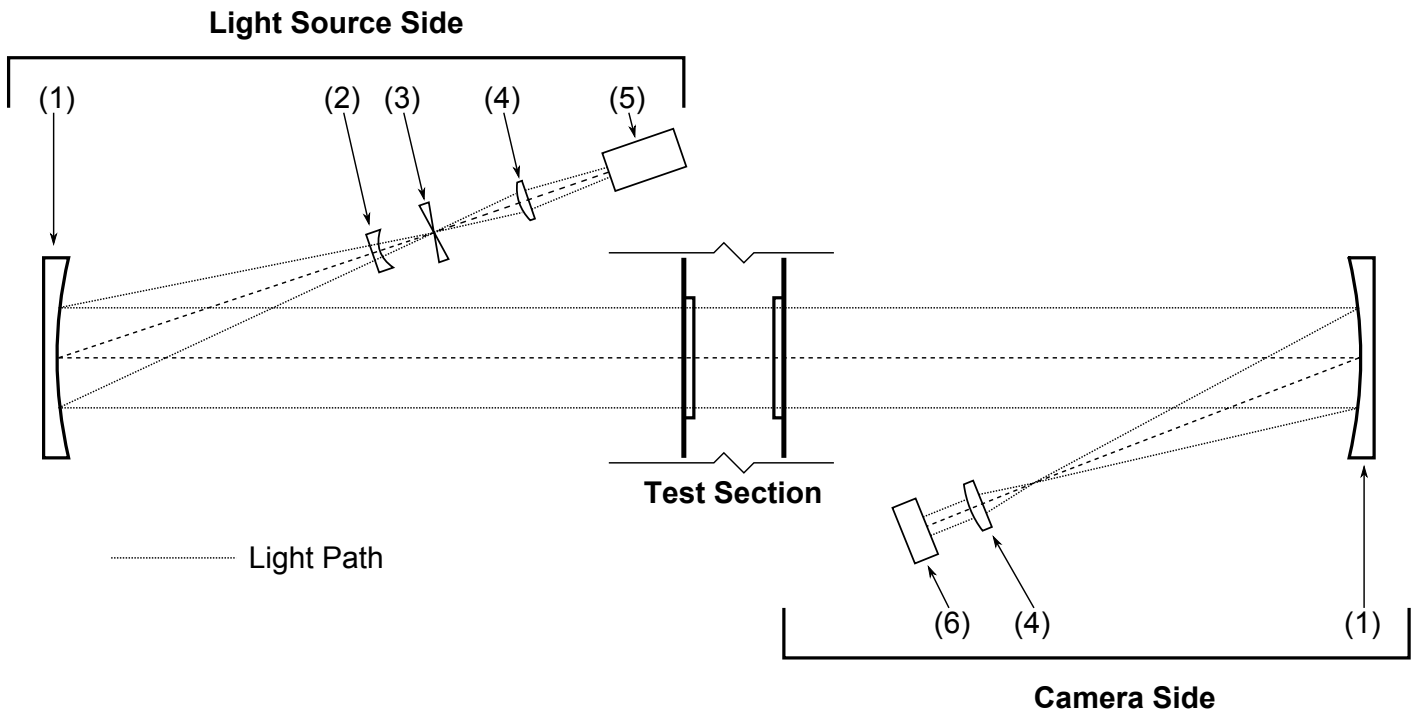


Figure 4.3: Flow Visualisation Layout

Table 4.6: Flow Visualisation Layout Specifications

Part Label	**Part Description**	**Part Label**	**Part Description**
(1)	Parabolic Mirror	(4)	Converging Lens
(2)	Cylindrical Lens	(5)	Xenon Light Source
(3)	Cut-off	(6)	Camera

Chapter 5 Numerical Method

5.1 Computational Fluid Dynamics

In order to select the wedge angles required for experimental testing, a commercial CFD package (Fluent 14) was used. Numerical results were obtained over a Mach number range from 1.34 to 1.61 to compare to previous numerical results by Rubidge[13] and corresponded to the available Mach number range in both the LBST and MSAST. The results were post processed in Tecplot 360 (2014 Release 1).

5.1.1 Physical Geometry

The geometry of the numerical domain modelled the internal dimensions of the LBST. A section before the test piece was included that was equal to the height of the fluid domain to allow for sufficient shock formation before the test piece. The outlet was simply set to a wall as the simulation is considered to be finished when either the reflected shock reflects off the upper wall and meets the triple point or when the incident shock reaches the end of the wedge. Figure 5.1 represents a typical geometry for a 30° wedge test case, note that $L = 450$mm which corresponds to the height of the LBST test section:

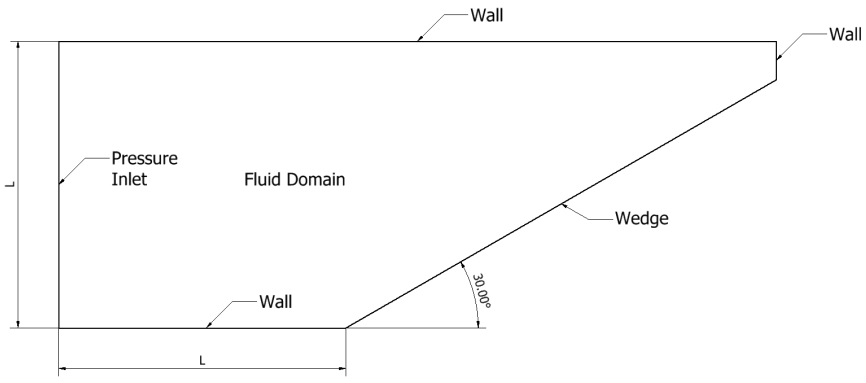


Figure 5.1: A typical geometry for a 30° Wedge

5.1.2 Mesh

Initially the entire fluid domain was meshed with 2mm quadrilateral cells. Mesh refinement was performed to resolve the KHI occurring along the shear layer of the Mach Reflection. The mesh was adapted according to gradients of density and velocity magnitude with the following threshold values (based off Rubidge[26]):

Refine Threshold:

$M_s = 1.34, 1.46$ **- 0.005**

$M_s = 1.61$ **- 0.015**

Coarsen Threshold:

$M_s = 1.34, 1.46$ **- 0.01**

$M_s = 1.61$ **- 0.03**

Maximum Level of Refinement - 5

Adaption Interval - Dependent on Mach Number

A magnified view of the refined mesh is shown in Figure 5.2 for a 30° wedge and incident shock strength $M_s = 1.46$:

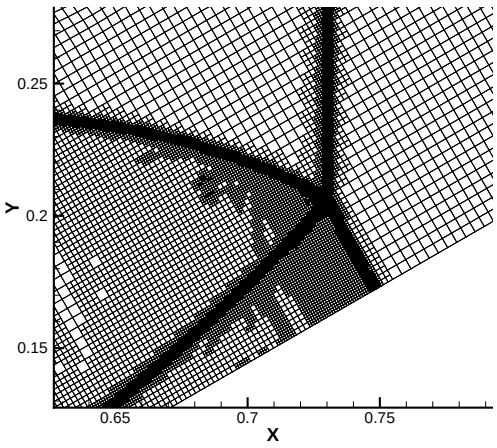


Figure 5.2: Refined mesh in the vicinity of the triple point for a 30° Wedge, $M_s = 1.46$

5.1.3 Settings

Air as an ideal gas was chosen to be the working fluid in the domain. The same solver settings were used as those in Rubidge[26].

5.1.3.1 Solver Settings

Time: Unsteady Second Order

Type: Density Based

Viscous Model: Inviscid

Energy Equation: On

Formulation: Explicit

Flux Type: Roe-FDS

Spacial Discretisation:

Gradient: Least Squares Cell Based

Flow: Third Order MUSCL

Transient Formulation: Second Order Implicit

5.1.3.2 Solution Initialisation

The fluid domain was initialised with the following conditions:

Ambient Pressure - 83300 Pa

Ambient Temperature - 293K

Courant Number - 2

A journal file was created for each of the Mach number cases, this ensured the settings were consistent across all of the simulations. For the pressure inlet shown in Figure 5.1 the following conditions were specified from Table 5.1:

Table 5.1: Pressure Inlet Initial Conditions

Mach Number M_s	**Total Gauge Pressure (Pa)**	**Supersonic Initial Pressure (Pa)**	**Inlet Temperature (K)**
1.34	184411.32	160619.06	370.70
1.46	240528.17	193272.66	403.52
1.61	329501.56	238025.59	448.50

5.1.3.3 Preliminary Results and Wedge Angle Selection

In order to decide on the initial wedge angles to be tested experimentally in the LBST, preliminary CFD was used to ascertain the type of reflection that occurred over a range of Mach numbers that could be obtained. Note that three wedges were previously manufactured for the LBST having wedge angles of $5°, 10°$ and $15°$. The results are summarised in the following Table 5.2 where the type of reflection is designated as either a vN/G/V (von Neumann/Guderley/Vasilev Reflection) or SMR (Single Mach Reflection); a '-' indicates a case that was not run:

Table 5.2: Preliminary CFD Results for the LBST

	Wedge Angle θ_w				
Mach Number	5°	10°	15°	30°	40°
1.34	vN/G/V	vN/G/V	vN/G/V	SMR	SMR
1.46	vN/G/V	vN/G/V	-	SMR	SMR
1.61	vN/G/V	-	-	SMR	SMR

From the above table it is clear that the current wedge models produced reflections in the weak Mach Reflection region, therefore new wedge models were required to be manufactured with higher wedge angles in order to study the shear layer occurring in a Single Mach Reflection. For the LBST experimental testing a 30° and 40° wedge angle was chosen as a SMR resulted over a large range of Mach numbers. Shown in Figure 5.3 is a magnified result for the 30° wedge at Mach 1.61, clearly showing development of the KHI along the shear layer, thus validating the wedge angle selection for this study.

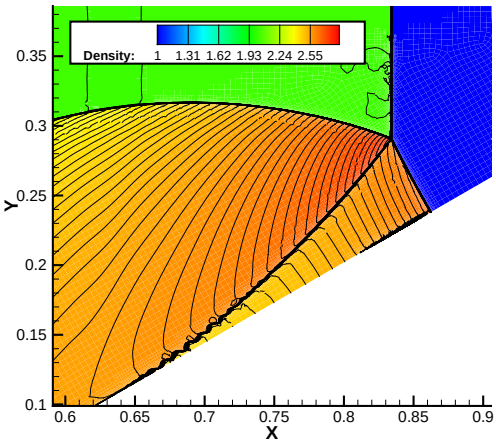


Figure 5.3: Contours of density of a Single Mach Reflection occurring on a 30° Wedge, $M_s = 1.61$

Chapter 6 Results and Discussion

6.1 Experimental Results

The experimental and theoretical results are presented and discussed below. A large scale shock tube was used initially and final testing was completed in a smaller scale shock tube utilising a wide range of wedge angles.

6.1.1 LBST Experimental Results

The LBST was used initially for experimental purposes following the preliminary CFD study outlined in 5.1. A 30° and 40° wedge were manufactured for testing at a scale larger than conventional shock tubes. The purpose of the study was to obtain images of large scale Mach Reflection and to visualise the Kelvin-Helmholtz Instability occurring along the shear layer as a follow up to the work of Rubidge and Skews[13]. It was hoped that the larger scale would help to characterise the periodicity of the vortex structures along the shear layer. During testing of the 40° wedge, failure of the bolts retaining one of the optical windows occurred; this led to the one optical window cracking and the subsequent shut down of the experimental facility for the rest of the year. Due to time constraints a conventional shock tube (the MSAST) was used for the rest of the testing with wedge angles ranging from 25° to 38°.

The results from the 30° wedge are shown in Figures 6.1, 6.2 and 6.4. The Mach numbers used for testing were Mach 1.27, 1.37 and 1.44 at local atmospheric conditions of 83300 Pa. The flow is from left to right with the wedge surface rotated to be horizontal. A shadowgraph flow visualisation setup was used in the experiment as the fine detail of the shear layer visualised in Rubidge and Skews[13] was not required for this study. A clear SMR develops on the wedge surface and moves along it. Note that each image is a separate test where the light source delay (in μs) was increased to obtain an image of the flow field at a later time. The measured Mach number varied by approximately ± 0.01. The results for the low Mach number case are

presented last in Figure 6.4 due to there being no visible increase in shear layer thickness. A direct comparison can be made between the two higher Mach numbers as the shear layer thickness is measurable.

From the earliest time delay at both of the higher Mach numbers shear layer growth is visible from the triple point. As the SMR progresses up the wedge surface the triple point follows a linear trajectory in relation to the wedge surface. This allows the shear layer to develop for a longer time before coming into contact with the wedge surface and is therefore at a larger scale than previous experiments by Rubidge and Skews[13]. A direct comparison between Figure 6.1 (d) and 6.2 (c) reveals a slight increase in shear layer thickness as the Mach number is increased, this is more pronounced nearer the wedge surface. A braided structure is visible within the shear layer: this is the Kelvin-Helmholtz Instability. The instability does not occur along the entire length of the shear layer, this differs from splitter plate experiments of Brown and Roshko[17] where the KHI vortices are visible at the trailing edge of their experiment. The reason for this may be due to the impulsive start of the shear layer caused by the pseudo-steady Mach Reflection compared to the steady flow passing over a splitter plate of Brown and Roshko[17].

The curvature of the Mach stem at the triple point decreases with increasing Mach number and will eventually become a straight shock perpendicular to the wedge surface at much higher Mach numbers. At the highest Mach number, compressions are visible emanating from the wedge surface at the foot of the Mach stem, this is most likely due to the surface roughness of the painted wedge or may be due to the double sided tape lining the edge of the wedge.

The following angles were measured at the triple point: incident shock to reflected shock (ω_{IR}) and incident shock to Mach stem (ω_{IM}). The triple point trajectory (χ) could not be measured from the wedge apex as it was not visible during testing, successive test images were used to measure the triple point trajectory. The accuracy to which the triple point trajectory could be measured is $\pm 1^{\circ}$.

Using the experimental data, a MATLAB program was written that required user input of the testing conditions (P_0 and T_0), wedge angle (θ_w), incident Mach number M_s and measured shock angles (ω_{IR}, ω_{IM}). As expected for the weak shock domain, the boundary conditions across the shear layer were not met when Three Shock Theory was used. Using the oblique shock analysis resulted in solutions that were within the boundary condition limits calculated in Olim and Dewey[12].

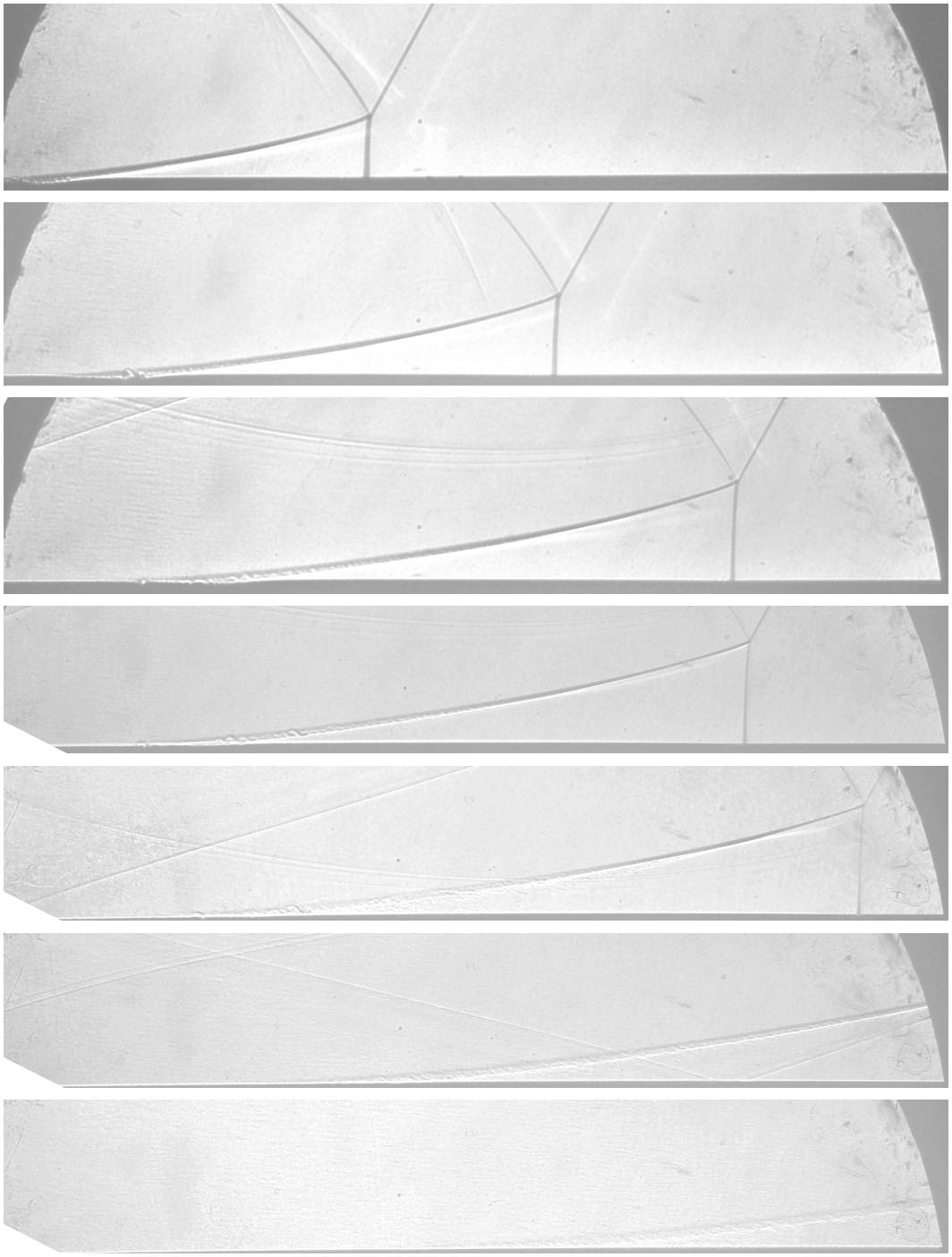


Figure 6.1: Shear layer development for the 30° Wedge. $M_s = 1.37$. (a) $3100\mu s$, (b) $3200\mu s$, (c) $3300\mu s$, (d) $3350\mu s$, (e) $3400\mu s$, (f) $3600\mu s$, (g) $3800\mu s$

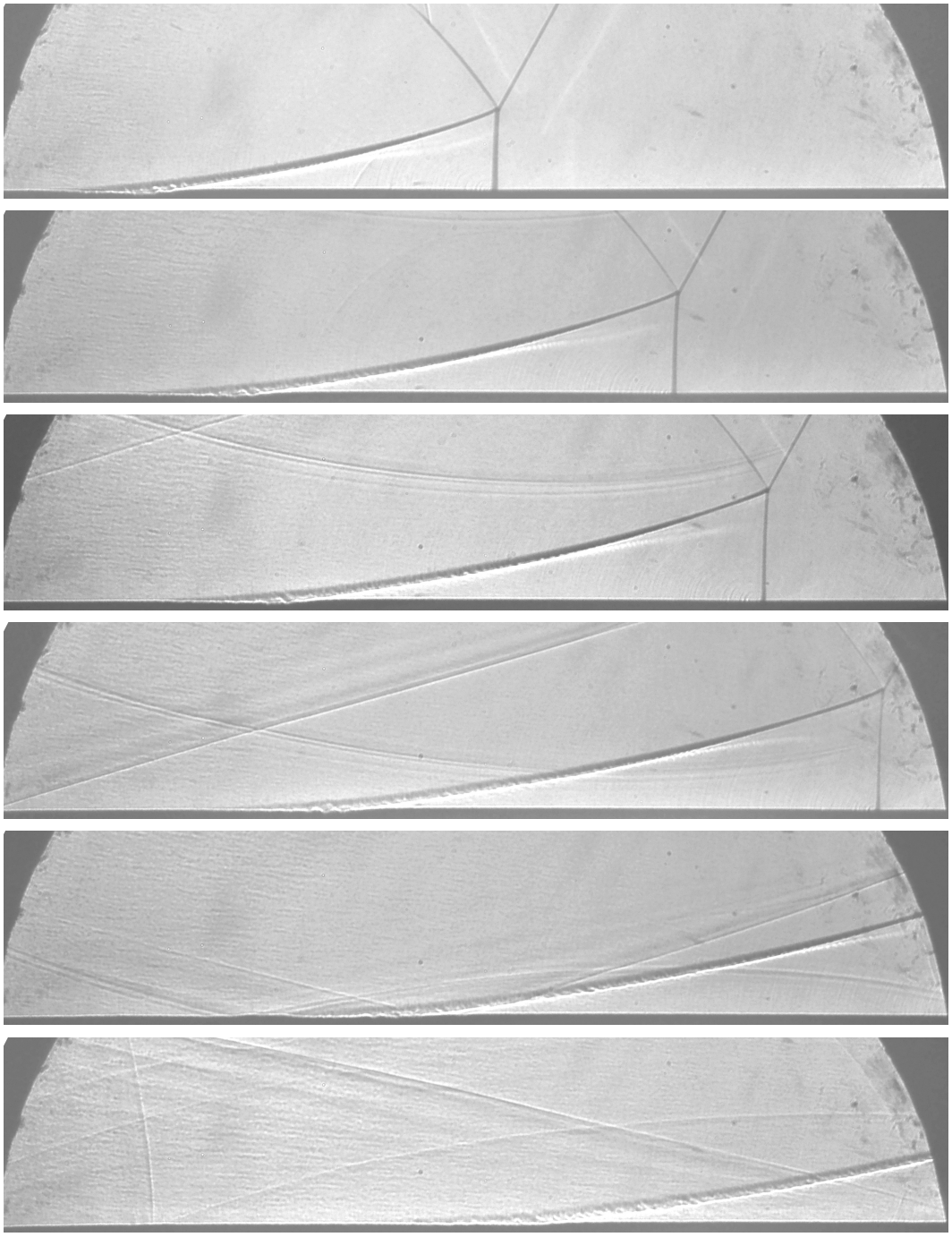


Figure 6.2: Shear layer development for the 30° Wedge. $M_s = 1.44$. (a) 3000μs, (b) 3100μs, (c) 3150μs, (d) 3200μs, (e) 3300μs, (f) 3400μs

The velocity ratio ($r = U_3/U_2$), density ratio ($s = \rho_3/\rho_2$), shear velocity (ΔU), convective velocity (U_c) and convective Mach number (M_c) were calculated for the shear layer. U_c and M_c were calculated using equations in Papamoschou and Roshko[22]. A summary of the measured experimental data is shown in Table 6.1.

Table 6.1: Measured angles and calculated shear layer data

θ_w [°]	M_s [-]	χ [°]	ω_{IR} [°]	ω_{RS} [°]	ω_{IM} [°]	r [-]	s [-]	ΔU [m/s]	U_c [m/s]	M_c [-]
30	1.27	4.1	48.6	84.7	158.0	0.864	1.049	46.47	318.89	0.0602
30	1.37	4.3	58.5	80.8	156.7	0.794	1.070	74.58	325.11	0.0938
30	1.44	5.4	61.4	78.4	155.6	0.787	1.035	77.97	328.38	0.0945

The increase in Mach number results in a decrease in velocity ratio across the shear layer and associated increase in shear velocity (ΔU). The denser fluid is on the low speed side (as s > 1) of the layer: this inhibits the growth rate of the shear layer according to Rikanati et al.[24]. A comparison to the CFD undertaken in Section 5.1 confirms this in Figure 5.3. The shear layer growth rate was measured by importing the experimental images into a CAD package and fitting a constant radius curve through the centre of the shear layer. The visual thickness δ_{vis} was measured at discrete points from the triple point. Shown in Figure 6.3 is the measured thickness for two different shock strengths. The error in measuring the thickness is estimated at ±0.25mm and distance from the triple point ±2mm. The visual growth rate δ'_{vis} was obtained by fitting a line of best fit through the data points and is approximately the same for both Mach numbers ($\delta'_{viz} = 0.013$).

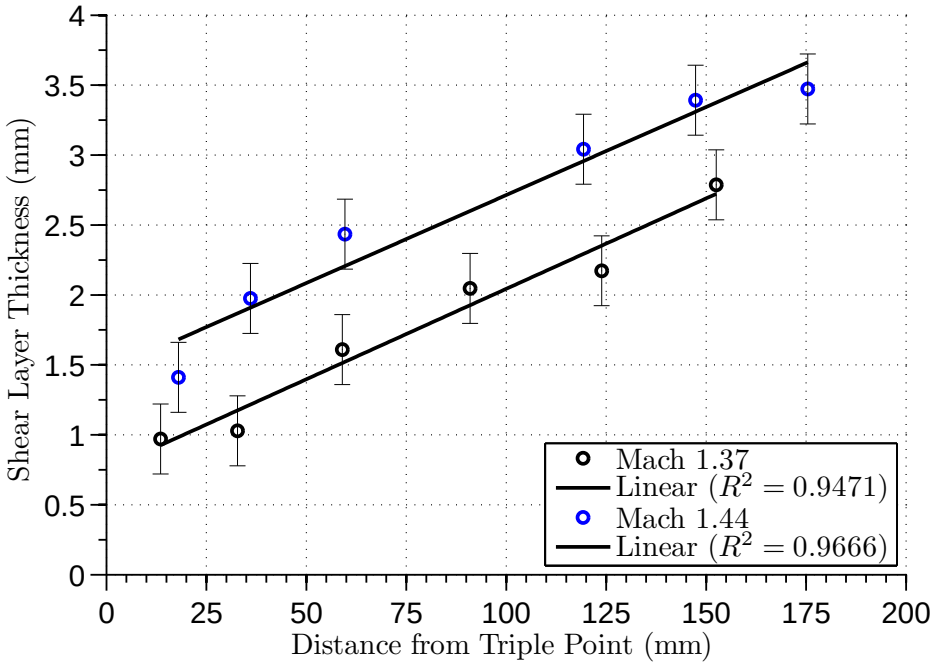


Figure 6.3: Measured Shear Layer Thickness from the LBST

Although a velocity shear is present across the shear layer of a Mach reflection, it is clear from Table 6.1 that compressibility does not play a large role in the growth of the mixing layer due to the convective Mach numbers being low. When comparing the visual growth

rates to the model proposed by Rikanati et al.[14], their theoretical growth rates were similar. A detailed discussion of the shear layer growth rates and spread angle is provided in Section 6.4.

The lowest Mach number results are presented in Figure 6.4. No visual growth of the shear layer from the triple point is apparent however, much further along the shear layer a single structure resembling the Kelvin-Helmholtz Instability is visible and grows in time as it convects downstream in the triple point frame of reference. The single instability was not visible with the triple point in the test section window field of view, but only at later times as seen in Figure 6.4 (b) - (f). An important distinction to make is that relative to the triple point the structure is convecting downstream i.e. away from the triple point, but in the laboratory reference frame the structure, shear layer and Mach reflection are moving from left to right along the wedge surface. The reason for this single occurrence of the instability is unknown and requires further verification. Also evident is a thickening of the shear layer close to the single instability in Figure 6.4 (e) and (f). The boundary layer on the wedge surface is much thicker than in the higher Mach number images and has a repeating structure similar to that found by Rubidge and Skews[13].



Figure 6.4: Shear layer development for the 30° Wedge. $M_s = 1.27$. (a) 3800μs, (b) 4000μs, (c) 4200μs, (d) 4400μs, (e) 4600μs, (f) 4800μs

6.1.2 MSAST Experimental Results

As discussed in Section 6.1.1 the remainder of the experimental testing was conducted in the MSAST. A wide range of wedge angles was chosen to serve as a complimentary study to the work undertaken using the LBST. The importance of the measuring from the wedge apex was also considered when designing the test pieces. The length of the wedges chosen ensured that the wedge apex was visible in the test section window field of view. Furthermore the use of the MSAST allowed for higher incident shock Mach numbers to be generated than in the LBST. Preliminary work was undertaken to evacuate the driven section of the MSAST to obtain Mach numbers in the range $M_s > 1.8$ however, due to time constraints this could not be utilised due to the automated software of the shock tube requiring an update.

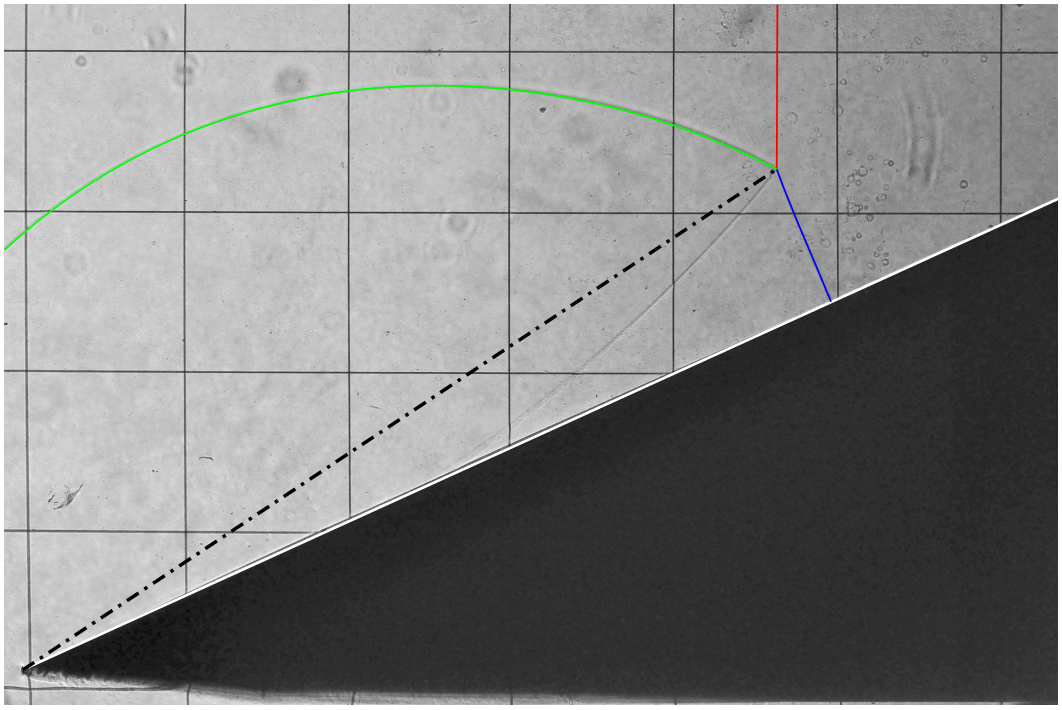
A shadowgraph flow visualisation setup was used in the experiment as the fine detail of the shear layer visualised in Rubidge and Skews[13] was not required for this study. Measurements of the angles between various shocks was the main focus of this work as well as obtaining the spread angle of the shear layer.

The original images for each wedge angle are presented in Figures 6.5 and 6.7. Only the high Mach number images for each wedge are presented in this section as the greatest difference between wedge angles is evident here (the remainder may be found in Appendix B). Each shock (incident, reflected and Mach stem) has been overlaid with different coloured lines for clarity; the wedge surface and triple point trajectory are also indicated for qualitative analysis. A zoomed in rotated image near the triple point of each wedge angle is presented in Figures 6.6 and 6.8, this allows for direct comparison of the shear layer thickness as the Mach number is varied for each wedge angle.

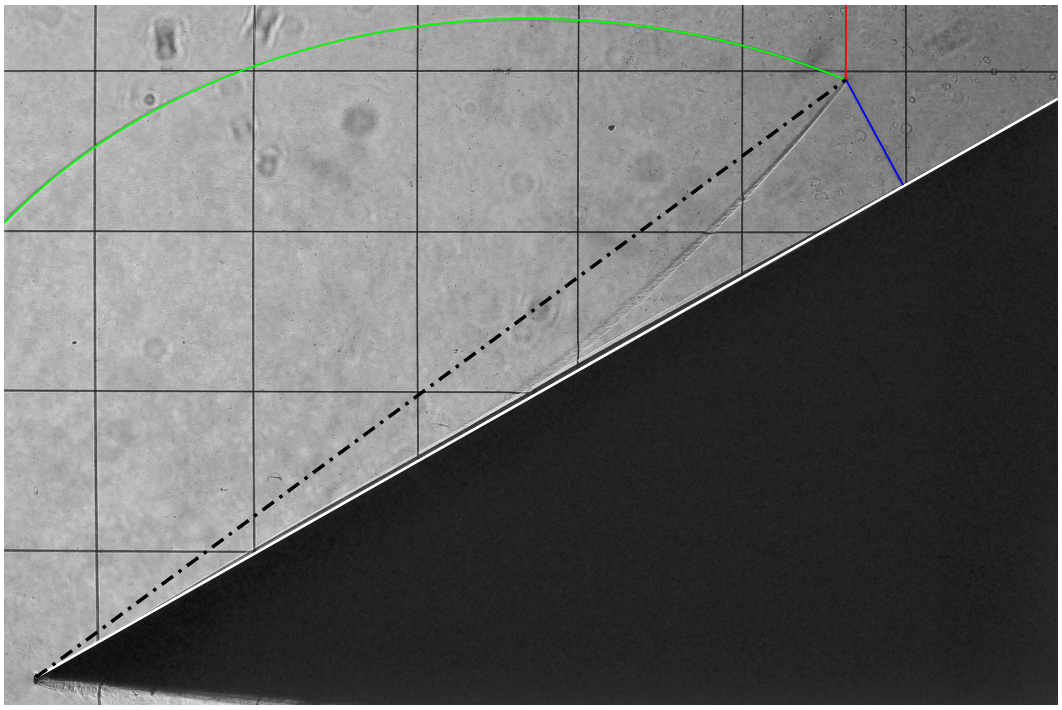
A qualitative analysis of the images is provided below:

For a fixed incident shock Mach number:

- The triple point trajectory decreases with increasing wedge angle
- The incident to reflected shock angle increases with increasing wedge angle
- The curvature of the Mach stem at the triple point decreases with increasing wedge angle
- The overall shape of the reflected shock decreases in curvature i.e. flattens out with increasing wedge angle
- The shear layer thickness increases and the KHI is evident closer to the triple point with increasing wedge angle



(a)



(b)

Figure 6.5: Single Mach Reflection with highlighted features (Incident Shock, Reflected Shock, Mach Stem, Triple Point Trajectory - Black, Wedge Surface - White): (a) $\theta_w = 25°$. $M_s = 1.585$, Time Delay: $1550\mu s$ (b) $\theta_w = 30°$. $M_s = 1.583$, Time Delay: $1550\mu s$

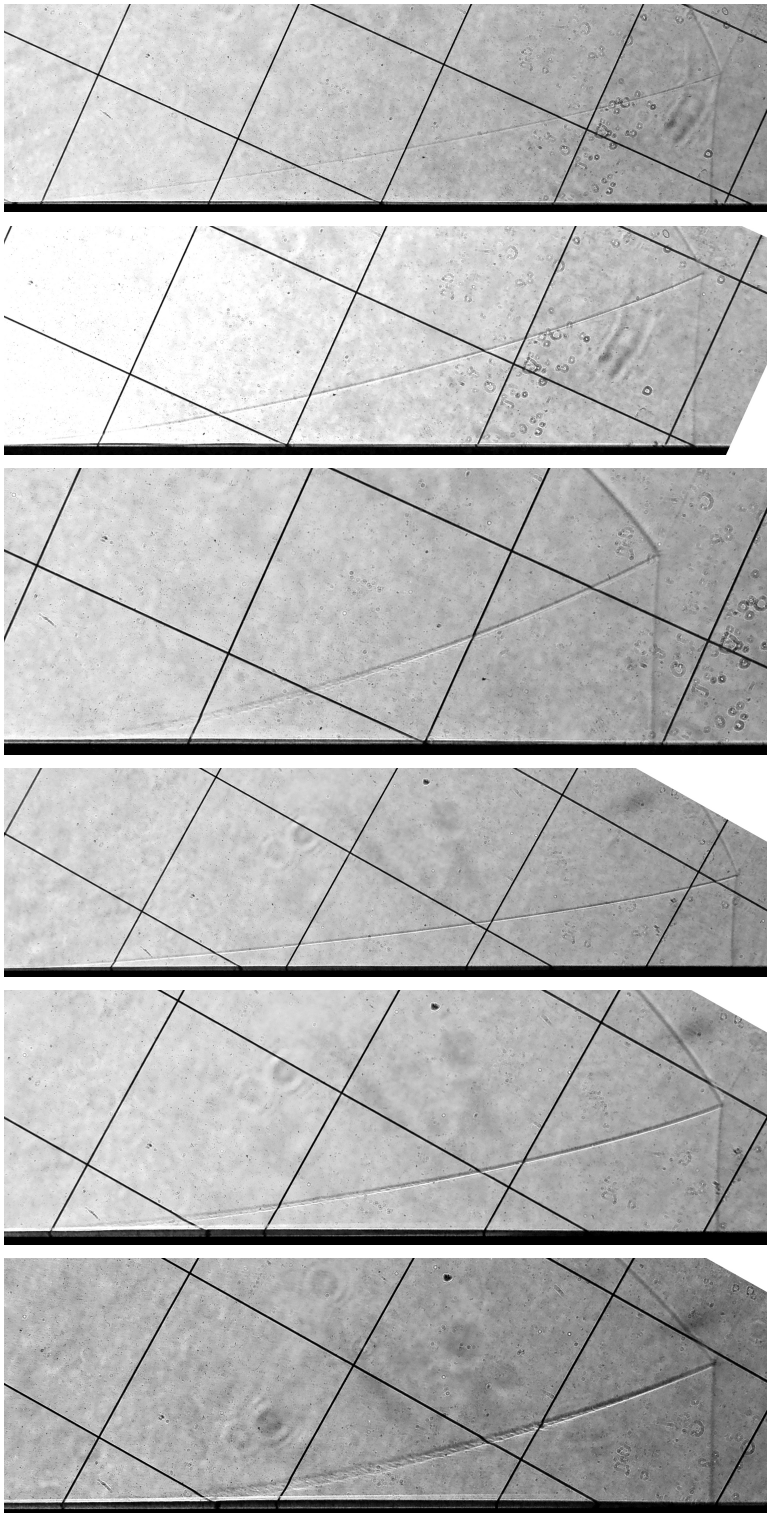
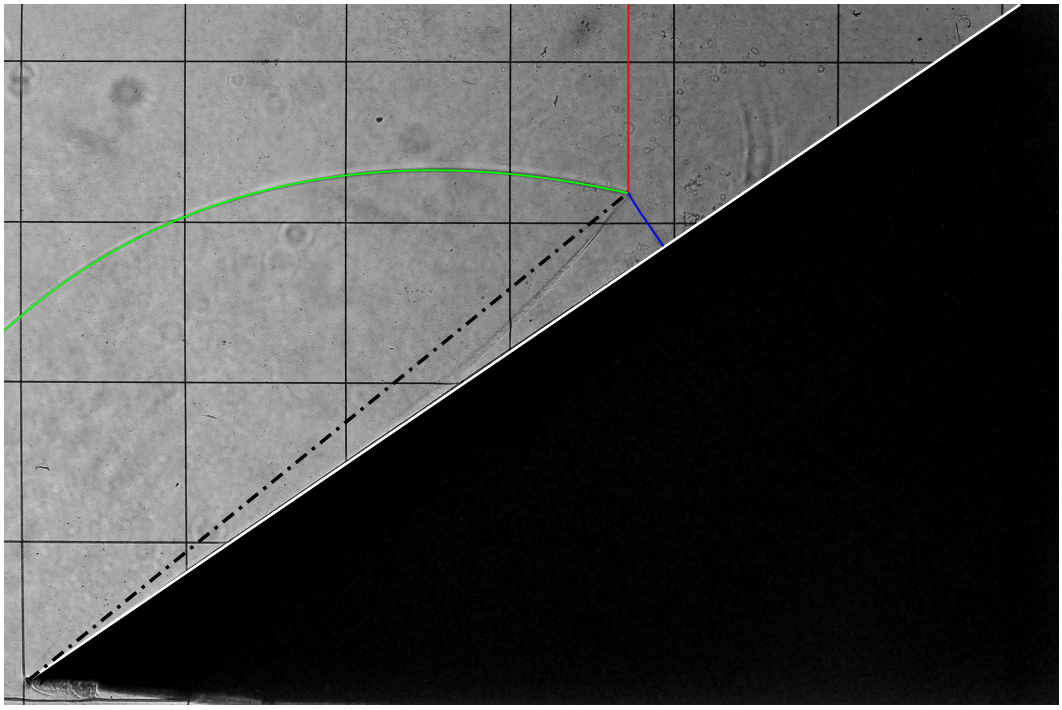
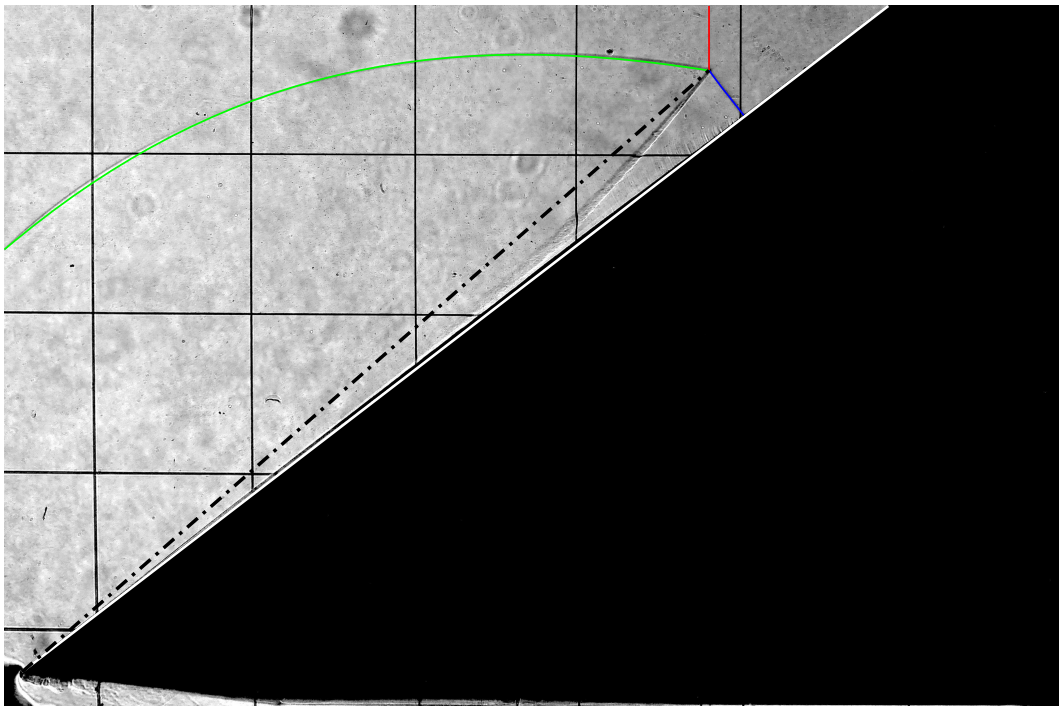


Figure 6.6: Shear layer development for the 25° Wedge. Corresponding Incident Shock Mach number and time delay: (a) $M_s = 1.309$, $1925\mu s$ (b) $M_s = 1.447$, $1750\mu s$ (c) $M_s = 1.585$, $1550\mu s$. Shear layer development for the 30° Wedge: (d) $M_s = 1.309$, $1900\mu s$ (e) $M_s = 1.441$, $1700\mu s$ (f) $M_s = 1.583$, $1550\mu s$



(a)



(b)

Figure 6.7: Single Mach Reflection with highlighted features (Incident Shock, Reflected Shock, Mach Stem, Triple Point Trajectory - Black, Wedge Surface - White): (a) $\theta_w = 35°$. $M_s = 1.587$, Time Delay: $1550\mu s$ (b) $\theta_w = 38°$. $M_s = 1.593$, Time Delay: $1500\mu s$

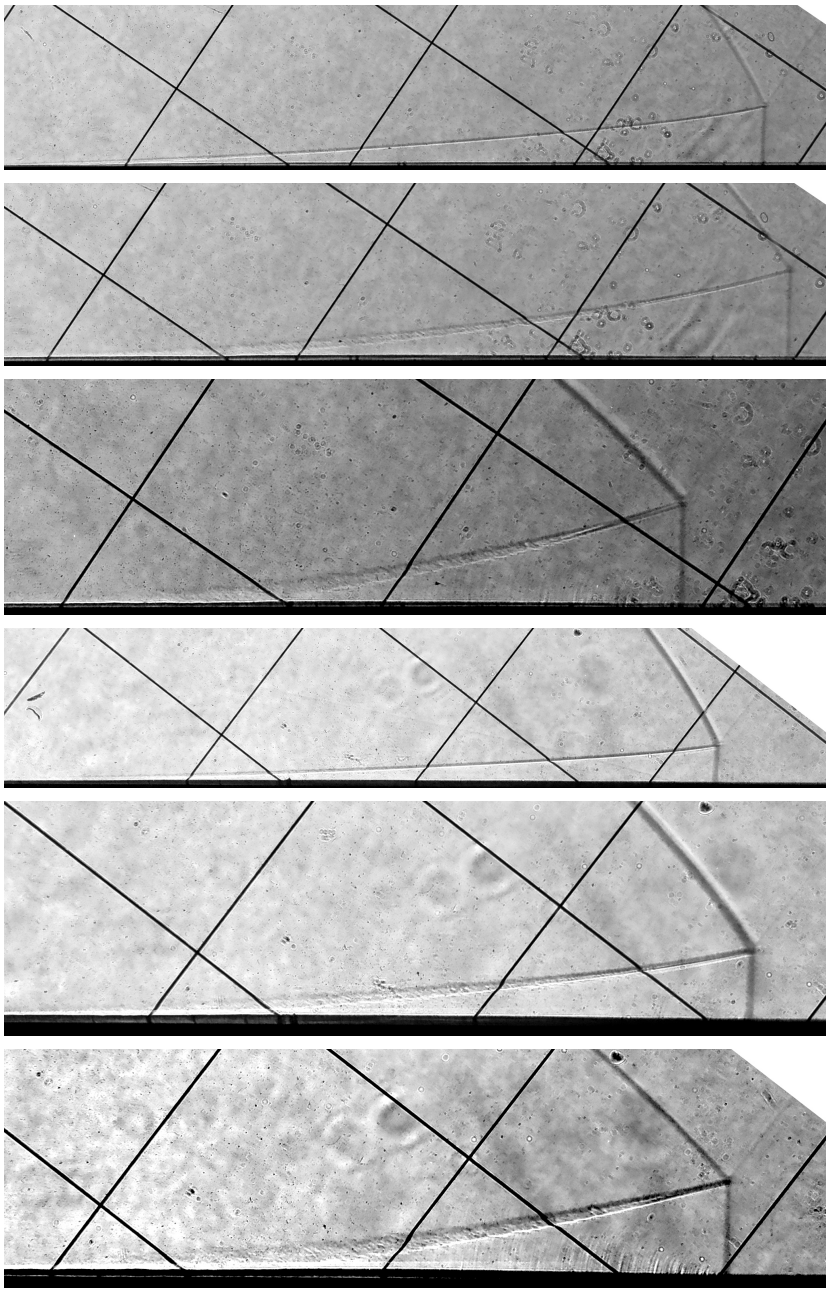


Figure 6.8: Shear layer development for the 35° Wedge. Corresponding Incident Shock Mach number and time delay: (a) $M_s = 1.313$, $1925\mu s$ (b) $M_s = 1.447$, $1750\mu s$ (c) $M_s = 1.587$, $1550\mu s$. Shear layer development for the 38° Wedge: (d) $M_s = 1.304$, $1850\mu s$ (e) $M_s = 1.442$, $1650\mu s$ (f) $M_s = 1.593$, $1500\mu s$

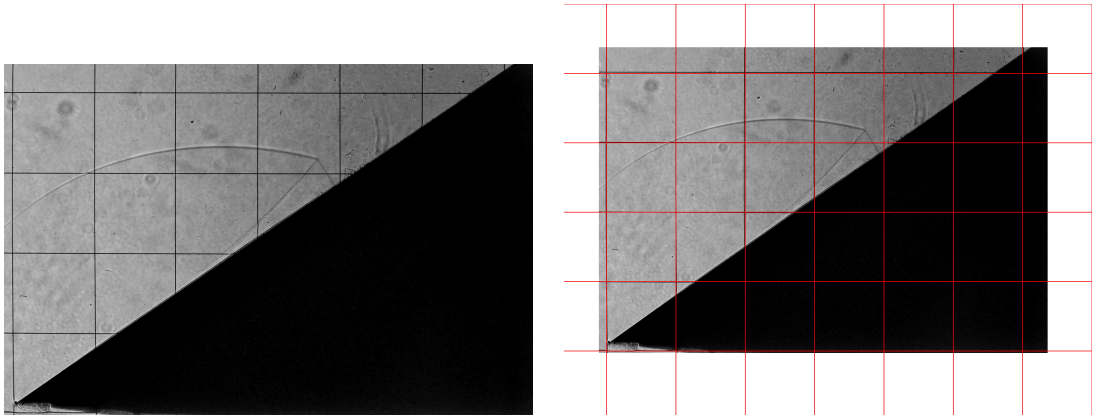
For a fixed wedge angle:

- The incident to reflected shock angle increases as the incident Mach number increases
- The curvature of the Mach stem decreases at the triple point with increase in Mach number. The shape of the Mach stem approaches that of a straight shock perpendicular to the wedge at higher Mach numbers. This is one of the basic assumptions of Three Shock Theory as given in Equation 1.13
- The shear layer thickness increases as the incident Mach number increases

Notes regarding other flow features:

- A turbulent separation bubble is present for all wedge angles at the leading edge of the wedge. This is due to the finite angle on the underside of the wedge that was machined to elevate the wedge apex and protect it from being damaged. A large gradient is present for the 38° wedge visible in the lower left corner of Figure 6.7 (b) due to the stronger vortex formed at the leading edge there
- Compressions are visible emanating from the wedge surface at the foot of the Mach stem at higher wedge angles. This may be due to the double sided tape lining the side of the wedges acting as a perturbation source
- For all images there are small grey circles in the background of each image. The optical windows were cleaned with acetone between wedge changes to remove any dust particles but these small circles could not be removed and are probably some form of glue from a previous experiment in the MSAST

The previous qualitative analysis is supported by the following quantitative study. A 25mm grid was overlaid on the test section for scaling purposes and for image distortion correction as discussed in Section 4.3.1. The images were imported into a free image manipulation program (GIMP v2.8.14) and a grid of pitch 50mm was overlaid on the image (the pitch of the grid is simply a multiple of the actual grid, 50mm was chosen for convenience). Each image was then scaled so that the test section grid matched the virtual grid as shown in Figure 6.9. The optical distortion was found to be greatest vertically (10.8%) compared to horizontally (8.6%). Although the optical distortion is minimal, the grid correction was still performed for each image as accurate measurements of the triple point trajectory are required for the analysis undertaken in Section 6.2.2.



(a) (b)

Figure 6.9: (a) $\theta_w = 35°$, $M_s = 1.587$ Original Image (b) Image corrected for grid distortion with virtual grid overlaid in red

The following shock angles were measured, shown in Figure 6.10 with a description below:

- χ: Triple Point Trajectory Angle
- ω_{IR}: Incident to Reflected Shock Angle
- ω_{RS}: Reflected Shock to Shear Layer Angle
- ω_{IM}: Incident Shock to Mach Stem Angle
- ω_{MS}: Mach Stem to Shear Layer Angle
- θ_E: Mach Stem Deficit Angle. Deviation of the Mach stem angle from a line projected perpendicular to the wedge surface from the triple point, this is equivalent to angle μ in Skews[8]

The angles were measured at least 5 times for each image, with a combined total of over 300 angular measurements being taken. The true wedge angle was also measured by measuring the angle between the incident shock and wedge surface, this was later used to calculate the complimentary wall angle ($\theta_w + \chi$). A statistical analysis was performed on the raw data following the procedure outline in Kirkup[27]. The mean ($\bar{x}$) and standard deviation (σ) were calculated for each angular measurement, the uncertainty may then be calculated by Equation 6.1.

$$\sigma_{\bar{x}} = \frac{\sigma}{\sqrt{n}} \tag{6.1}$$

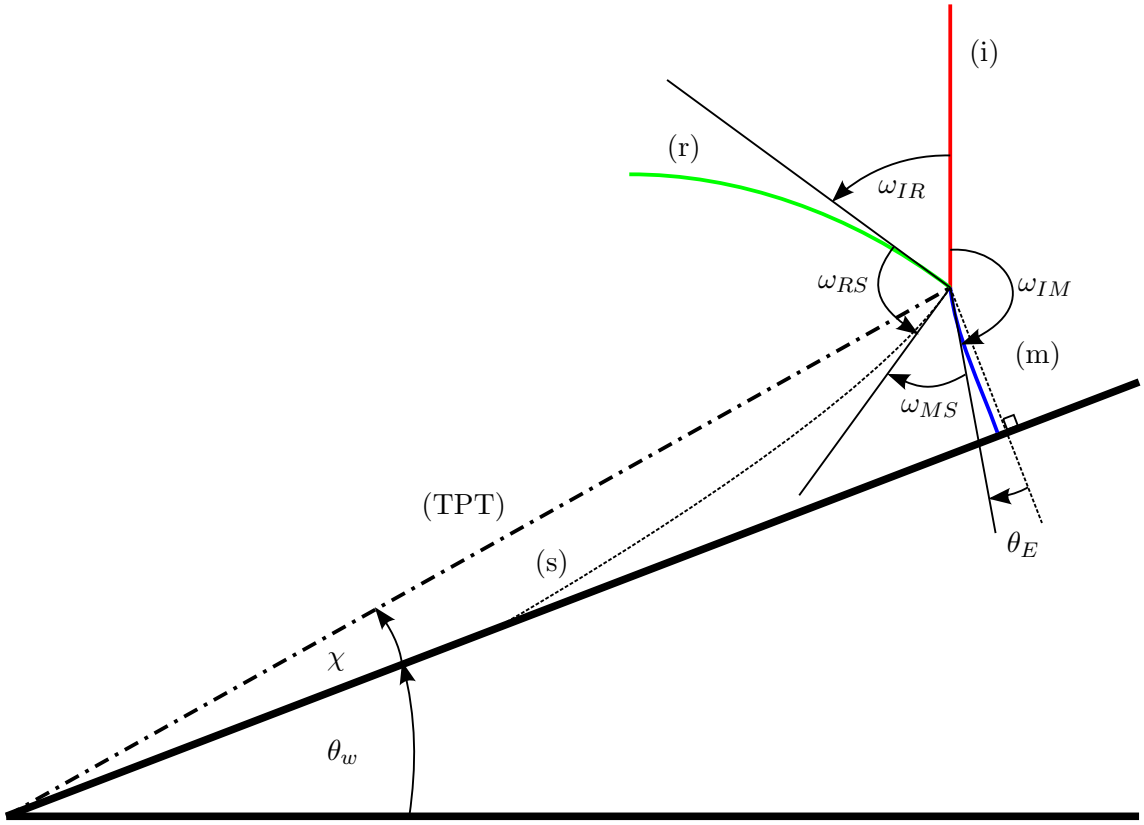


Figure 6.10: Schematic of measured angles

Where n is the number of repeated angular measurements. The 95% confidence interval for each measurement lies in the $[\bar{x} - 2\sigma_{\bar{x}}, \bar{x} + 2\sigma_{\bar{x}}]$ range[27]. The 95% confidence interval was used as the error bars in the following figures. Note that each measurement has its own uncertainty associated with it due to the varying degrees of accuracy that each angle could be measured. Note that the uncertainty for incident shock Mach number is ± 0.0005; this quantity is almost unreadable on the axis scale presented here, therefore the horizontal error bars were increased for clarity on all figures.

The triple point trajectory angle as a function of wedge angle vs Mach number is shown in Figure 6.11. Over the limited experimental Mach number range the triple point trajectory increases linearly with Mach number and decreases with higher wedge angles. The trajectories for the 35° and 38° wedge are closer together than the lower wedge angles; this is expected as the higher the wedge angle the closer the reflection configuration is to the transition wedge angle ($\theta_{w,transition}$) for a specific Mach number. The lower trajectories at higher wedge angles indicate that the triple point trajectory $\chi \to 0$ as $\theta_w \to \theta_{w,transition}$; a higher wedge angle is required for transition to occur when the Mach number is increased.

The following Figures 6.12 and 6.13 show the measured angles in a clockwise direction from the incident shock to the shear layer. The incident to reflected shock angle (ω_{IR}) increases as the wedge angle and incident Mach number is increased. This results in the reflected

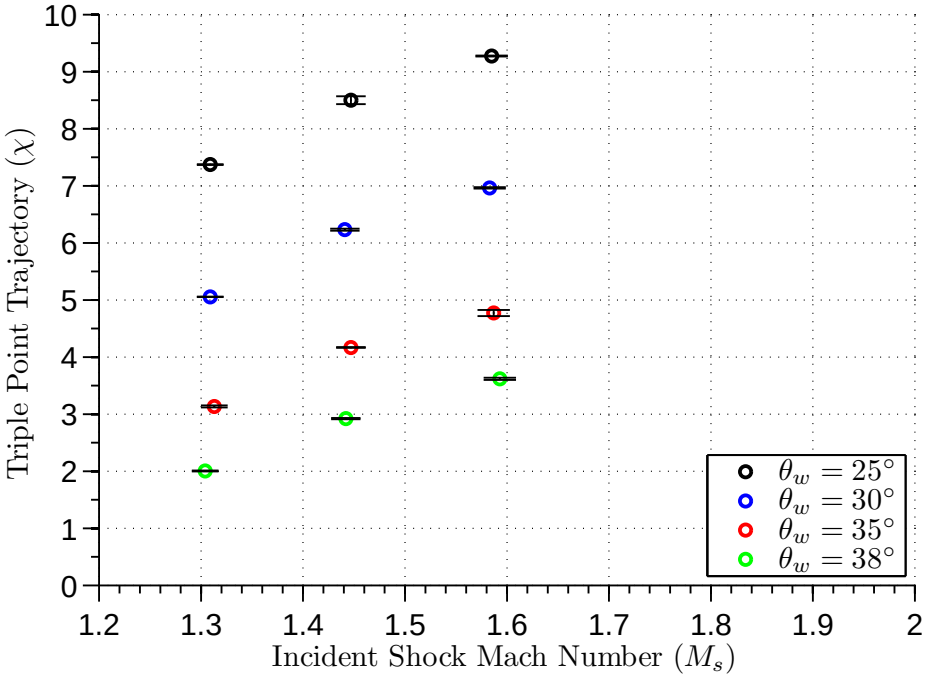


Figure 6.11: χ vs M_s

shock flattening out at the higher Mach numbers (visible in Figure 6.7 (a) and (b)). The change in ω_{IR} is the largest of all of the measured angles and differs by approximately 15° over the Mach number range. The angle ω_{RS} decreases in a non-linear manner with increase in Mach number with the highest angles occurring for the lower wedge angles. The reason for this non-linearity may be attributed to the gas behind the reflected shock being double-shocked as it passes through the incident and then reflected shock. The reflected shock is always significantly thicker than the incident shock, whether this is due to an interaction of the reflected shock on the window boundary layer or an optical effect requires further investigation.

Figure 6.14 and 6.15 show the measured angles in a counter-clockwise direction from the incident shock to the shear layer. The Mach stem shows some degree of curvature at the triple point and therefore these measurements have larger error bars associated with them. The curvature at the triple point is evident in the zoomed in Figures 6.6 and 6.8. The incident to Mach stem angle (ω_{IM}) decreases with increasing wedge angle, this is due to the curvature of the Mach stem at the triple point. Simple geometry reveals that if the Mach stem was perpendicular to the wedge surface at the triple point, an increase/decrease in triple point trajectory (i.e. a change in M_s) would not change the angle ω_{IM}. As will be subsequently shown the Mach stem is highly curved at lower wedge angles with a decrease in curvature as the wedge angle is increased for a fixed Mach number. The results for the 38° wedge indicate this as the decrease in ω_{IM} over the Mach number range is smaller than the lower wedge angles.

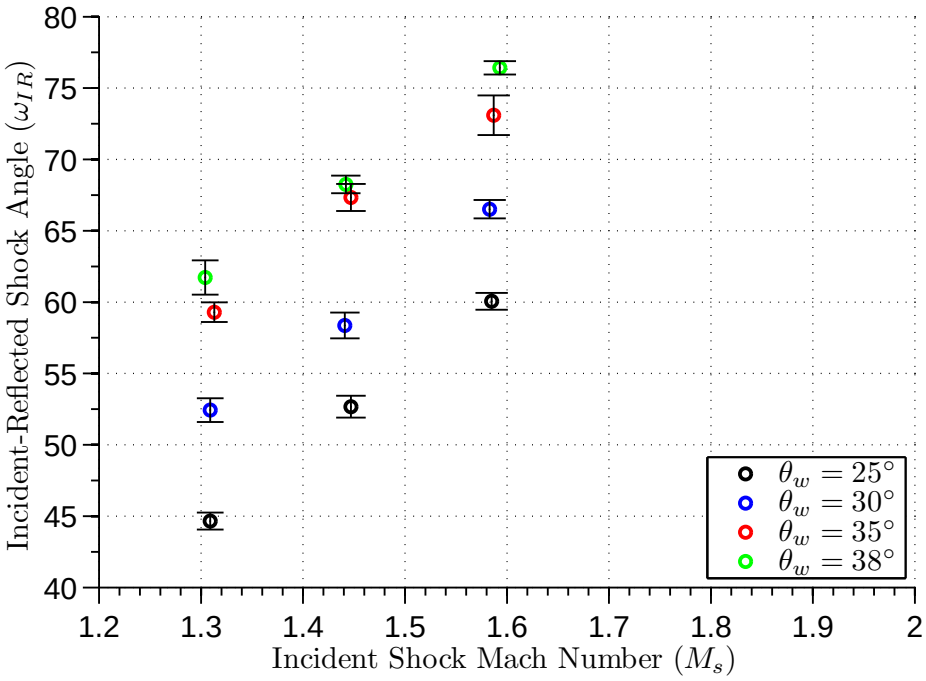


Figure 6.12: ω_{IR} vs M_s

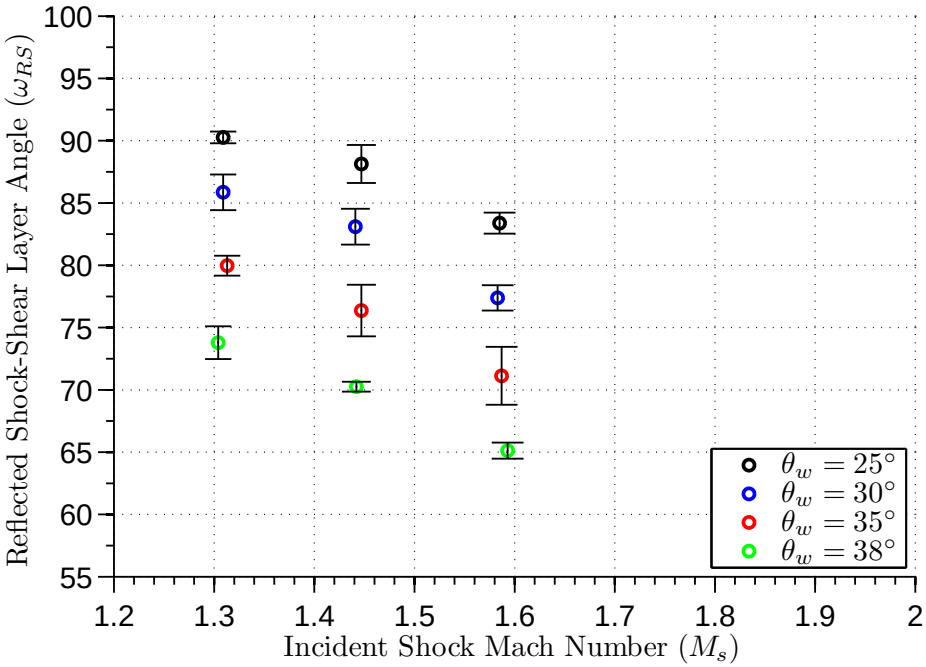


Figure 6.13: ω_{RS} vs M_s

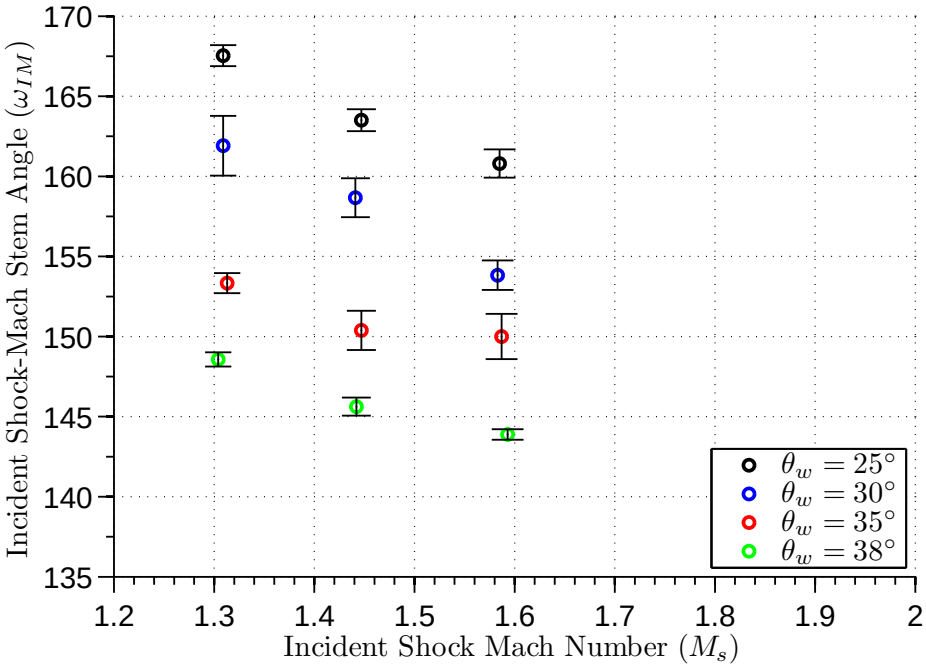


Figure 6.14: ω_{IM} vs M_s

The Mach stem to shear layer angle (ω_{MS}) results shown in Figure 6.15 exhibit the smallest change in angle as a function of Mach number. This is most likely due to the curvature at the Mach stem continuously adjusting to the required conditions at the triple point. The flow passing through the Mach stem is not double shocked as is the flow in the region behind the reflected shock. The 38° wedge results differ greatly from the lower wedge angles, this is due to the low triple point trajectory: the Mach stem is only slightly curved before becoming perpendicular to the wedge surface at the foot of the Mach stem.

The final results of the measured angles is shown in Figure 6.16. The deficit angle (θ_E) is a representation of how far off the Mach stem at the triple point is from being a straight shock perpendicular to the wedge surface. The highest uncertainty is associated with these measurements but the same trend is apparent for all wedge angles. The deficit angle decreases for all wedge angles as the Mach number is increased. This once again supports the assumption by a simple extrapolation that at stronger Mach numbers ($M_s > 2$) the Mach stem is a straight shock perpendicular to the wedge surface ($\theta_E \to 0$).

In order to make the results independent of wedge angle, the complimentary wall angle ($\theta_w + \chi$) is often used (Skews[8],Olim and Dewey[12]). The same angles that were plotted in Olim and Dewey[12] were selected for comparison (ω_{IR} and ω_{IM}) as these two angles are representative of the overall Mach reflection geometry. The incident to reflected shock angle (ω_{IR}) is shown in Figure 6.17 as a function of Mach number. There is a strong dependence on Mach number with an approximate increasing linear relationship existing when plotted

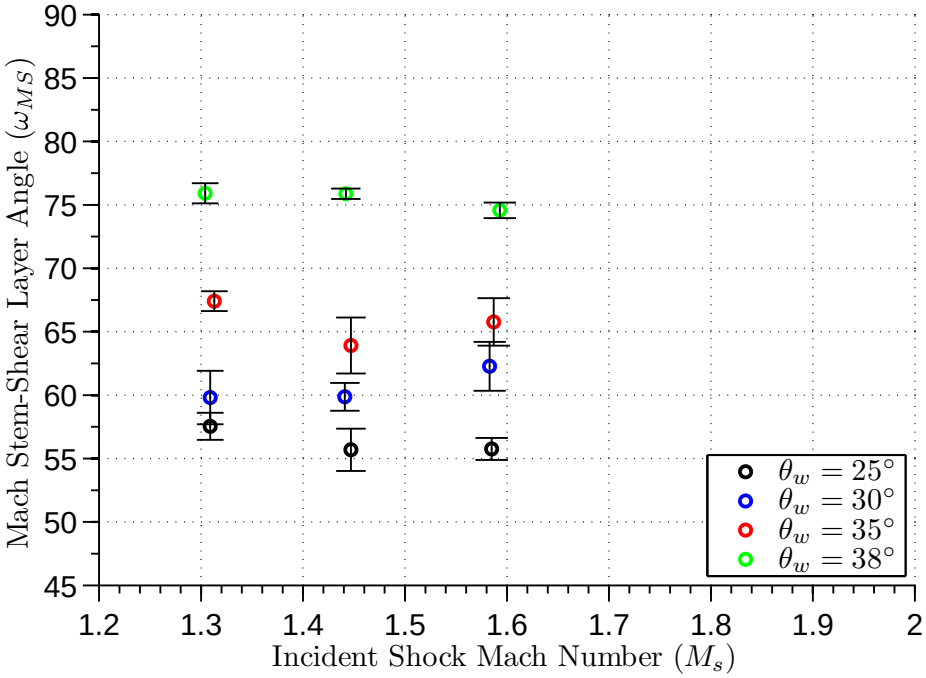


Figure 6.15: ω_{MS} vs M_s

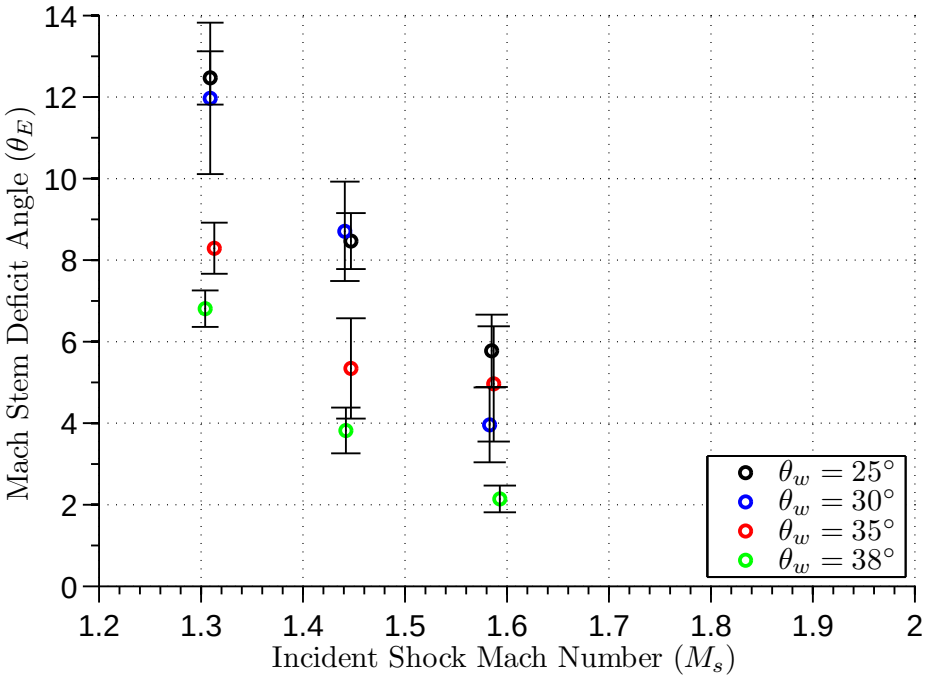


Figure 6.16: θ_E vs M_s

against the complimentary wall angle. The incident shock to Mach stem angle (ω_{IM}) is shown in Figure 6.18. The relationship with the complimentary wall angle is surprisingly linear given the highest uncertainty occurred when measuring the Mach stem angle, this indicates a dependence on wedge angle only.

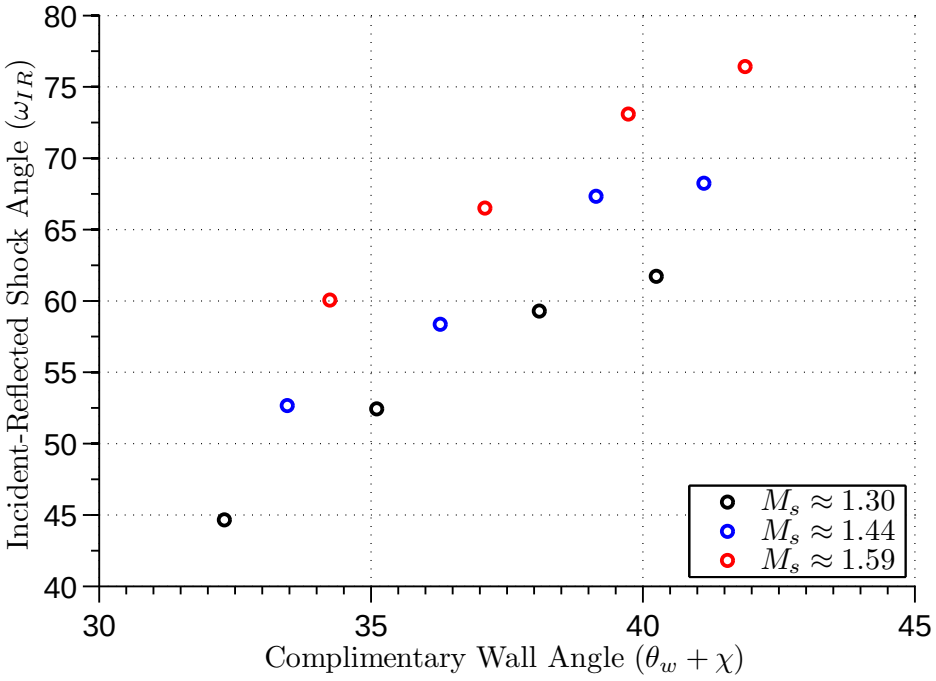


Figure 6.17: ω_{IR} vs $\theta_w + \chi$

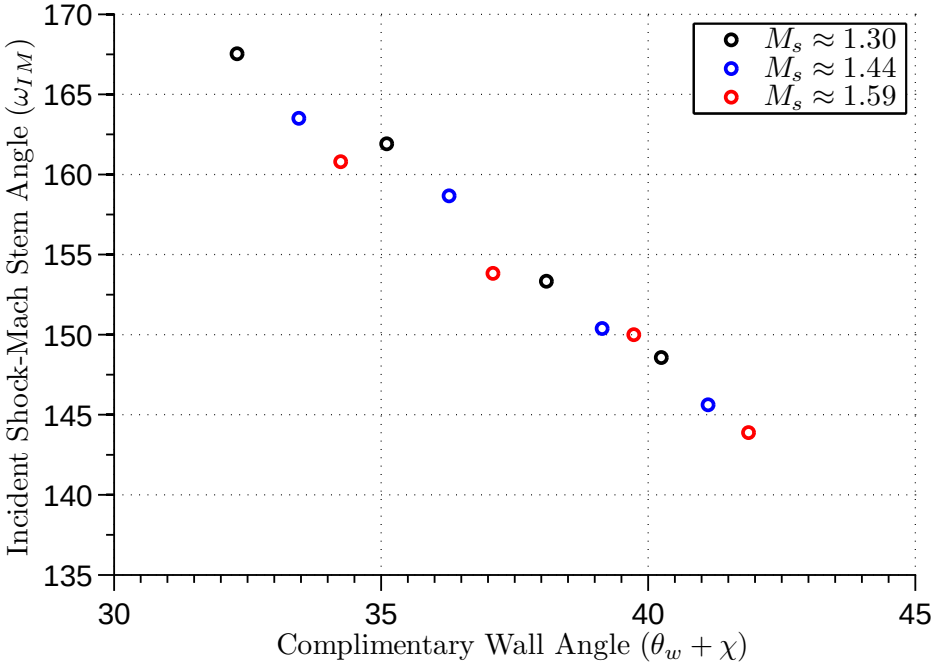


Figure 6.18: ω_{IM} vs $\theta_w + \chi$

6.1.3 Comparison of LBST and MSAST Results

A comparison can be made between the images obtained at the same Mach number in each experimental facility. The self-similarity of the shear layer is assessed by comparing results obtained for the 30° wedge at $M_s = 1.44$. A comparison of the different wedge models used is depicted in Figure 6.19. The LBST wedge model is much larger in size than the conventional wedge model used in the MSAST.

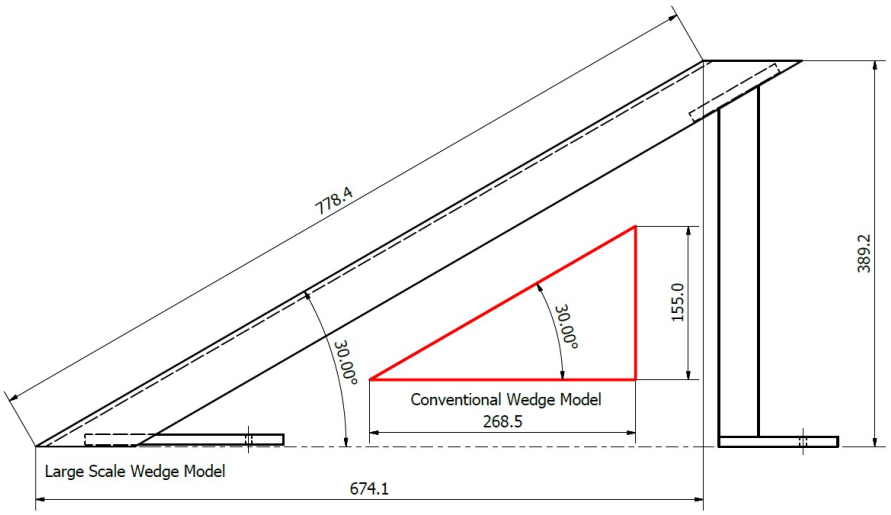
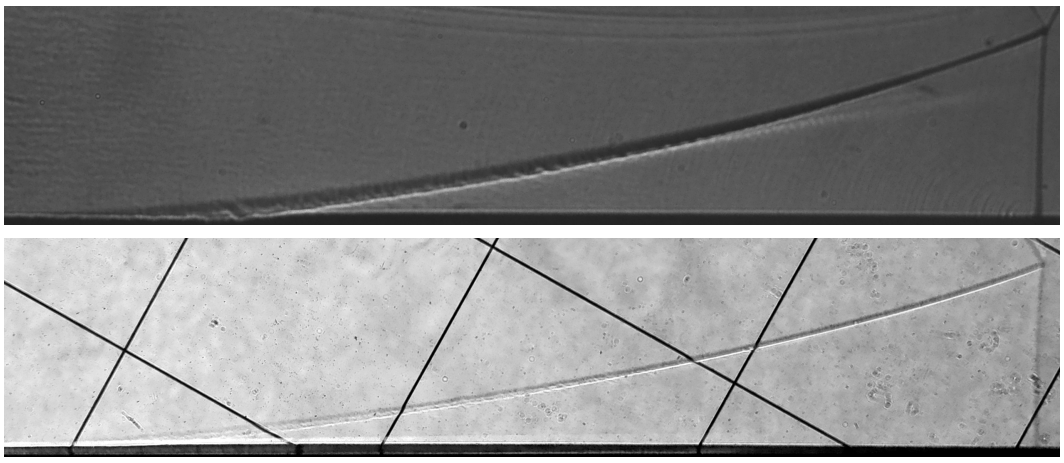


Figure 6.19: Comparison of facility wedge sizes (dimensions in mm)

The same optical setup was used in both experiments, a comparison of each image scaled by Mach stem height is shown in Figure 6.20. The larger scale experiment reveals a thicker shear layer and less discernible KHI structures within the layer itself. This may be an optical effect due to the wider test section in the LBST and requires further verification. A comparison of the growth rate for each shear layer is discussed in detail in Section 6.4.



(a)

(b)

Figure 6.20: Comparison of SMR's obtained at $M_s = 1.44$ in the (a) LBST (b) MSAST

The visual growth rate of the shear layer in the LBST was found to be similar to the results obtained in the MSAST and by Rubidge and Skews[13] using the same facility. The scale of the experiment in the LBST is approximately three times larger than the MSAST. As the study of pseudo-steady Mach Reflection has no length scale associated with it as it is self-similiar, the effect of a scale increase is minimal on the Reynolds number (Re). This is confirmed by the current study in the LBST. The advantage of the larger scale is that the KHI structures are larger and develop over a longer period as discussed in Section 6.1.1.

6.2 Three Shock Theory for Mach Reflection

This section presents a detailed description of the Three Shock Theory program that was used to compare the experimental results to the theory described by von Neumann[5, 6]. A comparison of the current code to the results obtained by Ben-Dor[10] is given as an introduction. The MATLAB Code may be found in Digital Appendix D.

6.2.1 Ben-Dor 1987 Validation

The detailed work of Ben-Dor[10] closely examined the Mach reflection configuration obtained experimentally to the original three shock theory for a strong incident shock $M_s = 2.71$. A discrepancy was found between the experimentally measured angles and the theoretical solution. A computer code was written in MATLAB R2010B similar to the one used by Ben-Dor. The solution method differed in the following way:

1. The simplified shock equations were used (Equations 1.3 to 1.7) instead of the original Rankine-Hugoniot equations used by Ben-Dor[10]
2. A simple bracketing method was used to converge to the three shock solution very rapidly (this method is given in Chapra[28]). Newton-Raphson was used by Ben-Dor[2] due to the available computational power at the time
3. Ben-Dor solved for the pressure and deflection boundary conditions simultaneously. In the new code, the pressure boundary condition was maintained across the shear layer and the Mach stem shock angle was solved for until a certain shear layer divergence criterion was met

Equation 1.3 was re-arranged to give an explicit solution for the Mach stem shock angle (ϕ_3) as a function of Mach number (M_0) and pressure ratio (P_3/P_0):

$$\phi_3 = \arcsin\left(\sqrt{\frac{(P_3/P_0 - 1)\left(\frac{\gamma+1}{2\gamma}\right) + 1}{M_0^2}}\right) \tag{6.2}$$

The boundary conditions for Three Shock Theory are repeated below for convenience with reference to Figure 6.21. The shock and flow angles are shown in Figure 6.21 for convenience.

$$p_2 = p_3 \tag{6.3}$$

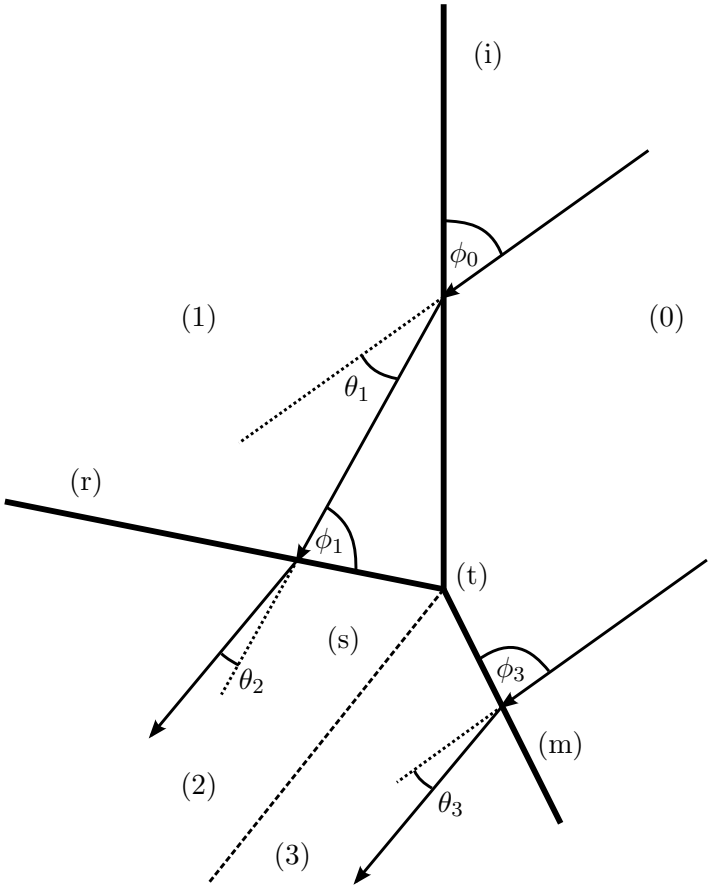


Figure 6.21: Confluence of three shocks at the triple point of a Mach Reflection with definition of angles and flow regions

$$\theta_1 - \theta_2 = \theta_3 \tag{6.4}$$

The solution is found as follows:

1. The initial conditions of the system are entered; these include the incident shock strength (M_s), complimentary wall angle ($\theta_w + \chi$) and pressure and temperature ahead of the shock (P_0 and T_0)
2. The frame of reference is transformed to the triple point and the flow properties are solved for in Region (1)
3. The reflected shock angle (ϕ_1) is then varied from the Mach angle (i.e. the weakest shock possible) to being perpendicular to the flow (i.e the transition condition to one of the vN/G/V Reflection configurations[1]) in small increments
4. For each reflected shock angle the flow in Region (2) is solved for, this then sets the required boundary conditions for that particular ϕ_1 angle:
   (a) The total deflection across the incident and reflected shock is solved for ($\theta_1 - \theta_2$)

(b) The pressure ratio across the reflected shock (p_2/p_1) is normalised by the pressure in front of the incident shock by the following simple relation:

$$\frac{p_3}{p_0} = \frac{p_2}{p_1} \times \frac{p_1}{p_0} \tag{6.5}$$

(c) Equation 6.2 allows for the Mach stem shock angle to be solved for a given pressure ratio. The flow in Region (3) is then calculated, of specific interest is the deflection angle θ_3. This may be compared to the required angle from Equation 6.4

(d) Based on Equation 6.4 the divergence of the shear layer is then calculated for a given reflected shock angle ϕ_1. The correct solution is reached when the value of the divergence is zero or sufficiently small e.g. $(< 10^{-3})^\circ$

The following Figures 6.23 to 6.25 represent all possible reflected shock angles where a solution could be obtained for the Mach stem shock angle, given the initial conditions for Ben-Dor's study. Upon closer inspection of Equation 6.2 it is evident that $\phi_3 \to 90^\circ$ as:

$$P_3/P_0 \to \frac{\left(M_0^2 - 1\right)(2\gamma)}{\gamma + 1} + 1 \tag{6.6}$$

The graphical representation of this is the well known shock polar (shown in Figure 6.22); for a given shock strength a maximum pressure ratio is achievable by an oblique shock. The incident shock is represented by the blue polar, the flow in Region (1) is where the reflected shock polar originates from. The intersection of the two polars is the three shock solution with the flow properties in Region (2) and (3) being obtained from the required shock angles. Equation 6.2 is the reason why only a limited range of reflected shock angles returns a result for the Mach stem angle: the pressure ratio at certain required Mach stem angles is not achievable by even the strongest shock possible at this Mach number (i.e. a normal shock to the oncoming flow $\phi_3 = 90^\circ$).

Figures 6.23 show the possible shear layer divergence angle (ϵ) as the reflected shock and Mach stem angles are varied. Note that as described above the angles are not varied independently. The divergence of the shear layer increases to a maximum as the reflected shock angle is increased from the Mach angle as seen in Figure 6.23. Close to the Mach angle the divergence is approximately 0°. After reaching a maximum value the divergence decreases rapidly in a region where small changes in reflected shock angle affect the divergence greatly. At a certain reflected shock angle the divergence crosses over the x-axis and divergence becomes negative i.e. the flow is converging at the triple point: an aphysical solution. The corresponding Mach stem angle is shown in Figure 6.23, this angle varies over a much wider range than the reflected shock angle.

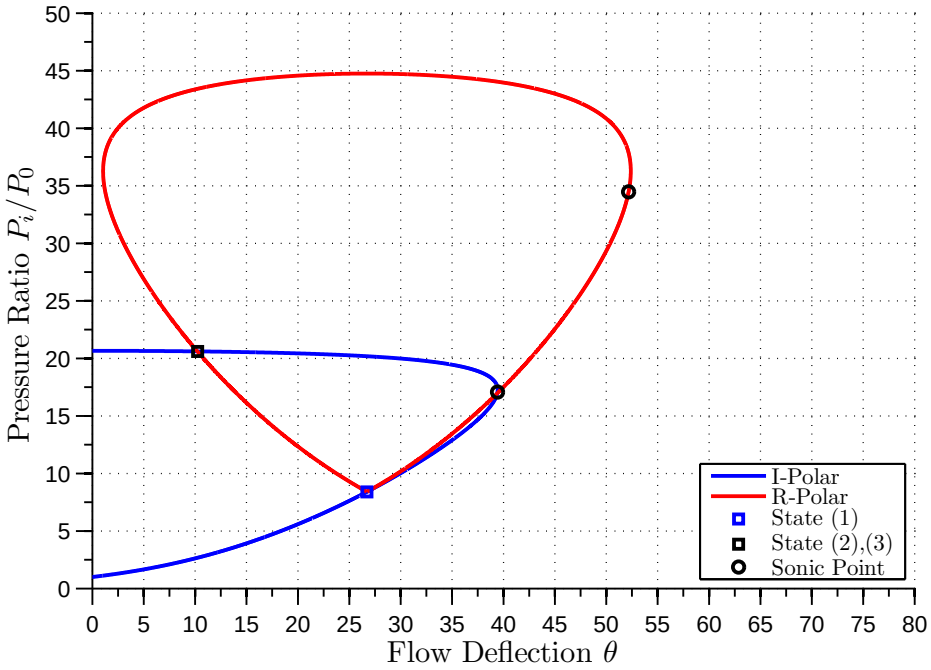


Figure 6.22: Shock Polar representation of Ben-Dor's data

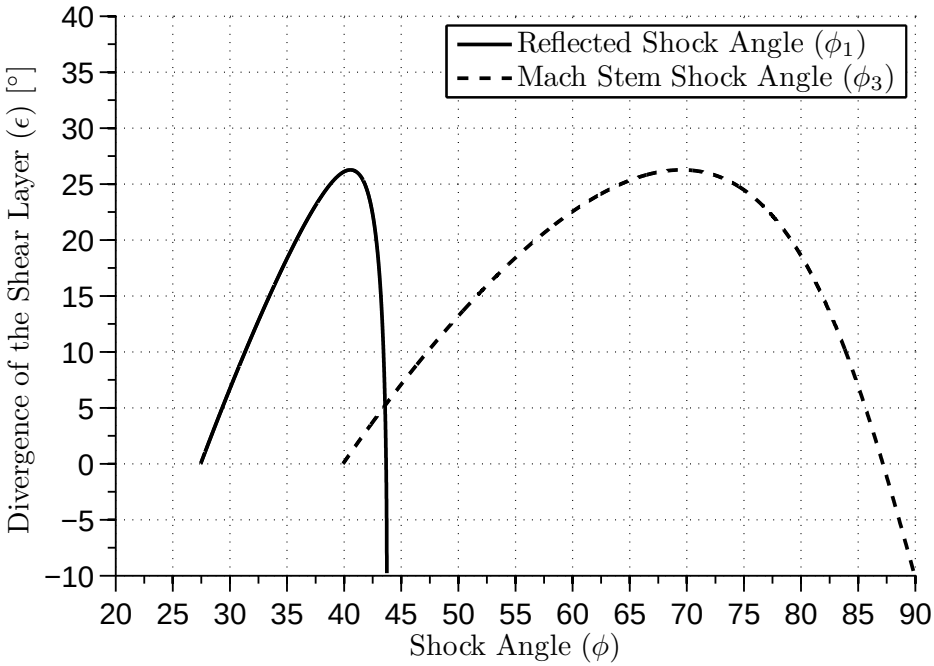


Figure 6.23: Shock Angle (ϕ) vs Shear Layer Divergence (ϵ)

Due to three possible solutions existing for the three shock solution, the same angles were plotted against the Mach number of the flow behind the Mach stem (M_3). This is shown in Figure 6.24. A comparison of Figure 6.23 and 6.24 reveals that for the smallest reflected shock angle, the flow behind the Mach stem is supersonic; this is physically not possible as it requires an additional shock wave to redirect flow along the wall. This phenomena has not been observed experimentally, therefore the second solution may be neglected for the Single Mach Reflection configuration. Closer examination of the second solution revealed that it occurred at the point State (1) in Figure 6.22 and is considered to be a numerical solution only. A third solution does exist if the shock polar in Figure 6.22 is examined however this corresponds to the vN/G/V Reflection boundary condition for Three Shock Theory i.e. $\theta_1 + \theta_2 = \theta_3$, this form of the boundary condition was excluded by the numerical simulation.

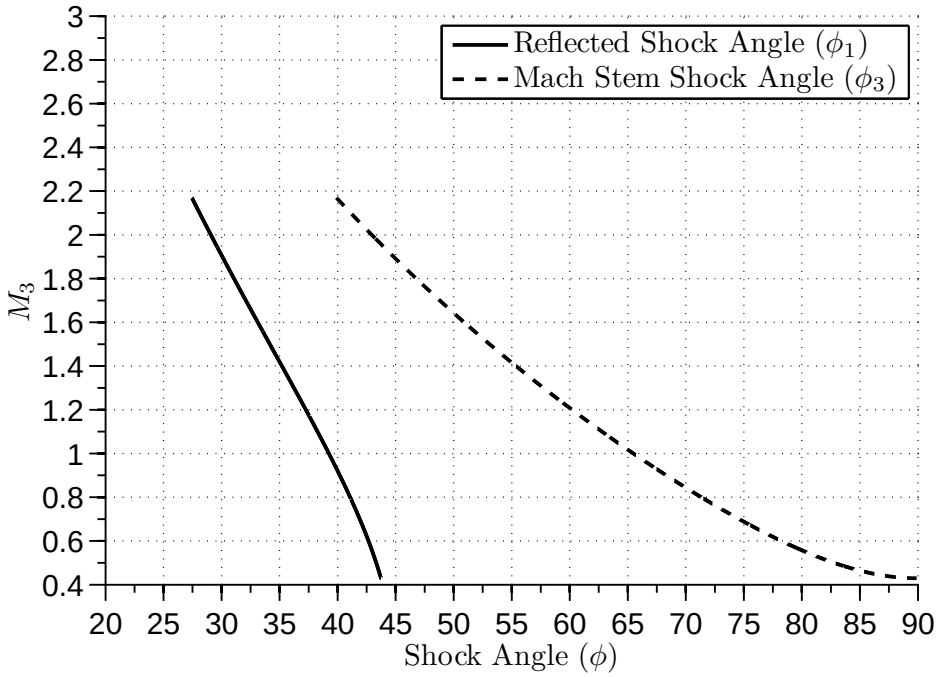


Figure 6.24: Shock Angle (ϕ) vs M_{03}

The velocity and density ratio across the shear layer is plotted against the reflected shock angle in Figure 6.25. From here it can be seen the velocity ratio change is much greater as the reflected shock angle is varied. Both ratios decrease with increasing angle ϕ_1, where the flow properties are the same across the shear layer at the Mach angle of the reflected shock. The velocity ratio curve tends towards zero at a certain angle ϕ_1 whilst the density ratio curve appears to flatten out and tend towards a finite ratio.

The three shock solution simply occurs when the shear layer divergence angle is zero; this may be found numerically by increasing the reflected shock angle until the divergence value becomes negative. The solution then exists in the small range near that angle and is found by a simple bracketing method to ensure quick convergence. Table 6.2 shows the numerical

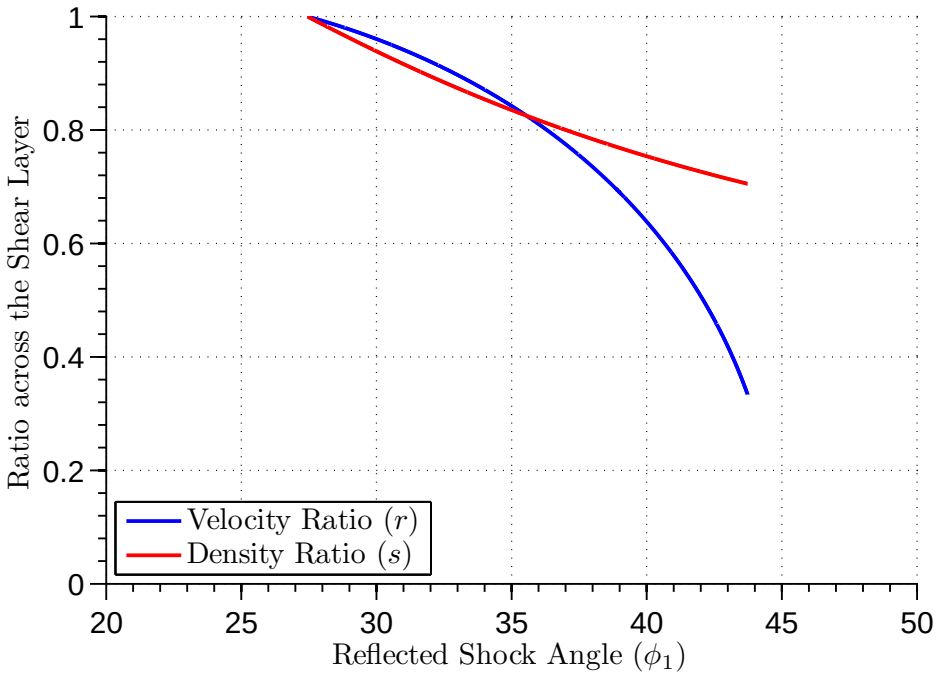


Figure 6.25: Reflected Shock Angle (ϕ_1) vs Velocity and Density Ratio

code results compared to Ben-Dor's results for a perfect gas model under the same input conditions:

Model	Flow Region	M	P [mmHg]	Shock Angle ϕ[°]	Deflection θ[°]
Ben-Dor 1987[10]	(0)	4.231	760	39.9	-
	(1)	2.171	6404	43.64	26.73
	(2)	1.537	15707	-	16.49
	(3)	0.441	15707	87.18	10.24
Numerical Code	(0)	4.2248	760	39.9	-
	(1)	2.1699	6385	43.6734	26.7171
	(2)	1.5361	15661	-	16.4935
	(3)	0.4409	15661	87.1655	10.2238

Table 6.2: Comparison of Ben-Dor's[10] results to the numerical code

As can be seen in Table 6.2 the numerical code matches closely the results of Ben-Dor[10]. Small discrepancies exist between each of the dataset values; this may be attributed to the slightly different approaches to the problem discussed previously. With the numerical code validated, it can then be used in the following sections to compare experimental data from Section 6.1 to Three Shock Theory.

6.2.2 Comparison of Three Shock Theory to Experimental Results

With the numerical code validated in the previous section, a comparison is made to the experimental results. The complimentary wall angle is used for the x-axis as it ensures the results are independent of wedge angle. Note that the theoretical calculations assume the Mach stem is perpendicular to the wall at the triple point, it is well known that this is not the case experimentally as discussed in Section 6.1.2. Shown in Figure 6.26 is the theoretical comparison of the incident to reflected shock angle. As expected, poor agreement is obtained for all Mach numbers especially at the lower complimentary wall angles. There is no correlation between the Mach 1.30 and 1.44 results and the theory. Some agreement is obtained for the Mach 1.59 results between complimentary wall angles of 35° to 40°.

Figure 6.27 shows the theoretical comparison of the incident shock to Mach stem angle. Above complimentary wall angles of 40° excellent agreement is obtained as the theoretical curves collapse to the same line. The same general trend is observed for all Mach numbers however the theory does not permit solutions at complimentary wall angles less than 35°. Once again, poor agreement is obtained for the lower Mach numbers where experimental results are obtained where the theory does not permit a solution.

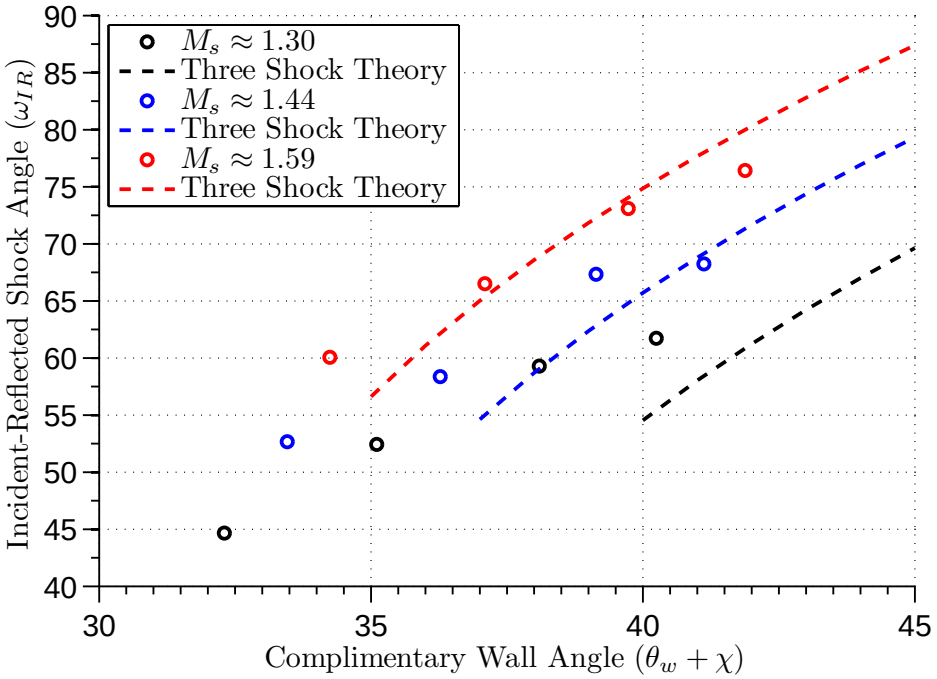


Figure 6.26: Comparison of experimental shock angles to Three Shock Theory for ω_{IR}

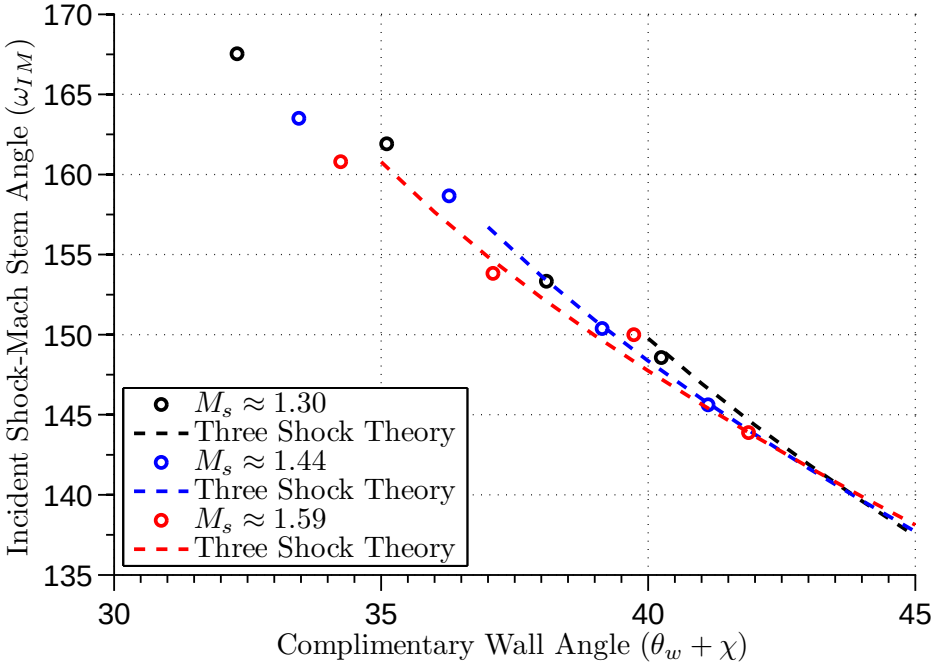


Figure 6.27: Comparison of experimental shock angles to Three Shock Theory for ω_{IM}

6.2.3 Theoretical results for Complimentary Wall Angle ($\theta_w + \chi$)

The theoretical results for a fixed Mach number on the various Mach reflection parameters such as triple point trajectory angle and the different flow properties in each region are assessed below. The theoretical triple point trajectory angle for a fixed Mach number (for this example a Mach number of 1.30 was chosen) versus the complimentary wall angle is shown in Figure 6.28. The triple point trajectory angle decreases with increasing ($\theta_w + \chi$) value. Oscillations are present in the results as the trajectory approaches 0°.

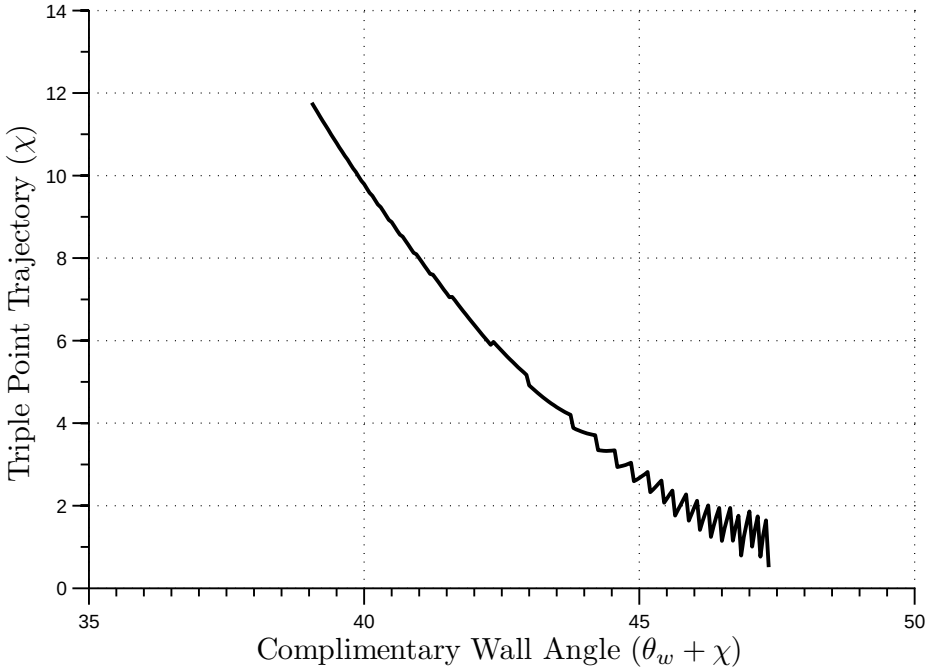


Figure 6.28: Triple Point Trajectory (χ) vs Complimentary Wall Angle ($\theta_w + \chi$) for $M_s = 1.30$

The flow Mach numbers were plotted against ($\theta_w + \chi$) in Figure 6.29. The flow Mach number in Region (2) and (3) behind the reflected shock is subsonic for all ($\theta_w + \chi$) values and corresponds to a Single Mach Reflection (Skews[8],Olim and Dewey[12] and Ben-Dor and Glass[2]). As expected the solutions that exist for all ($\theta_w + \chi$) values imply the Mach number in Region (1) is supersonic, if this was not the case there would be no need for a reflected shock.

The reflected and Mach stem shock angles are plotted in Figure 6.30. The reflected shock angle decreases from the strongest possible shock ($\phi_1 = 90°$) to a finite value. Conversely, the Mach stem shock angle increases to the strongest possible shock ($\phi_3 = 90°$), for ($\theta_w + \chi$) values beyond that there exists no three shock solution as discussed in Section 6.2.1.

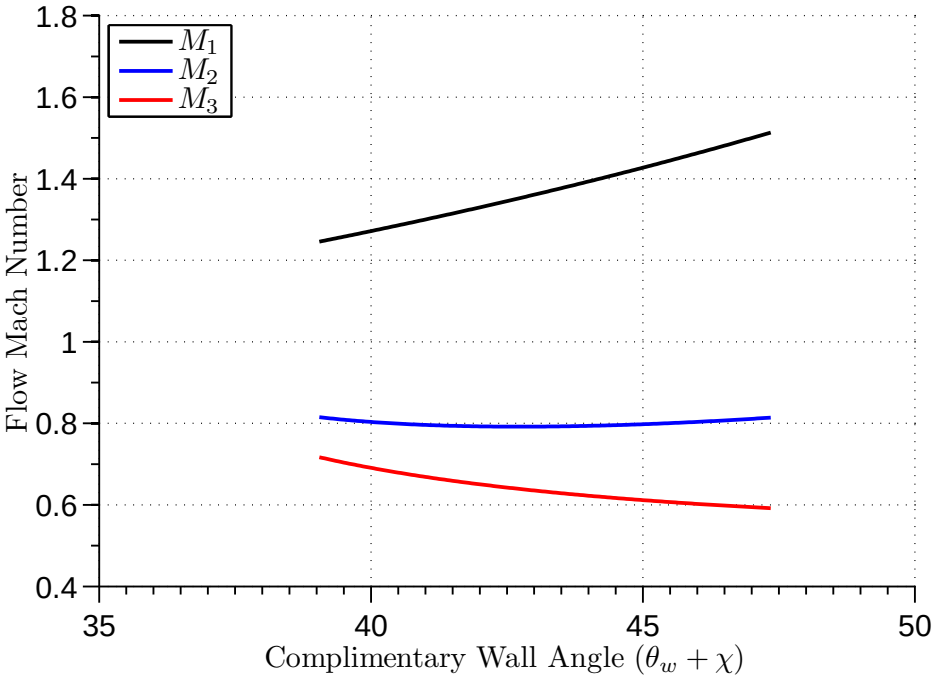


Figure 6.29: Flow Mach Number vs Complimentary Wall Angle ($\theta_w + \chi$) for $M_s = 1.30$

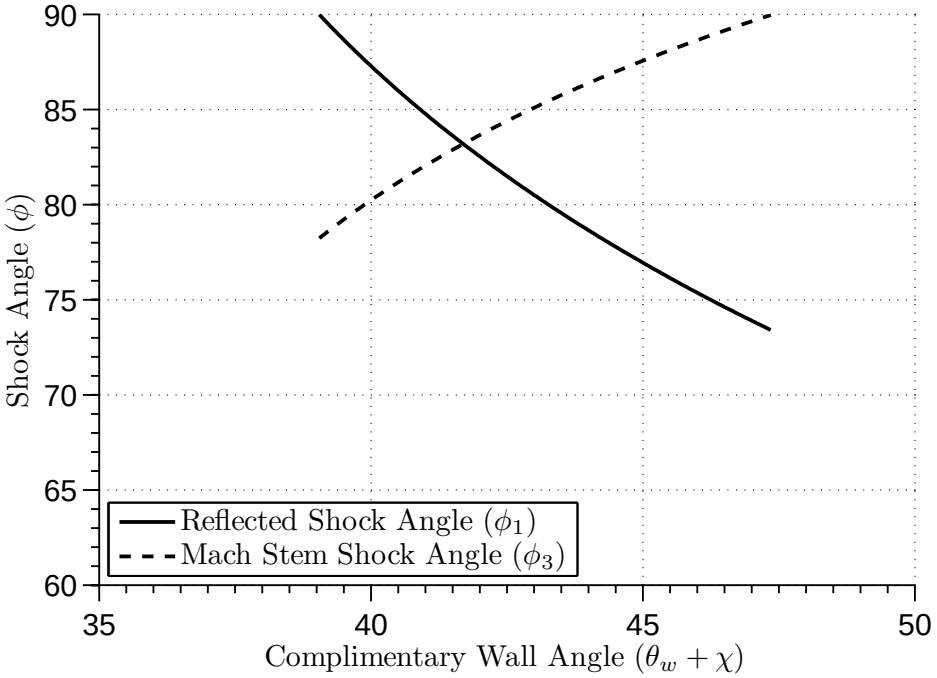


Figure 6.30: Shock Angle (ϕ) vs Complimentary Wall Angle ($\theta_w + \chi$) for $M_s = 1.30$

6.3 Oblique Shock Analysis: MSAST Experimental Results

As shown previously in Section 6.2.2 the application of Three Shock Theory to the Mach number domain being investigated shows poor agreement; an oblique shock analysis based off the experimentally measured shock angles was undertaken identical to that in Section 6.1.1. Due to the larger dataset available from the testing conducted in the MSAST, a graphical approach to compare the results as a function of wedge angle is provided below.

Note that due to the oblique shock analysis undertaken, an exact solution that satisfies the boundary conditions across the shear layer is unlikely, therefore the limits described by Olim and Dewey[12] in their analysis are adopted for the present study. Shown in Figure 6.31 is the normalised pressure difference across the shear layer (ΔP).

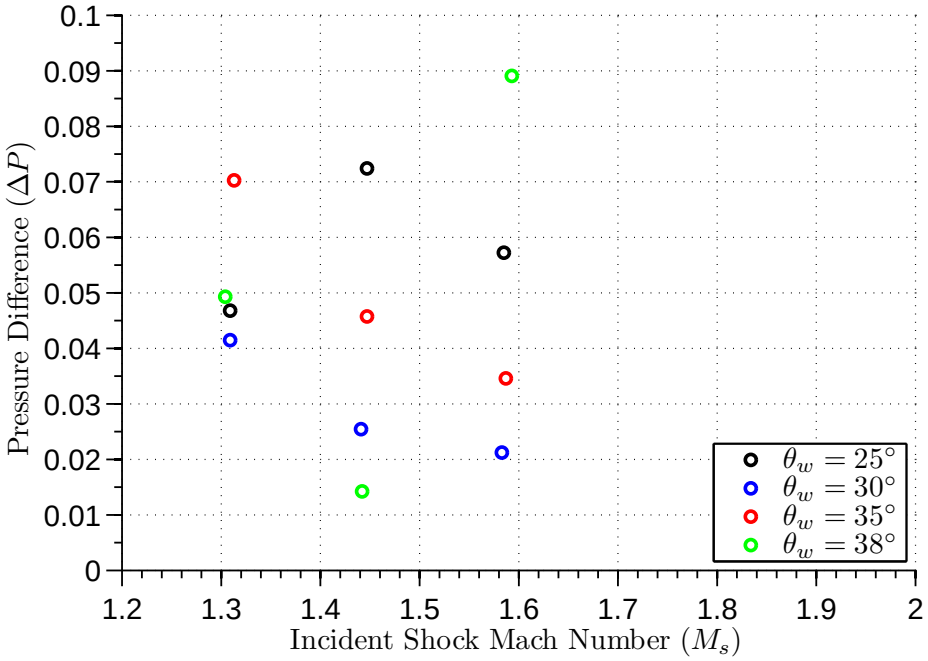


Figure 6.31: Pressure difference across the shear layer

For all measured angles the pressure difference across the shear layer is well below the limit set by Olim and Dewey of 0.128[12] and is therefore considered negligible. Therefore it can be concluded that the angular shock measurements are of the highest accuracy possible. The corresponding shear layer divergence angle is shown in Figure 6.32, from here it can be seen that only 5 cases are below the minimum divergence specified in Olim and Dewey of 0.8°. In general the divergence decreases with increasing Mach number as solutions to Three Shock Theory are obtainable at these Mach numbers. The effect of changing the wedge angle shows no meaningful correlation, this is most likely due to each measurement having its own uncertainty associated with it, with some uncertainties larger than others.

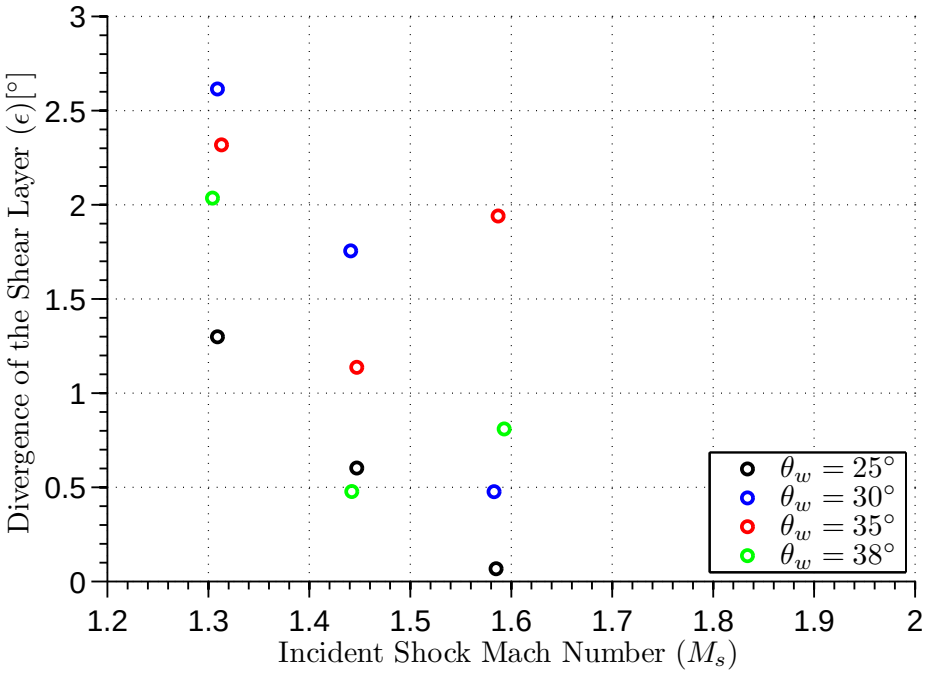


Figure 6.32: Divergence across the Shear Layer

The shear velocity (ΔU) and convective Mach number (M_c) are plotted in Figure 6.33 and 6.34 respectively. A reminder that the convective Mach number is given by:

$$M_c = \frac{U_1 - U_c}{a_1} \tag{6.7}$$

where U_1 is the high speed side of the shear layer, corresponding to the flow in Region (2) and a_1 is the local sound speed calculated from oblique shock relations. The convective velocity of the KHI structures is given by:

$$U_c = \frac{a_2 U_1 + a_1 U_2}{a_1 + a_2} \tag{6.8}$$

where U_2 is the low speed side of the shear layer, corresponding to the flow in Region (3). The above Equation 6.8 may be used as the flows have the same specific heat ratio γ and real-gas effects have been ignored. From Figure 6.33 the velocity difference across the shear layer increases with increasing Mach number and wedge angle. This correlates well with the previous Section 6.1.2 where the shear layer thickness increased as a function of Mach number and wedge angle. It is well documented (Brown and Roshko[17],Papamoschou and Roshko[22]) that an increase in shear velocity results in a thickening of the shear layer; this was observed experimentally.

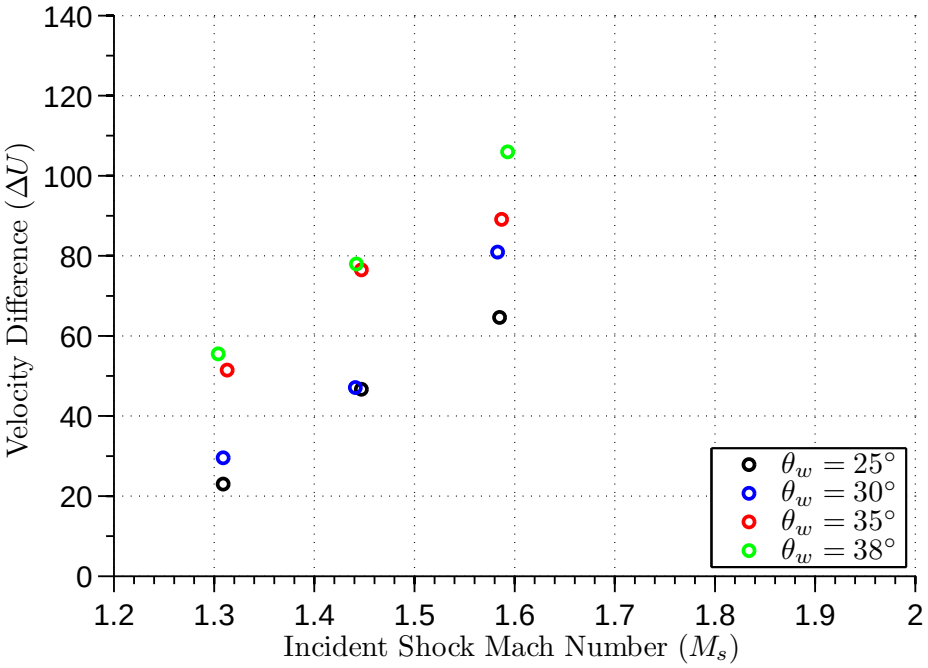


Figure 6.33: Velocity difference across the Shear Layer

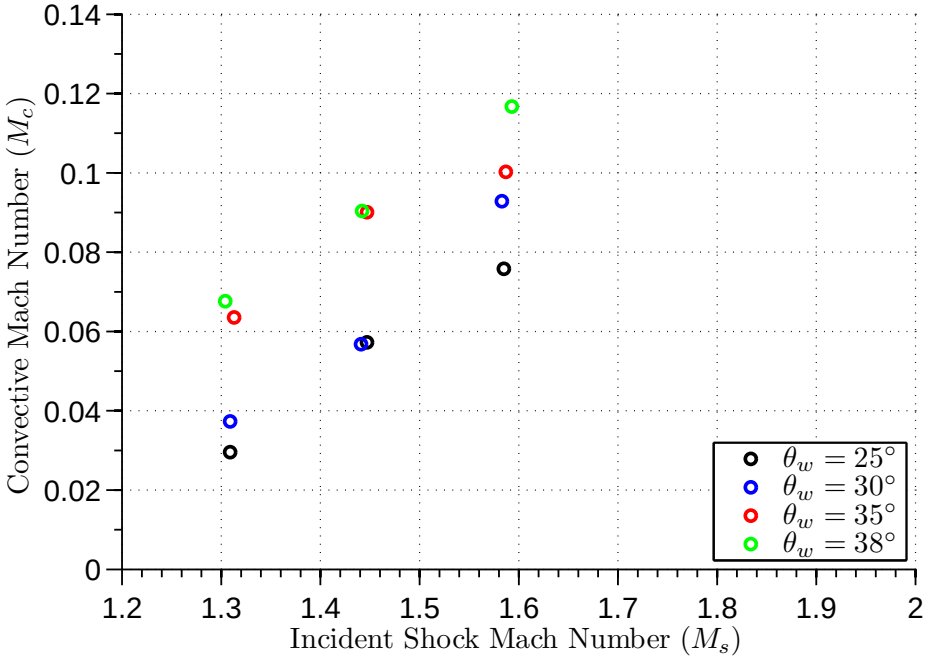


Figure 6.34: Convective Mach Number

The convective Mach numbers are low ($M_c < 0.12$) for all test cases. However, the values increase with increasing Mach number and wedge angle due to the increasing flow velocities on either side of the shear layer. The increase in M_c values indicate that an increase in wedge angle or Mach number causes an increased effect of compressibility. According to Papamoschou and Roshko[22] this effect is only noticed beyond M_c values greater than 0.4, therefore the shear layer thickness should increase with increasing shear velocity for all experimental cases which was previously noted in Section 6.1.2.

The effect of compressibility is not included in the visual growth rates proposed by Brown and Roshko[17] or Dimotakis[20]. In the Mach number domain considered and for all wedge angles used, compressibility effects have a negligible effect on the growth rate of the shear layer. The main factor contributing to the growth rate is therefore the velocity and density ratio where the oblique shock analysis allows for these values to be calculated.

The velocity ratio (r) is show in Figure 6.35. The velocity ratio across the shear layer decreases with increasing wedge angle and Mach number. This implies the shear layer growth rate increases as the wedge angle and Mach number is increased; which was verified experimentally. The density ratio (s) is shown in Figure 6.36. The density ratio decreases for wedge angles greater than 30° with increasing Mach number. For all wedges except for the 38°, the density ratio is greater than 1 for the Mach 1.30 tests. The importance of this was noted by Rikinati et al.[24], where $s > 1$ inhibits the growth of the shear layer. The visual growth rates were almost negligible at the lower Mach numbers for these wedge angles, this correlates well with the oblique shock analysis. This is further verified for the 25° wedge where the density ratio ($s \approx 1$) for all Mach numbers.

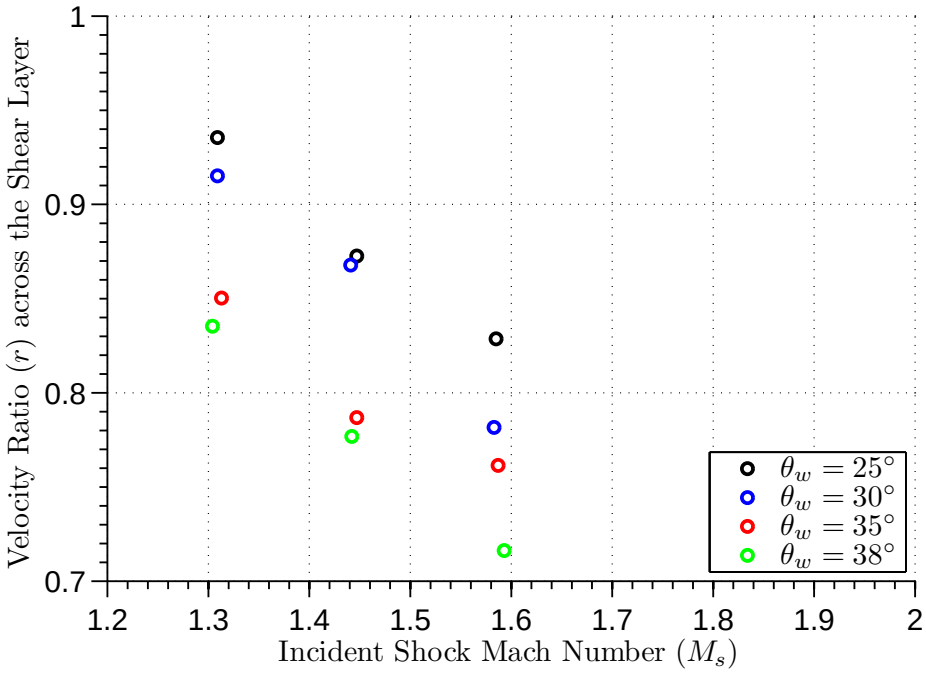


Figure 6.35: Velocity Ratio across the Shear Layer

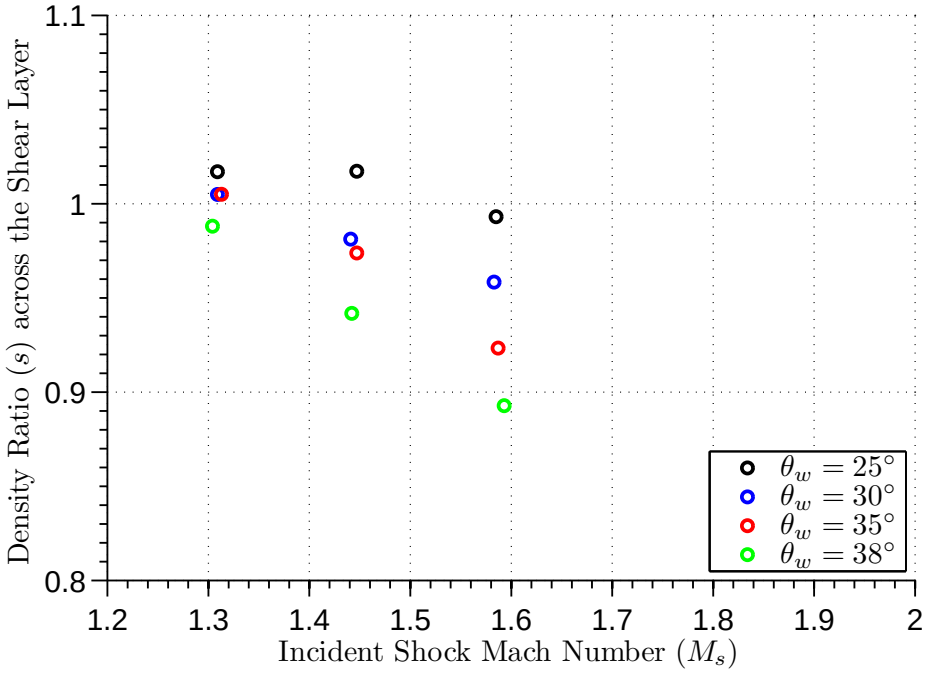


Figure 6.36: Density Ratio across the Shear Layer

6.4 Shear Layer Growth Calculations

In order to investigate the effect of different velocity and density ratios across the shear layer have on the growth rate, various equations were plotted from Papamoschou and Roshko[22]. Previously derived expressions from Brown and Roshko[17] were only applicable to constant density shear layers, while this may be applicable to the lower wedge angle results, the 38° density ratios are significant. The follow up derivation by Dimotakis[20] included the experimentally measured vortex spacing (l/x) from Brown's data and should be used with caution. The work of Chinzei et. al[21] bares no relevance to the present work as both flows in a Single Mach Reflection are subsonic. Papamoschou derived the same expression for the incompressible growth rate as Dimotakis. The similarity between the two Equations 6.9 and 6.10 is evident.

Dimotakis 1986[20]

$$\frac{\delta}{x} = 0.17\left(\frac{1-r}{1+rs^{1/2}}\right)\left[1+s^{1/2}-\frac{1-s^{1/2}}{1+2.9\left(\frac{1+r}{1-r}\right)}\right] \tag{6.9}$$

Papamoschou and Roshko 1988[22]

$$\delta'_{viz,0} = 0.17\frac{\Delta U}{U_c} = 0.17\frac{[1-r]\left[1+s^{1/2}\right]}{1+rs^{1/2}} \tag{6.10}$$

The visual growth rate (δ'_{viz}) is plotted against the variable $\lambda = \frac{1-r}{1+r}$ in Figure 6.37. Plotting growth rates against λ ensures the curves pass through the origin when $r = 1$ (corresponding to two flows of the same velocity i.e. zero velocity shear) and reach a maximum as $r \to 0$ (corresponding to the edge of a jet where one stream is at rest). The growth rate curves were plotted with constant density ratios of $s = 1/7, 1, 7$ as first used in Brown and Roshko[17]. The visual growth rates increase as the parameter λ increases which is attributed to a decreasing velocity ratio. The effect of increasing the density ratio is small as large density ratios across the shear layer are not easily attained. The growth rates are linear for equal densities across the shear layer where Equation 6.9 and 6.10 reduce to the growth rate equation found in Brown. At very low λ values i.e. high velocity ratios, the growth rates are practically independent of density ratio.

The convective velocity ratio was derived analytically by Dimotakis[20] and is given by Equation 6.11. The convective velocity ratio is simply the ratio U_c/U_1 and is shown in Figure 6.38 for the same density ratios mentioned previously.

$$r_c = \frac{1+rs^{1/2}}{1+s^{1/2}} \tag{6.11}$$

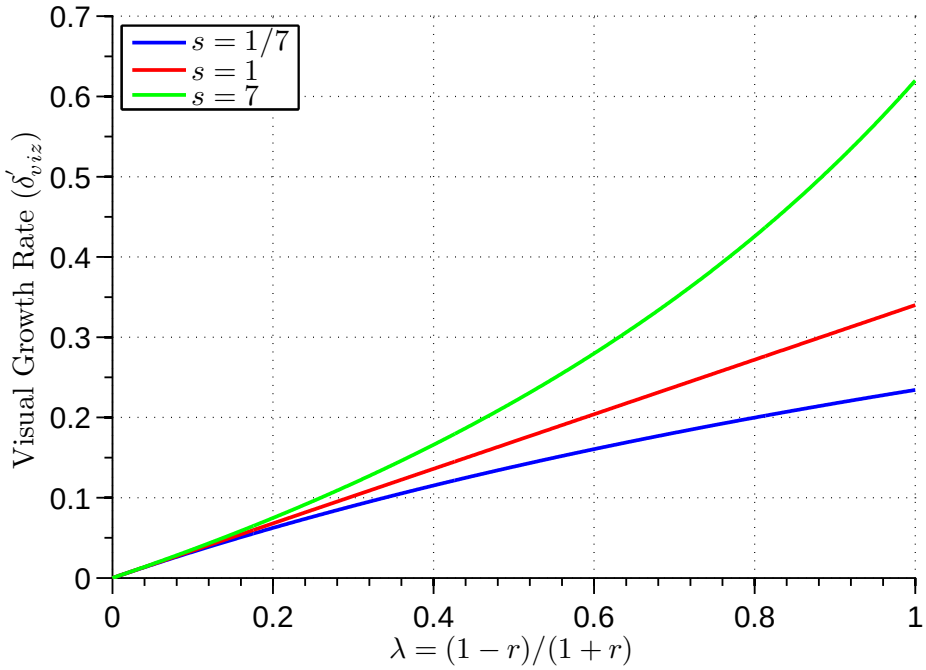


Figure 6.37: Visual Growth Rate (δ'_{viz}) vs λ

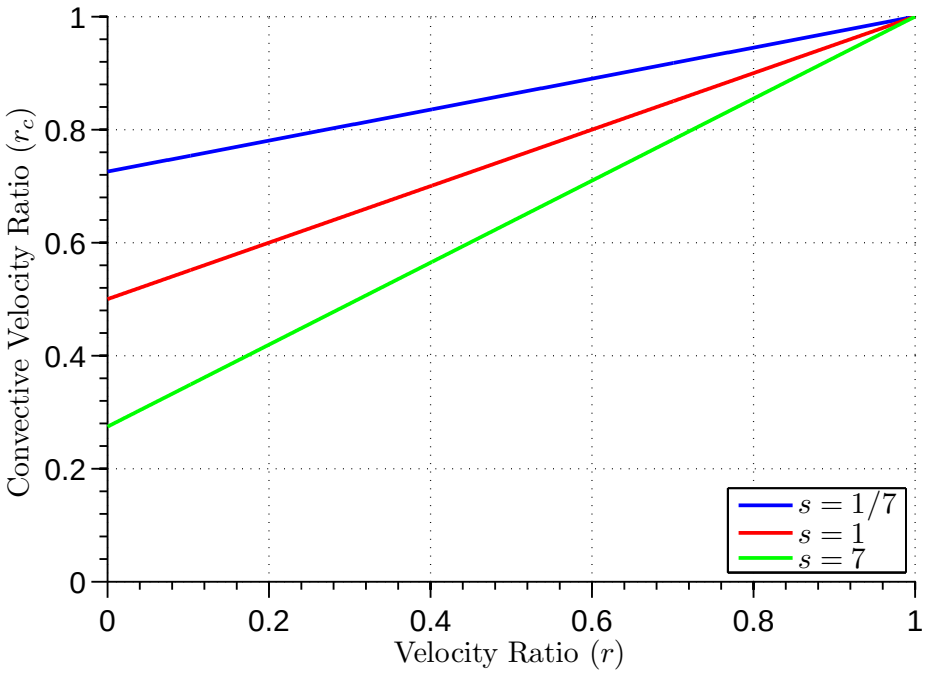


Figure 6.38: Convective Velocity Ratio (r_c) vs Velocity Ratio (r)

From Figure 6.38 it is clear that the convective velocity ratio $r_c \to 1$ with increasing velocity ratio in a linear fashion. The effect of increasing the density ratio affects decreases the values of r_c attained. This implies that the convective velocity of the structures within the shear layer decreases *with respect to* the high speed layer U_1.

The convective velocity ratio is plotted against the visual growth rate in Figure 6.39. The effect of increasing the density ratio, increases the growth rates attainable whilst decreasing the convective velocity ratio. This implies that a more rapidly growing shear layer is obtained with slower moving KHI structures relative to the high speed layer within it.

The visual growth rate was plotted against density ratio taking different velocity ratios as a parameter in Figure 6.40. For a fixed velocity ratio ($r > 0.4$) any change in density ratio has negligible effect on the growth rate attainable. This is relevant in the present study as the density ratios obtained from the oblique shock analysis were all in the region $0.89 < s < 1.02$, therefore the main influence on the growth rate of the shear layer can be attributed to velocity ratio alone.

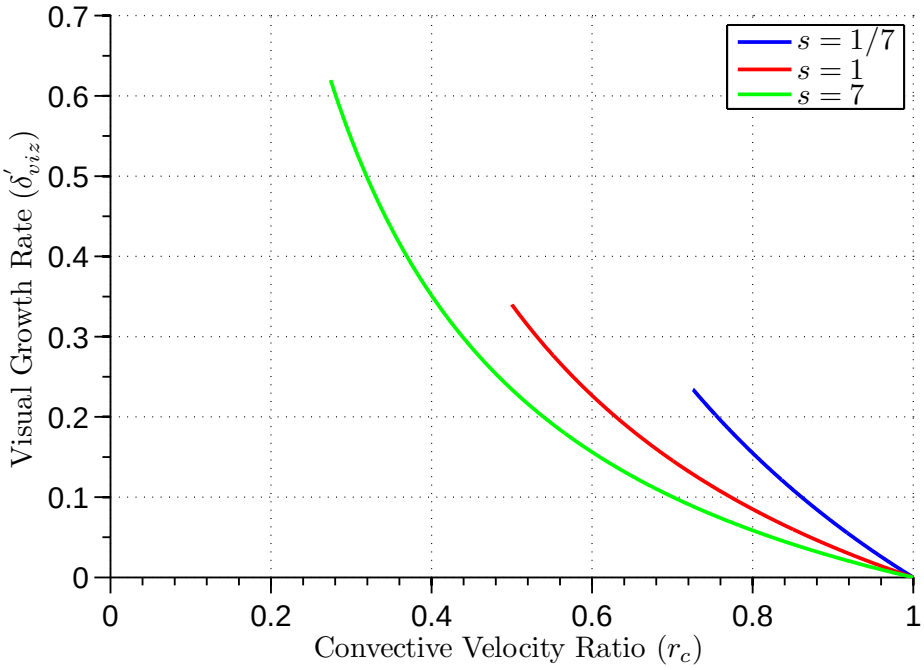


Figure 6.39: Visual Growth Rate (δ'_{viz}) vs Convective Velocity Ratio (r_c)

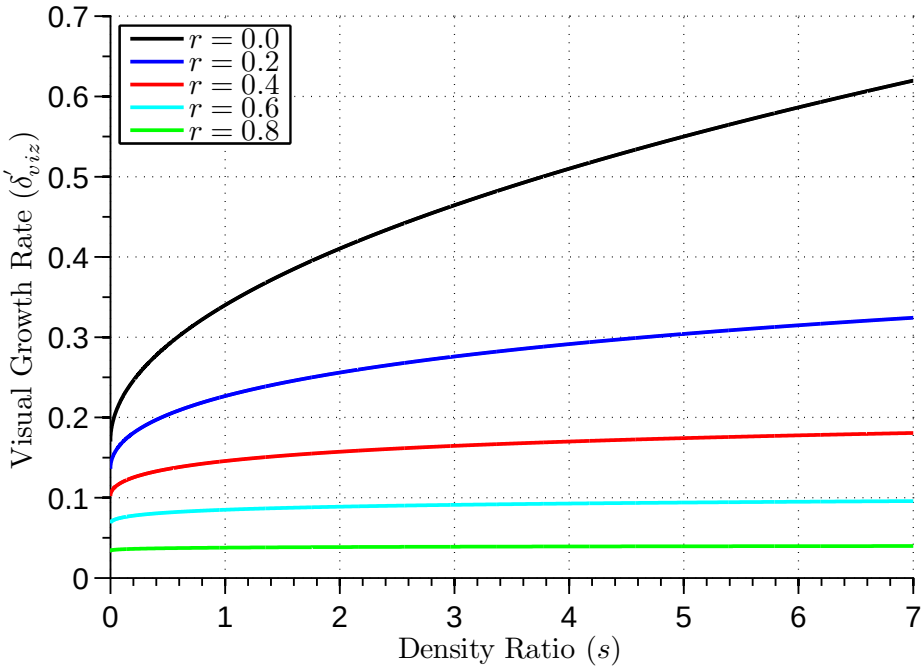


Figure 6.40: Visual Growth Rate (δ'_{viz}) vs Density Ratio (s)

6.4.1 Spread Angle Comparison to Experimental Results

The spread angle of the shear layer was measured at least 5 times to obtain a meaningful average. Due to the limited resolution available, the uncertainty was calculated using the same method as in Section 6.1.2. On average the uncertainties from the measured angles were in the region of $\pm 0.5°$. The spread of the shear layer was measured by constructing two straight lines along the upper and lower edge of the layer itself and measuring the angle between the two lines. Note that for all cases the thickness of the shear layer at the triple point was non-zero. This may be due to the finite exposure time of the light source used however, it is well documented that the region in the vicinity of the triple point is not governed by the Rankine-Hugoniot relationships (Skews[8]). The associated difficulties measuring the shear layer spread are summarised below:

- The shear layer grows from a finite thickness, this increases the difficulty in measuring the spread angle at the triple point
- In the Mach number domain used in the present study, a Single Mach Reflection is obtained for all test cases; this results in a curved shear layer due to the flow field being subsonic with respect to the triple point
- The 25° wedge yielded no measurable growth in shear layer thickness. For the 30° wedge, only the highest Mach number case yielded a usable result

The visual growth rate is simply related to the spread angle by:

$$\delta'_{viz} = 2tan\,(\theta_{spread}) \tag{6.12}$$

A comparison to the theoretical visual growth rates from Papamoschou and Roshko[22] is shown in Figure 6.41 with the inclusion of results from Rubidge and Skews[13]. The growth rates are very low when compared to the available data from Brown and Roshko[17] Figure 2.8. The theoretical curves agreement is summarised as follows:

- Reasonable agreement is obtained for the 30° wedge results from Rubidge and Skews[13] for all Mach numbers as well as for the single measurement recorded in the present study. The LBST results agree well with the results of Rubidge and Skews within the experimental accuracy
- Excellent agreement is obtained for the 35° and 38° wedges for the Mach 1.30 and 1.44 cases
- Poor agreement is obtained for the 35° and 38° wedges for the highest Mach number case. There could be a transition to turbulence occurring for these results and this could lead to an increased thickness of the shear layer. This requires further verification

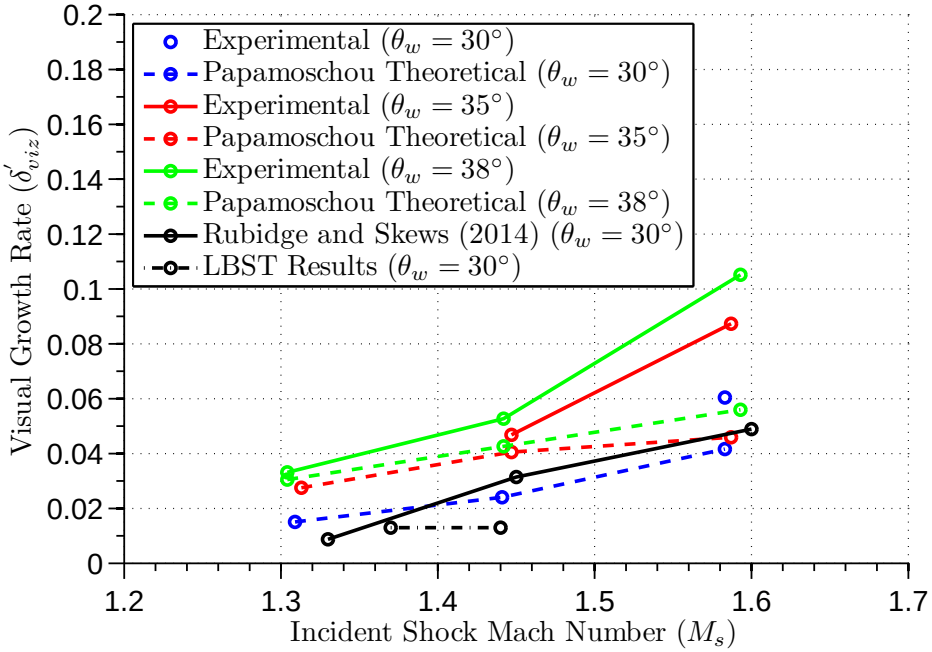


Figure 6.41: Visual Growth Rate (δ'_{viz}) comparison to theory from Papamoschou and Roshko[22]

The growth rate equations from Brown, Dimotakis and Papamoschou are all based off the assumption that there are structures within the shear layer. In the present study and the work of Rubidge and Skews[13], the KHI structures visible within the shear layer are only present approximately midway down the layer between the triple point and the wedge surface.

The work of Rikanati et al.[14] compared the spread angle of the shear layer to their large scale KHI growth rate model. Three Shock Theory was used to obtain the shear layer properties such as velocity and density ratio in order to calculate the spread angle in their study. Note that in the present study, Three Shock Theory does not apply for all cases and poor correlation is obtained due to the Mach number domain under consideration; therefore the results from the oblique shock analysis are used instead. The growth rate equation used by Rikanati was plotted in Figure 6.43 with the results from Papamoschou transformed by Equation 6.12 shown in Figure 6.42 for comparison. The equation derived in Rikanati et al.[14] is given in Equation 6.13.

$$\frac{\delta}{x} = (0.38 \pm 0.02) \frac{S}{1 - 2f_d\left(\rho_1, \rho_2\right) S} \times f_{HiMach}\left(\frac{\Delta U}{a}\right) \tag{6.13}$$

The term f_{HiMach} is used to compensate for the effect of compressibility, previously attributed to the convective Mach number[22]. As it is a function of $\Delta U/a$, originally determined from Three Shock Theory, the accuracy to which it may be applied remains questionable. The oblique shock analysis revealed that the values of $f_{HiMach} \approx 1$ for the present study, once again reinforcing that the shear layer of a Single Mach Reflection in the $M_s < 1.5$ domain is not affected by compressibility effects.

A comparison of the theoretical models of Papamoschou and Rikanati et al. in Figure 6.42 and 6.43 reveals very little difference. The inclusion of compressibility in Rikanati's model has no distinct advantages for the present study. The differences between the two models is mainly due to the value of the empirical constants used. Rikanati's theory shows better agreement with the experimental data simply due to the larger constant of 0.38.

The inclusion of the shear layer divergence angle into Three Shock Theory was undertaken by Ben-Dor[11] and resulted in poor agreement with experimental data. Due to the good agreement obtained using an oblique shock analysis in the present study, it can be concluded that the shear layer diverges due to the velocity ratio and the associated shear velocity across it. Further work to include the effect of transition to turbulence is required for the growth rate model.

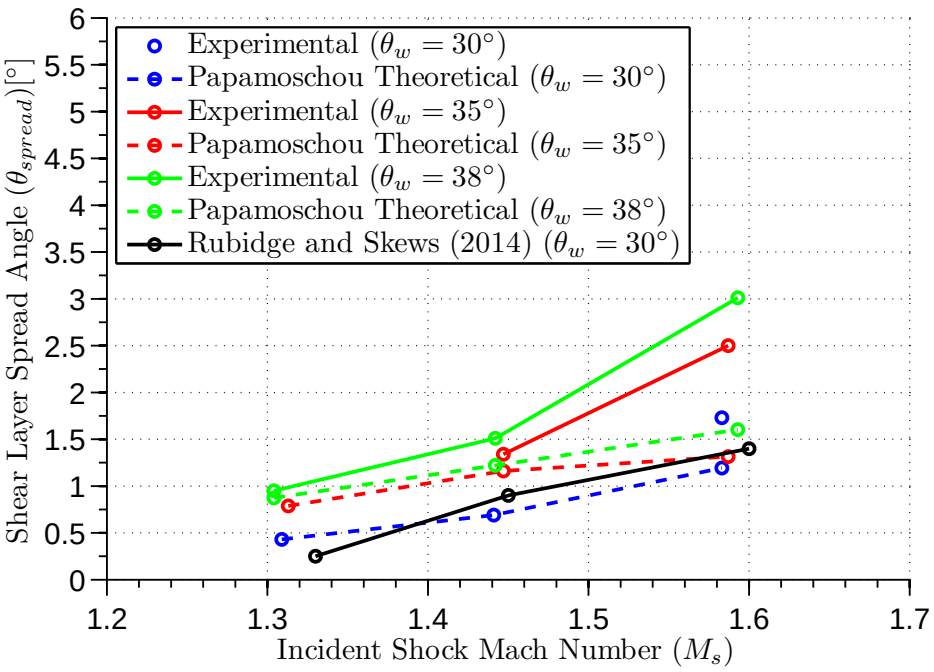


Figure 6.42: Spread angle comparison to theory from Papamoschou and Roshko[22]

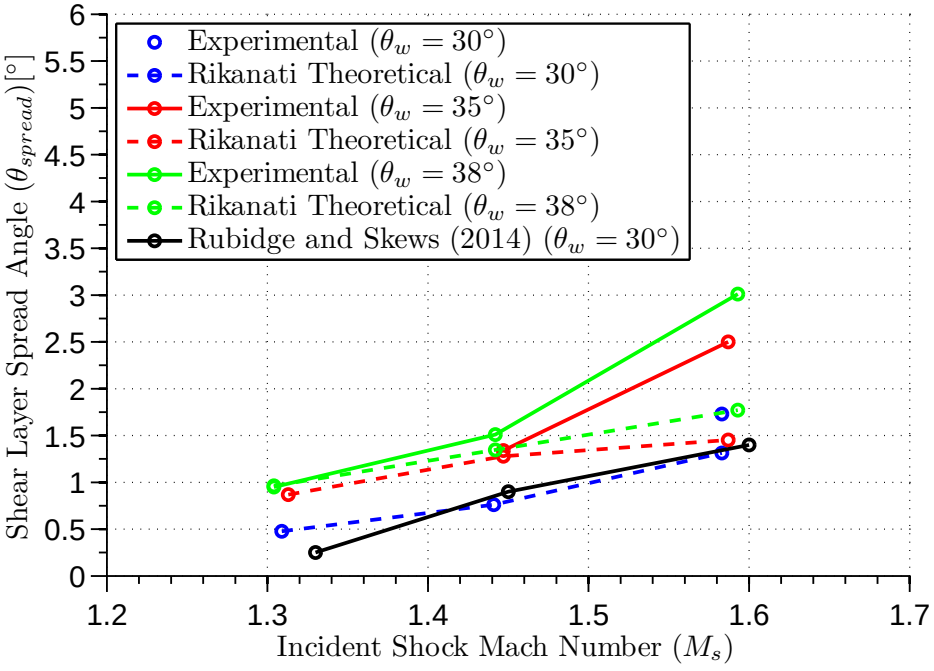


Figure 6.43: Spread angle comparison to theory from Rikanati et al.[14]

Chapter 7 Conclusions

A study of the shear layer of a Single Mach Reflection was undertaken in two facilities at different scales. The large scale facility (the LBST) was used initially but due to an incident where one of the optical windows was damaged, testing was completed in a smaller scale automated shock tube (the MSAST). The investigation was conducted in the $1.27 < M_s < 1.59$ domain in the wedge angle range $25^\circ < \theta_w < 38^\circ$.

Results from the LBST:

- The testing in the LBST was conducted at a much larger scale than previous experiments. A Single Mach Reflection occurring on a 30° wedge was studied over a range of incident shock Mach numbers ($1.27 < M_s < 1.44$). No visible increase in shear layer thickness was observed for the $M_s = 1.27$ case, but rather a large scale KHI structure was present and grew in size as it convected downstream in the triple point reference frame. A measurable change in thickness of the shear layer occurred for the $M_s = 1.27, 1.37$ cases. The visual growth rates were measured at discrete distances from the triple point and were found to be approximately equal within the experimental accuracy. The growth rates were found to be low due to the low velocity shear across the layer. The convective Mach numbers (M_c) were calculated from an oblique shock analysis and were found to be low, indicating the effects of compressibility on the shear layer are negligible. A comparison to previous work undertaken by Rubidge and Skews[13] revealed the shear layer in the large scale experiment was thicker at a similar Mach number, this was due to the larger scale of the experiment. The growth rates were found to be similar when compared to results in the MSAST within the experimental accuracy.

Results from the MSAST:

- The testing in the MSAST was used a complimentary study where a wide range of wedge angles were used ($\theta_w = 25^\circ, 30^\circ, 35^\circ, 38^\circ$) in conjunction with higher Mach numbers

($1.30 < M_s < 1.59$). The experimental images were corrected for optical distortion and measured multiple times to ensure the highest accuracy possible. The effect of increasing the wedge angle resulted in a decreasing triple point trajectory as well as decreased curvature of the Mach stem at the triple point. The curvature of the Mach stem is significant as Three Shock Theory assumes it is perpendicular to the wedge surface at the triple point. An increase in Mach number or wedge angle increases the angle ω_{IR} and decreases the angle ω_{IM}. When plotted against the complimentary wall angle ($\theta_w + \chi$), the results for ω_{IR} increase linearly and are strongly influenced by Mach number whilst the results for ω_{IM} decrease linearly and only depend on wall angle. The shear layer thickness increased as the Mach number or wedge angle was increased. An oblique shock analysis reinforced the previous conclusions reached from the LBST results: the effect of compressibility on the shear layer is negligible. The larger spread angle of the shear layer at higher wedge angle or Mach number is attributed to the decreasing velocity ratio across the layer. The 25° wedge angle spread angle could not be measured as the growth of the shear layer is inhibited due to $s \approx 1$.

Shock angle comparison to Three Shock Theory:

- A numerical code for calculating the theoretical shock angle according to the boundary conditions of Three Shock Theory was validated using the results from Ben-Dor[10]. As expected and in accordance with previous work by other researchers, poor agreement was obtained between the theory and measured experimental angles. Some agreement was obtained for the $M_s = 1.59$ results but not for all wedge angles.

Shear Layer growth rate comparison to theory:

- The shear layer spread angles were measured from the MSAST results and were converted to corresponding growth rate measurements. Previously derived growth rate equations were assessed with the incompressible relation of Papamoschou and Roshko[22] and the large-scale KHI growth rate model of Rikanati et al.[14] being chosen for experimental comparison. Decent agreement was obtained for the 30° wedge for both models as well as the 35° and 38° wedges at Mach 1.44. Poor agreement is obtained at the higher Mach numbers, this is attributed to the breakdown of the shear layer into turbulence and an increased growth rate. Rikanati's model shows the closest agreement due to the higher value of the empirical constant present in their equation.

Chapter 8 Recommendations for Future Work

The current work examined a limited range of parameters in the (M_s,θ_w) domain for studies of the shear layer of a Mach Reflection. Recommendations for future work are given below:

- **Testing at higher Mach numbers**: In both experimental facilities used the maximum Mach number was limited by safety requirements and in the case of the MSAST by the automated software program. In order to obtain higher Mach numbers in the range $M_s > 1.6$ the driven section of each facility would need to be evacuated using a vacuum pump. This would require additional instrumentation and a modification to the LBST test section, whilst for the MSAST additional instrumentation and an update to the automation software would be required. Testing at higher Mach numbers $1.6 < M_s < 2.2$ would allow for the study of Transitional Mach Reflection to be undertaken, improving the shock angle measurements due to the reflected shock being planar in the vicinity of the triple point. Direct comparison to Three Shock Theory may also be made in this M_s domain.
- **Increasing the wedge angle range**: Shear layer spread angle measurements proved inconclusive for the two higher wedge angles used for the higher Mach number cases. Therefore more data points are required at wedge angles close to transition. A 40° wedge could be manufactured for the MSAST to compare to the untested wedge in the LBST of the same angle.
- **Improvements to the flow visualisation setup**:
  - In order to improve the accuracy of the shock angle measurements a higher resolution single shot camera could be used in conjunction with a shorter duration light source. Different optical flow visualisation methods could be used such as holographic interferometry (as used by Rikanati et al. [14]) where the gas density can be calculated directly from the fringes.
  - The use of a high speed camera of sufficient resolution would allow for accurate measurements of the triple point trajectory as well as the assessment of the self-similarity of the shear layer and the three shock structure. Measurements of the

convective velocity of the KHI structures within the shear layer could be estimated using multiple frames from the high speed camera.

- **Modifications to Three Shock Theory**:
  - Further work using a modified Three Shock Theory is to be undertaken. A modification which relaxes the boundary condition that the Mach stem is perpendicular to the wedge surface at the triple point could yield an improved agreement with experimental data. An additional equation is required to solve the three shock system without this boundary condition, a choice of either the angle ω_{IR} or ω_{IM} in addition to the triple point trajectory will be required as an input.
  - The theoretical values for convective Mach number (M_c) are to be plotted in the (M_s, θ_w) plane as a function of θ_w. From there, the regions where compressibility has an effect on the shear layer growth can be obtained.

References

[1] G. Ben-Dor. *Shock-wave Reflection phenomena*. 2nd. Springer, 2007.

[2] G. Ben-Dor and I. I. Glass. 'Domains and boundaries of non-stationary oblique shock-wave reflexions. 1. Diatomic gas'. In: *Journal of Fluid Mechanics* 92 (1979), pp. 459–496. DOI: 10.1017/S0022112079000732.

[3] J. D. Anderson. *Modern compressible flow: with historical perspective*. McGraw-Hill series in aeronautical and aerospace engineering. McGraw-Hill, 2004. ISBN: 9780071241366.

[4] H. Li and G. Ben-Dor. 'A parametric study of Mach reflection in steady flows'. In: *Journal of Fluid Mechanics* 341 (1997), pp. 101–125.

[5] J. von Neumann. *Oblique Reflection of Shocks*. Tech. rep. Explosives Research Report No. 12. Bureau of Ordinance, Washington DC: Navy Department, 1943a.

[6] J. von Neumann. *Refraction, intersection and reflection of shock waves*. Tech. rep. NAVORD Report 203-45. Bureau of Ordinance, Washington DC: Navy Department, 1943b.

[7] C. K. Law and I. I. Glass. 'Diffraction of strong shock waves by a sharp compressive corner'. In: *CASI Transactions* 4 (1971), pp. 2–12.

[8] B. W. Skews. 'The flow in the vicinity of a three-shock intersection'. In: *CASI Transactions* 4 (2 1971), pp. 99–107.

[9] L. G. Smith. *Photographic investigation of the reflection of plane shocks in air*. Tech. rep. OSRD Report 6271. 1945.

[10] G. Ben-Dor. 'A reconsideration of the three-shock theory for a pseudo-steady Mach reflection'. In: *Journal of Fluid Mechanics* 181 (1987), pp. 467–484. ISSN: 1469-7645. DOI: 10.1017/S0022112087002179.

[11] G. Ben-Dor. 'Structure of the contact discontinuity of nonstationary Mach reflections'. In: *AIAA* 28.7 (1990), pp. 1314–1316. DOI: 10.2514/3.25213.

[12] M. Olim and J. Dewey. 'A revised three-shock solution for the Mach reflection of weak shocks (1.1¡Mi¡1.5)'. In: *Shock Waves* 2.3 (1992), pp. 167–176. ISSN: 0938-1287. DOI: 10.1007/BF01414639.

[13] S. R. Rubidge and B. W. Skews. 'Shear-layer instability in the Mach reflection of shock waves'. In: *Shock Waves* 24.5 (2014), pp. 479–488. ISSN: 0938-1287. DOI: 10.1007/s00193-014-0515-6.

[14] A. Rikanati et al. 'Shock-Wave Mach-Reflection Slip-Stream Instability: A Secondary Small-Scale Turbulent Mixing Phenomenon'. In: *Phys. Rev. Lett.* 96.17 (2006), p. 174503. DOI: 10.1103/PhysRevLett.96.174503.

[15] N. Michio. 'Chapter 4.1 - Shock Tubes and Tunnels: Facilities, Instrumentation, and Techniques'. In: *Handbook of Shock Waves*. Ed. by G. Ben-Dor, O. Igra and T. Elperin. Burlington: Academic Press, 2001, pp. 553–585. ISBN: 9780120864300. DOI: http://dx.doi.org/10.1016/B978-012086430-0/50012-9.

[16] H. Kleine. 'Chapter 5.1 - Measurement Techniques and Diagnostics: 5.1 Flow Visualization'. In: *Handbook of Shock Waves*. Ed. by G. Ben-Dor, O. Igra and T. Elperin. Burlington: Academic Press, 2001, pp. 683–IV. ISBN: 9780120864300. DOI: http://dx.doi.org/10.1016/B978-012086430-0/50017-8.

[17] G. L. Brown and A. Roshko. 'On density effects and large structure in turbulent mixing layers'. In: *Journal of Fluid Mechanics* 64 (04 1974), pp. 775–816. ISSN: 1469-7645. DOI: 10.1017/S002211207400190X.

[18] D. W. Bogdanoff. 'Compressibility Effects in Turbulent Shear Layers'. In: *AIAA* 21.6 (1983), pp. 926–927. DOI: 10.2514/3.60135.

[19] D. W. Bogdanoff. 'Interferometric Measurement of Heterogeneous Shear-Layer Spreading Rates'. In: *AIAA* 22.11 (1984), pp. 1550–1555. DOI: 10.2514/3.8817.

[20] P. E. Dimotakis. 'Two-Dimensional Shear-Layer Entrainment'. In: *AIAA* 24.11 (1986), pp. 1791–1796. DOI: 10.2514/3.9525.

[21] N. Chinzei et al. 'Spreading of two-stream supersonic turbulent mixing layers'. In: *Physics of Fluids* 29.5 (1986), pp. 1345–1347. ISSN: 00319171. DOI: 10.1063/1.865698.

[22] D. Papamoschou and A. Roshko. 'The compressible turbulent shear layer: an experimental study'. In: *Journal of Fluid Mechanics* (1988), pp. 453–477. ISSN: 1469-7645. DOI: 10.1017/S0022112088003325.

[23] S. A. Ragab and J. L. Wu. 'Linear instabilities in two-dimensional compressible mixing layers'. In: *Physics of Fluids A: Fluid Dynamics* 1.6 (1989), pp. 957–966. ISSN: 08998213. DOI: 10.1063/1.857407.

[24] A. Rikanati, U. Alon and D. Shvarts. 'Vortex-merger statistical-mechanics model for the late time self-similar evolution of the Kelvin-Helmholtz instability'. In: *Physics of Fluids* 15.12 (2003), pp. 3776–3785. DOI: 10.1063/1.1624837.

[25] M. W. Seitz. 'Shock wave interaction with porus, compressible foams'. PhD thesis. School of Mechanical, Industrial and Aeronautical Engineering, 2001.

[26] S. R. Rubidge. 'Kelvin-Helmholtz instability on the Mach reflection shear layer'. MA thesis. School of Mechanical, Industrial and Aeronautical Engineering, 2012.

[27] L. Kirkup. *Experimental methods: an introduction to the analysis and presentation of data*. Wiley, 1994. ISBN: 0471335797.

[28] S. Chapra. *Applied Numerical Methods with MATLAB for Engineers and Scientists*. McGraw-Hill, 2012. ISBN: 9780073401102.

Appendix A Detailed Test Piece Drawings

A.1 LBST Test Pieces

The LBST 30° wedge model drawings consist of the following:

- A complete assembly of the wedge: Figure A.1
- An assembly of the rear support arm: Figure A.2
- The wedge channel: Figure A.3
- The wedge attachment foot: Figure A.4
- The wedge corner attachment foot: Figure A.5
- The wedge channel attachment foot: Figure A.6
- The wedge rear support bar: Figure A.7

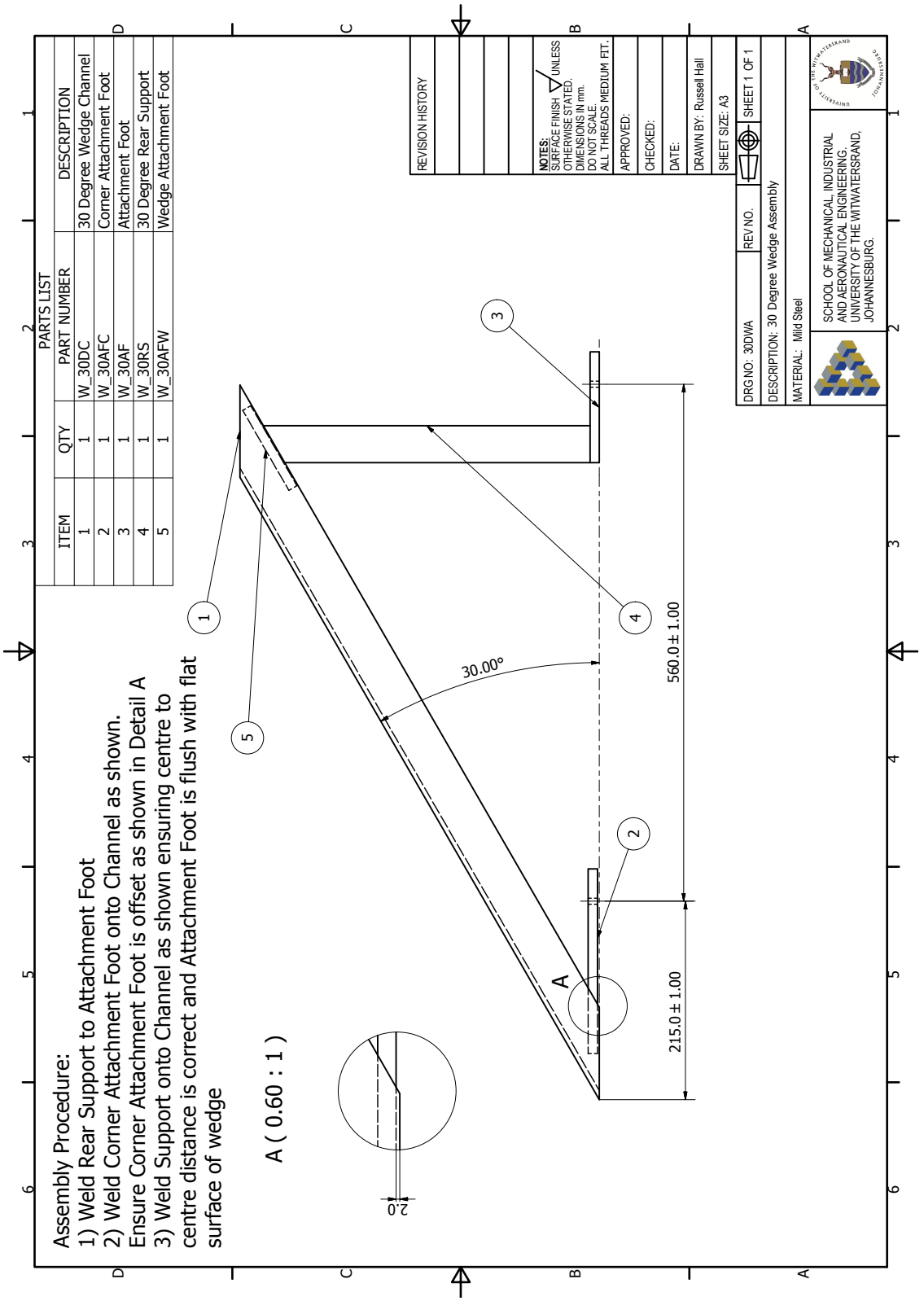


Figure A.1: 30° Wedge Assembly

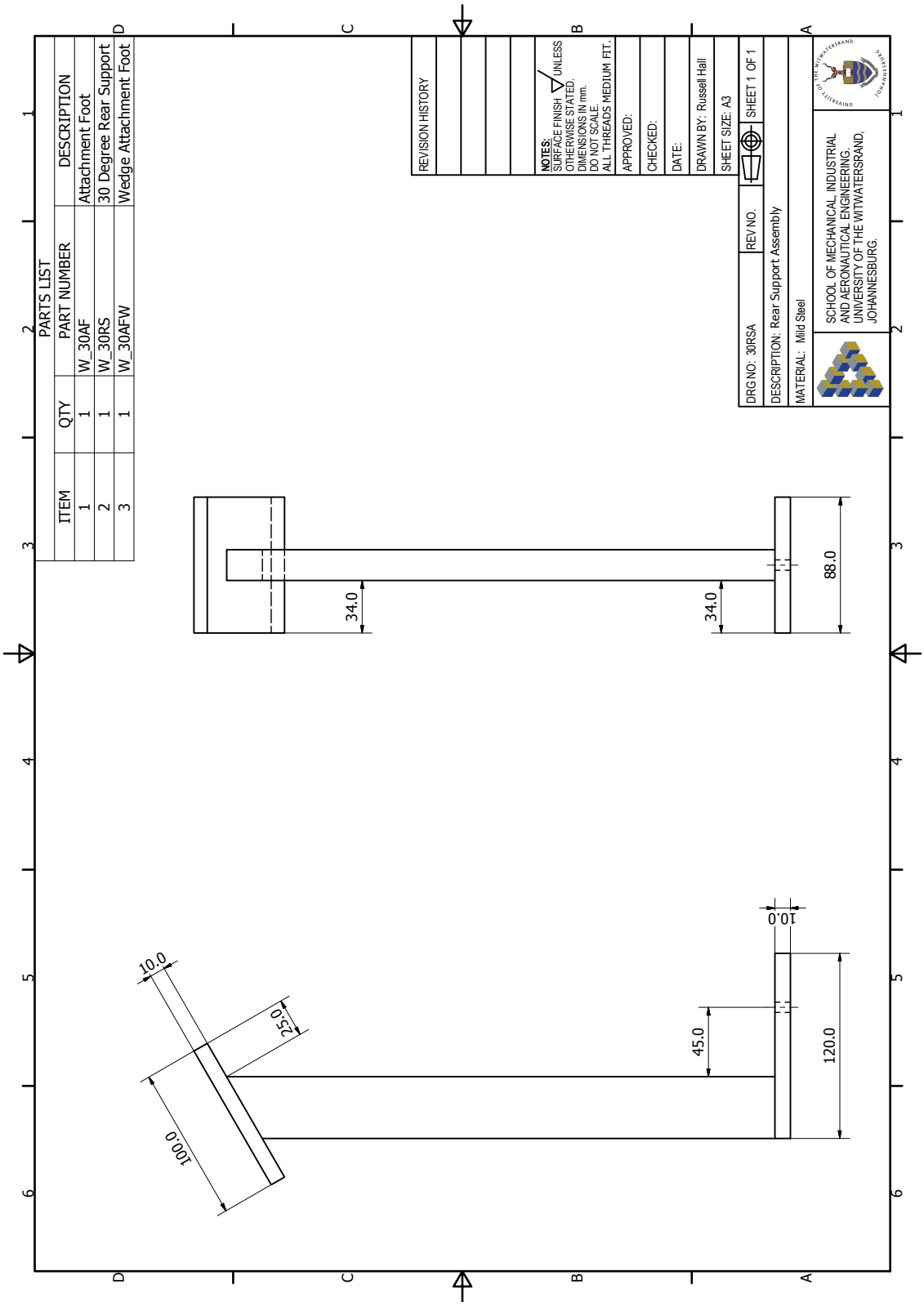


Figure A.2: 30° Wedge Rear Support Assembly

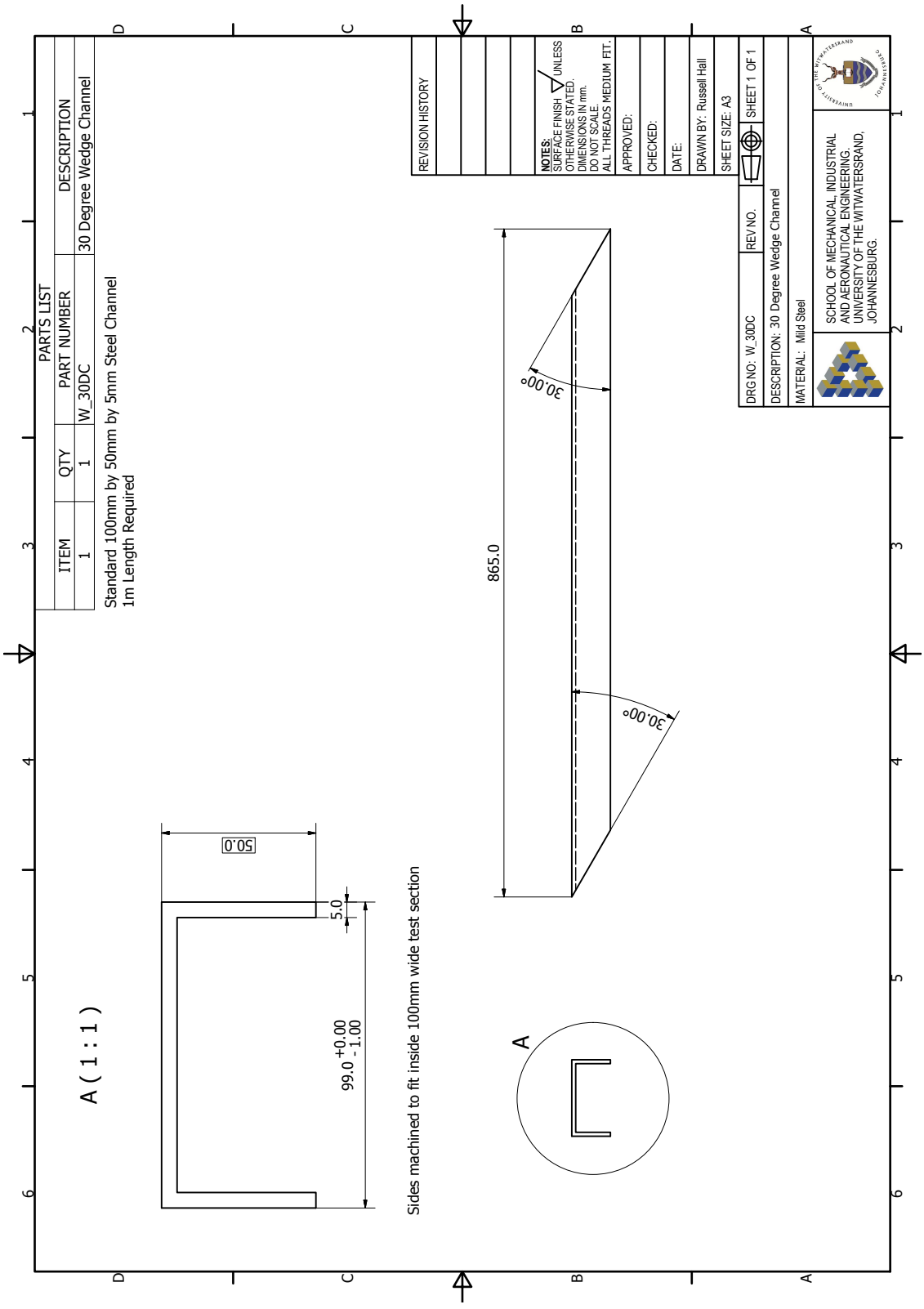


Figure A.3: 30° Wedge Channel

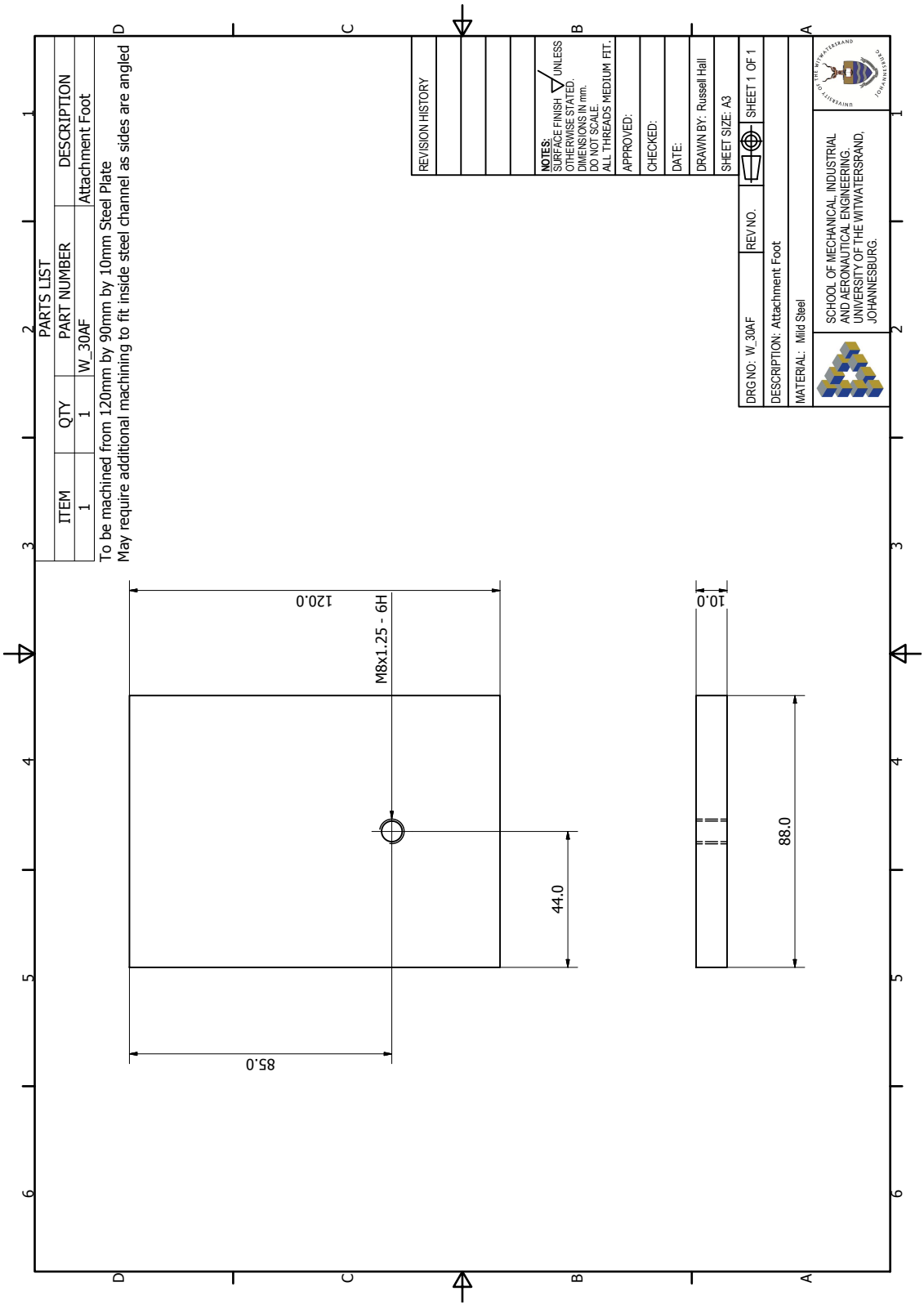


Figure A.4: 30° Wedge Attachment Foot

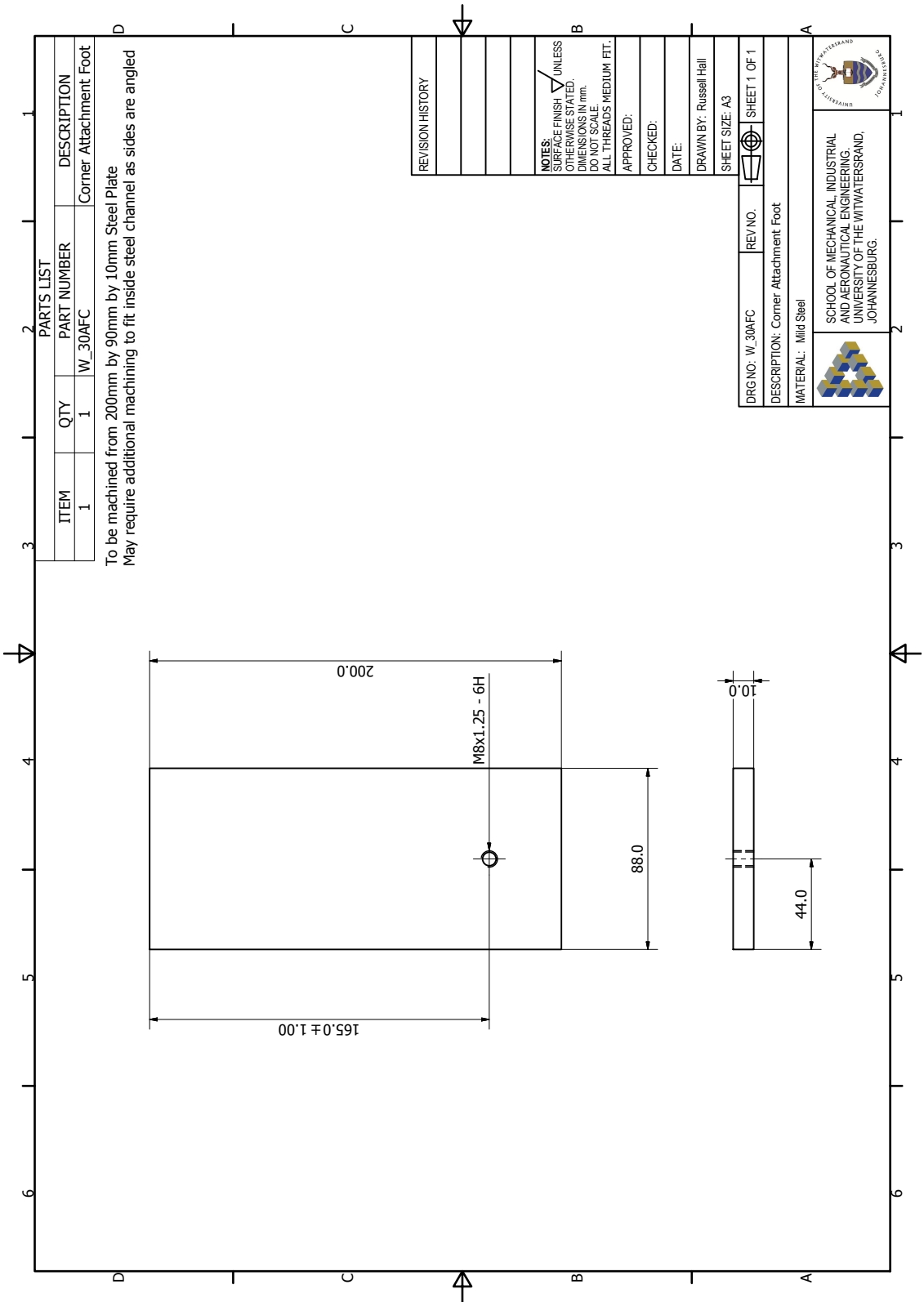


Figure A.5: 30° Wedge Corner Attachment Foot

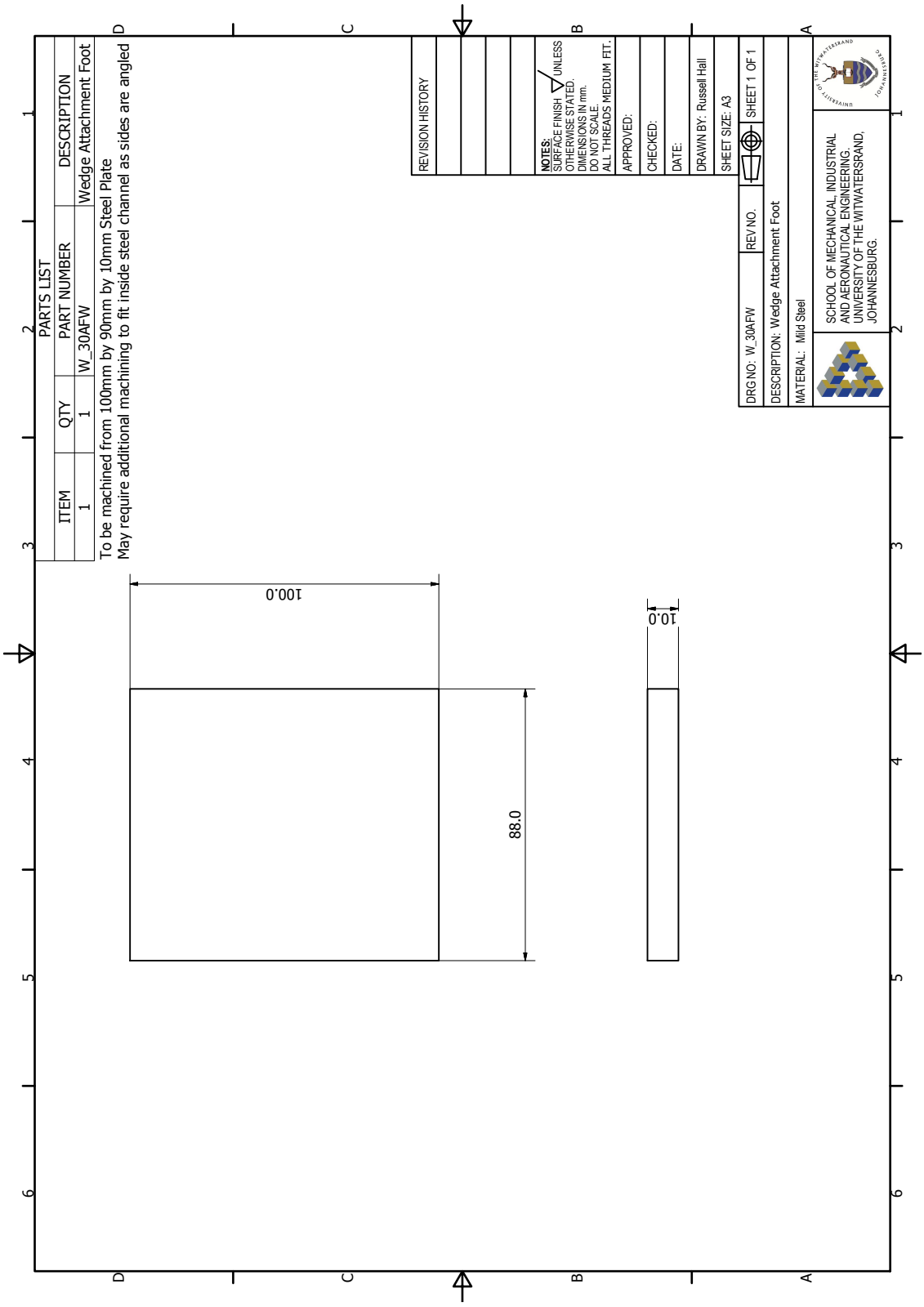


Figure A.6: 30° Wedge Channel Attachment Foot

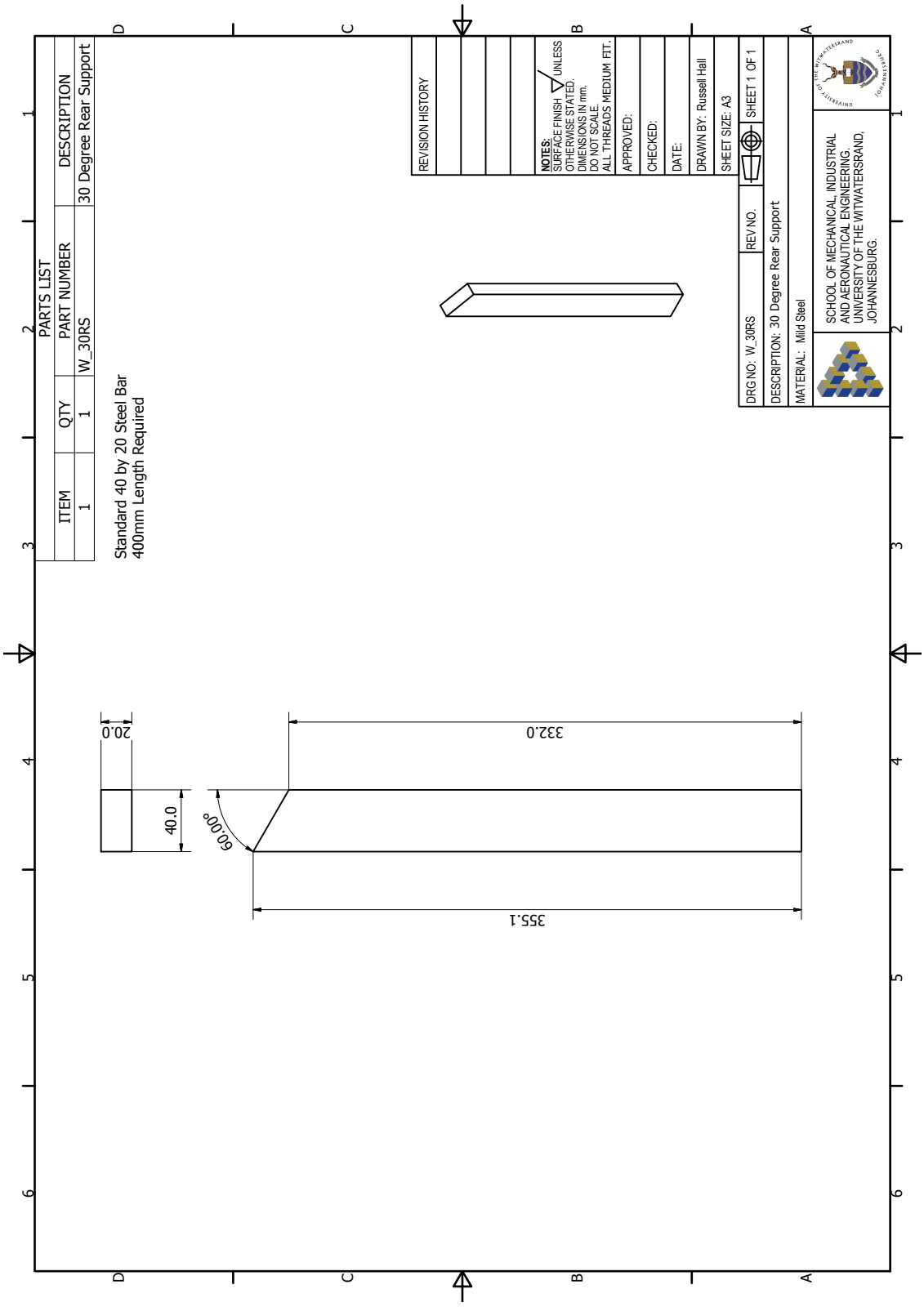


Figure A.7: 30° Wedge Rear Support

A.2 MSAST Test Pieces

The MSAST $25°, 30°$ and $35°$ wedge model drawings consist of the following:

- The $25°$ wedge model: Figure A.8
- The $25°$ wedge CNC path: Figure A.9
- The $25°$ wedge mounting holes: Figure A.10
- The existing $30°$ wedge modification: Figure A.11
- The existing $30°$ wedge modification side view: Figure A.12
- The $35°$ wedge model: Figure A.13
- The $35°$ wedge CNC path: Figure A.14
- The $35°$ wedge mounting holes: Figure A.15
- The $25°$ and $35°$ wedge spacer: Figure A.16

The $38°$ wedge was previously used by Rubidge and Skews[13] and consists of the following:

- The $38°$ wedge model: Figure A.17
- The $38°$ wedge spacer: Figure A.18

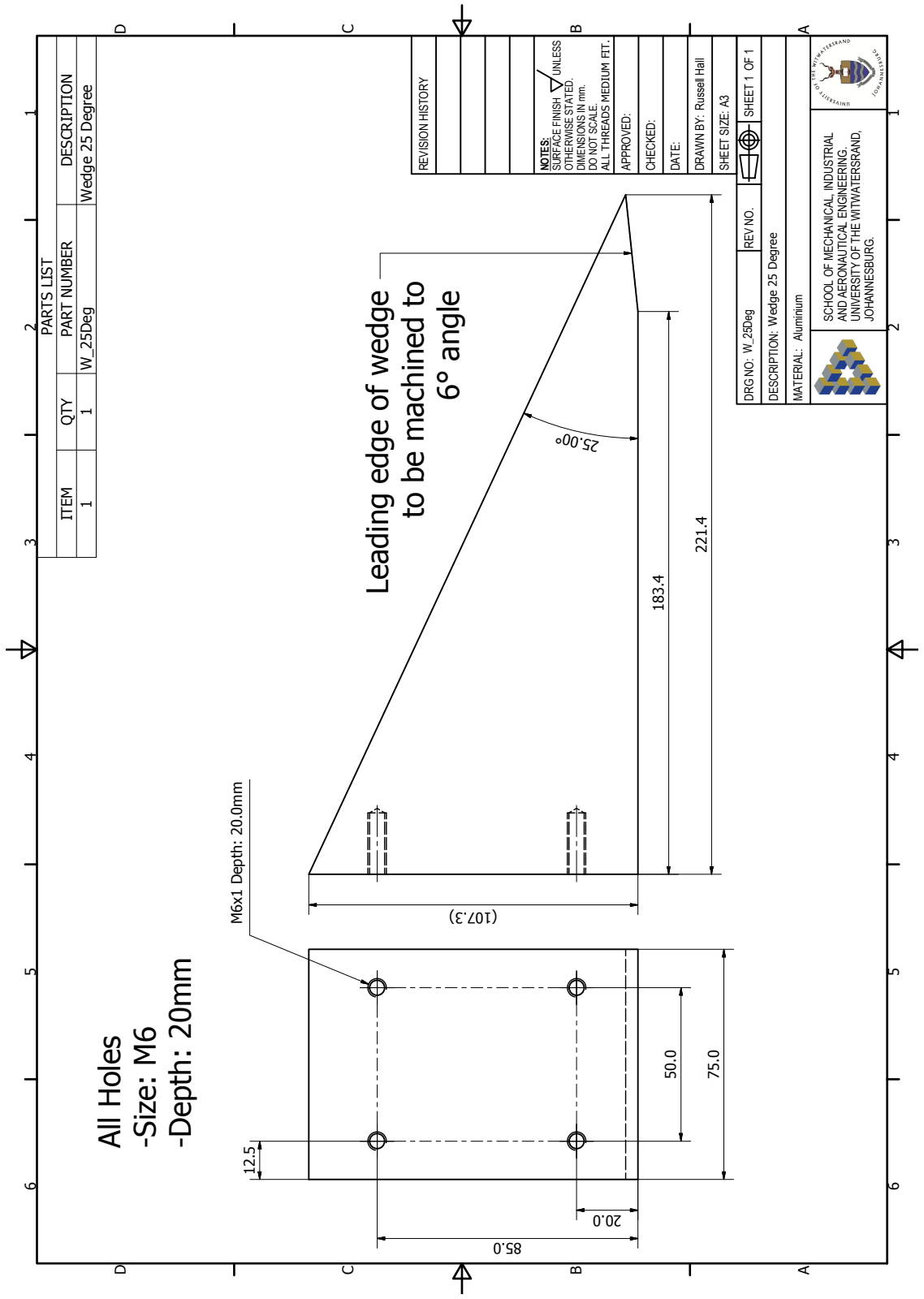


Figure A.8: 25° Wedge Model

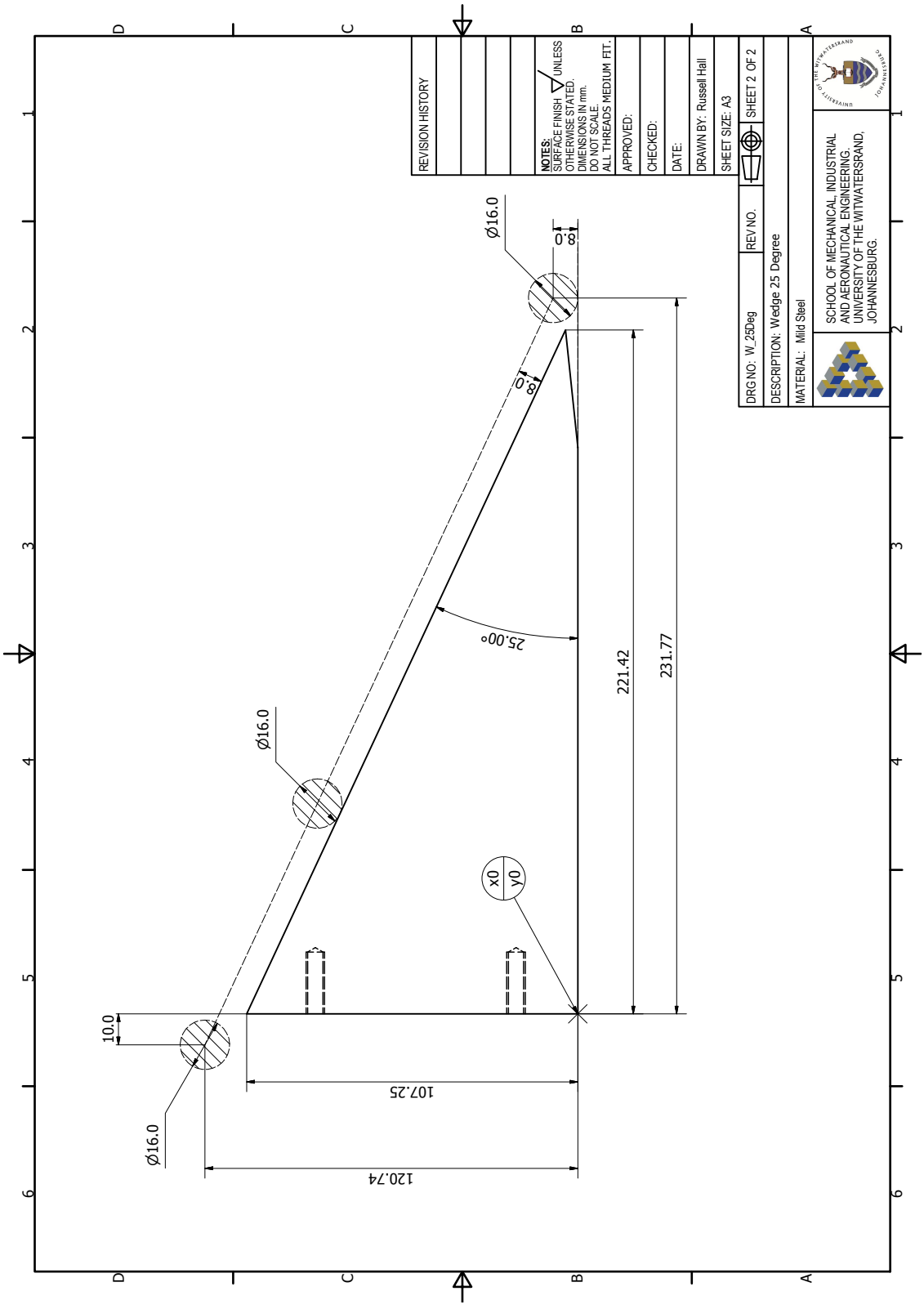


Figure A.9: 25° Wedge Model CNC Path

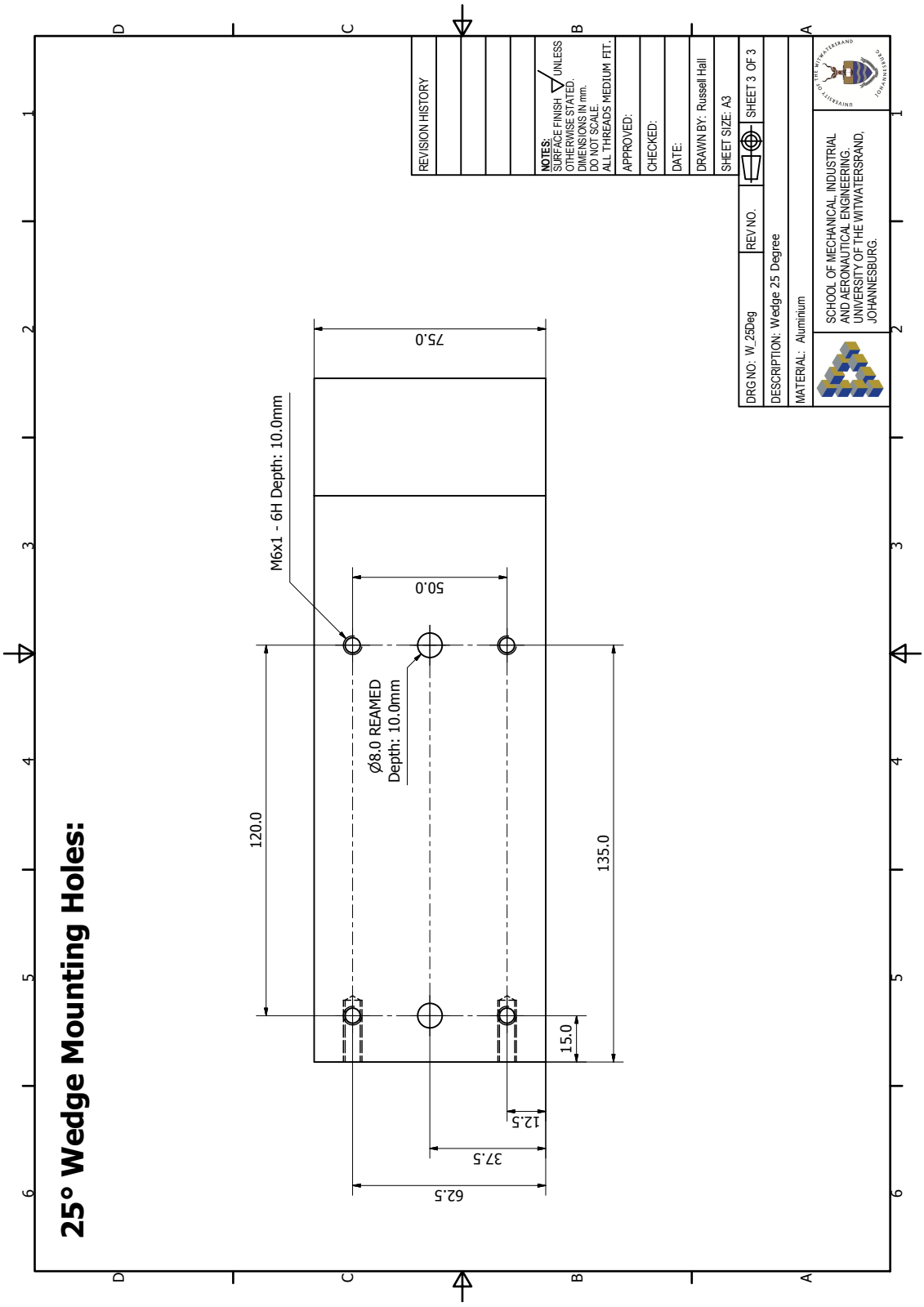


Figure A.10: 25° Wedge Model Mounting Holes

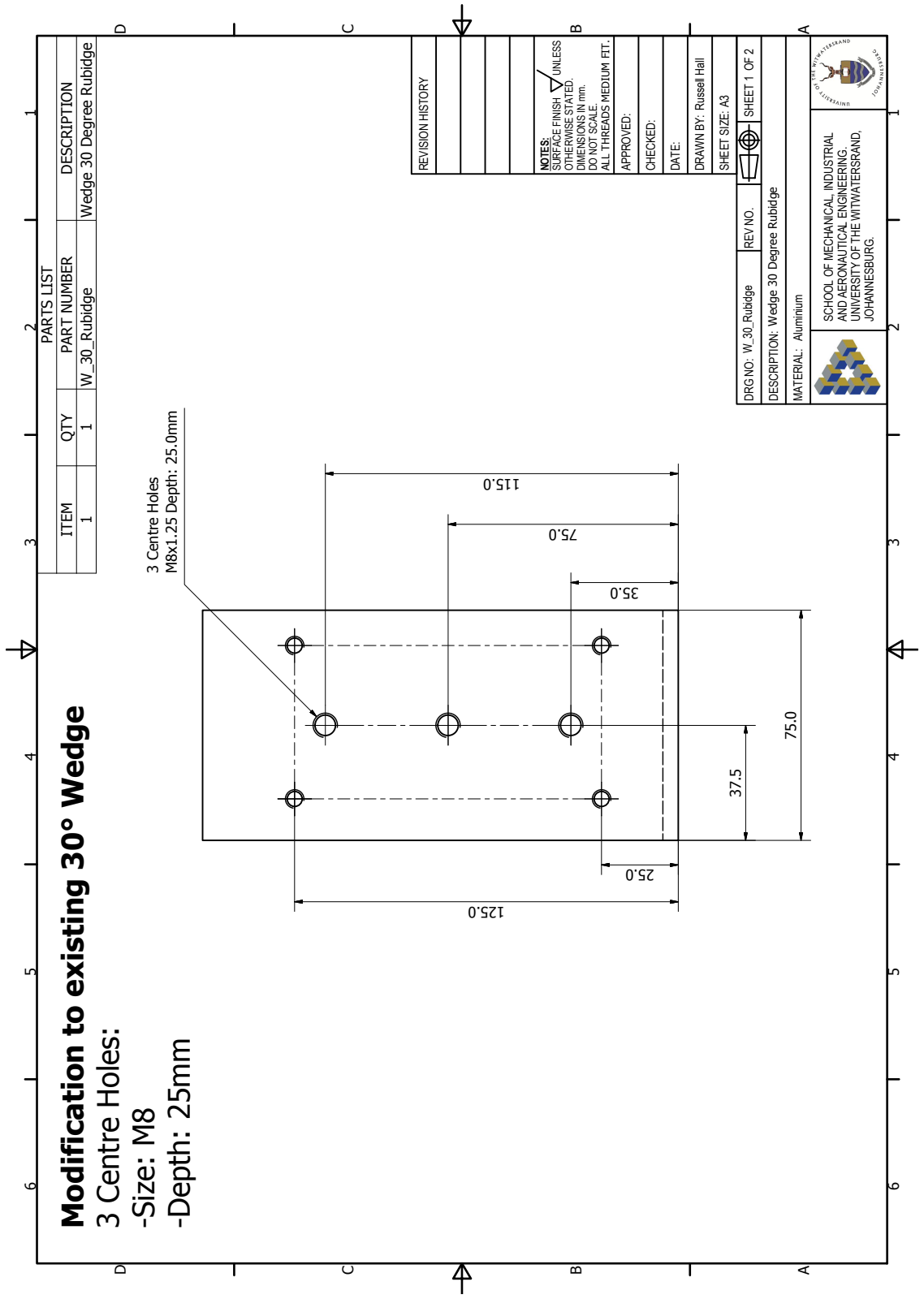


Figure A.11: 30° Wedge Model Modification

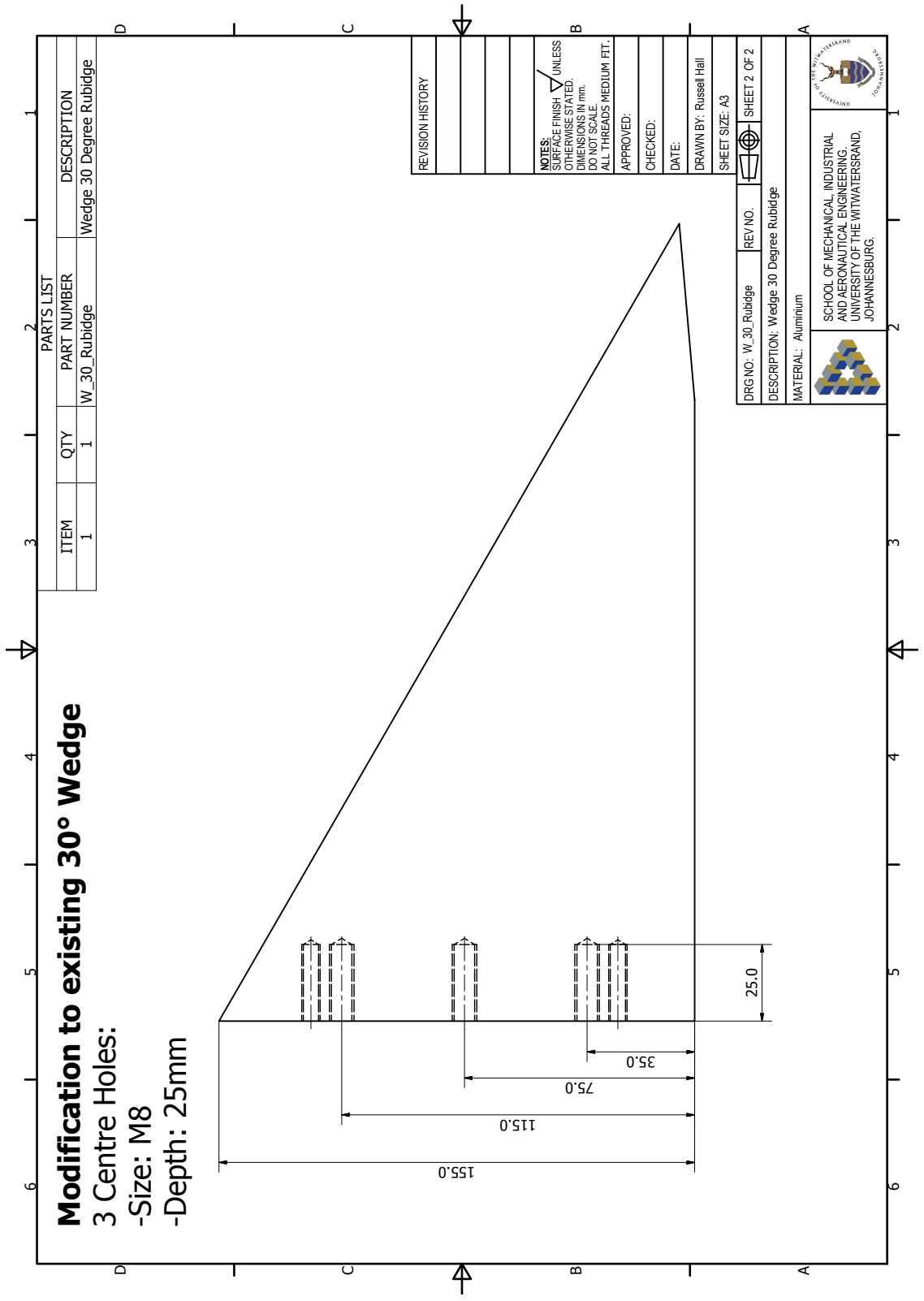


Figure A.12: 30° Wedge Model Modification Side View

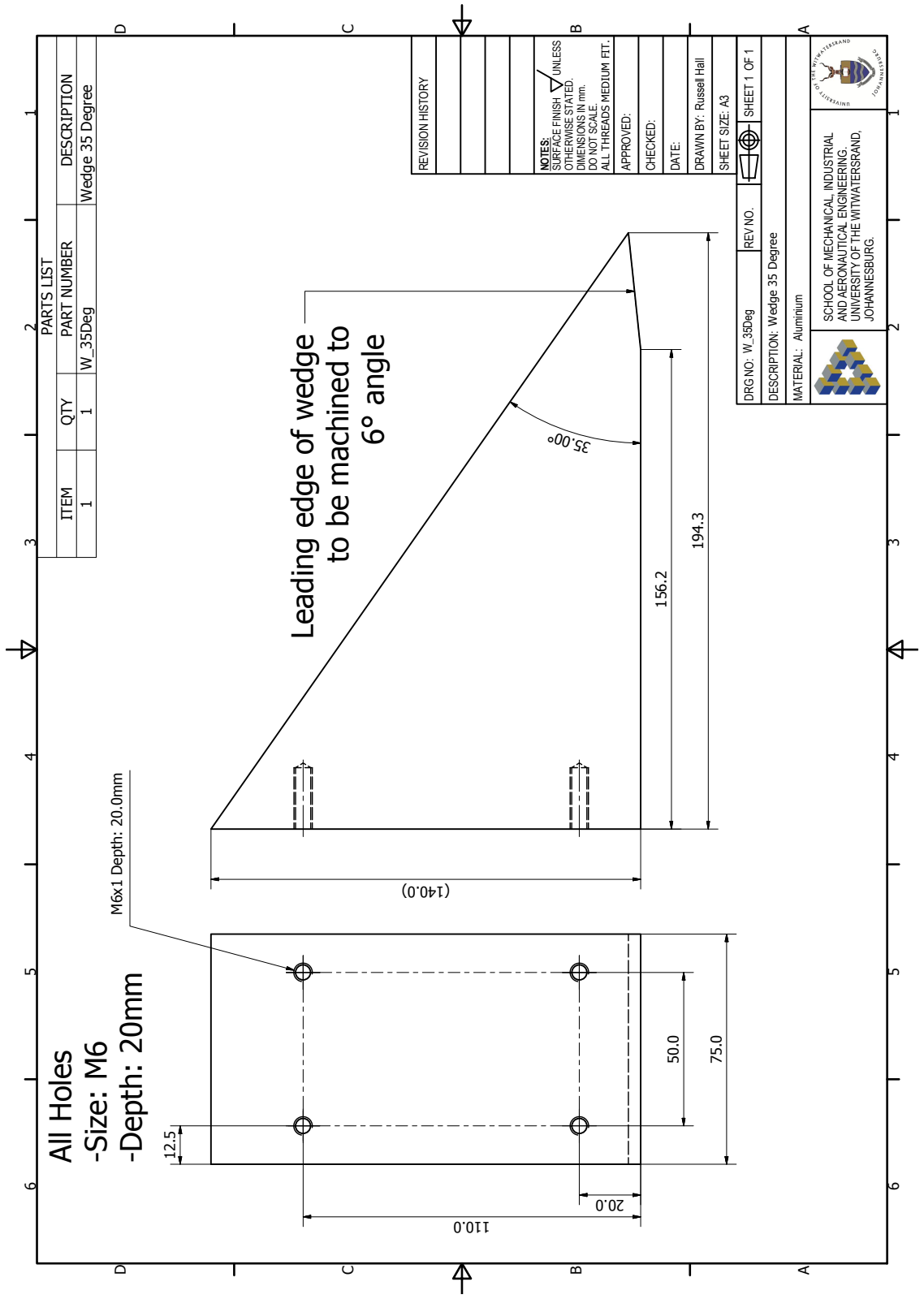


Figure A.13: 35° Wedge Model

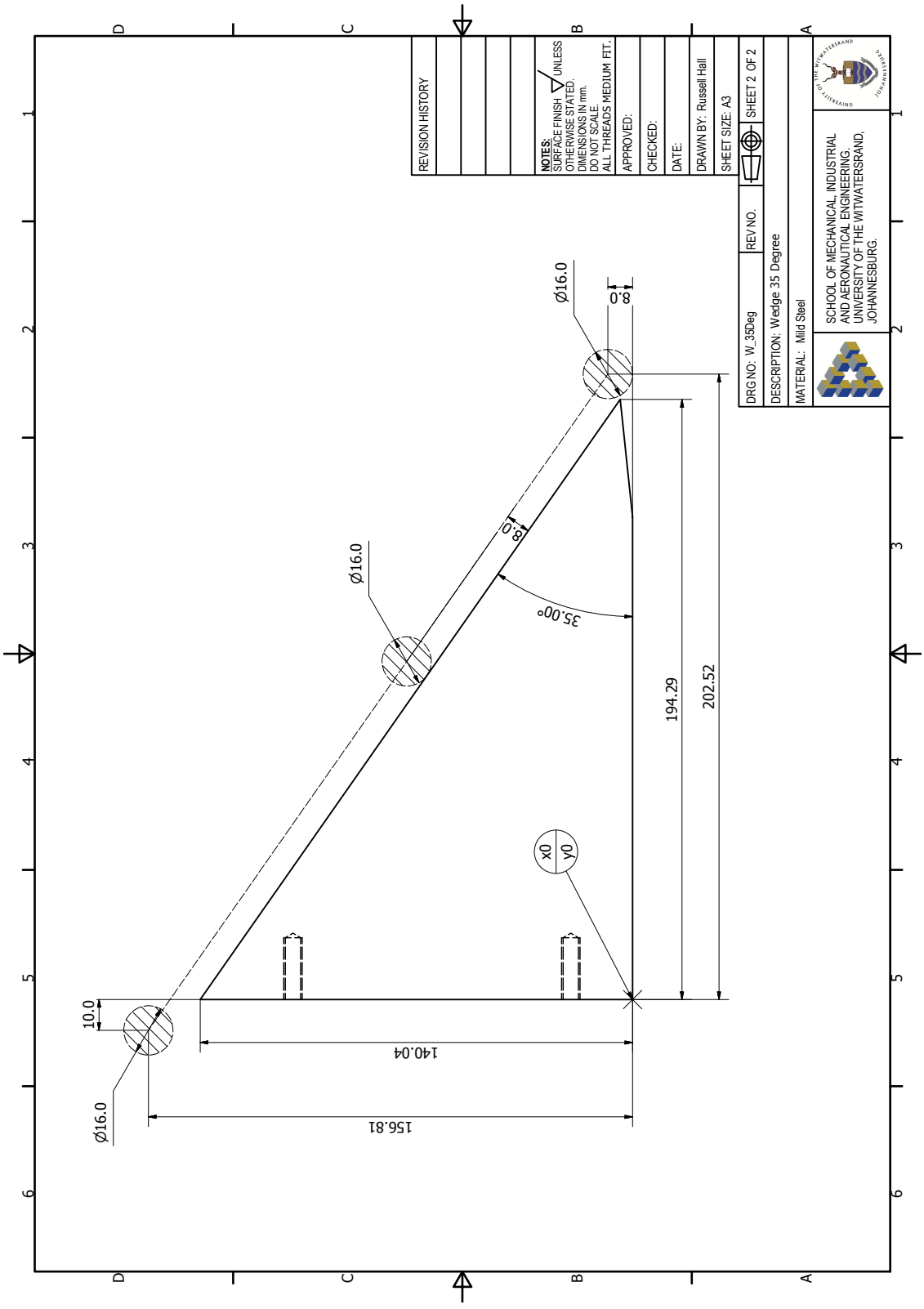


Figure A.14: 35° Wedge Model CNC Path

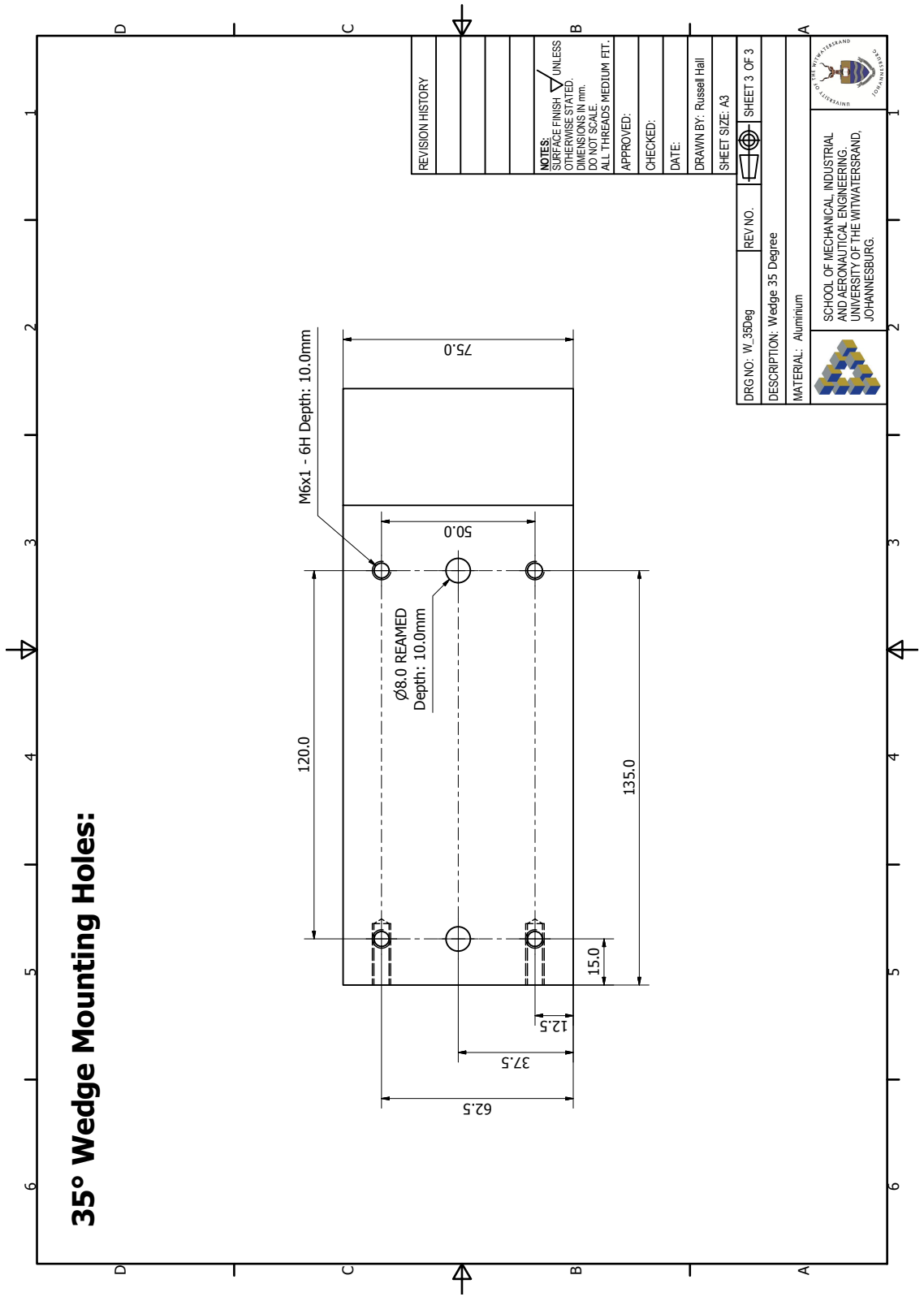


Figure A.15: 35° Wedge Model Mounting Holes

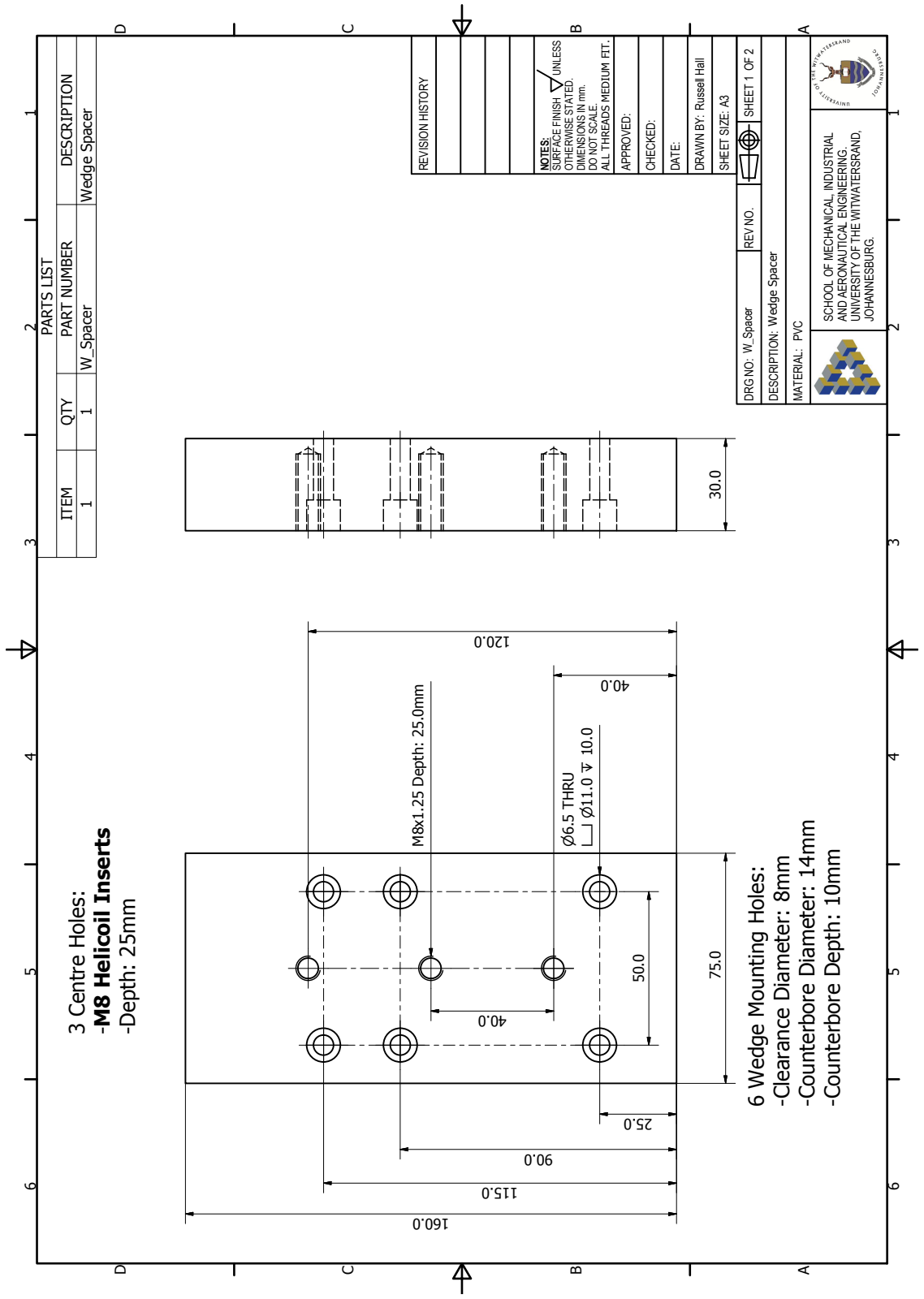


Figure A.16: The 25° and 35° Wedge Spacer

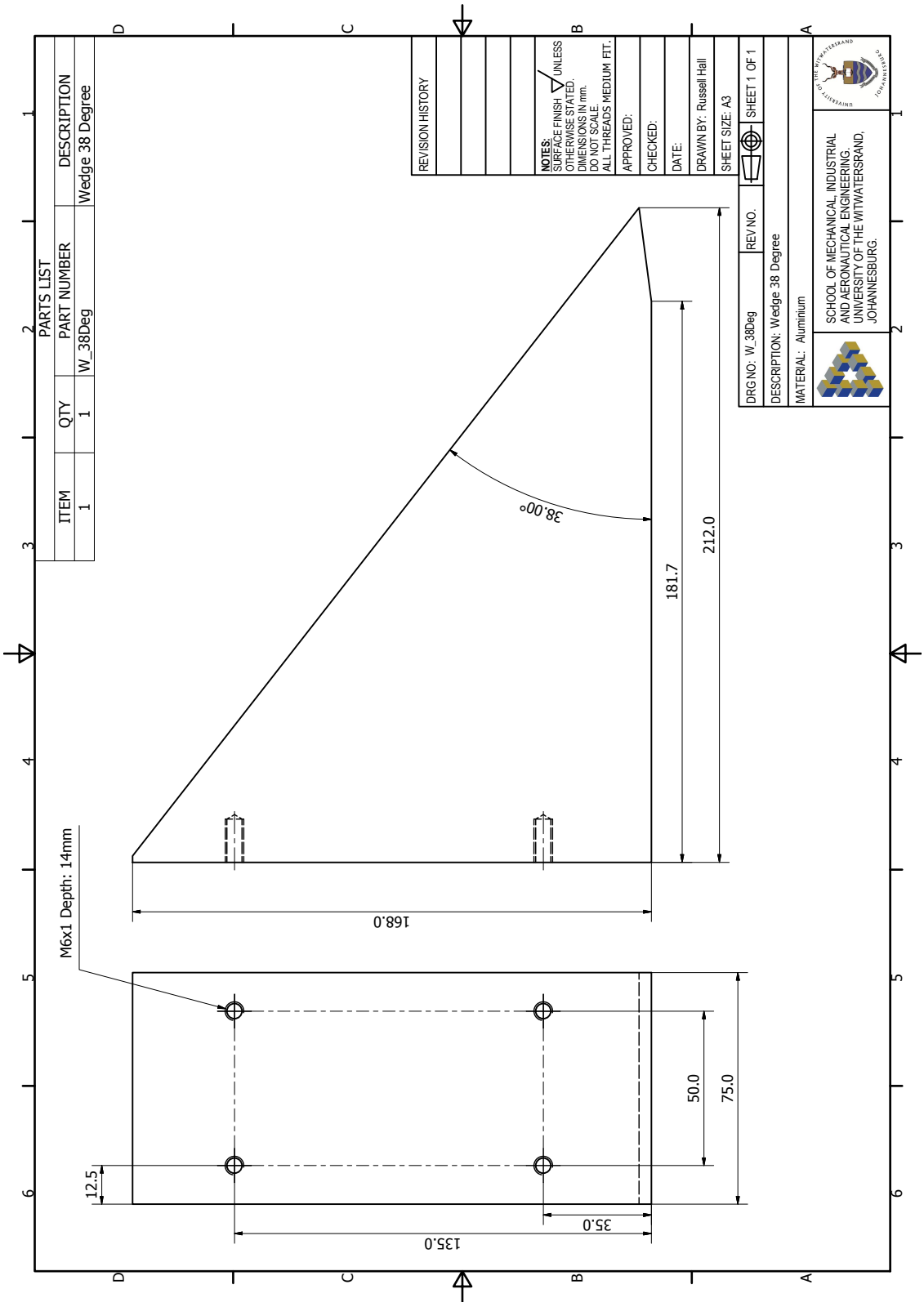


Figure A.17: 38° Wedge Model

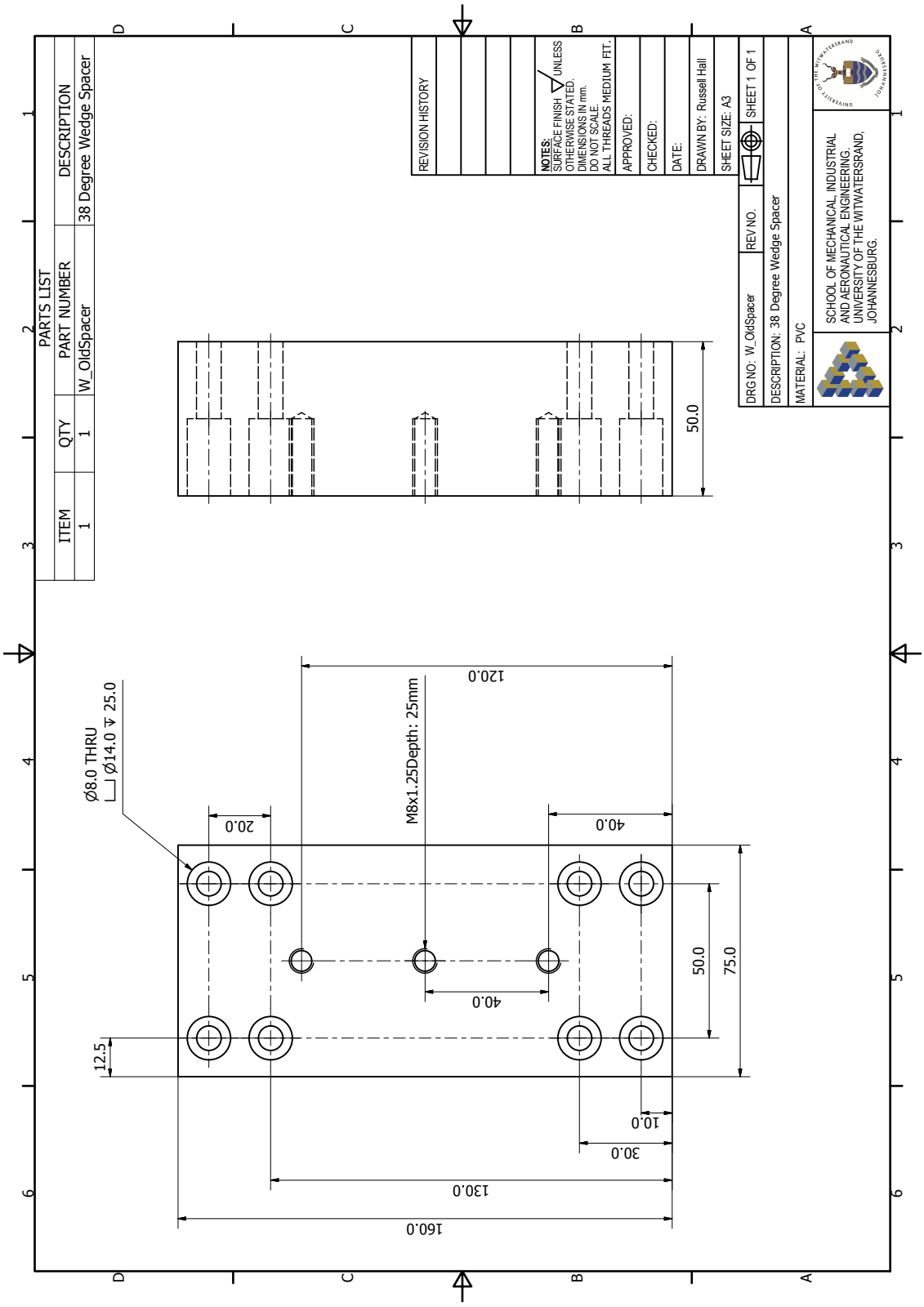
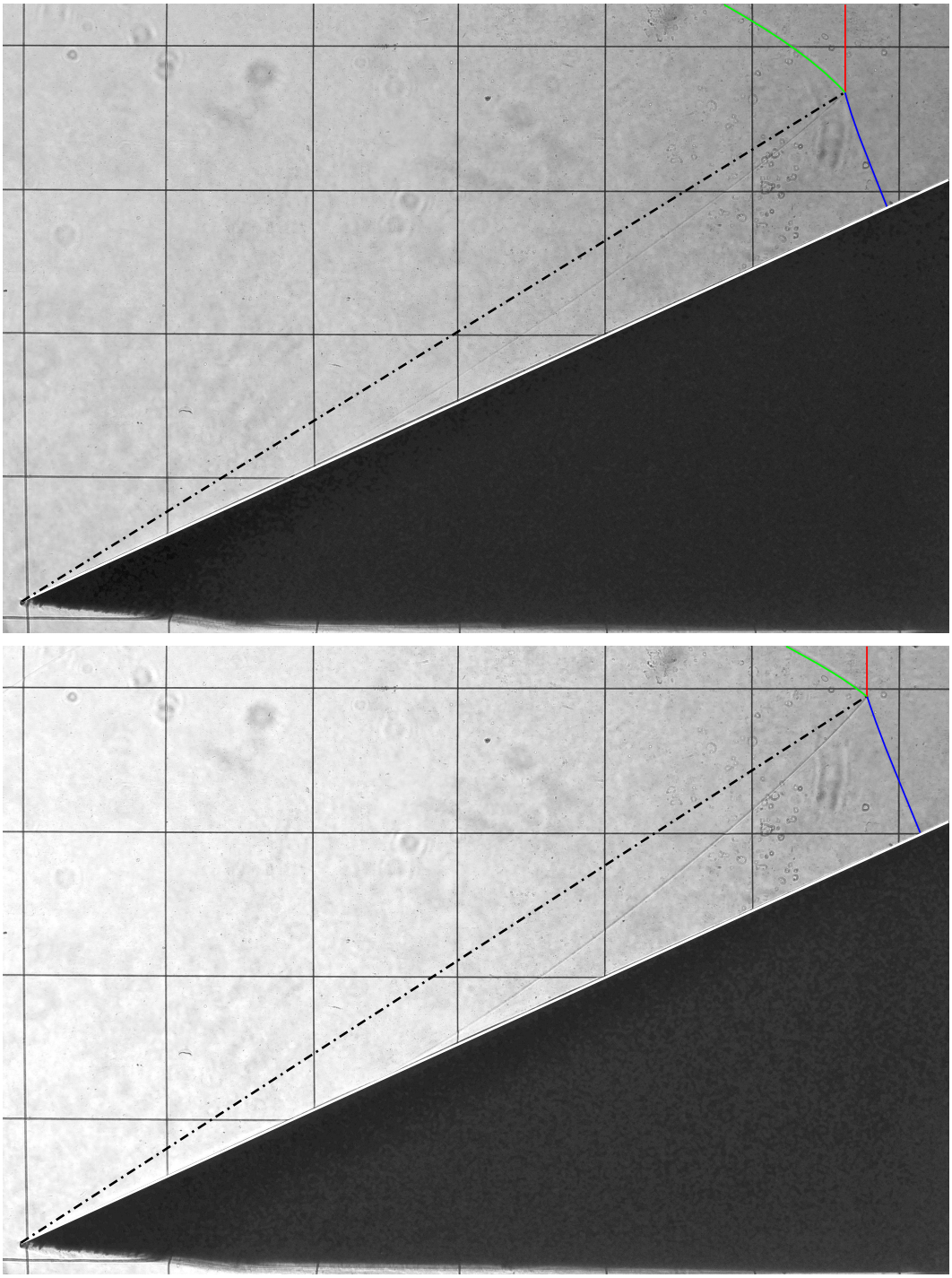


Figure A.18: The 38° Wedge Spacer

Appendix B MSAST Experimental Images

The following pages provide the annotated experimental images for the $M_s \approx 1.30$ and $M_s \approx 1.44$ results:

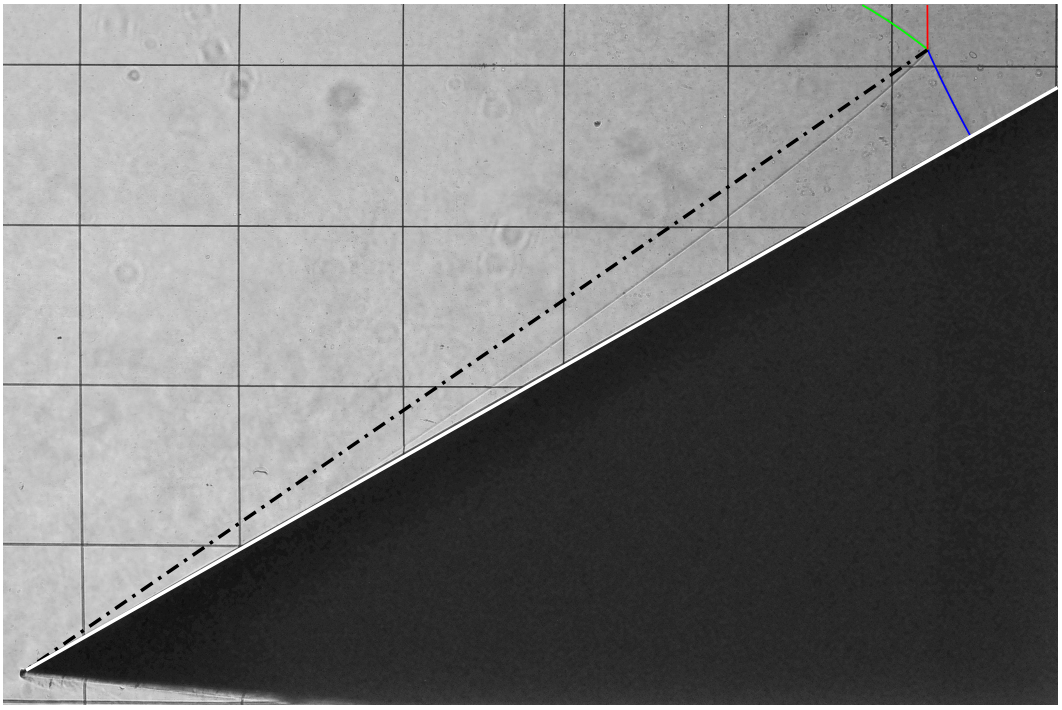
- 25° Wedge: Figure B.1
- 30° Wedge: Figure B.2
- 35° Wedge: Figure B.3
- 38° Wedge: Figure B.4



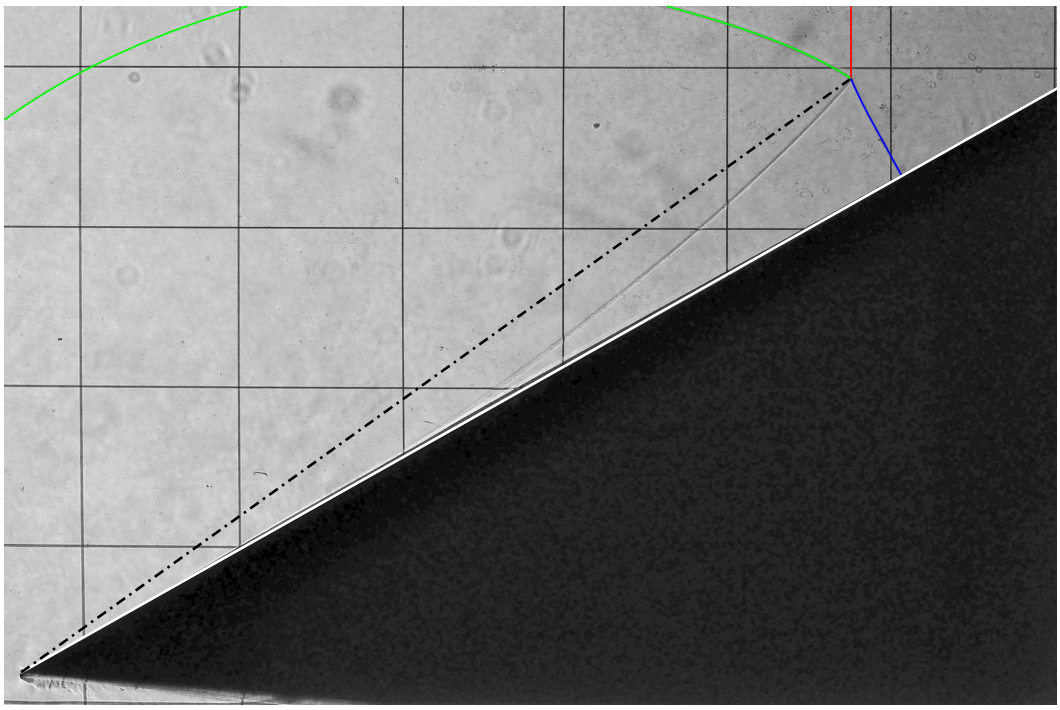
(a)

(b)

Figure B.1: Single Mach Reflection with highlighted features for the $\theta_w = 25°$ wedge (Incident Shock, Reflected Shock, Mach Stem, Triple Point Trajectory - Black, Wedge Surface - White): (a) $M_s = 1.309$, Time Delay: $1925\mu s$ (b) $M_s = 1.447$, Time Delay: $1750\mu s$

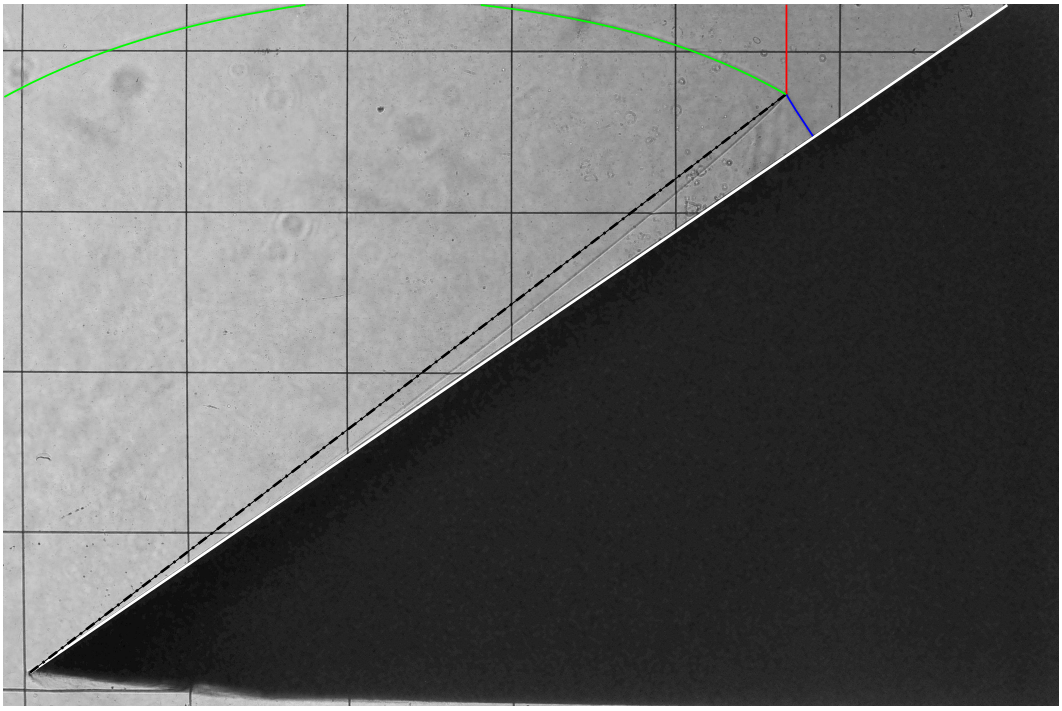


(a)

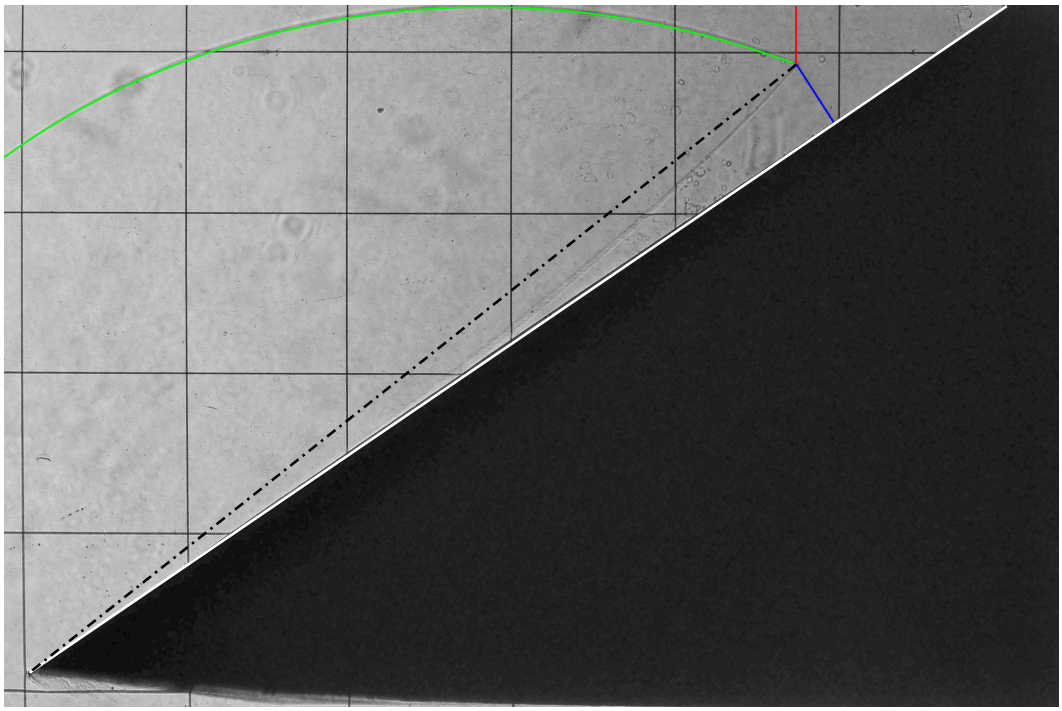


(b)

Figure B.2: Single Mach Reflection with highlighted features for the $\theta_w = 30°$ wedge (Incident Shock, Reflected Shock, Mach Stem, Triple Point Trajectory - Black, Wedge Surface - White): (a) $M_s = 1.309$, Time Delay: $1900\mu s$ (b) $M_s = 1.441$, Time Delay: $1700\mu s$

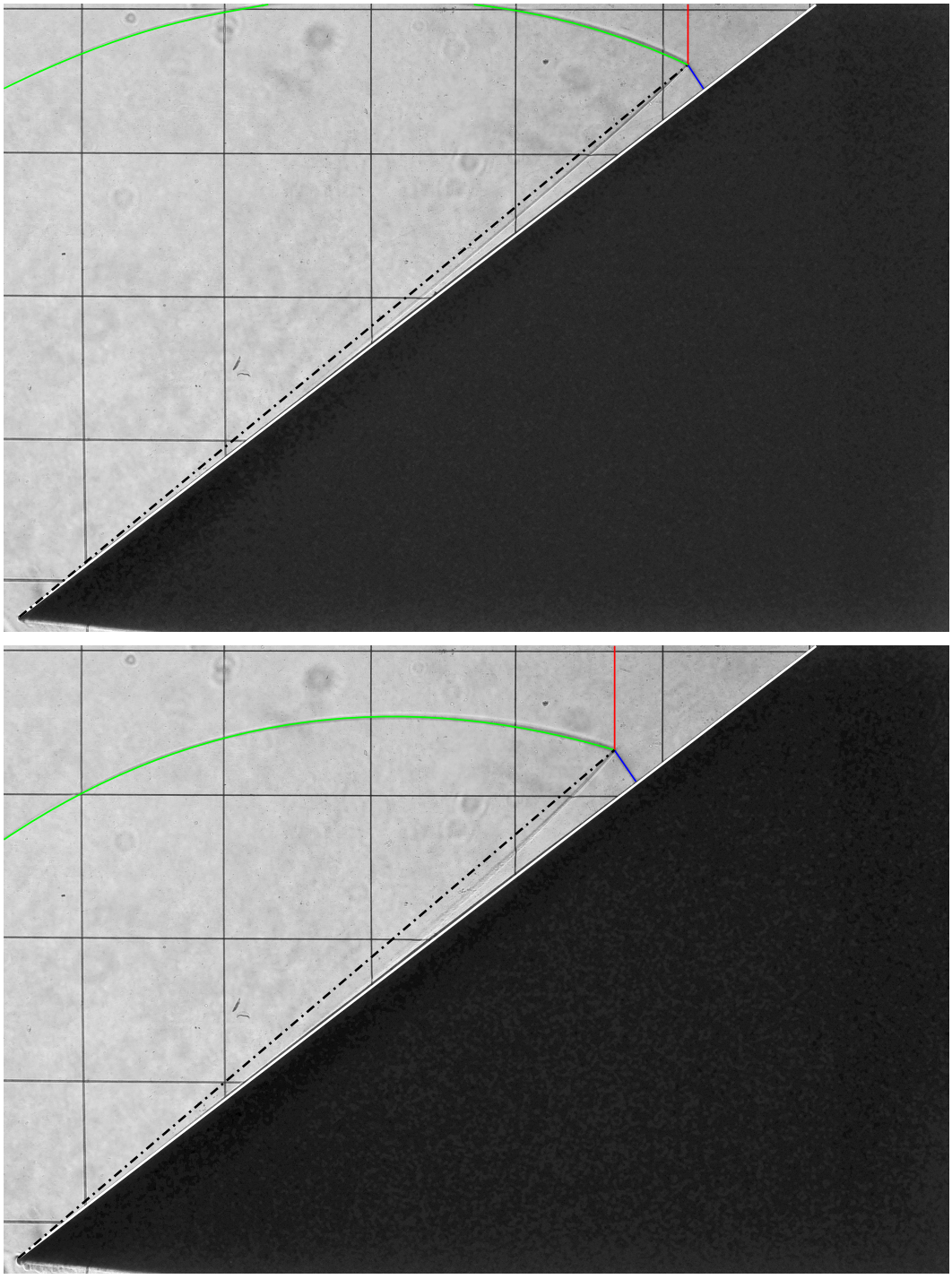


(a)



(b)

Figure B.3: Single Mach Reflection with highlighted features for the $\theta_w = 35°$ wedge (Incident Shock, Reflected Shock, Mach Stem, Triple Point Trajectory - Black, Wedge Surface - White): (a) $M_s = 1.313$, Time Delay: $1925\mu s$ (b) $M_s = 1.447$, Time Delay: $1750\mu s$



(a)

(b)

Figure B.4: Single Mach Reflection with highlighted features for the $\theta_w = 38°$ wedge (Incident Shock, Reflected Shock, Mach Stem, Triple Point Trajectory - Black, Wedge Surface - White): (a) $M_s = 1.304$, Time Delay: $1850\mu s$ (b) $M_s = 1.442$, Time Delay: $1650\mu s$

Appendix C Supplementary Three Shock Theory Results

The following pages provide additional Three Shock Theory results for $M_s \approx 1.44$ and $M_s \approx 1.585$ cases:

- Triple Point Trajectory vs Complimentary Wall Angle $M_s = 1.44$: Figure C.1
- Triple Point Trajectory vs Complimentary Wall Angle $M_s = 1.585$: Figure C.2
- Flow Mach number vs Complimentary Wall Angle $M_s = 1.44$: Figure C.3
- Flow Mach number vs Complimentary Wall Angle $M_s = 1.585$: Figure C.4
- Shock Angle vs Complimentary Wall Angle $M_s = 1.44$: Figure C.5
- Shock Angle vs Complimentary Wall Angle $M_s = 1.585$: Figure C.6

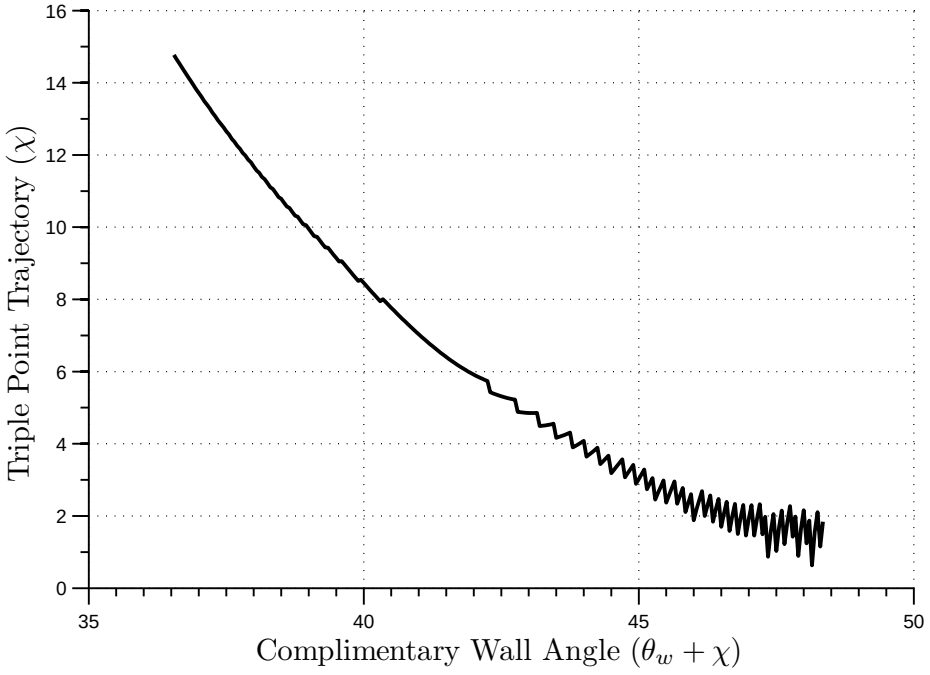


Figure C.1: Triple Point Trajectory (χ) vs Complimentary Wall Angle ($\theta_w + \chi$) for $M_s = 1.44$

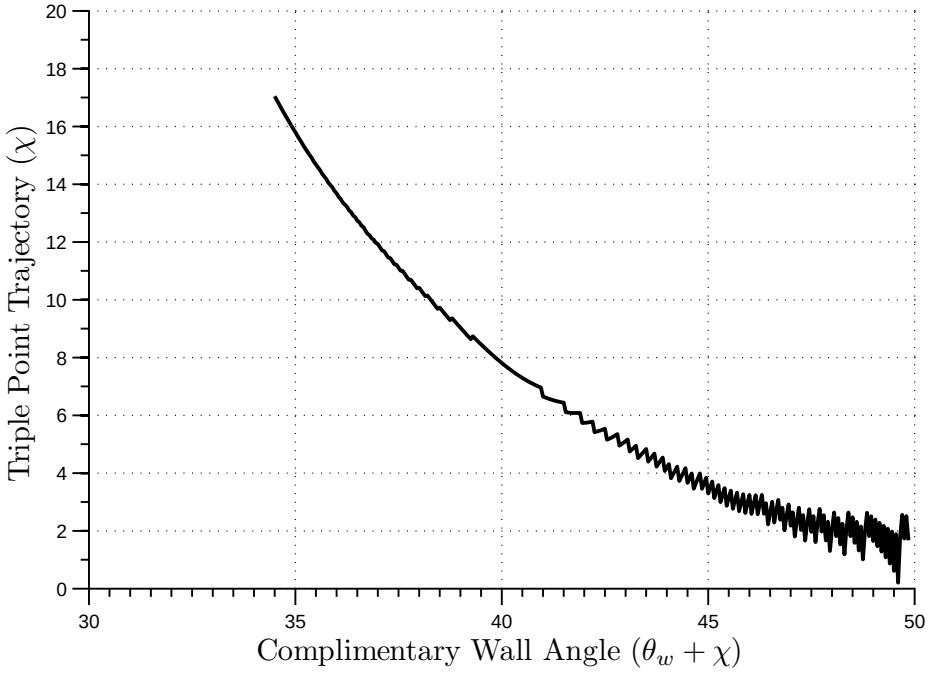


Figure C.2: Triple Point Trajectory (χ) vs Complimentary Wall Angle ($\theta_w + \chi$) for $M_s = 1.585$

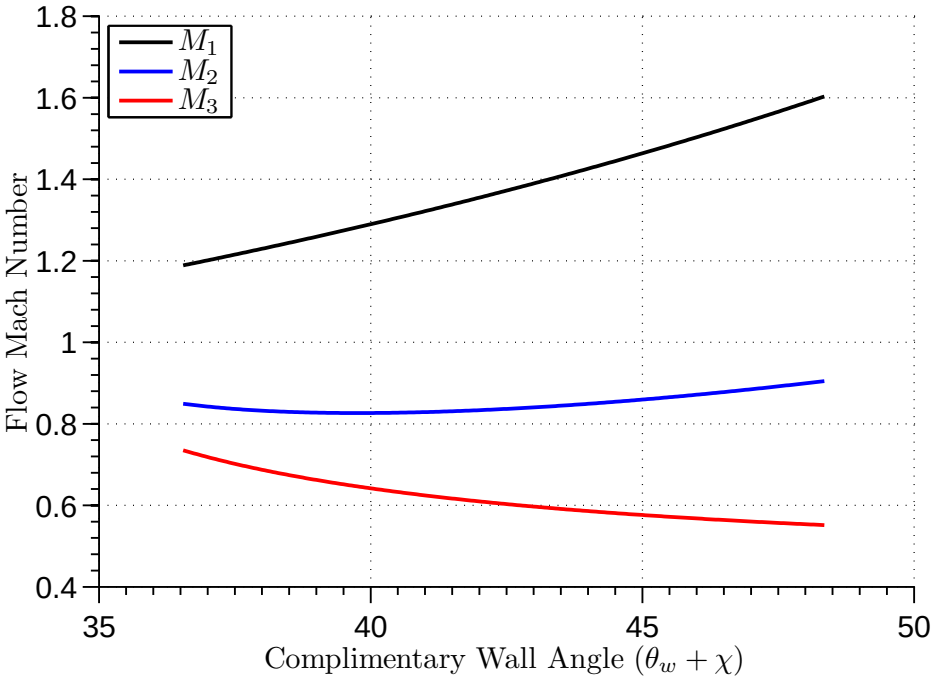


Figure C.3: Flow Mach Number vs Complimentary Wall Angle ($\theta_w + \chi$) for $M_s = 1.44$

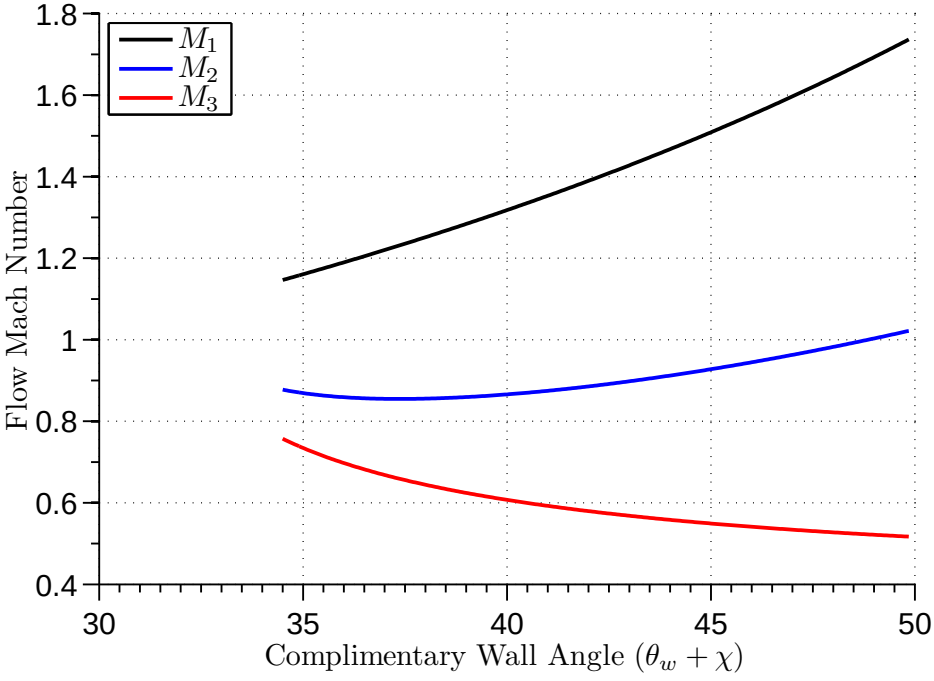


Figure C.4: Flow Mach Number vs Complimentary Wall Angle ($\theta_w + \chi$) for $M_s = 1.585$

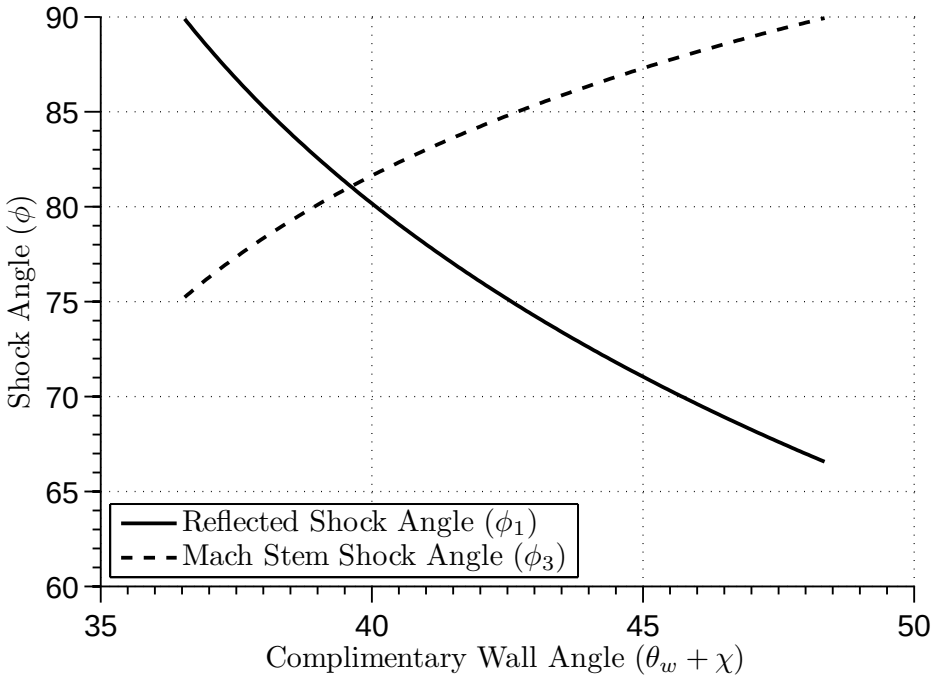


Figure C.5: Shock Angle (ϕ) vs Complimentary Wall Angle ($\theta_w + \chi$) for $M_s = 1.44$

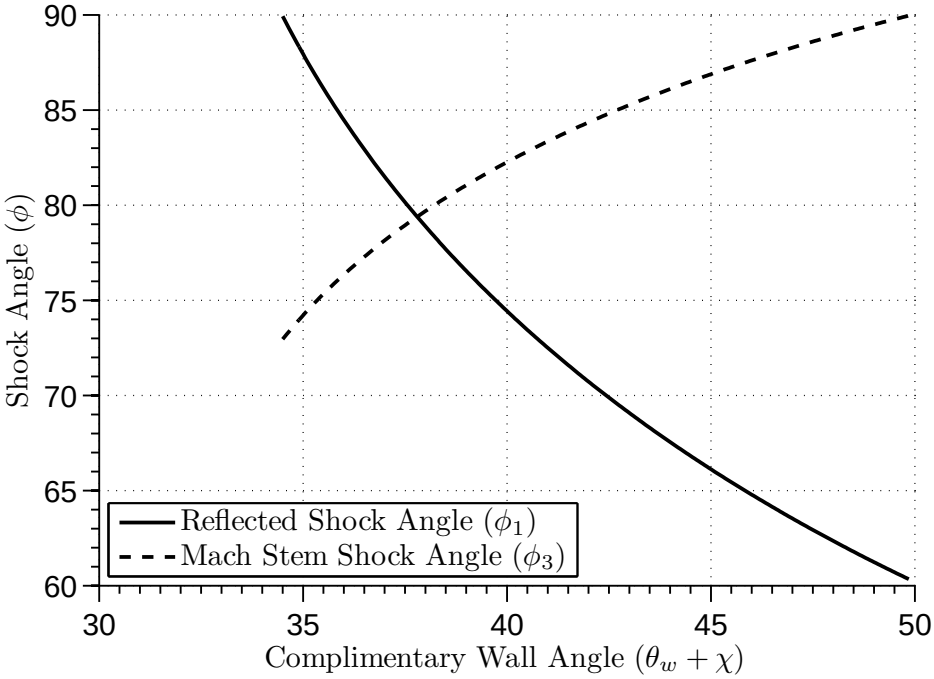


Figure C.6: Shock Angle (ϕ) vs Complimentary Wall Angle ($\theta_w + \chi$) for $M_s = 1.585$

Appendix D Digital Appendix

The Digital Appendix consists of the following sections:

- D.1: The preliminary CFD results using the LBST geometry
- D.2: Experimental Images from the LBST and MSAST
- D.3: Three Shock Theory MATLAB Code
- D.4: Shear Layer MATLAB Code
- D.5: Engineering Drawings of Test Pieces
- D.5: Shock Angle Measurement CAD Files and Excel Sheets